Teleseismic Transmission and Reflection Tomography

by

Scott A. Burdick

B.S., Purdue University (2006)

Submitted to the Department of Earth, Atmospheric, and Planetary Science
in partial fulfillment of the requirements for the degree of

Doctor of Philosophy in Geophysics

at the

MASSACHUSETTS INSTITUTE OF TECHNOLOGY

February 2014

Author ....
Department of Earth, Atmospheric, and Planetary Science
January 8, 2014

Certified by ... .
Robert D. van der Hilst
Schlumberger Professor of Earth and Planetary Sciences
Thesis Supervisor

Accepted by..... ....
Robert D. van der Hilst
Schlumberger Professor of Earth and Planetary Sciences
Head, Department of Earth, Atmospheric and Planetary Sciences

Teleseismic Transmission and Reflection Tomography

by

Scott A. Burdick

Submitted to the Department of Earth, Atmospheric, and Planetary Science
on January 8, 2014, in partial fulfillment of the
requirements for the degree of
Doctor of Philosophy in Geophysics

Abstract

The aim of seismic tomography is to determine a model of Earth properties that best explain observed seismic data. In practice, the limitations placed on our observations and computational capabilities force us to make a number of decisions about the scales and parameterizations of models, the nature of the data considered, and the approximations to wave propagation that connect the two.

This thesis will consider three divergent approaches to seismic tomography spanning different representations of Earth structure at different scales, using different parts of the teleseismic wavefield, and solving the inverse problem with different approximations to the wave equation and different optimization methods. In choosing each of these approaches, we address two major decisions that influence the tomographic process: First, what relative value do we place on an less approximate treatment of wave physics versus the ability to incorporate as much information as possible in our inversion? Second, how can we use novel data to better constrain smooth seismic structure in regions that were previously unresolved?

The first project presents a global ray-theoretical *P*-wave model that encompasses millions of traveltime picks. In this inversion, the addition of data from the dense USArray Transportable Array to global catalog data allows us to image the structure of the Eastern United States with unprecedented resolution and make a robust evaluation of the spatial scales of the heterogeneity. The second project develops a finite frequency approach to turning wave transmission tomography using a computationally efficient one-way wave propagation on curvilinear coordinates. The use of overturning coordinate systems allows for the application of wave equation tomography to phases previously unused in other one-way schemes. The final project presents a novel approach to wave-equation teleseismic reflection tomography using free surface multiples. The use of these multiply reflected phases helps to localize heterogeneity in the model to within layers of Earth structure. This project spans the final two chapters and includes the theoretical developments and an inaugural application to *SsPmp* data from the Hi-CLIMB array in Tibet.

Thesis Supervisor: Robert D. van der Hilst
Title: Schlumberger Professor of Earth and Planetary Sciences

Acknowledgments

As a "long-tenured" graduate student, I have been aided by several generations of faculty, students, postdocs, and administrators. It startles me now to recall that I've been at MIT longer than half of my thesis committee. As such, any set of acknowledgments cannot be complete.

First I must thank my advisor, Rob van der Hilst. His ability to see far afield from his lofty vantage point into the future of seismology was never short of inspiring. After leaving a meeting with Rob, I always felt like I could step up and solve the world. I'm grateful to have had a chance to learn from a scientist of his stature. I also owe a great debt of gratitude to our constant collaborator Maarten de Hoop. Maarten's mathematical expertise and rigor helped breathe life into all of our concepts.

I thank the rest of my thesis committee, Sam Bowring, Alison Malcolm, and Germán Prieto. The fruitful conversations I have had with each of them helped me look up from the narrow corner of seismology I sometime tend to focus on and see how it fits into the broader picture of Earth science. I thank the members of my Generals committee, Stéphane Rondenay and Brad Hager, who helped mold my understanding of how scientific research is actually done in those somewhat rocky early years.

I would also like to thank my colleagues at the Array Network Facility at Scripps, particularly Luciana Astiz and Frank Vernon. Without their skillfulness at traveltime picking, my Ph.D. might have lasted 40 years or more.

I have been lucky to share data, codes, expertise, and office space with a series Rob's students. In particular, I have been pleased to work directly with Chang Li, Xuefeng Shang, Chunquan Yu, and Eva Golos. I have also been happy to work with members of our academic "extended family" in Maarten's group, especially Shen Wang, with whom I have worked on a number of projects.

One of the greatest things about working on a Ph.D. at MIT has been the opportunity to meet the next generation of brilliant, ground-breaking geoscientists and drink beer, watch football, and wreak general mischief with them. During my time at MIT, Nate Dixon, Christy Till, Mike Krawczynski, Noah McLean, Gabi Melo, Terry Blackburn, Jimmy Elsenbeck, Seth Burgess, Fred Pearce, Einat Lev, Junlun Li, and David Forney, among many others, have played major roles in my social and academic life. Here's hoping for a future of fruitful collaborations and many, many more beers.

In addition to the students, I want to acknowledge the Euro Postdoc Squad, with whom I have had many insightful and constructive discussions which occasionally touched on seismology. Thomas Gallot, Lizzie Day, Bérénice Froment, Dylan Mikesell (honorary), Piero Poli and early members Pierre Gouedard and Tim Seher have all made the department a really edifying place to spend my days.

In the last couple of years, racing with the MIT Cycling Team has been a tremendous source of energy and serenity. The sweetness and decency of my teammates has been as uplifting as it is confounding to my grizzled old heart. I'll always appreciate that the major breakthrough in the reflection tomography project came as I was cramming work hours in between rides at training camp. Furthermore, the wonderful folks on the cyclocross team have made me feel like waking up at 5 AM, driving to rural Rhode Island, smearing capsaicin ointment on my legs, and riding my bike into a mud puddle at near freezing temperatures is truly the sanest thing I have done during the course of my education.

A special thanks to Bradley E. G. Palmer, whose name now appears in an MIT thesis.

I never could have made it this far without the love and support of my most excellent family. I'm incredibly lucky to have a Mom and a Dad who nurtured my interests in science from the start. You started teaching me about the world the moment you brought me home from the hospital, you took me on regular trips to the library when I was a kid, you didn't think twice about sending me off to study physics in the far-away land of Indiana, and you didn't get too fussy when you found out that academics don't make a whole lot of money. Any success I have in life I owe largely to you. I appreciate my brother David and sister Laura for being there for me through this long and sometimes arduous process. They may not have nurtured my interests in science early on, but I really couldn't ask for a better couple of siblings.

Finally, I dedicate this thesis to my nephew Leonardo Vollink in the hope that he will always let his curiosity get the better of him.

Contents

3 One-way wave propagation for finite-frequency tomography on curvilinear coordinates 67

4 Reverse-time migration-based reflection tomography using teleseismic free surface multiples 97

List of Figures

Chapter 1

Introduction

Abstract

The aim of seismic tomography is to determine a model of the Earth's seismic properties that best explain observed data. In practice, the limitations placed on our observations and computational capabilities force us to make a number of decisions about the scales and parameterizations of models, the nature of the data considered, and the approximations of wave propagation that connect the two. In this thesis, I will consider three approaches to seismic tomography spanning different representations of Earth structure, using data from different parts of the teleseismic wavefield, and solving the inversion problem with different wave physics and different optimization methods. The first project will present a global adaptable grid *P*-wavespeed inversion using traveltime residuals. The second will present a finite frequency approach to turning-wave transmission tomography using one-way wave propagation on curvilinear coordinates. The final project will present a novel approach to teleseismic reflection tomography using free surface multiples and an application to 2-D array data from Tibet.

1.1 Variations on Seismic Tomography

The seismological forward problem is most generally defined as

$$G(m) = d, \tag{1.1}$$

where m are Earth's seismic properties, d are the observed data, and G is the Green's function that relates the two. The Earth constantly runs this forward problem in real time all around us, but the planet is too vast, the seismic properties too numerous and our ability to make observations too limited to make use of all of it. Seismologists thus commonly turn to a pale form of this grand problem, the discrete linearized case,

$$\mathbf{Gm} = \mathbf{d}, \tag{1.2}$$

and, limited by aperture, by time, by funding, and by computational capabilities, make a series of decisions about which part of the problem to focus on. In this formulation, the model $\mathbf{m}$ can represent a variety of different seismic properties from bulk sound speed to anisotropic elastic parameters, the data $\mathbf{d}$ can be any number of seismic phase picks, waveforms, or other observations, and the forward operator $\mathbf{G}$ admits to many different approximations of wave physics.

In seismic tomography, we wish to use observed data to find our way back to Earth properties that are otherwise difficult to directly measure at the surface. That is, we want to solve for $\mathbf{m}$. Due to the over-determined nature of most seismic problems and to computational limitations, the inverse $\mathbf{G}^{-1}$ is not always so easy to determine. The inversion for $\mathbf{m}$, then, is accomplished finding minimum value of a chosen error function, $\mathcal{J}[\mathbf{m}]$, a measure comparing seismic observations to their estimated values based on our model. One well-trod approach involves minimizing the L_2 norm between the modeled and observed data,

$$\mathcal{J}[\mathbf{m}] = ||\mathbf{d}_{obs} - \mathbf{Gm}||_2, \tag{1.3}$$

but $\mathcal{J}$ admits to a number of different forms. Furthermore, a variety of approaches can be applied to minimize $\mathcal{J}$ in order to optimize $\mathbf{m}$.

There are myriad ways to perform seismic tomography. Tomography can be applied to a wide variety of Earth problems using an even wider variety of methods. Choosing a path to follow involves asking a number of questions: what are we interested in knowing about the Earth? What type of data is available and in what volumes? How accurate and how fast does our modeling need to be? What can our computational facilities handle? In the following sections we will address the implications that these and other questions have upon the choice of tomographic analyses.

1.1.1 $\mathbf{m}$

Ideally, our tomographic inversion should be motivated by interest in a particular geological question. The model $\mathbf{m}$ should be designed to provide an answer, and the data and methodology needed to recover it should subsequently follow. (This is not always the case, of course. Often seismologists become more fixated on the methods than the models.) So we first ask: What scope of model is needed to address our geological question? What part of the Earth are we pursuing? If we endeavor to better constrain convection in the deep mantle, we need to invert for a full mantle model. If we are interested in a regional tectonic question or in prospecting for hydrocarbons in the crust, a less extensive model will be more suitable. The dimensionality of the model also depends on the question we wish to answer. If the structure we are interested in varies little in one direction, perhaps a 2- or 2.5-D cross-section suffice.

Next, what properties are we interested in determining? Often we can adequately express the model in terms of an acoustic wavespeed; sometimes is it vital to find both compressional and shear wave velocity. For applications like constraining volatile content, the ratio between them is particularly informative. If we wish to interrogate the mineral structure and flow direction, it will be necessary to employ an anisotropic model.

Once we know the volumes and properties we wish to measure, how will we parameterize the model? We can search for smooth variations in seismic properties that are expressible in terms of smooth basis functions, but perhaps we hope to constrain discontinuities as well. The choice of our Green's function solution place may also place requirements on our parameterization, often obliging us to define seismic properties on regularly spaced nodes or volumes.

Finally, are there any *a priori* assumptions that go into the model? We can attempt to recover the absolute velocity structure, but often it is more convenient invert for a deviation from a 1-D background model. It is possible to constrain the model in regions not resolved by a particular method to values derived by other means. For instance, global body wave inversions with poor resolution in the crust often make use of crustal corrections based on surface wave models. Assumptions can also be made about the positions of discontinuities. Assumptions about the depths of the core-mantle boundary and mantle transition zone interfaces are usually baked into tomography using reflected phases, and surface wave tomography studies often make use of Moho structure determined by receiver function analysis.

1.1.2 d

Data is where reality creeps into the inversion process. The quality, quantity, location and type of observations **d** determine to a large extent what truth can be recovered about the target velocity structures. Illumination of the model by seismic phases in the data is the key to tomography, and investigators rarely have much control over where and when sources will occur. Passive-source tomography (as opposed to methods using active sources like explosions, airguns, or Vibroseis trucks) rely on naturally occurring seismicity to provide illumination of the subsurface. Unfortunately, earthquakes are notoriously unpredictable. The locations, magnitudes, frequency content, and source-time functions of seismic sources all place limitations on what kind of information can be extracted for model optimization.

Illumination is further constrained by the ability to place and maintain seismic arrays. High density array deployments are typically short term, making the number and quality of observed events uncertain. Full-mantle tomography suffers from the extreme expense of making measurements at the 70% of the Earth covered by water. Divisions as geologically meaningless as political boundaries can undermine the availability of data. For example, the Transportable Array component of USArray provides high quality data throughout the western US, but its coverage ends at 49° N, not because it's where any interesting terranes or mantle features end, but because it's where Canada begins. (The array extends into southern Ontario and Quebec in the east.)

Caveats noted, once we have the data in hand, which part of it do we hope to use? First, the particular phases and polarizations will be heavily influenced by what model we hope to uncover. Tomographic studies can make use of waves traveling directly from the seismic source, waves reflecting once or more off of discontinuities in velocity. If we hope to uncover the velocity structure of the crust and upper mantle with good vertical resolution, surfaces waves may be suitable. If we want to invert for the long-wavelength multiscale structure of the full Earth, we might consider normal modes. If we wish to know about the anisotropic structure of a the region, it could be useful to involve both SV and SH phases.

The data volume will naturally be chosen based on the geological question at hand and the illumination of the model region, but beyond that, we must determine how these measurements are defined. On one hand, we can look at individual traveltimes of identifiable seismic phases. These can be determined either by picking their arrival time or by correlating their arrival between different stations. On the other hand, the amplitude and phase information the entire wavefield can be treated at once through waveform inversion methods. On the third hand, new methods make it possible to constrain tomographic models based not on data in the time domain, but on images of reflectivity in depth.

1.1.3 G

The forward modeling operator uses some approximation of seismic wave propagation in order to generate data based on model parameters. The choice of G is intimately related to type and quantity of the data measured and the computational facilities available. Due to computational constraints, G has been estimated using ray theory for much of tomography's history. This approach relies on an asymptotic high-frequency approximation to the wave equation, but as discussed above, seismic data has a limited bandwidth. Especially in the case of teleseismic data, finite frequency effects can play an important role, as different frequencies sample different model scales differently. Finite frequency approximations of the wave equation that can explicitly handle these problems come with various levels of various levels of accuracy and computational expense. The question of how to approach the forward problem has immediate ramifications on the type and quantity of data that can be used, and ultimately on what sort of models can be recovered.

In spite of their relatively low accuracy, ray theoretical approaches allow us to quickly invert for models using vast amounts of data. As the volumes of data from stations across the globe continue to increase, these methods will continue to be useful for some time to come. Within the framework of ray theory, a few additional decisions apply. Raypaths can be computed in a 1-D background model or they can be updated during the inversion based on the 3-D velocity structure at an increased computational cost. Some of the finite frequency effects can be accounted for by projecting the sensitivity on to 3-D volumetric "fat rays" which encompass the first Fresnel zone. Furthermore, it is possible to follow the Born approximation and find finite-frequency sensitivity kernels which, under a specific set of circumstances (i.e. no caustics, known source-time function), resemble "banana doughnuts" in the global Earth.

On the opposite end of the spectrum, it is possible to treat a small number of high-quality data using more accurate approximations to the wave equation. One such method is the Spectral Finite Element Method (SPECFEM) which propagates all anisotropic, elastic seismic phases, including surface waves, to a high degree of accuracy on a structured 3-D mesh that includes discontinuous structure. The extreme computational expense of such approaches (forward modeling of global seismic events up to 1 Hz is presently out of reach, to say nothing of an iterative inversion with those frequencies) drives our search for faster solutions with accuracy appropriate for the problems at hand.

Between these end-members, there are a plethora of other modeling operators that are able to incorporate more data than SPECFEM but are able to overcome the difficulties with caustics and finite frequency inherent in ray theory. Based on the problem as hand and the data used, the wave equation can be solved in the time domain or the frequency domain, elastic or acoustic, isotropic or anisotropic. The full wave equation can be solved, or speed can further be increased by considering propagation in one direction using a one-way wave equation solution.

1.1.4 $\mathcal{J}$

Once we have chosen our models and forward operators, we must also ask how we intend to compare the resulting modeled data with our observations. We can try to minimize the difference between observed traveltimes and theoretical ones determined in a starting model or the difference between modeled and observed waveforms. We can compare the waveforms with an L_2 norm, which can be unstable when they begin out of phase with each other, but we may be better off comparing them by cross correlation, which is more robust but less sensitive. For image domain problems, we can choose from a number of error functions which do not directly compare the modeled data and observations, but instead judge the success of image formation. For situations where we have good enough data coverage, we can apply extended image annihilation. For more sparse datasets we might instead try to minimize the residual differences between different single-source images.

What sort of other constraints do we need to add to our inversion? These requirements are often applied through the error function. We might want to damp the amplitude of model variations in order to hold it close to the starting value. We can maintain a level of smoothness by applying damping between adjacent model parameters. We may want to ensure updates for different seismic properties to correlate with each other.

Finally, given the error function, how will we minimize it? Due to the large number of model parameters and the high cost of forward modeling common to most seismic studies, optimization approaches like grid search and Monte Carlo methods that rely on large numbers of forward problems with different parameter combinations are typically not considered. For seismic inverse problems, there are two major approaches that most studies follow, which we will detail below.

If the problem we've chosen is linearized, we can we minimize $\mathcal{J}$ via a least squares inversion. In effect we can set the derivative of Equation 1.3 to zero and solve for $\mathbf{m}$. Since $\mathbf{G}$ is typically not a square matrix and can't be inverted, the classic approach is to multiply all terms by the transpose $\mathbf{G}^T$. Then the problem becomes

$$\mathbf{m} = \left(\mathbf{G}^T\mathbf{G}^{-1} + \lambda\mathbf{I}\right)\mathbf{G}^T\mathbf{d}, \tag{1.4}$$

where a damping term, λ, is used to ensure stability. Depending on the problem, one inversion may be sufficient for determining the model; otherwise the process can be applied iteratively.

If our problem is more computationally intensive, we can consider inverting for $\mathbf{m}$ using a steepest descent approach. In this case, we will determine $\frac{\partial \mathcal{J}}{\partial \mathbf{m}}$, the gradient of the error function with respect to the model parameters. Instead of finding the this sensitivity by calculating the forward problem for a perturbation in each model parameter, we can use the Seismic Adjoint Method to calculate it using only one forward and one adjoint propagation. We then update the model iteratively according to

$$\mathbf{m}_i = \mathbf{m}_{i-1} - \alpha \frac{\partial \mathcal{J}}{\partial \mathbf{m}}, \tag{1.5}$$

where α is the multiplier that minimizes $\mathcal{J}$ along that line. Once we know the update direction, we can apply a number of optimization algorithms to find our best fit model such as conjugate gradient. If the problem is large enough, we may want to use limited-memory LBGS. Convergence can be improved by solving for the second derivative of the error function and applying a Gauss-Newton scheme.

1.2 Thesis Structure

This thesis will present three quite dissimilar takes on seismic tomography making use three different parts of the wavefield, modeling the data using three different solutions to the wave equation, and solving for models at three different scales with three different optimization approaches. In spite of their variability, each of the three approaches deals with the tradeoff between bigger data volumes and more accurate wave propagation. Each also addresses the use of new parts of the seismic wavefield for resolving previously unresolved seismic structure.

The flood of high quality broadband data pouring in from the USArray Transportable Array invites thorough investigation of the mantle beneath the United States, including the application of established tomographic methods on a grand scale. With a station spacing of 70 km and a baseline eventually extending coast to coast, the Transportable Array (TA) provides the ideal dataset to perform tomography with resolution in North America not previously seen in global mantle models. **Chapter 2** presents a global *P* wave inversion using TA data in concert with global catalog data. From 2007 to present, we have been updating the global model with incoming *P* phase traveltime picks from the Array Network Facility and sharing the resulting model volumes with the geophysics community. The sensitivity of the traveltimes to mantle wavespeeds is determined by ray tracing through the 1-D *ak135* model, and the spacing of the model grid is adapted in regions without ray coverage. The linear inversion is performed by least squares. Although this approach to tomography has long been established and its wave physics is approximate compared to wave equation methods, the application to the TA dataset allows us to make powerful observations in regions which previously were sparsely instrumented. As USArray rolled out across the country from the tectonically active west to the more stable east, our tomography models revealed heterogeneity in the tectonically inactive and previously poorly sampled provinces east of the Rocky Mountains to have similar spatial scales but lower relative amplitudes compared to heterogeneity in the west.

While ray theoretical methods can be powerful and computationally fast, the asymptotic frequency assumption discards useful scale information from the data. One way to keep computational costs down while keeping accuracy up is by using a one-way wave equation. Common in the exploration industry in the mid-2000's, one-way approaches are limited by the fact that waves can only propagate in one direction at a time, making it difficult to account for backscatter and turning waves. Motivated by the presence of turning waves like teleseismic phases in global seismology and near-vertical elements like salt flanks in the exploration setting, **Chapter 3** develops a one-way propagator on curvilinear coordinates. By finding a coordinate system where waves do not overturn, we can model complicated propagation using fast solvers. The method presented uses a finite difference scheme based on a rational approximation of the single square root operator. In this chapter we also develop a finite frequency transmission tomography using the seismic adjoint method for use with the one-way wave equation. We formulate our inverse using perturbation theory and present the resulting sensitivity kernels.

The next two chapters develop a novel form of reflection tomography for teleseismic free surface multiples inspired by methods established in exploration seismology. The growing availability of high-quality regional data inspires us to consider new phases that might help us to better constrain seismic properties in the lithosphere and upper mantle. In particular, teleseismic conversions and free surface multiples are regularly used to create images of structures like the crust-mantle boundary (Moho) and the lithosphere-asthenosphere boundary (LAB). Through the use of reflection tomography, information about the smooth background model can be inferred from the consistency of these images. Using these reflected phases has the advantage of localizing velocity updates to the volumes above the discontinuities, whereas teleseismic transmission tomography tends to have very poor vertical resolution in the lithosphere. This helps reduce the null space and enhance the uniqueness of the inversion. **Chapter 4** describes the theoretical development of a reflection tomography approach that optimizes the smooth background model by minimizing the correlation power between single-source images away from zero depth shift. An acoustic Helmholtz operator is used to both create the images through reverse-time migration and to determine the sensitivity kernel for update via conjugate gradient. The gradient here is determined by an application of the Augmented Lagrange Method.

An initial application of the reflection tomography method to the 2-D HICLIMB array is presented in **Chapter 5**. The Hi-CLIMB spans the central Tibetan Plateau from the Himalaya to the Qiangtang terrane and is aimed at investigating the collision between the Indian and Eurasian plates. Seismic studies performed using the high quality broadband data from the array have recovered a sharp Moho reflection beneath the Lhasa and Qiangtang terranes, separated by a zone of relative complexity beneath the Bangong-Nujiang suture and evidence of downwelling lithosphere from both plates. For this study, we apply our reflection tomography method to critically reflected SsP_mp phases, which are excellent for creating strong single-source images of the Moho. These data include events that arrive at a high angle of obliquity with the strike of the array, which reduces the resolving power of the method but helps provide the angular coverage required for the inversion. We present both the results of RTM imaging of the Moho and crustal discontinuities and the estimate of smooth velocity structure in the crust recovered by reflection tomography.

Finally, the conclusions of the thesis are presented in **Chapter 6**. Future work based on this thesis, particularly the theoretical extensions and applications for the reflection tomography presented in Chapters 4 and 5, are discussed in depth.

Appendices A-E contain the published updates to the MITP_USA model described in Chapter 2. **Appendix A** presents the first community model MITP_USA_2007NOV, as well as the methodology used and a comparison to models created with USArray TA datasets at intervals between February and November 2007. **Appendix B** presents model MITP_USA_2008DEC and resolution analysis of the gap in the Juan de Fuca slab beneath the High Lava Plains in Oregon imaged in the MIT model and others. **Appendices C, D, and E** are brief research notes presenting models MITP_USA_2010JAN, MITP_USA_2011MAR, and MITP_USA_2013JAN, respectively.

Several of the chapters presented here have been submitted for publication or are in preparation. There is, therefore, some redundancy in the models and theory presented in different chapters. Appendices A-E have been published as research notes in *Seismological Research Letters.* Chapter 2 briefly summarizes the results from the papers presented in the appendix and is in preparation for submission to *Earth and Planetary Science Letters.* Chapter 3 is the core of a paper written for the General Exam, augmented with further theoretical development on transmission tomography. Chapter 4 is published in *Geophysical Journal International* and Chapter 5 is in preparation for submission to *Geophysical Research Letters.*

Chapter 2

Structure and scale of the mantle heterogeneity beneath the United States from traveltime tomography

Abstract

Since its inception in 2004, the Transportable Array (TA) component of USArray has furnished the seismic community with ever-growing volumes of high-quality seismic data as it rolls across the continental United States. These data provide an unprecedented opportunity to recover the structure of the upper mantle with higher resolution than was previously possible in many regions. Although full-wave equation tomography methods, which take into account the true multi-scale nature of the mantle, will eventually be applied to the broadband waveforms yielded by USArray, traditional ray theoretical approaches to continue to yield useful first-order tomographic images. At regular time intervals from 2007 to 2013, we performed a global P-wave traveltime inversion for velocity heterogeneity in the mantle using USArray TA and global catalogue data and the results were released to the seismic community. The evolution of these community models clearly shows the enhancements that the addition of USArray TA data have on our ability to resolve structure in the mantle. The current model, MITP_USA_2013JAN, uses TA data up to January 2013 from stations extending east into the Appalachians. The 2013JAN model resolves features in the center of the continent, including the Midcontinental Rift system, the New Madrid Seismic Zone, and the Reelfoot Rift, unseen in previous iterations. The uniformity of the array coverage provided by the TA further allows us to compare and quantify the scale and amplitude of heterogeneity from region to region. Local scale analysis performed using wavelet decomposition shows that the scales of heterogeneity in actively deforming regions are also present in stable blocks, but with lower relative amplitude.

2.1 Introduction

The continental United States can, in a broad sense, be divided into a tectonically active region stretching from the Pacific Ocean to Rocky Mountains and a relatively stable region to the east of the range. The west coast of the continent is home to an active margin, with the subduction of the Juan de Fuca and Gorda plates beneath North America occurring from Northern California to Vancouver Island and the strike-slip motion between the North American and Pacific plates along the San Andreas Fault. The ongoing subduction of the ancient Farallon plate has driven much of the deformation in the west, including the Cenozoic uplift of the Rockies and extension of the Basin and Range province. In the northwest, the Columbia River flood basalts and Snake River Plain/Yellowstone hotspot track are thought to be related to a mantle plume. The eastern half of the continent consists of a stable craton bordered to the east by an ancient orogeny. The craton is composed in much of the midwestern region of a Proterozoic platform. A small segment of the Archaean Superior Province extends into the US at the Great Lakes. The Paleozoic Appalachian Highlands lie to east, bordered by a passive margin. In spite of the relative stability, several anomalies exist in the east including the New Madrid Seismic Zone, the Reelfoot Rift, and the Midcontinental Rift System. Figure 2-1 gives an overview of the tectonic provinces across the United States.

Before 2004, studies seeking to characterize the heterogeneity beneath the whole of the United States were limited to one of two approaches: either the piecemeal construction of a model from regional studies (Dueker et al., 2001) or relatively low-resolution tomography using global traveltimes or surface wave data (Li et al., 2008b; Montelli et al., 2004; Grand, 2002; Ritzwoller et al., 2002). The ability to resolve the differences between east and west was limited by the irregular station coverage between the regions – extremely dense along the San Andreas and other local points of interest in the west, and sparse or practically non-existent over large swaths of the east. Into this gap stepped the USArray Transportable Array. USArray TA, part of the seismological component of the national Earth Science program Earthscope, began progressing across the United States from west to east beginning in 2004. As of 2013, the final stations have been installed along the east coast. With a station spacing of $\sim$70 km and a baseline of thousands of kilometers, the TA has provided an unprecedented look at the upper mantle and transition zone beneath the continent.

In the near future, full wave equation approaches to seismic tomography using traveltime measures (De Hoop & Van der Hilst, 2005; Tromp et al., 2005; Zhao & Jordan, 2006), full waveform inversion (Fichtner et al., 2013) or reflected phases (Burdick et al. (2013), Chapter 4) will produce mantle models using USArray TA waveforms that accurately account for wave physics and the multi-scale nature of the Earth. Presently, however, classic linearized, ray theoretical approaches remain useful for determining the first-order mantle structure when dealing with massive volumes of data. Thus, in response to the ever-increasing catalog of USArray TA data, we have published a series of five *P* wave velocity models (Burdick et al., 2008, 2009, 2010, 2012, 2014), included here in Appendices A-E. The models are created by a global inversion of multiple *P* phase traveltime picks from USArray TA and global data from the International Seismological Centre. In order to make the based use of the dense USArray TA station spacing, inversions are performed on an adaptive grid that conforms to raypath density. Due to poor resolution of the crust, we apply a 3-D crustal correction.

The current model, MITP_USA_2013JAN gives new insights into the outstanding questions about the mantle structure beneath the United States, including (1) the relationship between near-surface tectonic elements and deeper mantle processes, (2) the fate of subducted oceanic lithosphere in the mantle beneath the eastern US and implications for continental evolution, and (3) the quantitative differences between the tectonically active provinces west of the Rocky Mountains and the relatively more stable provinces to the east. On this last point, the broad baseline and uniform spacing of the Transportable Array present an unparalleled opportunity to perform a robust comparison between the provinces using local scale analysis.

This paper consists of three major parts. Section 2.2 consists of a brief description of the tomographic method and data used. In Section 2.3, the evolution of the MITP model with increasing USArray data is described, illuminating the effects of improved station coverage. Section 2.4 presents an indepth analysis of the current model, including a breakdown of heterogeneity by tectonic province and wavelet analysis.

2.2 Data and Tomographic Method

For the complete details of the method we refer to Li et al. (2008a) and Burdick et al. (2008), but here we include a brief description. We make use of the tomographic inversion method first applied in Li et al. (2006) to study the mantle beneath Tibet. This approach minimizes an the L2 norm between observed *P* phase traveltime picks and ray theoretical calculations in the spherically symmetrical 1-D global model *ak135* (Kennett et al., 1995). The cost function to be minimized also contains terms for norm and gradient damping, hypocenter mislocation, and a crustal correction.

The January 2013 update of the MITP model uses ~2,500,000 *P* phase traveltime residuals from USArray TA picked by the Array Network Facility (ANF), including 800,000 new residuals not used in previous models. The station locations for residuals are shown in Figure 2-2. These locations include 415 new TA stations spanning the Midwest and Gulf Coast and beginning to extend into the Appalachians. In addition to the TA picks, the inversion uses some 10 million teleseismic *P*, *pP*, *Pn*, and *PKP* from the International Seismological Centre (ISC), as reprocessed in Engdahl et al. (1998) (referred to hereafter as the EHB dataset).

In response to the uneven raypath coverage caused by the sparse and irregular distribution of stations and earthquake hypocenters, we perform the inversion using an adaptable parameterization. Beginning with uniform grid cells 0.35° × 0.35° × 45 km near the footprint of USArray TA and 1.4° × 1.4°× 45 km outside, cells are merged based on whether a sufficient number of rays are sampling a mantle volume. This approach allows our global inversion to make use of the dense station coverage in North America, making it possible to yield a model that approaches the resolution of regional studies (Bijwaard et al., 1998).

Figure 2-3 shows the adaptable grid for MITP_USA_2013JAN at a number of depths, as well as the average (2-D) diagonal of the grid cells. The inclusion of the EHB dataset in the inversion leads to some inconsistency in grid spacing across the continent, but the effect is much smaller than in models prior to TA. The average cell size is smallest (~35 km) beneath California and Yellowstone at depths down to 200 km. Elsewhere in the west and beneath the Ozarks and western coastal states, the grid size grows to ~50 km. Where data has been able to accumulate over the full deployment time, grid size beneath the remainder of the TA does not exceed 75 km. The fine grid size becomes more widespread with depth thanks to the spreading of the rays (and owing in part to the decrease of grid volume with decreasing radius). At 750 km, we increase the minimum allowable grid latitude and longitude due to the shrinking mantle volumes. The current implementation of the cell merging algorithm takes neither the azimuth nor the ray parameter of the rays into account, so regions where most incoming rays sit within a single plane (i.e. there are no crossing rays) may be poorly resolved in spite of their fine grid spacing. This is the case off of the west coast of the continent and at other array boundaries. For that reason, we cannot consider grid spacing to have a 1-to-1 relationship with resolution.

Due to the relatively steep incidence angles with which the teleseismic P phases arrive, our method has poor sensitivity in the crust. As such, without a correction term, strong crustal heterogeneity would map into the mantle. To mediate this effect, we add a term to the cost function that holds the velocities in the crust near the values from the global reference model CRUST 2.0 (Bassin et al. (2000), available online at *http://mahi.ucsd.edu/Gabi/crust2.html*).

2.3 Evolution of the MITP model

Between 2008 and 2013, we released a series of five research notes that presented global P wave models with fine parameterization in the continental United States in response to incoming USArray TA picks. The progressive improvement of the scales and structure imaged beneath the array show without question the value of the USArray experiment. Figures 2-4 and 2-4 give an overview of improvements over the years. Since model updates began in 2008, the number of USArray TA picks has expanded to comprise roughly 20% of the data used in the global inversion, a denser dataset than is available anywhere else. These picks have refined our estimates of seismic velocity structure particularly in regions east of the Rockies where data was previously unavailable.

Burdick et al. (2008) presented the first community model, MITP_USA_2007NOV, in addition to two earlier iterations of the model using USArray TA data and one with EHB data only. The USArray TA stations used for the final published model, shown as red triangles in Figure 2-2, extend from the west coast inland to 110 W, covering much of the Basin and Range Province, as well as the Columbia Plateau and Yellowstone hotspot. The TA data included ~600,000 picks from over 3,000 teleseismic events. Compared with global models constructed without USArray data available at the time of its release (e.g. Montelli et al. (2004); Grand (2002)) the 2007NOV model shows fine structures in the upper mantle connected to regional tectonic features. The model shows the Cascadian subduction as a thin high velocity zone from Vancouver to the Mendocino Triple Junction with variation along-strike, in particular, a much lower amplitude is seen around the High Lava Plains in Oregon. The upper mantle expression of the Yellowstone hotspot is also seen as a low velocity linear feature extending northeast from the northern extent of the Basin and Range. Any connection with deeper heterogeneity remains unresolved in this model due to lack of crossing raypaths.

MITP_USA_2008DEC (Burdick et al., 2009) added ~390,000 USArray TA picks from 2,000 new events to the inversion. In addition to new picks from previously installed stations, the dataset added picks from stations extending over the Rocky Mountains and into the Great Plains (Figure 2-2, orange triangles). The major improvements from the previous model were focused in the Pacific Northwest, where additional data had accumulated, and in New Mexico and West Texas. The geometry of the Cascadian subduction and the slab hole at the High Lava Plains are shown to be robust, the contrast between the Yellowstone hotspot and the surrounding Wyoming Craton increases, and the boundary of the of the slow Basin and Range and the fast interior region of the Colorado Plateau becomes well defined. This model cannot yet distinguish whether the stable continent to the east of the Rockies lacks heterogeneity due to still-sparse data coverage.

The next update, MITP_USA_2010JAN (Burdick et al., 2010), added ~280,000 picks from 1,500 events, inclusive of picks from stations extending to 96 W (Figure 2-2, yellow triangles). This new station coverage gave the first real look at the structure of the Great Plains. In this model, the scale and variability of heterogeneity in the upper mantle beneath the Plains states do not appear to change in response to increased ray coverage and model grid refinement. Better continuity beneath subducted slabs in the west and fast anomalies in the east can be seen. Most crucially, beneath the eastern edge of the array, what once was a large undifferentiated fast blob begins to separate into distinct elements from the cool cratonic lithosphere and remnants of the ancient Farallon subduction in the mantle.

MITP_USA_2011MAR (Burdick et al., 2012) included some ~260,000 new picks from 3,500 events. The USArray TA stations at this time had rolled into Gulf Coast states, extending north to the Superior Province (Figure 2-2, blue triangles). Refinements to the model are most pronounced in shallow mantle Great Plains due to further data accumulation and the mantle transition zone beneath the Plains and western sections of the Central Lowlands and Gulf Coast due to improved ray coverage. This update begins to give indication of variations among different tectonic blocks in the stable center of the continent. The fast signature of the cold crust becomes stronger and more confined laterally. The fast anomaly due to the Ouachita Mountains and Ozark Plateau begins to come into focus. The Farallon slab beneath the Great Plains becomes narrower due to the refinement in the model grid at transition zone depths.

The latest *P* wave model, MITP_USA_2013JAN (Burdick et al., 2014) includes nearly two years of additional TA data, bringing the total number of picks to ~2,500,000. The stations extend through the entire Gulf Coast, the Midwest, the western reach of the Appalachians, and into Ontario (Figure 2-2, purple triangles). The model resolution improves tremendously in the Ozark Plateau, the Central Lowlands, and the Coastal Plain, revealing fine scale structure, albeit of a low relative amplitude, throughout the eastern half of the continent. The results of this final inversion, shown in Figures 2-6 and 2-7, are analyzed in more detail in the following sections.

2.4 Current model interpretation

2.4.1 Pacific Mountain System

The far west provinces bordering on the Pacific Ocean are the most densely instrumented region in the US and show the highest degree of variation. The Pacific Border province is generally characterized by low velocities in comparison to the adjacent Cascade-Sierra system. Here the model is able to resolve velocity contributions from individual mountain ranges. At depths down to 200 km, the Klamath Mountains region exhibits velocity lows of about -1.5% which correspond spatially to a gravity low. South of the San Francisco Bay, the California Coastal Ranges show similar low velocities but without the corresponding gravity lows. The California Trough is indistinct in velocity from the Coastal Ranges, but at its northern and southern ends, there is a sharp contrast with the Sierra Nevada, giving some of the strongest gradients in the model. The velocity beneath the Sierra is average to slow apart from a fast anomaly at the southern edge. At depths from 50 to 150 km the northern and central regions of the Sierra have similar velocity and gravity structure to the Basin and Range. The Cascade Mountains are marked by the strongest high velocity anomalies (up to 2.5% at 100 km) in the western half of the U.S. These anomalies are strongest in the Northern and Southern Cascades, with a distinct weakening of the trend beneath central Oregon.

2.4.2 Columbia River–Yellowstone magmatic system

The northwestern sector of the United States is host to a relatively recent spate of magmatic events. The eruption of the Columbia River and Steens Mountain Basalts occurred at 17-14 Ma, followed by the initiation of the Yellowstone–Snake River Plains and High Lava Plains trends. The former trends to the northeast along the Snake River Plain and terminates at Yellowstone, while the latter extends northwest, terminating at the Newberry Caldera. The magmatism in the region has been variously interpreted to be the result of a deep mantle plume (Camp & Ross, 2004; Jordan et al., 2004) or subduction driving mantle dynamics (Humphreys et al., 2000; Fouch, 2012).

Figure 2-8 show the gravity and tomography in the region encompassing the magmatism. The fast, thin linear structure related to the subducted Juan de Fuca subduction runs north-south along the coast, but weakens at depths from 100 km to 200 km beneath the High Lava Plains, coincident with the extent of low seismicity along the slab (Wong, 2005). The cross section in figure 2-8(c) shows a strong Juan de Fuca slab descending to the transition zone before intersecting the fast anomaly of the Idaho Batholith. The slab is continuous apart from a distinct hole in the in the otherwise continuous Juan de Fuca slab beneath in this area.

The Columbia Plateau registers lower velocities, culminating in a velocity low of -2.8% at the Yellowstone hotspot. The province's only strong positive velocity anomaly is a 1.0% peak beneath the Blue Mountain Region. The slow anomaly, which tracks along the Snake River Plain at depths down to 250 km, correlates with a local gravity high for the length of the plain, then connects in the south with the Basin and Range slow region instead of following along the Payette River section. The Walla Walla Plateau also shows strong slow velocity structure correlated in space with a gravity high. In Figure 2-8(d), the slow anomaly continues downward to 300 km where it weakens before reappearing at strength beneath the 660 km discontinuity. This appears to be a robust feature in a number of tomography models (Schmandt & Humphreys, 2010; James et al., 2011) and suggests that deep mantle processes are at least somewhat involved.

2.4.3 Basin and Range and Colorado Plateau

The Basin and Range province (Figure 2-9) is a broad zone of extension caused by the motion between the Pacific and North American plates. At depths down to 200 km, the Basin and Range appears as one of the slowest provinces of the continent, with the Great Basin in particular seeing velocities as low as -2.7% at 50 km. The southern sections of the province have slightly higher velocities, with the relatively fast region of the Sonoran Desert corresponding to a local gravity high, while the rest of the province is characterized by a gravity low.

Bordering the Basin and Range to the east is the relatively stable and seismically fast Colorado Plateau. Observations of lithospheric reflections by Lekic & Fischer (2013) have shown that the interior sections of the Colorado Plateau have deeper, more diffuse discontinuities, while the outer parts have strong, shallow reflections more similar to the Basin and Range. Figure 2-9(b) shows that at shallow depths, sections of the Colorado Plateau vary with respect to their proximity to the Basin and Range. The High Plateaus of Utah, the Grand Canyon and the Datil Mountains share similar velocity structure to the Basin and Range down to 200 km depth. The interior sections of the Plateau, the Uinta Basin, Navajo, and particularly the Canyonlands are faster, with velocities up to 0.6%. The model exhibits a sharper gradient between the two sections of the Colorado Plateau than between the Plateau and the Basin and Range. Based on the relative lack of deformation of the outer portions of the Plateau, this suggests that the low velocities are due to magmatic reworking of the lithosphere rather than stretching (Roy et al., 2005).

2.4.4 Rocky Mountains

With a few exceptions, the Rocky Mountains have a low Bouguer anomaly, but the velocity structure beneath the range displays a good deal of variability from the north to south. The Northern Rockies, apart from the slow section related to the Yellowstone hotspot, have a fast structure at depths down to 400 km, with a fast fingerlike structure extending down past 600 km. The Middle Rockies vary strongly, with somewhat faster sections in the north and around the Great Salt Lake. The Wind River Range, which sticks out into the Wyoming Basin, has a particularly high velocity anomaly of 1.5% down to 100 km. The Wyoming Basin, a block of relatively low deformation, is of average to low velocity. The gradient between the basin and the Wind River Range is particularly sharp and corresponds to a very strong gradient in the gravity anomaly. The Southern Rockies bordering the Colorado Plateau exhibit the slowest velocity structure of the range, with velocities around -1.0% down to 300 km, correlating with a gravity low.

2.4.5 Eastern United States

The central region of the United States to the east of the Rocky Mountains is characterized by high seismic velocities, less variable topography, and a recent history of tectonic stability. The North American craton, including the Great Plains, Central Lowlands, and Superior Upland provinces, was previously poorly instrumented; USArray TA data now allows for a much richer analysis. Typically, there is a sharp change between the velocity structure of the Rocky Mountain System and the relatively smooth structure of the Great Plains province. Although they are lower in amplitude, there are however still subtle velocity variations between the sections. There is a relatively strong gradient between the fast Black Hills (1%) and the surrounding Missouri Plateau down to 150 km, as well as at the boundary of the Edwards Plateau in Central Texas. The Edwards and Missouri Plateaus are faster than average down to 300 km, while the sections bordering the Southern Rockies, the Piedmont and Raton Basin, are slower. The transition between the Great Plains and the high velocities of the Central Lowland is relatively smooth. The Central Lowlands, comprised of Paleozoic strata, are bordered to the north by the Superior Upland, part of the Archaean-aged Canadian Shield. These provinces, which are part of the continental craton, register the highest average velocity structure, with fast anomalies extending to 200-250 km depth.

Between the Central Lowlands and the Gulf Coast is a region of relative complexity in the velocity model. The Interior Highlands (Figure 2-10) are marked by strong variation within the provinces and at the boundaries of adjacent regions. The Springfield-Salem Plateaus have a strong (greater than 2%) fast anomaly to 200 km, which stands in contrast to the slightly slower surrounding regions. The Ouachita Mountains are underlain by a slow anomaly at 50 km with some small scale variation beneath the center of the range. The low velocity structure is similarly situated with a gravity low. Further to the east, the Interior Low Plateaus do not exhibit much fine scale correlation between the velocity model and the physiographic sections of the province. The province is underlain by a fast anomaly that starts out focused under the Nashville Basin at shallow depths, but broadens out as it continues to depths of 600 km or more. It is likely here that the data are not yet able to distinguish between the general fast structure of the craton and the underlying slab fragments.

The velocity at shallow depths beneath the Coastal Plain is relatively homogeneous. The West Gulf Coastal Plain has a uniform velocity of -0.5% between Texas and Alabama down to 300 km, which is considerably lower than surrounding regions. The velocity structure beneath the alluvial plain of the Mississippi River holds to the same region-wide trends apart from its northern extent where it terminates in the Reelfoot Rift system. The relative slow zone ends to the east in Georgia, where a fast anomaly extends down from the southerly end of the Appalachian Range. Current station coverage has only begun to resolve the Appalachian region on a fine scale, but the lithospheric structure beneath the Appalachians is slower than in the adjacent craton. The velocity heterogeneity across the ranges does not at coarse scales (on the order of 3°) appear to be consistent along the strike.

2.4.6 Rift Systems

Within the relatively stable craton of the continent there exist several failed Proterozoic-age rift systems, including the Mid-Continental Rift, which spans the Superior Upland and Central Lowlands, and the Reelfoot Rift, which lies within the Coastal Plain and surrounding provinces and includes the New Madrid Seismic Zone. These ancient rifts are associated with gravity highs due to the emplacement of basalt associated with rifting. They often register as low velocity zones in the crust and shallow mantle due to sedimentation and the increased density of mantle material.

Figure 2-11 focuses on the region surrounding the Mid-Continental rift. The gravity field shows a major anomaly due to the rift, which runs from Lake Superior, through the Superior Upland, and into the plains of Iowa and Nebraska. The velocity structure follows the line of this rift. An anomaly of 0.3% cuts through the much faster ($\sim$2%) region surrounding it. The current data do not reveal the second branch of the rift that runs through the center of Michigan. Cross sections in Figures 2-11(c) and 2-11(d) demonstrate that the low velocity signature of the rift extends only $\sim$100 km into the mantle.

The Reelfoot Rift, a reactivated Precambrian rift zone, extends from the Coastal Plain into the region between the Interior Highlands and Low Plateaus (Figure 2-10(d)). The northwest extension of the rift includes the New Madrid Fault, a zone of anomalous intracontinental seismicity, which manifests itself as a linear slow anomaly corresponding to a local gravity high. Figure 2-10(c) shows the strong velocity anomaly from the fault zone extending deep into the upper mantle. The depth of the velocity anomaly suggests that the fault is susceptible to external stress from the mantle (Pollitz & Mooney, 2013). Opposite the New Madrid Seismic Zone, a slow feature extends to the northeast and may be related to the Wabash Valley Seismic Zone.

2.4.7 Local scale analysis

One of the great open questions that the Transportable Array was designed to answer is whether the variation in seismic velocity is consistent between the tectonically active west and stable east. Prior to the advent of USArray TA, the station coverage in the United States was highly irregular and focused in areas of specific geological interest – the San Andreas Fault system, the Yellowstone hotspot, the New Madrid Seismic Zone and many others. Models created with such data could easily mistake ray coverage for inherent complexity in seismic structures. The uniformity of station spacing from USArray TA presents an opportunity to finally resolve whether tectonically stable provinces like the Great Plains and Central Lowland evince the same type of heterogeneity as actively deforming regions like the Basin and Range. The differences in scale and amplitude between these regions will help answer the question of whether major heterogeneity is simply the result of dynamic changes in the mantle or if heterogeneity can be "locked in" and preserved through prolonged periods of inactivity. Previous research notes (Burdick et al., 2012, 2014) have concluded that the scale of heterogeneity to the east of the Rockies has a similar scale to that in the west, but a lower relative amplitude of variation. Analyses of traveltime delays generated in a variety of *P* and *S* wave models in Lou & van der Lee (2013) suggest that the variation is not dependent on the characteristics of the tectonic province. The consistent coverage afforded by the TA invites further quantitative measures of variation in heterogeneity between the provinces.

Wavelet decomposition, which is used to represent functions in both position and scale, has been used to investigate and interpret a variety of 2-D and 3-D Earth properties. This wavelet analysis improves on Fourier analysis for our purposes by giving additional information about the structural wavelengths from region to region. Wavelets have proved useful in discerning the effective elastic plate thickness from the spatial coherence of gravity anomaly and topography (Audet, 2011) and for localizing the seismic anisotropy (Simons et al., 2003). Similar analyses have also been applied to seismic tomography models in order to quantify and localize structural properties (Simons et al., 2011). Piromallo et al. (2001) used wavelet analysis to investigate the continuity of velocity structures in the mantle transition zone beneath Europe. Carannante (2008) applied similar wavelet correlations to compare between different global tomography models.

Wavelet power analysis

Here we apply a simple set of wavelet analyses to better quantify the dominant scales of heterogeneity beneath the United States and and between its tectonic provinces. After projecting onto Cartesian coordinates, we apply a continuous wavelet transform to 2-D layers of the velocity model, v :

$$w(a,\mathbf{y}) = \frac{1}{a}\int v(\mathbf{x})\psi\left(\frac{\mathbf{x}-\mathbf{y}}{a}\right)d\mathbf{x}, \tag{2.1}$$

$w(a,\mathbf{y})$ is the resulting wavelet decomposition, $\mathbf{x} = (x_1, x_2)$ are the 2-D coordinates in the model domain, $\mathbf{y} = (y_1, y_2)$ are coordinates in the wavelet domain, and a is the scale factor. Following Piromallo et al. (2001) and Perrier et al. (1995), we choose as our wavelet ψ as

$$\psi(\mathbf{x}) = \frac{\partial^4}{\partial x^4} exp\left(\frac{-|\mathbf{x}|^2}{2}\right), \tag{2.2}$$

the fourth derivative of the Gaussian function, due to its regularity properties.

To find the relative importance of each scale length, we can make a simple measurement of the wavelet power spectrum:

$$P(a) = \int |w(a,\mathbf{y})|^2 d\mathbf{y}. \tag{2.3}$$

This measurement is analogous to the Fourier power spectrum, with the advantage that the integration can be done over subsets of $\mathbf{y}$, yielding information about the relative power between different regions. Using this measure, we will investigate the differences in scale length and power of the heterogeneity between the various tectonic provinces.

Wavelet analysis results

Figure 2-12 shows the results of the continuous wavelet decomposition (Equation 2.1) of the 2013JAN model at a number of depths and wavelet scales, a. The wavelet picture gives some interesting insight as to which features are dominant at which scales. At scales $\sim$100 km and less, the abundance of tightly spaced arrays along the west coast and around Yellowstone appears to still have an effect. At shallow depths, these images are dominated by the Cascadia subduction south of the High Lava Plains, the Sierra Nevada root, and to a lesser extent by the Yellowstone Hotspot. Wavelet amplitude elsewhere in the US is muted, but the boundary between the Basin and Range and the inner Colorado Plateau and between the Rockies and the Great Plains can faintly be seen.

At scales of $\sim$200 km, the heterogeneity in the wavelet images becomes more widespread. Yellowstone is the largest-amplitude feature at this scale. The Cascadia subduction zone and the Idaho Batholith also have a strong presence, and the slab window beneath the High Lava Plains is especially pronounced in this view. In the east, the Mid-continental Rift and Reelfoot Rift stand out amid faster patches.

Around 375 km, widespread features like the Basin and Range begin to show up. In the upper 200 km, the Ozark Plateau, Superior Province, and Edwards Plateau in Texas appear as a strong fast anomalies, while the western Coastal Plain shows as a broad slow anomaly. The continuation of the Yellowstone Hotspot beneath 660, while already visible at shorter scales, is much stronger here. At this scale, we begin to see the features related to ancient subduction. From 800 km down, fast anomalies interpreted as the Cascadian root surround the show Yellowstone anomaly.

For shallow depths at wavelet scales between 600 and 1000 km, wavelet analysis yields a picture of the continent much like those available from early global tomography. The west is dominated by the Basin and Range and Columbia Plateau/Cascadia subduction, and the east is an undifferentiated fast zone. The fragments of the Farallon slab reign at depths from the transition zone down. At $\sim$650 km scale, discontinuous pieces of the Farallon can be seen beneath the southeast in addition to major sections of the Cascadia slab beneath Colorado. At longer scales, the continuous slab wall dominates.

An investigation of the wavelet power (Equation 2.3) reveals some general patterns concerning the scale of heterogeneity in the model. Figure 2-13 (a) shows that the heterogeneity is generally stronger at shallow depths across all scales. This pattern is broken between scale lengths of 300-600 km, where the heterogeneity is stronger in the transition zone than it is directly above the 410 discontinuity. For depths greater than 800 km, maximum power is yielded at a scale length of $\sim$700 km, while at shallower depths the power continues to increase beyond 1000 km scales. Figure 2-13 (b) plots the same data, but emphasizes the variation of power with depth. In this view, it is clear that the model has a local power maximum across a broad range of wavelet scales in the transition zone. This observation suggests that the horizontal scale of stagnating slabs in the transition zone is on the order of 300-600 km.

Scale comparison of tectonic provinces

Before performing the wavelet analysis to investigate the differences between provinces, it is worthwhile to consider the effects of irregular model gridding. As discussed in the method section, we perform our global inversion on an adaptable 3-D grid. Figure 2-3 shows that the average grid spacing at depths of 200 km or less is smallest beneath the Pacific Border and Sierra/Cascades range as well as parts of the Rockies and Yellowstone. The grid cells in these regions have diagonals as low as 35 km in length, while the remainder of the cells beneath the footprint of USArray have diagonals between 50 and 75 km. It is therefore not useful to compare wavelet power at scales shorter than this.

Figure 2-14 shows the spectral power averaged over individual tectonic provinces. Some provinces were merged together because they make up a larger tectonic devision (the provinces of the Rocky Mountains, Interior Highlands, and Appalachian are all considered apiece) or because of geographical convenience (the Superior Upland is too small in area to consider alone.) The bottom right inset shows the outlines of the merged provinces. To determine the wavelet power spectra, the wavelet transform of the full continent was taken and the resulting power was summed over the area of the individual provinces. Localizing the integration in this way means that the power measure is affected by heterogeneity from nearby provinces, particularly for small provinces and long wavelet scales. For this reason we have limited the scales to 350 km and less.

The resulting power measures show that the power throughout all provinces generally increases with wavelet scale up to 350 km. The colored lines at the right of each plot show the wavelet power by depth as in 2-13 (b), and the black lines to the left give the averaged grid size in each province for comparison. The amplitude of the power continues to increase with scale length, but beyond 350 km it is no longer correlated with regional structure and therefore is not useful for this analysis. The general pattern of wavelet power is quite similar between the regions The peak power across all scales and provinces is near the surface, where we image the strongest heterogeneity, except in the Pacific Mountain system where the maxima are between 100 and 200 km depth (at longer scales this may owe to the narrowness of the province). In all regions, power tapers off with depth, but sees an additional peak at or around transition zone depths. Heterogeneity in provinces west of the Rockies tends to have greater power at upper mantle depths than those east of the range, but it shows similar power overall in the transition zone and below. The power is lowest in the Appalachians and Coastal Plain where the least USArray TA data is currently available for our inversion.

The locations of the secondary peaks in power in the transition zone appear to roughly correspond with the fragments of subducted slab, suggesting that this is a good measure for determining regions where mantle convection is playing a stronger role. Beneath the Pacific system, the secondary peak is missing or is indistinguishable from the strong heterogeneity at shallow depths. Beneath the Columbia Plateau and Basin and Range provinces, the peak is sharp and constrained to ~500 km depth. In the Great Plains and Central Lowlands, the peak is broad and low, and it sits around 600 km, which corresponds to the depth of inferred Farallon fragments.

2.5 Discussion and Conclusions

A global inversion of *P* phase picks from USArray Transportable Array and global catalogue data has been used to constrain the *P* velocity structure of the mantle beneath North America. The major findings of this analysis are:

(1) The segmented structure of the Juan de Fuca slab beneath the High Lava Plains makes it difficult to reconcile our observations with the plume model suggested by the continuity of the slow structure beneath Yellowstone down to the lower mantle.

(2) In spite of the relatively small amount of deformation it has undergone, the velocity

structure of the outer part of the Colorado Plateau is more similar in velocity structure to the Basin and Range province.

(3) Whereas the Mid-Continental Rift only produces a low velocity zone down to lithospheric depths, the velocity signature of the failed rift encompassing the New Madrid Seismic Zone extends to 300 km, suggesting that the seismicity there may be influenced by mantle stresses.

(4) Analysis of wavelet power spectra shows that heterogeneity is strongest in the upper 300 km of the mantle across spatial scales from 100 to 1000 km and that longer scales dominate at upper mantle depths. The power spectra also peak in the mantle transition zone at scales from 300 to 600 km, suggesting this is the main horizontal scale of slab fragments at those depths.

(5) Power spectra localized to individual tectonic provinces show that the fine scale of heterogeneity long imaged in the western US is also present in regions to the east previously seen as homogeneous, albeit at a lower relative amplitude.

(6) The peak in power spectra inferred to be caused by slab-related heterogeneity gets deeper in depth and longer in scale from west to east.

The study presented here is far from the only one to invert for smooth Earth structure using USArray data. The TA experiment has spurred the creation of a multitude of tomographic models of the mantle beneath the US using a variety of approaches at both global and regional scales. Regional models have been made using body waves arrivals (Roth et al., 2008; Schmandt & Humphreys, 2010; James et al., 2011) and joint body and surface inversions (Obrebski et al., 2011). Global and continental scales have included finite frequency traveltimes (Sigloch & Mihalynuk, 2013) surface waves and normal modes (Ritsema et al., 2011), and have inverted for wavespeed and density (Simmons et al., 2010) and anisotropy (Panning et al., 2010; Nettles & Dziewonski, 2008). All of the models include the major tectonic features seen in the MITP models, but they vary significantly in structure and amplitude across all scales.

Quantifying the variations in heterogeneity between these models and determining which structures are robust between them will be useful in providing a more accurate understanding of mantle processes. A number of metastudies have been performed to evaluate the similarities and differences across the array of mantle models. Pavlis et al. (2012) made a qualitative comparison of the models with regards to the Farallon slab. Lou & van der Lee (2013) looked at the predicted spread in traveltime residuals to measure model accuracy. Becker (2012) looked at the correlation between models and built a composite model based on the consistent features. Along the lines of the later study, wavelet analysis of the type done here and in Carannante (2008) will prove useful in determining the locations and scales of structures common to all models. Simple wavenumber domain analysis of correlations will necessarily miss the differences in scale exhibited by the models due to varied parameterization, methodology, and type of data used.

2.6 Acknowledgments

We thank the National Science Foundation for continued funding of the EarthScope program and the USArray team and the Incorporated Research Institutions for Seismology. We also thank our colleagues at the Array Network Facility at the University of California San Diego for providing the traveltime picks used in the creation of our model. This work is supported by NSF grant EAR-0951901.

Bibliography

Audet, P., 2011. Directional wavelet analysis on the sphere: Application to gravity and topography of the terrestrial planets, *Journal of Geophysical Research: Planets*, **116**(E1).

Bassin, C., Laske, G., & Masters, G., 2000. The current limits of resolution for surface wave tomography in North America, *EOS*, **81**(B4).

Becker, T. W., 2012. On recent seismic tomography for the western United States, *Geochemistry Geophysics Geosystems*, **13**.

Bijwaard, H., Spakman, W., & Engdahl, E. R., 1998. Closing the gap between regional and global travel time tomography, *Journal of Geophysical Research-Solid Earth*, **103**(B12), 30055–30078.

Burdick, S., Li, C., Martynov, V., Cox, T., Eakins, J., Mulder, T., Astiz, L., Vernon, F. L., Pavlis, G. L., & van der Hilst, R. D., 2008. Upper mantle heterogeneity beneath North America from travel time tomography with global and USArray Transportable Array data, *Seismological Research Letters*, **79**, 384–390.

Burdick, S., Hilst, R. D., Vernon, F., Martynov, V., Cox, T., Eakins, J., Mulder, T., Astiz, L., & Pavlis, G., 2009. Model update December 2008: Upper mantle heterogeneity beneath North America from travel time tomography with global and USArray Transportable Array data., *Seismological Research Letters*, **80**, 638–645.

Burdick, S., van der Hilst, R. D., Vernon, F. L., Martynov, V., Cox, T., Eakins, J., Karasu, G. H., Tylell, J., Astiz, L., & Pavlis, G. L., 2010. Model update January 2010: Upper mantle heterogeneity beneath North America from traveltime tomography with global and USArray Transportable Array data, *Seismological Research Letters*, **81**(5), 689–693.

Burdick, S., van der Hilst, R. D., Vernon, F. L., Martynov, V., Cox, T., Eakins, J., Karasu, G. H., Tylell, J., Astiz, L., & Pavlis, G. L., 2012. Model update March 2011: Upper mantle heterogeneity beneath North America from traveltime tomography with global and USArray Transportable Array data, *Seismological Research Letters*, **83**(1), 23–28.

Burdick, S., de Hoop, M. V., Wang, S., & van der Hilst, R. D., 2013. Reverse-time migration-based reflection tomography using teleseismic free surface multiples, *Geophysics Journal International*, **in press**.

Burdick, S., van der Hilst, R. D., Vernon, F. L., Martynov, V., Cox, T., Eakins, J., Karasu, G. H., Tylell, J., Astiz, L., & Pavlis, G. L., 2014. Model update January 2013: Upper mantle heterogeneity beneath North America from traveltime tomography with global and USArray Transportable Array data, *Seismological Research Letters*, **in press**.

Camp, V. E. & Ross, M. E., 2004. Mantle dynamics and genesis of mafic magmatism in the intermontane Pacific Northwest, *Journal of Geophysical Research-Solid Earth*, **109**(B8).

Carannante, S., 2008. *Multiresolution spherical wavelet analysis in global seismic tomography*, Ph.D. thesis, Univeresita di Bologna.

De Hoop, M. V. & Van der Hilst, R. D., 2005. On sensitivity kernels for 'wave-equation' transmission tomography, *Geophysical Journal International*, **160**(2), 621–633.

Dueker, K., Yuan, H., & Zurek, B., 2001. Thick structured Proterozoic lithosphere of Western North America, *GSA Today*, **11**(12), 4–9.

Engdahl, E. R., van der Hilst, R., & Buland, R., 1998. Global teleseismic earthquake relocation with improved travel times and procedures for depth determination, *Bulletin of the Seismological Society of America*, **88**(3), 722–743.

Fichtner, A., Trampert, J., Cupillard, P., Saygin, E., Taymaz, T., Capdeville, Y., & Villasenor, A., 2013. Multiscale full waveform inversion, *Geophysical Journal International*, **194**(1), 534–556.

Fouch, M. J., 2012. The Yellowstone Hotspot: Plume or not?, *Geology*, **40**(5), 479–480.

Grand, S. P., 2002. Mantle shear-wave tomography and the fate of subducted slabs, *Philosophical Transactions of the Royal Society of London Series a-Mathematical Physical and Engineering Sciences*, **360**(1800), 2475–2491.

Humphreys, E. D., Dueker, K., Schutt, D. L., & Smith, R. B., 2000. Beneath Yellowstone: Evaluating plume and nonplume models using teleseismic images of the upper mantle, *GSA Today*, **10**, 1–6.

James, D. E., Fouch, M. J., Carlson, R. W., & Roth, J. B., 2011. Slab fragmentation, edge flow and the origin of the Yellowstone hotspot track, *Earth and Planetary Science Letters*, **311**(1-2), 124–135.

Jordan, B. T., Grunder, A. L., Duncan, R. A., & Deino, A. L., 2004. Geochronology of age-progressive volcanism of the Oregon High Lava plains: Implications for the plume interpretation of yellowstone, *Journal of Geophysical Research-Solid Earth*, **109**(B10).

Kennett, B. L. N., Engdahl, E. R., & Buland, R., 1995. Constraints on seismic velocities in the Earth from travel-times, *Geophysical Journal International*, **122**(1), 108–124.

Lekic, V. & Fischer, K., 2013. Contrasting lithospheric signatures across the western United States revealed by Sp receiver functions, *Earth and Planetary Science Letters*, **submitted**.

Li, C., van der Hilst, R. D., & Toksöz, A. N., 2006. Constraining P-wave velocity variations in the upper mantle beneath Southeast Asia, *Physics of the Earth and Planetary Interiors*, **154**(2), 180–195.

Li, C., van der Hilst, R. D., Engdahl, E. R., & Burdick, S., 2008a. A new global model for P wave speed variations in Earth's mantle, *Geochemistry Geophysics Geosystems*, **9**, Q05018.

Li, C., van der Hilst, R. D., Meltzer, A. S., & Engdahl, E. R., 2008b. Subduction of the Indian lithosphere beneath the Tibetan Plateau and Burma, *Earth and Planetary Science Letters*, **274**(1), 157 – 168.

Lou, X. & van der Lee, S., 2013. Notes on continental structure and formation from observed and predicted North American teleseismic delay times, *Earth and Planetary Science Letters*, **submitted**.

Montelli, R., Nolet, G., Masters, G., Dahlen, F. A., & Hung, S. H., 2004. Global P and PP traveltime tomography: rays versus waves, *Geophysical Journal International*, **158**(2), 637–654.

Nettles, M. & Dziewonski, A. M., 2008. Radially anisotropic shear velocity structure of the upper mantle globally and beneath North America, *Journal of Geophysical Research-Solid Earth*, **113**(B2).

Obrebski, M., Allen, R. M., Pollitz, F., & Hung, S.-H., 2011. Lithosphere-asthenosphere interaction beneath the western United States from the joint inversion of body-wave traveltimes and surface-wave phase velocities, *Geophysical Journal International*, **185**(2), 1003–1021.

Panning, M. P., Lekic, V., & Romanowicz, B. A., 2010. Importance of crustal corrections in the development of a new global model of radial anisotropy, *Journal of Geophysical Research-Solid Earth*, **115**.

Pavlis, G. L., Sigloch, K., Burdick, S., Fouch, M. J., & Vernon, F. L., 2012. Unraveling the geometry of the Farallon plate: Synthesis of three-dimensional imaging results from USArray, *Tectonophysics*, **532**, 82–102.

Perrier, V., Philipovitch, T., & Basdevant, C., 1995. Wavelet spectra compared to fourier spectra, *Journal of Mathematical Physics*, **36**(3), 15061519.

Piromallo, C., Vincent, A. P., Yuen, D. A., & Morelli, A., 2001. Dynamics of the transition zone under Europe inferred from wavelet cross-spectra of seismic tomography, *Physics of the Earth and Planetary Interiors*, **125**(14), 125 – 139.

Pollitz, F. F. & Mooney, W. D., 2013. Seismic structure of the central {US} crust and shallow upper mantle: Uniqueness of the reelfoot rift, *Earth and Planetary Science Letters*, **in press**.

Ritsema, J., Deuss, A., van Heijst, H. J., & Woodhouse, J. H., 2011. S40RTS: a degree-40 shear-velocity model for the mantle from new Rayleigh wave dispersion, teleseismic traveltime and normal-mode splitting function measurements, *Geophysical Journal International*, **184**(3), 1223–1236.

Ritzwoller, M. H., Shapiro, N. M., Barmin, M. P., & Levshin, A. L., 2002. Global surface wave diffraction tomography, *Journal of Geophysical Research-Solid Earth*, **107**(B12).

Roth, J. B., Fouch, M. J., James, D. E., & Carlson, R. W., 2008. Three-dimensional seismic velocity structure of the northwestern United States, *Geophysical Research Letters*, **35**(15).

Roy, M., MacCarthy, J. K., & Selverstone, J., 2005. Upper mantle structure beneath the eastern Colorado Plateau and Rio Grande rift revealed by Bouguer gravity, seismic velocities, and xenolith data, *Geochemistry, Geophysics, Geosystems*, **6**(10).

Schmandt, B. & Humphreys, E., 2010. Complex subduction and small-scale convection revealed by body-wave tomography of the western United States upper mantle, *Earth and Planetary Science Letters*, **297**(3-4), 435–445.

Sigloch, K. & Mihalynuk, M. G., 2013. Intra-oceanic subduction shaped the assembly of Cordilleran North America, *Nature*, **496**(7443), 50–+.

Simmons, N. A., Forte, A. M., Boschi, L., & Grand, S. P., 2010. GyPSuM: A joint tomographic model of mantle density and seismic wave speeds, *Journal of Geophysical Research-Solid Earth*, **115**.

Simons, F. J., van der Hilst, R. D., & Zuber, M. T., 2003. Spatiospectral localization of isostatic coherence anisotropy in Australia and its relation to seismic anisotropy: Implications for lithospheric deformation, *Journal of Geophysical Research: Solid Earth*, **108**(B5).

Simons, F. J., Loris, I., Nolet, G., Daubechies, I. C., Voronin, S., Judd, J. S., Vetter, P. A., Charlety, J., & Vonesch, C., 2011. Solving or resolving global tomographic models with spherical wavelets, and the scale and sparsity of seismic heterogeneity, *Geophysical Journal International*, **187**(2), 969–988.

Tromp, J., Tape, C., & Liu, Q. Y., 2005. Seismic tomography, adjoint methods, time reversal and banana-doughnut kernels, *Geophysical Journal International*, **160**(1), 195–216.

Wong, I. G., 2005. Low potential for large intraslab earthquakes in the central Cascadia subduction zone, *Bulletin of the Seismological Society of America*, **95**(5), 1880–1902.

Zhao, L. & Jordan, T. H., 2006. Structural sensitivities of finite-frequency seismic waves: a full-wave approach, *Geophysical Journal International*, **165**(3), 981–990.

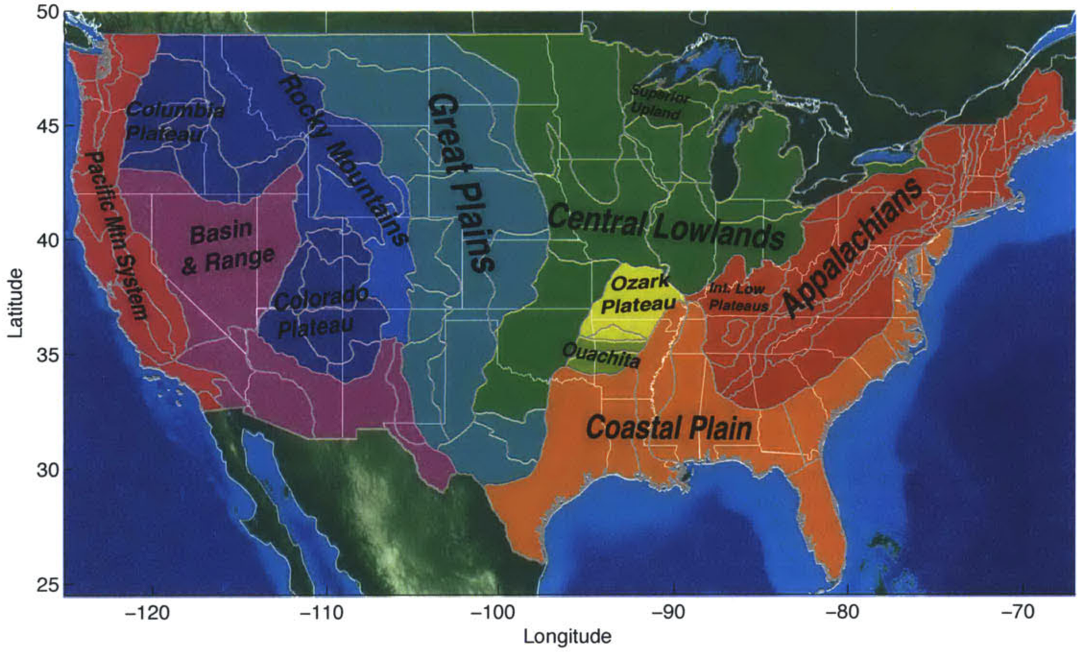

Figure 2-1: Major geological provinces of the United States (http://tapestry.usgs.gov/physiogr/physio.html) illuminated by USArray Transportable Array.

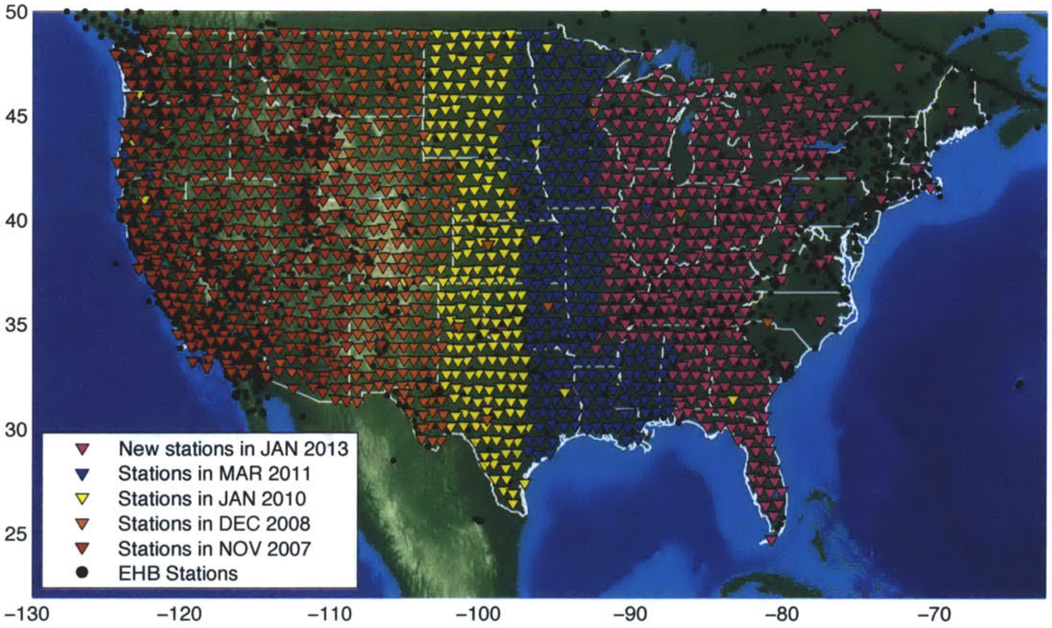

Figure 2-2: The progression of USArray TA stations used in MITP model updates. Red triangles represent station locations used in the November 2007 inversion, orange – December 2008, yellow – January 2010, blue – March 2011, purple – January 2013. Black dots show the locations of the EHB dataset in North America.

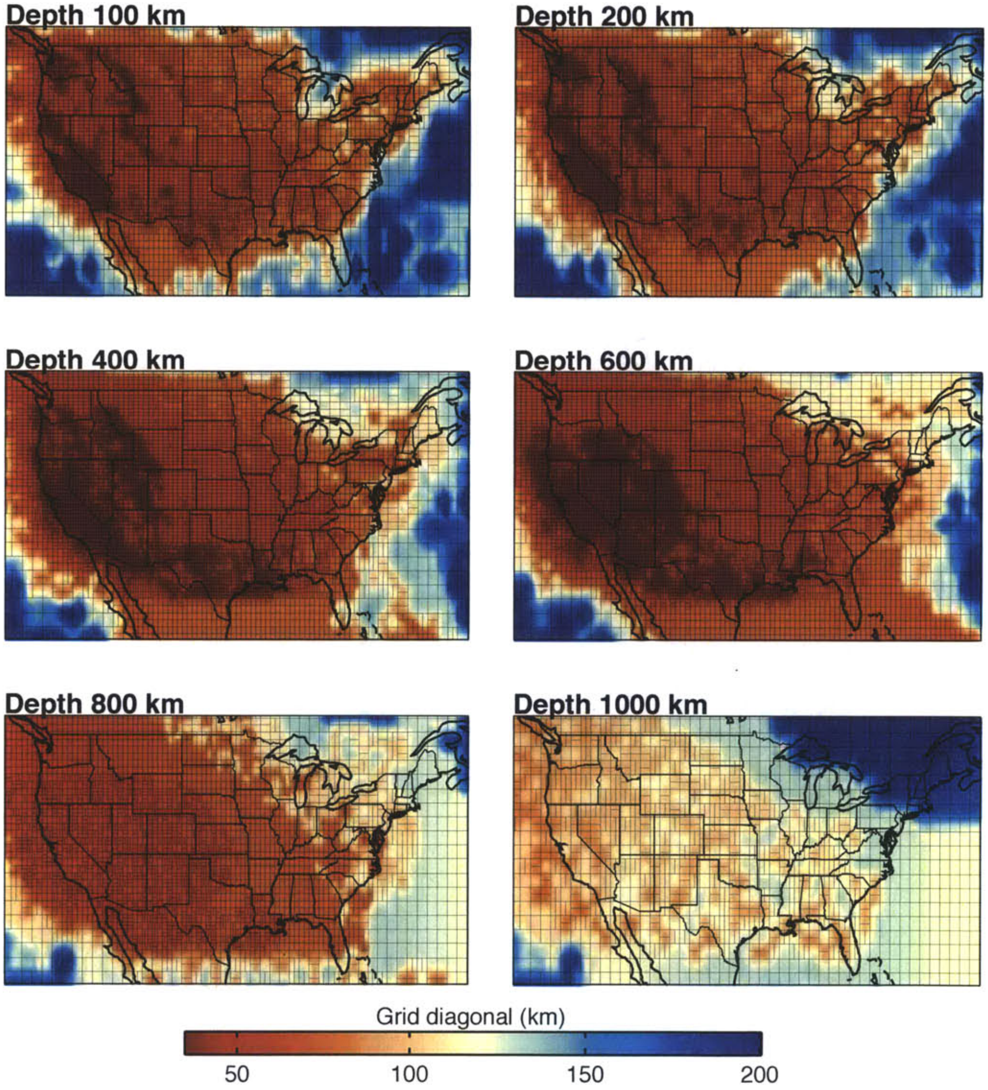

Figure 2-3: Irregular grid structure and various depths in the 2013JAN model. Colors correspond to an interpolation of the diagonal lengths of the irregular grid cells.

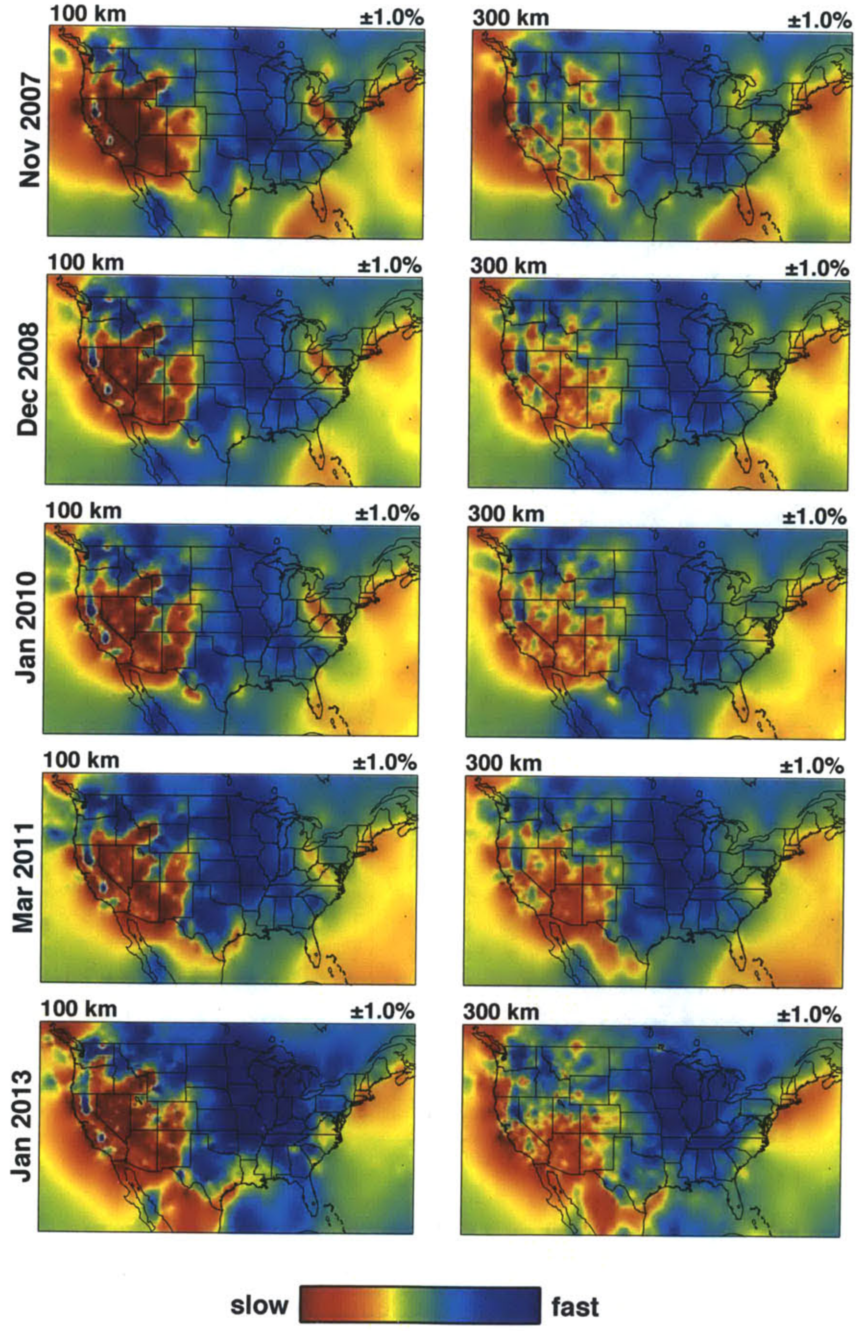

Figure 2-4: Iterations of the MITP community model at depths of 100 and 300 km.

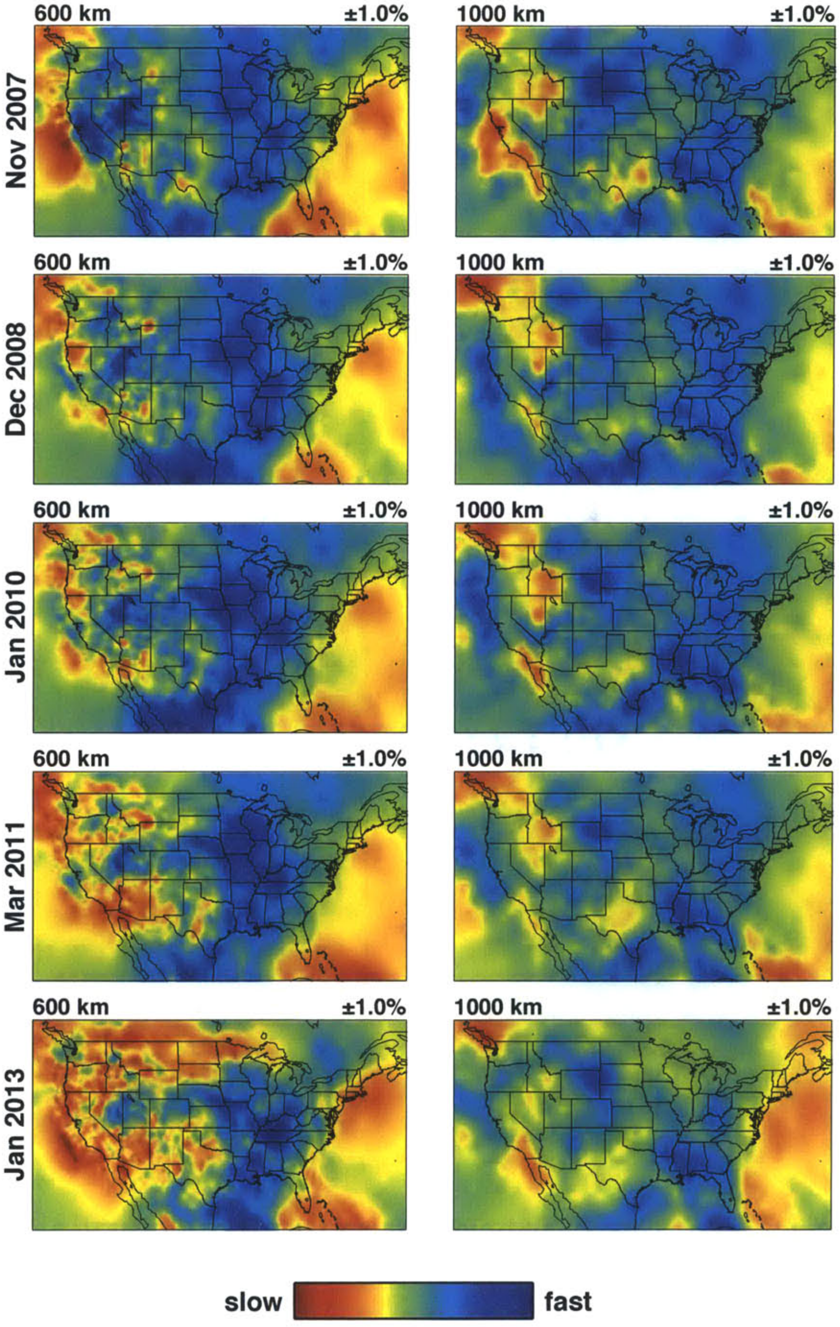

Figure 2-5: Iterations of the MITP community model at depths of 600 and 1000 km.

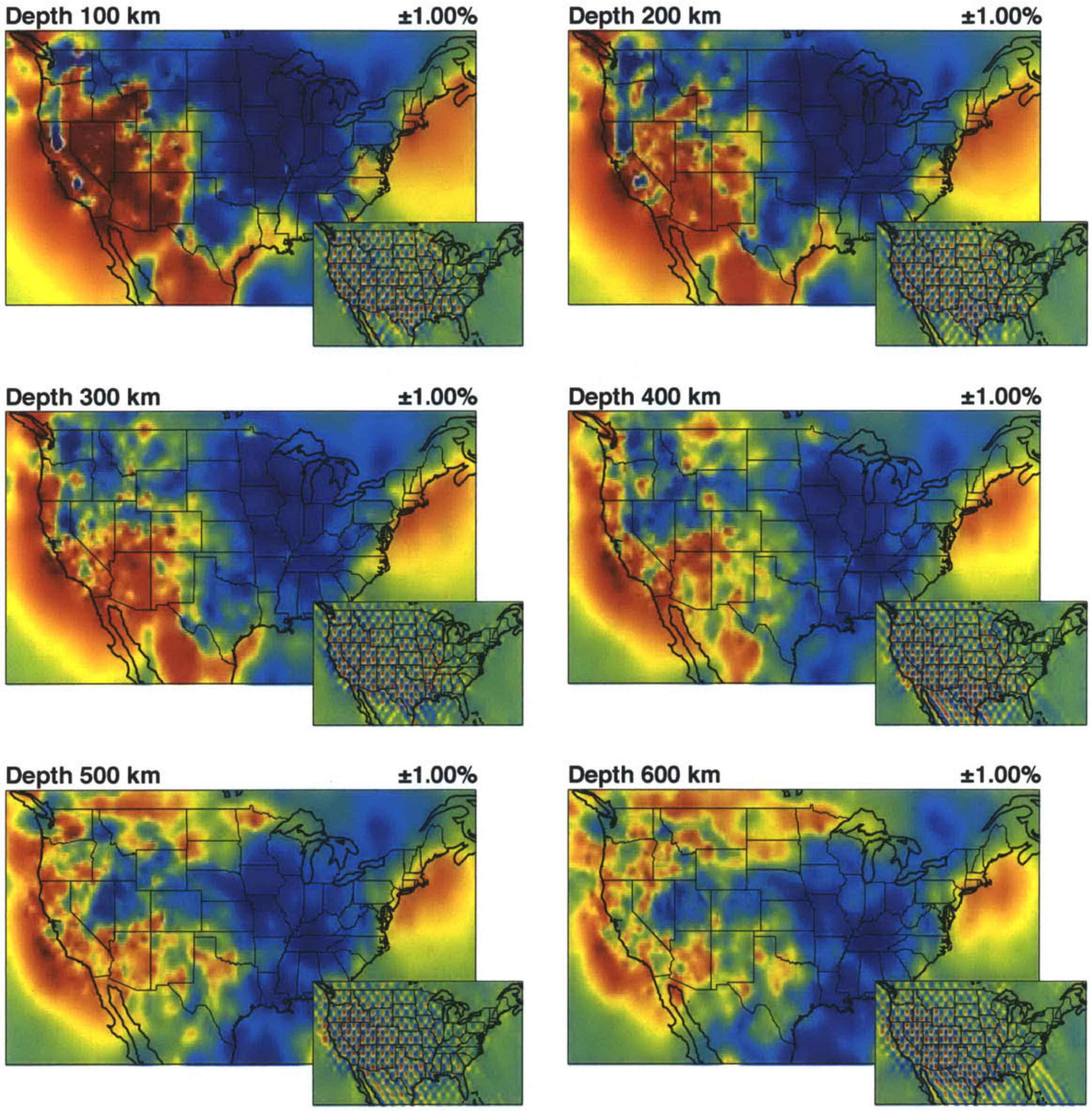

Depth 100 km ±1.00%

Depth 200 km ±1.00%

Depth 300 km ±1.00%

Depth 400 km ±1.00%

Depth 500 km ±1.00%

Depth 600 km ±1.00%

Figure 2-6: Maps and checkerboard resolution tests in MITP_USA_2013JAN at depths of 100, 200, 300, 400, 500 and 600 km. Fast regions are displayed as blue and slow regions are red. Resolution tests show the ability of the inversion to recover heterogeneity on the order of 1.5° by 1.5°.

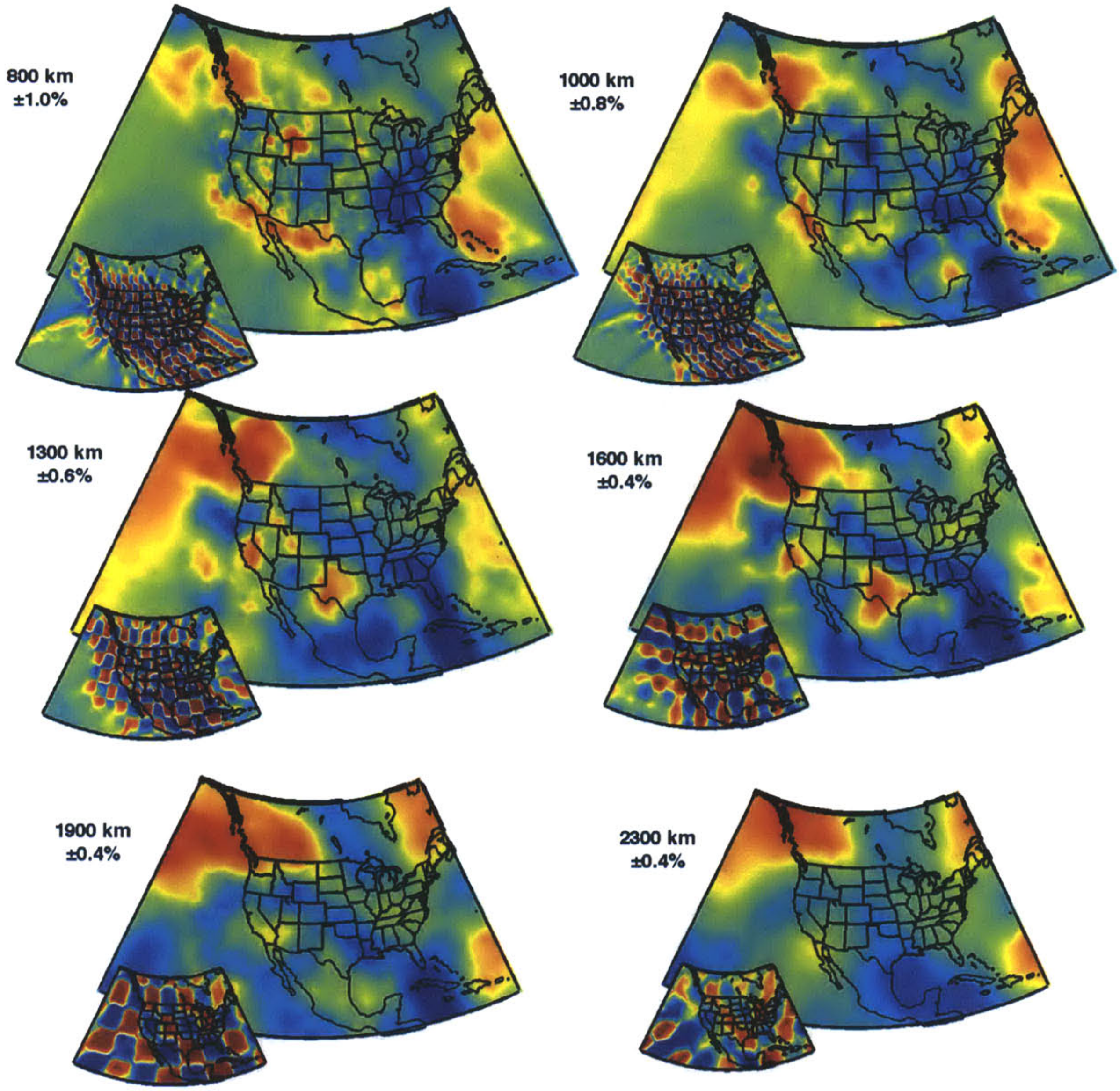

Figure 2-7: Maps and checkerboard resolution tests in MITP_USA_2013JAN at depths of 800, 1000, 1300, 1600, 1900 and 2300 km. The size of the figures is scaled based on the surface array of the region at the given depths. The checkerboard width is 1.5° by 1.5° at 800 and 1000km, 3° by 3° at 1300 and 1600 km, and 5° by 5° at 1900 and 2300 km.

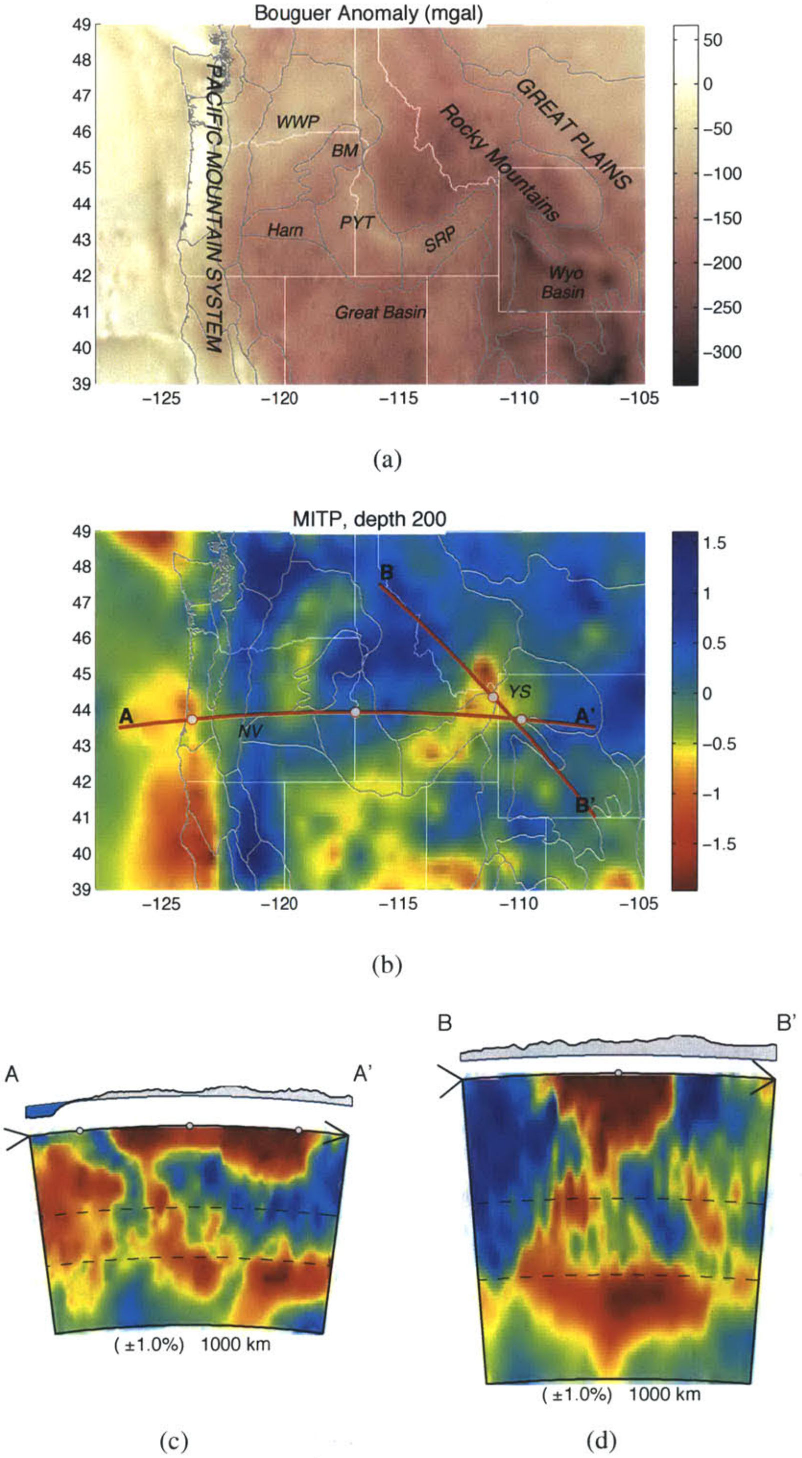

(a)

(b)

(c)

(d)

Figure 2-8: P velocity heterogeneity at the Yellowstone and the Columbia Plateau (a) Bouguer gravity anomaly in the region. Abbreviations: Walla Walla Plateau (WWP), Blue Mountain (BM), Payette (PYT), Harney (Harn), Snake River Plain (SNP) (b) MITP model at 200 km depth with Yellowstone (YS) and the Newberry Caldera (NV) marked. Red lines denote locations of cross sections for (c) and (d). (c) The subducted Juan de Fuca slab with the hole beneath the High Lava Plains. (d) The Yellowstone Hotspot signature at depth.

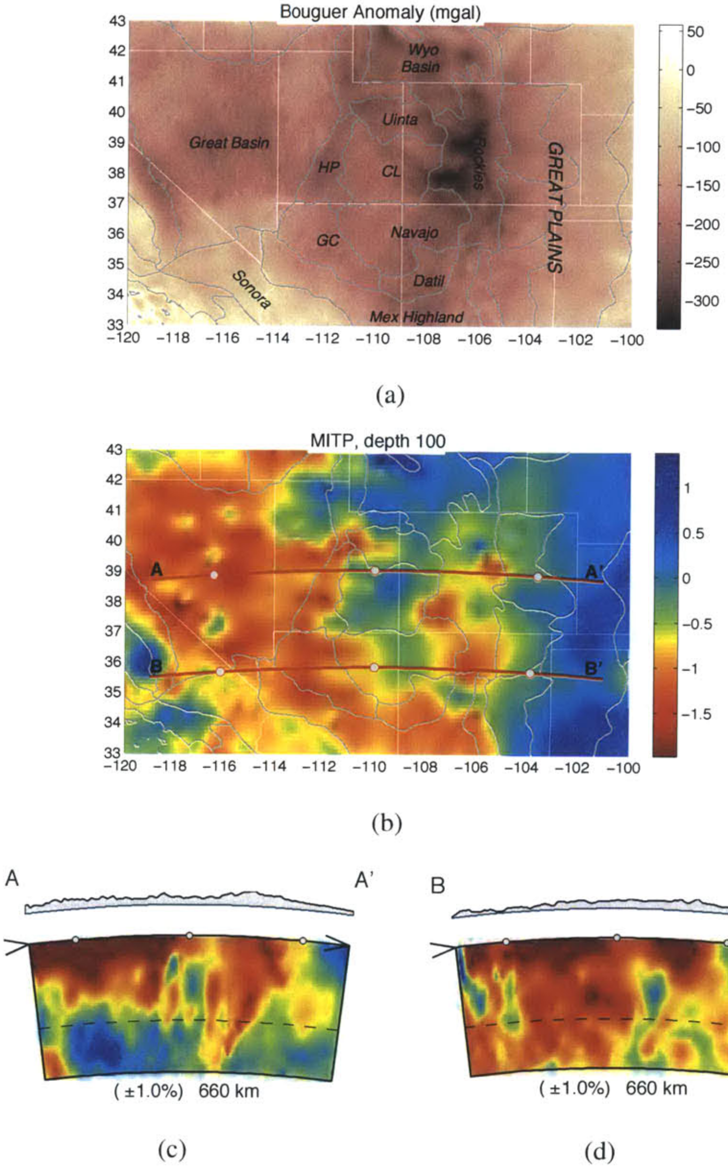

Figure 2-9: P velocity heterogeneity at and around the Colorado Plateau (a) Bouguer gravity anomaly in the region. Abbreviations: Uinta Basin (UB), High Plateaus (HP), Canyon Lands (CL), Grand Canyon (GC). (b) MITP model at 100 km depth. Cross sections in (c) and (d) show the variation from the Basin and Range to the Plateau.

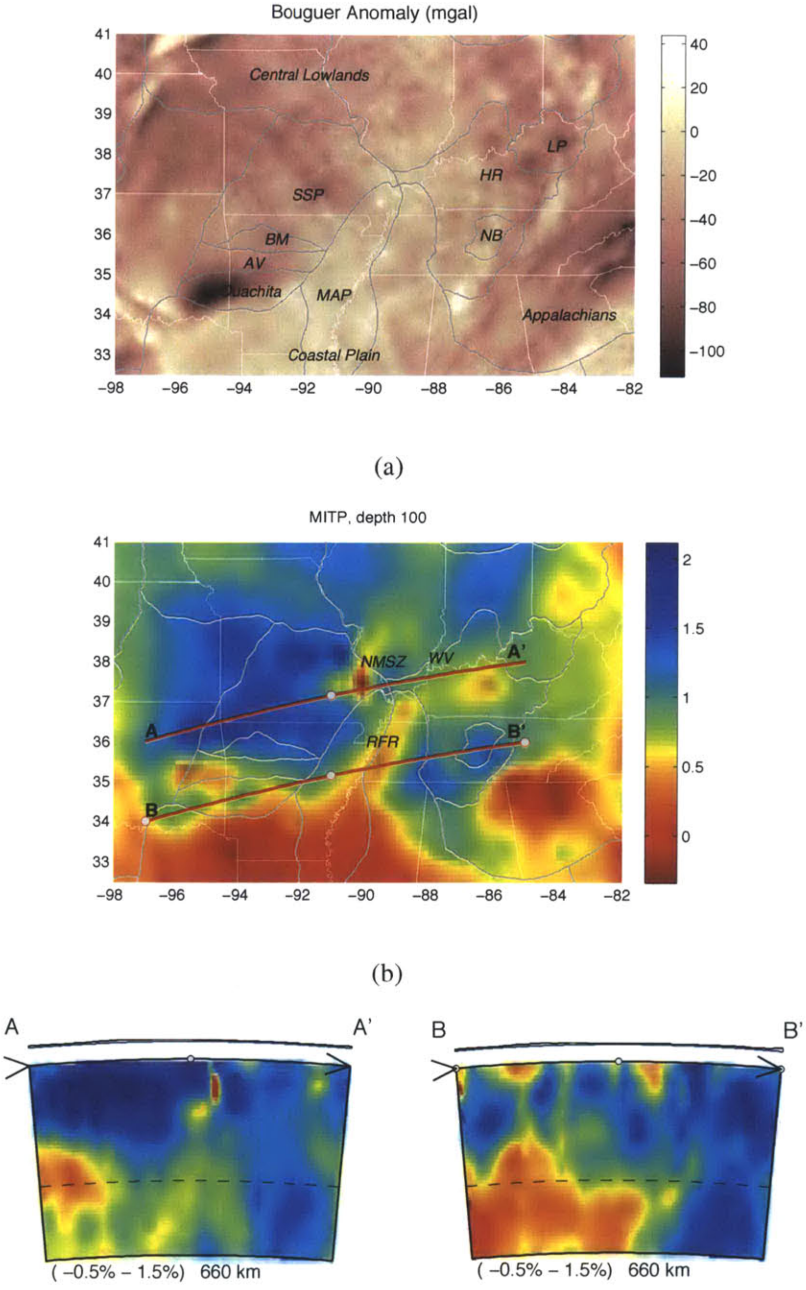

(a)

(b)

(c)

(d)

Figure 2-10: P velocity heterogeneity in provinces including the Interior Highlands Interior Low Plateaus. (a) Bouguer gravity anomaly in the region. Abbreviations: Springfield-Salem Plateaus (SSP), Boston Mountains (BM), Arkansas Valley (AV), Mississippi Alluvial Plain (MAP), Nashville Basin (NB), Highland RIM (HR), and Lexington Plain (LP). (b) MITP model at 100 km depth. Features include New Madrid Seismic Zone (NMSZ), Reelfoot Rift (RFR), and Wabash Valley Seismic Zone (WV). Red lines denote locations of cross sections in (c) and (d).

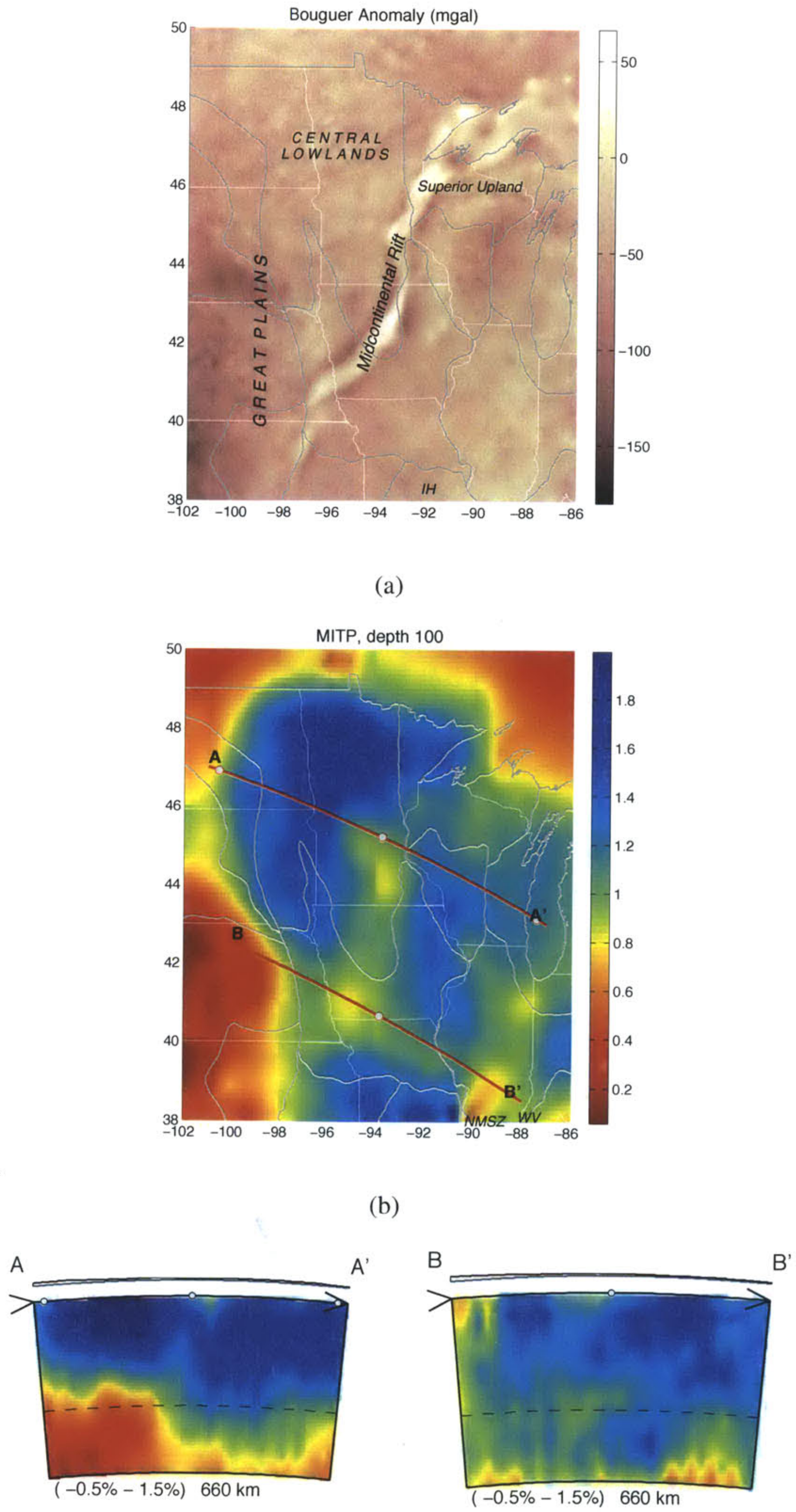

(a)

(b)

(c)

(d)

Figure 2-11: P velocity heterogeneity at the Midcontinental Rift System (a) Bouguer gravity anomaly in the region showing a strong gravity high along the location of the failed rift. (b) MITP model at 100 km depth. Cross sections (c) and (d) show the shallow signature of the rift.

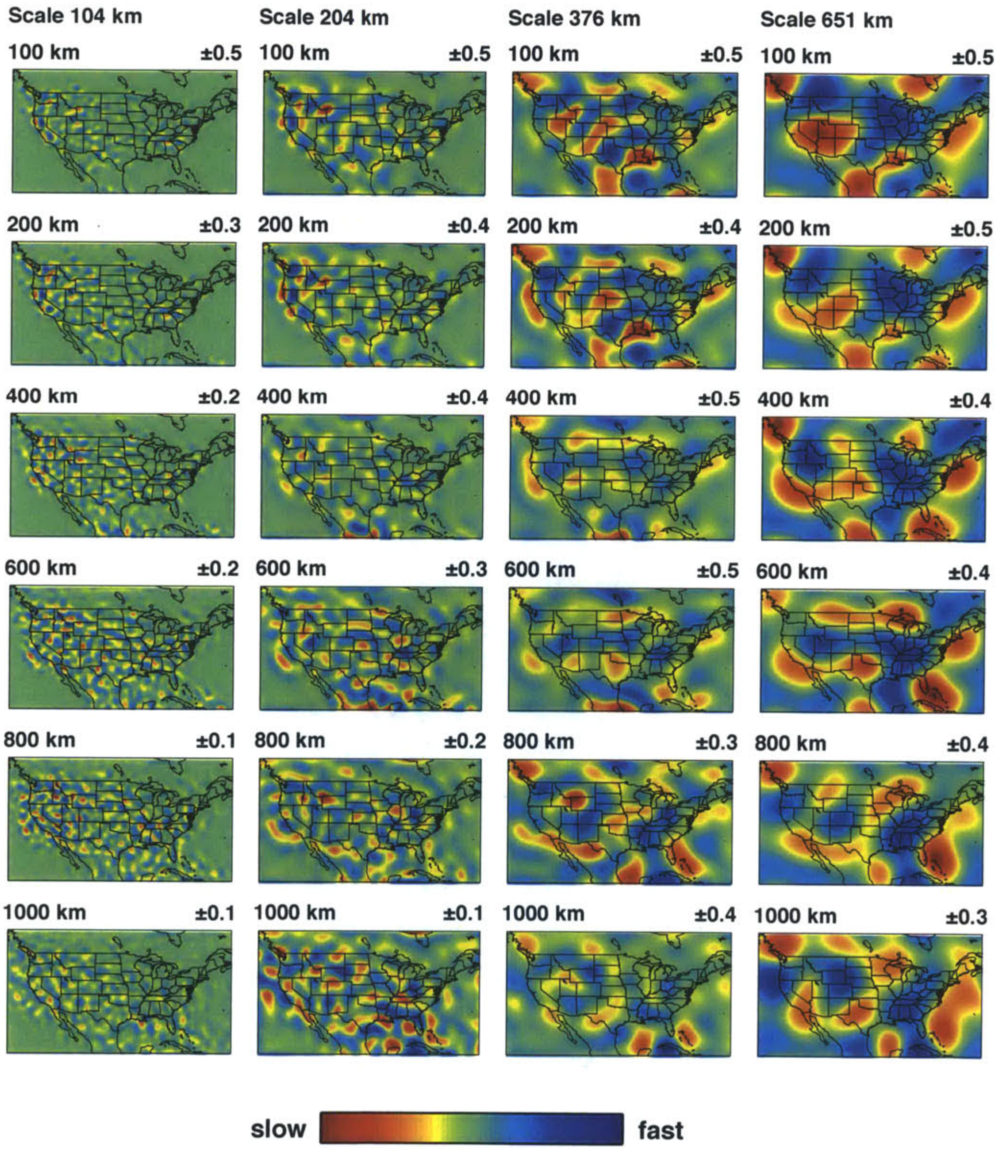

Figure 2-12: Continuous wavelet transform of the 2013 MITP model at various depths and length scales.

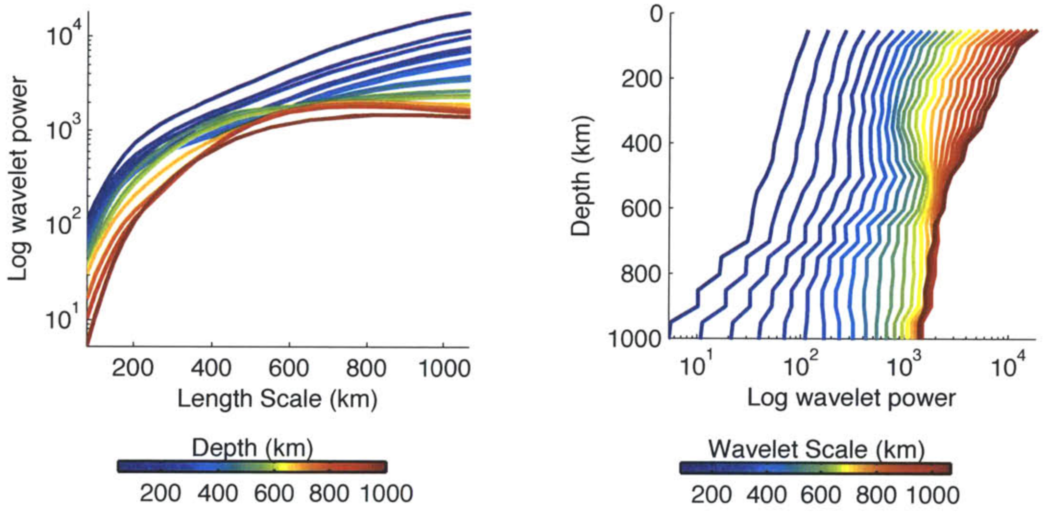

(a) (b)

Figure 2-13: Two different views of the wavelet power spectrum for the entire continental United States. (a) Log power according to wavelet length scale. Each colored line corresponds to the power for one depth between 50 and 1000 km. (b) Depth profiles of log wavelet power. Each line represents the power for one scale length from 100 to 1024 km.

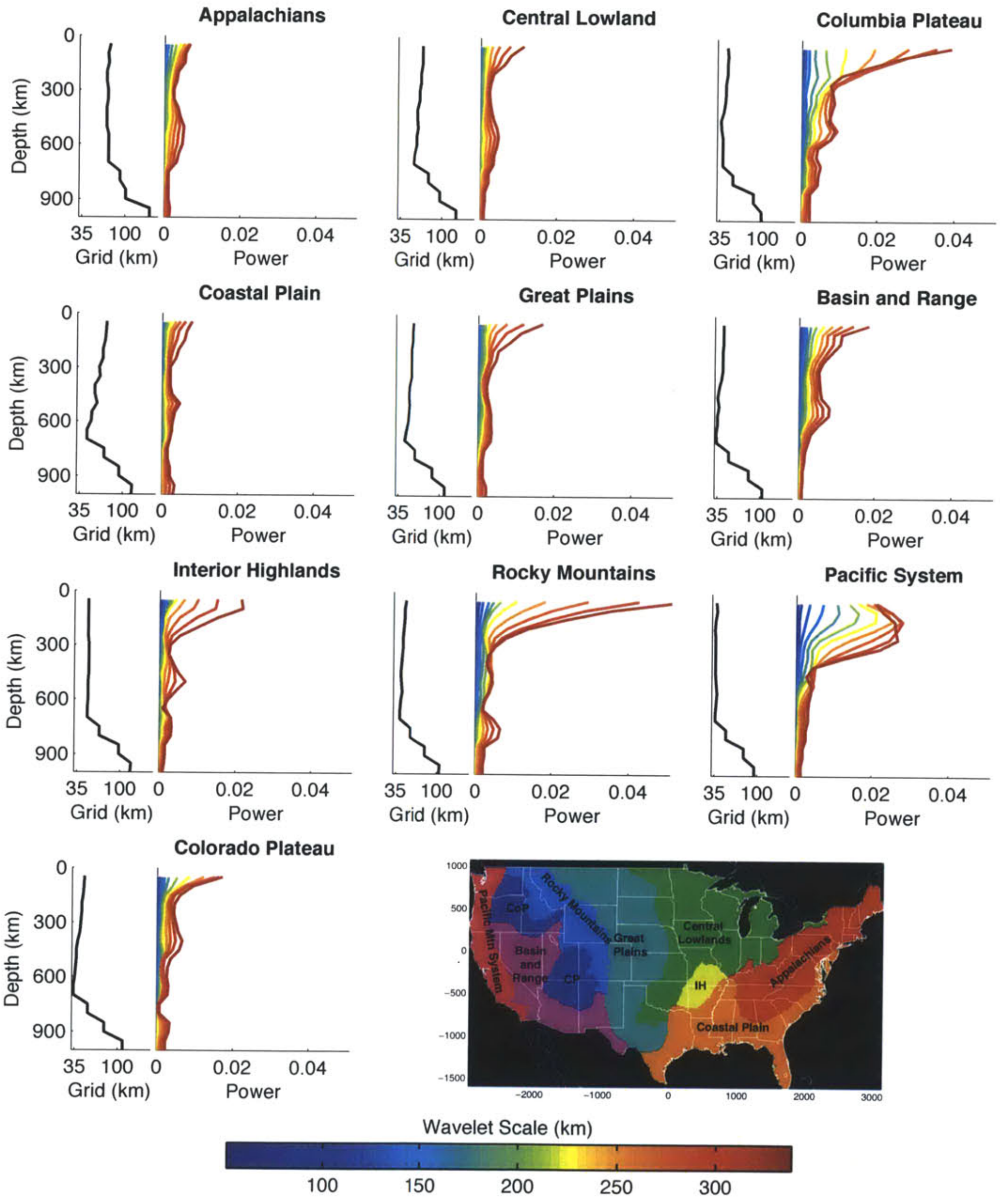

Figure 2-14: Depth profiles of regional wavelet power. Each line represents the power for one scale length from 100 to 376 km.

Chapter 3

One-way wave propagation for finite-frequency tomography on curvilinear coordinates

Abstract

In order to make use of the high-quality broadband seismic data pouring in from projects like USArray, it has become vital to develop tomography methods which make use of more of the wavefield when inverting for tomographic images. Finite-frequency wave equation tomography, using both transmitted and reflected components of the wavefield, offers the ability to utilize a greater part of the recorded data for imaging seismic heterogeneity at different scales. This added accuracy comes at a price, however, since wave equation methods are generally more computationally expensive. For higher computational efficiency in dealing with the large volumes of data, wavefield continuation can be carried out by large angle one-way wave propagators. These propagators cannot handle situations where turning waves occur, e.g. teleseismic studies or reflections off of lateral faults. To accommodate such geometries, a transformation to curvilinear coordinates where wavefront does not travel horizontally in one pseudodepth coordinate is necessary. To this end, we develop a computationally efficient curvilinear one-way propagator based on a rational approximation. By applying the seismic adjoint method to downward propagated data, we produce Fréchet sensitivity kernels on curvilinear coordinates which can be used to optimize a tomographic model.

3.1 Introduction

The abundance of broadband array data generated by projects such as USArray calls for the development of novel approaches to high-resolution tomography. Although ray theory-based approaches to tomography, such as the multi-scale method used by Li et al. (2008)

and Burdick et al. (2008), have been vital in illuminating large-scale mantle structure, additional information can be extracted from the broadband wavefield by accounting for finite-frequency effects. Instead of projecting data mismatch over ray paths defined by an asymptotic high frequency approximation, it can be projected onto a finite-frequency sensitivity kernel (Dahlen et al., 2000). This approach enables the proper interpretation of the effects of different frequencies on the resolution of different spatial scales. Furthermore, it allows lower frequency data to constrain smooth medium variations before high frequencies define small scale structure for improved speed and stability in the inversion (see Pratt (1999), for instance).

At the same time, analytical approaches to finite-frequency tomography fail to take into account the complicated nature of the wavefield in a 3-D, caustic-forming Earth (De Hoop & Van der Hilst, 2005). The most computationally efficient way to determine finite-frequency model updates is the seismic adjoint method, first developed by Tarantola (1984), which is based on the interation of a forward propagated source with a backward propagated "adjoint source" based on the error measure. Although determining the model gradient via the seismic adjoint method is much faster than individually perturbing each element of the tomographic model, the two propagation steps for each event in the data can still be quite computationally intensive. While propagation techniques such as Spectral Element Method (Tromp et al., 2008) are highly accurate, they may not represent the most useful means of computing wavefields for iterative updates in an efficient manner. In order to overcome the heavy computational expense inherent in tomographic inverse problems, we wish to make use of fast one-way wave equation migration techniques that have been developed in exploration seismology.

We develop our methodology with general application to transmission tomography and reflection tomography (known as migration velocity analysis (MVA) in the exploration setting) in mind. Two possible difficulties exist in the application of these methods to regional tectonic problems. First, one-way propagation does not allow for the possibility of wavefronts traveling horizontally or overturning, limiting the applicability to teleseismic phases. Second, most one-way techniques are developed for local scale surveys where Cartesian geometry is a good approximation to the true shape of the Earth. If we wish to do regional scale tomography or use phases that overturn in depth, such as lateral faults or underside reflections from discontinuities, while still taking advantage of these fast, accurate methods, we must carry out our propagation in a curvilinear coordinate system. Though previous studies have investigated coordinate systems generated by the rays associated with propagation (Sava & Fomel, 2005), we define curvilinear coordinates suited to a particular tectonic or geological setting. The coordinate transformation is based on a pseudodepth direction in which the waves of interest propagate. The one-way wave equation can then be transformed into this new coordinate system. In this paper, we will cast the curvilinear one-way equation into a computationally efficient thin-slab propagator based on the rational approximation. The propagated wavefield will then be used to calculate finite-frequency kernels for use in tomographic inversions.

3.2 One-way wave propagation in curvilinear coordinates

For application of wave-equation tomography to exploration and local scale problems, a Cartesian grid is an apt approximation of the Earth. However, for continental scale arrays such as USArray or for global applications, the curvature of the Earth cannot be ignored. Additionally, there exist many situations where turning waves occur, such as most teleseismic phases, or reflections off of vertical faults or salt flanks in exploration seismology. For one-way propagation, we require that the waves do no travel horizontally before encountering a scattering point or a receiver. To accommodate situations such as salt flank reflections or turning waves in strongly heterogeneous media, we transform the one-way wave equation into curvilinear coordinates.

3.2.1 Transforming the wave equation

We denote the cartesian coordinate system with horizontal coordinates x_1 and x_2 and vertical coordinate z. The curvilinear coordinate system is then denoted by $\tilde{x}_1 = \tilde{x}_1(x_1, x_2, z), \tilde{x}_2 = \tilde{x}_2(x_1, x_2, z)$, and pseudodepth coordinate $\tilde{z} = \tilde{z}(x_1, x_2, z)$. The pseudodepth coordinate is required to be orthogonal to the other coordinates, while the lateral coordinates need not be orthogonal. The Riemannian transformation metric in three dimensions is given by

$$\tilde{g}_{ij} = \frac{\partial(x,z)^l}{\partial(\tilde{x},\tilde{z})^i}\delta_{lk}\frac{\partial(x,z)^k}{\partial(\tilde{x},\tilde{z})^j} = \begin{pmatrix} \tilde{g}_{11} & \tilde{g}_{12} & 0 \\ \tilde{g}_{21} & \tilde{g}_{22} & 0 \\ 0 & 0 & \tilde{g}_{33} \end{pmatrix}_{ij}, \tag{3.1}$$

where we sum over repeated indices. δ_{lk} is the Kronecker delta function and $\frac{\partial(x,z)^j}{\partial(\tilde{x},\tilde{z})^i}$ represents the derivative of the j^{th} Cartesian coordinate according to the i^{th} curvilinear coordinate. Using the notation where subscripts represent the transformation from Cartesian to curvilinear and superscripts represent the inverse transformation, the inverse metric is given as $(\tilde{g}_{ij})^{-1} = \tilde{g}^{ij}$. For the purposes of this paper, we proceed in two dimensions, $\tilde{x} = \tilde{x}(x,z), \tilde{z} = \tilde{z}(x,z)$, but calculations can be extended to three dimensions.

The curvilinear acoustic wave equation is derived in Stolk & de Hoop (2007) via the variational formula by transforming the action functional into curvilinear coordinates according to the Riemannian metric and setting the its perturbation to zero. The resulting wave equation is:

$$\kappa \left|\frac{\partial(x,z)}{\partial(\tilde{x},\tilde{z})}\right| \frac{\partial^2 \tilde{u}}{\partial t^2} - \frac{\partial}{\partial \tilde{z}}\left(\alpha \frac{\partial \tilde{u}}{\partial \tilde{z}}\right) - \frac{\partial}{\partial \tilde{x}}\left(\rho^{-1}\left|\frac{\partial(x,z)}{\partial(\tilde{x},\tilde{z})}\right| \tilde{g}^{11}\frac{\partial \tilde{u}}{\partial \tilde{x}}\right) = f\left|\frac{\partial(x,z)}{\partial(\tilde{x},\tilde{z})}\right| \tag{3.2}$$

$$\kappa\,|\mathbf{g}|\,\frac{\partial^2 \tilde{u}}{\partial t^2} - \frac{\partial}{\partial \tilde{z}}\left(\rho^{-1}\,|\mathbf{g}|\,\tilde{g}_{33}\frac{\partial \tilde{u}}{\partial \tilde{z}}\right) - \frac{\partial}{\partial \tilde{x}}\left(\rho^{-1}\,|\mathbf{g}|\,\tilde{g}^{11}\frac{\partial \tilde{u}}{\partial \tilde{x}}\right) = f\,|\mathbf{g}|, \tag{3.3}$$

with $\alpha \equiv \rho^{-1}\tilde{g}_{33}\left|\frac{\partial(x,z)}{\partial(\tilde{x},\tilde{z})}\right|$, density $\rho(\tilde{x},\tilde{z})$ and compliance $\kappa(\tilde{x},\tilde{z})$. Transformation according to the action principle gives a proper acoustic wave equation on a Riemannian metric. With the assumption that $\rho(\tilde{x},\tilde{z})$ varies slowly, this simplifies to the curvilinear wave equation (Eq. 7) of Sava & Fomel (2005).

3.2.2 Directional decomposition

After Fourier transforming into the time frequency domain, we define the curvilinear wavefield as $\tilde{U}(\tilde{x},\tilde{z},\omega) = U(x(\tilde{x},\tilde{z}), z(\tilde{x},\tilde{z}),\omega)$. We write the resulting curvilinear Helmholtz equation as a first-order system in $\tilde{z}$.

$$\left(\frac{\partial}{\partial \tilde{z}} - i\omega A\right)\begin{pmatrix} \tilde{U} \\ -i\omega^{-1}\alpha\frac{\partial \tilde{U}}{\partial \tilde{z}} \end{pmatrix} = \begin{pmatrix} 0 \\ f\left|\frac{\partial(x,z)}{\partial(\tilde{x},\tilde{z})}\right| \end{pmatrix}, \tag{3.4}$$

where

$$A = \begin{pmatrix} 0 & \alpha^{-1} \\ \kappa\left|\frac{\partial(x,z)}{\partial(\tilde{x},\tilde{z})}\right| + \omega^{-2}\frac{\partial}{\partial \tilde{x}}\rho^{-1}\left|\frac{\partial(x,z)}{\partial(\tilde{x},\tilde{z})}\right|\tilde{g}^{11}\frac{\partial}{\partial \tilde{x}} & 0 \end{pmatrix}.$$

This allows us to derive the one-way wave equation by diagonalizing the system by finding its eigenvalues. In a self-adjoint formulation, the eigenvalues are found to be $\Gamma = (A_{12}^{1/2}A_{21}A_{12}^{1/2})^{1/2}$, with $c(\tilde{x},\tilde{z})^{-2} = \rho\kappa$. These values define the pseudodifferential vertical slowness operator, or the "square root operator:"

$$\Gamma = \sqrt{c^{-2}\tilde{g}_{33} + \omega^{-2}\frac{\partial}{\partial \tilde{x}}\tilde{g}^{11}\tilde{g}_{33}\frac{\partial}{\partial \tilde{x}}}. \tag{3.5}$$

A can then be written as a matrix product of a diagonal eigenmatrix Λ and the normalization matrix Q, with its inverse:

$$A = \mathrm{Q}\Lambda\mathrm{Q}^{-1} = \frac{1}{2}\begin{pmatrix} \Gamma^{-\frac{1}{2}} & \Gamma^{-\frac{1}{2}} \\ \mathcal{H}\Gamma^{\frac{1}{2}} & -\mathcal{H}\Gamma^{\frac{1}{2}} \end{pmatrix}\begin{pmatrix} \Gamma & 0 \\ 0 & -\Gamma \end{pmatrix}\begin{pmatrix} \Gamma^{\frac{1}{2}} & -\mathcal{H}\Gamma^{-\frac{1}{2}} \\ \Gamma^{\frac{1}{2}} & \mathcal{H}\Gamma^{-\frac{1}{2}} \end{pmatrix}, \tag{3.6}$$

where $\mathcal{H}$ is the Hilbert transform. By premultiplying the equation by Q^{-1}, the wavefield $\tilde{U}$ can be effectively split into upgoing and downgoing constituents where $\tilde{U}_+$ and $\tilde{U}_-$ are defined as

$$\begin{pmatrix} \tilde{U}_+ \\ \tilde{U}_- \end{pmatrix} \equiv \mathrm{Q}^{-1}\begin{pmatrix} \tilde{U} \\ -i\omega^{-1}\alpha\frac{\partial \tilde{U}}{\partial \tilde{z}} \end{pmatrix}.$$

The forcing function f is similarly split into an upgoing and downgoing components, with $f_\pm = \pm\frac{1}{2}\mathcal{H}\Gamma^{-\frac{1}{2}}$. The separation of the wave equation into upgoing and downgoing parts requires that $\frac{\partial}{\partial \tilde{z}}$ and Q commute, and therefore assumes c changes slowly with $\tilde{z}$. For the purposes of tomography, this constitutes a reasonable assumption, as propagation will be performed on a smooth background model, and any backscattering will be modeled separately using a Born scattering approximation. From several possible normalizations, we choose this particular Q because the coupling term ignored by this assumption includes only backscattering effects.

The square root operator represents only the principal symbol of the one-way equation. If $c, \tilde{g}^{11}$ or $\tilde{g}_{33}$ varies strongly with $\tilde{x}$, the action of square root operator on itself results in the wave equation plus some extra terms. In this case, the next term in the operator, the subprincipal operator, is necessary for the correct amplitude. For the purposes of cross correlation-based transmission and reflection tomography, the effects of wave amplitude may be slight, so the subprinciple symbol is omitted here. The final one way wave equation is then written in the form:

$$\frac{\partial}{\partial \tilde{z}}\tilde{U}_{\pm} \pm i\omega\Gamma\tilde{U}_{\pm} = f_{\pm}. \tag{3.7}$$

The fundamental solution for the one-way wave equation in the positive direction, $G_+ = G_+(\tilde{x}, \tilde{z}, \omega; \tilde{x}_0\tilde{z}_0)$, is then

$$\left(\frac{\partial}{\partial \tilde{z}} - i\omega\Gamma_+\right) G_+ = \delta(\tilde{x} - \tilde{x}_0)\delta(\tilde{z} - \tilde{z}_0). \tag{3.8}$$

3.3 Numerical scheme

3.3.1 Discretization of the single square root operator

Previous studies (Sava & Fomel, 2005; Sava et al., 2004) have investigated curvilinear coordinate systems conforming to the extrapolated high frequency wavefield, thereby reducing the need for high angular accuracy. If the coordinate system does not closely follow the direction of propagation or if the medium forms caustics, low order approximations are not adequate (Sava & Fomel, 2008). As we expect to determine the coordinate system based on known tectonic features, we desire an approximation with a balance high accuracy and low computation time. Thus, from a number of numerical approximations of the square root operator, we proceed via a (2,1) rational approximation, which is equivalent to the 3rd order Thiele approximation of de Hoop & de Hoop (1992). We use this approximation for its high angular accuracy and extendibility to three dimensions.

We generalize the method of Van Stralen et al. (1998) for use in curvilinear coordinates. Using the rational approximation, we seek to express the square root operator as the quotient of two Taylor series. For the desired angular accuracy, the series in the numerator is extended to the second degree and the series in the denominator to the first degree. Defining $\Xi \equiv -\tilde{g}_{33}^{-1/2}\frac{c}{\omega^2}\frac{\partial}{\partial\tilde{x}}\tilde{g}^{11}\tilde{g}_{33}\frac{\partial}{\partial\tilde{x}}\tilde{g}_{33}^{-1/2}c$, we have a self-adjoint rational representation of the single square root operation:

$$\begin{aligned}\Gamma &= \sqrt{\frac{\tilde{g}_{33}^{1/2}}{c}}\sqrt{1+\Xi}\sqrt{\frac{\tilde{g}_{33}^{1/2}}{c}}, \\ \Gamma^{III} &= \sqrt{\frac{\tilde{g}_{33}^{1/2}}{c}}\left(1+[1+\beta_3\Xi]^{-1}[\beta_1\Xi+\beta_2\Xi^2]\right)\sqrt{\frac{\tilde{g}_{33}^{1/2}}{c}},\end{aligned} \tag{3.9}$$

where we define the approximate square root equation as Γ^{III}. Solving for the coefficients yields $\beta_1 = 1/2, \beta_2 = 1/8, \beta_3 = 1/2$.

Comoving frame of reference

Next, in order to further improve computational accuracy and reduce discretization artifacts, we shift Γ into the comoving frame of reference (Claerbout, 1970). The function $\tau(\tilde{x})$ gives the approximate time it takes for a wave traveling in the pseudodepth coordinate to reach level $\tilde{z}$

$$\tau(\tilde{x}) = \int_0^{\tilde{z}} c^{-1}(\tilde{x},\zeta)\sqrt{\tilde{g}_{33}}d\zeta. \tag{3.10}$$

This allows for waves traveling straight downwards in $\tilde{z}$ to be modeled perfectly. After the applying a shift into the co-moving frame of reference, we rewrite the approximate one-way equation in the form:

$$\frac{\partial}{\partial\tilde{z}}\tilde{U} + i\omega\left(e^{i\omega\tau}\Gamma^{III}e^{-i\omega\tau} - \frac{\sqrt{g^{33}}}{c}\right)\tilde{U} = 0. \tag{3.11}$$

Discretization of the Laplace operator

We add additional accuracy at no additional computational cost by using an implicit implementation of the approximate Laplace operator (Mitchell & Griffiths, 1985).

$$\langle \Xi \rangle = (1 + a\Delta\tilde{x}^2\hat{\Xi})^{-1}\hat{\Xi} \tag{3.12}$$

where $\hat{\Xi}$ is the central difference discretization of Ξ in $\tilde{x}$. From the Taylor expansion, the value $a = 1/12$ is found.

Matrix system

With this approximation of the square root equation, we develop a "thin slab" propagator. The propagator will solve for the wavefield in each pseudodepth "slab" $\tilde{z}_i$ based on the slab above it, $\tilde{z}_{i-1}$. Before propagating, the wavefield in the first depth and any source function are acted on by the normalization operator Q^{-1}, which ensures accurate amplitude of propagation.

The solution of equation (3.7) is a product integral, and can be approximated with another (1,1) rational approximation, which leads to a finite difference scheme, accurate up to order $\Delta\tilde{z}^3$ (Richtmeyer & Morton, 1967).

$$\begin{aligned}\tilde{U}(\tilde{x}, \tilde{z}_i + \Delta\tilde{z}) &\approx e^{-i\omega\Delta\tilde{z}\Gamma^{III}(\tilde{x},\tilde{z}_i+\frac{1}{2}\Delta\tilde{z})}\tilde{U}(\tilde{x}, \tilde{z}_i) \\ &\approx \frac{1 - i\omega\Delta\tilde{z}\beta_4\Gamma^{III}}{1 + i\omega\Delta\tilde{z}\beta_4\Gamma^{III}}\tilde{U}(\tilde{x}, \tilde{z}_i).\end{aligned} \tag{3.13}$$

This operation can be written as the multiplication of the wavefield at slab $\tilde{z}$ by two matrices and the inverses of two matrices. The computationally intensive steps in this scheme are the inversion of one tridiagonal matrix and one five-banded matrix, both of dimension n_x, the number of nodes in the $\tilde{x}$ direction. These can be efficiently solved using a forward-backward substitution algorithm where the number of operations necessary is proportional to n_x (Golub & Van Loan, 1995). The propagated wavefield at each depth is then shifted out of the comoving frame and subjected to the normalization Q to find the final observable wavefield.

Parameter optimization

To further improve the angular accuracy of propagation, β_1, β_2, β_3, β_4, and a can be optimized. Denoting γ as the symbol of the square root slowness operator (the operator transformed into the wavenumber domain, in other words), Van Stralen et al. (1998) minimized the differences between the slowness operator and the group slowness of the approximate operator, γ_{group}, and the difference between the group slowness and phase slowness, γ_{phase}. Numerical anisotropy is given by $\gamma_{group} - \gamma$ and $\gamma_{phase} - \gamma_{group}$ gives the numerical dispersion. The optimized coefficients are $\beta_1 = 0.486, \beta_2 = 0.349, \beta_3 = 0.841, \beta_4 = 0.529$ and $a = 0.114$. These optimized coefficients hold for curvilinear coordinate systems. Figure 3-1 demonstrates the effect of the optimized parameters on the shape of the dispersion curve in polar coordinates compared to the analytically determined parameters.

3.3.2 Discretization of normalization operators

The discretization of Q requires the approximation of two pseudodifferential operators of the form $(1+\Xi)^{\pm\frac{1}{4}}$, with Ξ as above. This is achieved using a rational approximation to degree 2 in both the numerator and denominator.

$$\begin{aligned} \Gamma^{\frac{1}{2}} &= \left(\frac{\tilde{g}_{33}^{1/2}}{c}\right)^{\frac{1}{4}} (1+\Xi)^{\frac{1}{4}} \left(\frac{\tilde{g}_{33}^{1/2}}{c}\right)^{\frac{1}{4}} \\ &\approx \left(\frac{\tilde{g}_{33}^{1/2}}{c}\right)^{\frac{1}{4}} \frac{1+\alpha_1\Xi+\alpha_2\Xi^2}{1+\alpha_3\Xi+\alpha_4\Xi^2} \left(\frac{\tilde{g}_{33}^{1/2}}{c}\right)^{\frac{1}{4}}. \end{aligned} \tag{3.14}$$

The optimal parameters of the approximation were found using a least squares algorithm and are $\alpha_1 = 1.7854$, $\alpha_2 = 0.7854$, $\alpha_3 = 1.5623$, and $\alpha_1 = 0.5655$. The $\Gamma^{-\frac{1}{2}}$ operator inverts the numerator and denominator of the approximation, and is similarly accurate. These normalizations are applied to the wavefield before and after the complete propagation for each frequency. Figure 3-2 demonstrates the effect of the normalization of the propagation operator. The unnormalized propagator results in a directional source, while the application of the normalization operators leads to an isotropic source function, resulting in more accurate wide angle propagation.

3.3.3 Computational considerations for propagation

Perfectly matched layers

To prevent nonphysical reflections from the boundaries of the computational grid, it is necessary to use an absorbing boundary condition. Perfectly matched layers (PML) based on Collino (1997) were put into place on the $\tilde{x}$ boundaries. The PML is achieved by complexifying the Laplacian operator in the region where damping occurs.

$$\Xi \to -\tilde{g}_{33}^{-1/2}\frac{c}{\omega^2}\frac{i\omega}{i\omega+\sigma}\frac{\partial}{\partial\tilde{x}}\tilde{g}^{11}\tilde{g}_{33}\frac{i\omega}{i\omega+\sigma}\frac{\partial}{\partial\tilde{x}}\tilde{g}_{33}^{-1/2}c, \tag{3.15}$$

where $\sigma(\tilde{x}) = 0$ in the freely propagating medium and is determined to create the weakest reflection in the damping region. Figure 3-3 demonstrates the results of the propagator with perfectly matched layers on Cartesian coordinates. Due to the thin-slab propagator used, absorbing conditions are unnecessary at the lower $\tilde{z}$ boundary. The PML method is advantageous because no reflection is generated at the interface of the PML and the free medium. This allows for the damping parameter to be very strong, whereas standard damping requires a more gradual attenuation of the wave. The result is fewer damping layers in $\tilde{x}$ are required to attenuate unwanted waves, which is especially important in this method since the most computationally intensive steps in the numerical scheme are proportional to n_x.

Complexification of parameters

With $\tilde{k}_x^2$ equivalent to the symbol of Ξ, the real part of the square root operator is zero when $\tilde{k}_x^2 < 1$. However, the real part of the approximated operator is nonzero, which causes numerical artifacts. Further improvements can be made in the suppression of artifacts caused by postcritically propagating modes if we allow the approximation parameters and frequency to be complex. By allowing $\omega \to \omega(1-i\Omega)$ in equation 3.7, we introduce an amplification factor to each plane wave component of the propagating wave. This amplification factor is near unity for horizontal wavenumber $\tilde{k}_x^2 < 1$, and tapers off quickly at the critical values. The optimal complex values for the parameters of the approximations, the implicit finite difference variable, and the frequency were found by minimizing the imaginary parts of the phase and group slowness in addition to the numerical anisotropy and dispersion, as above.

These complex parameters, when multiplying the complex Laplacian operators needed for the perfectly matched layers, create singular changes in the medium properties, causing nonphysical reflections. In order to avoid interfering with the PMLs, the imaginary parts of the parameters are tapered near the computational boundaries.

3.4 Application to tomography

3.4.1 The seismic adjoint method

Finite frequency Fréchet kernels give the sensitivity of an error measure to various model parameters and are used to find the direction of the model update for iterative optimization. In wave-equation tomography schemes, these kernels are most efficiently calculated using the seismic adjoint method. In the adjoint method, the sensitivity is determined by an interaction of the forward propagated source with the back-propagated error function residual at points within the medium. Previous applications of the seismic adjoint method to transmission tomography have focused on the use of normal mode summation (De Hoop & Van der Hilst, 2005) or full-wave propagation (Tromp et al., 2008) in forward modeling and the back-propagation of residuals. Here, we draw transmission and reflection tomography together under the same framework by using our one-way propagator to model the data. Using thin-slab propagation allows us to build the kernel depth by depth, thereby reducing the cost of storing the entire forward and backward propagated wavefields.

3.4.2 Transmission tomography

The generalization of the one-way wave equation onto curvilinear coordinates makes it possible to apply fast one-way methods to transmission studies. Several different study geometries could benefit from tomography on curvilinear coordinates. For local seismicity, propagation could be modeled in overturning coordinates such as the polar coordinates in figure 3-4 when turning waves occur. For teleseismic body waves, it is possible to apply overturning coordinates where the surface geometry is spherical or sphereoidal. Apart from global applications, passive seismics are also becoming a useful tool in hydrocarbon exploration. Wave-equation transmission tomography using microseismicity caused by reservoir-induced earthquakes can be performed.

In Appendix 3.A we develop a cross correlation-based transmission tomography approach for use with our curvilinear one-way propagator. We wish to minimize the traveltime difference between the observed and forward modeled arrivals of particular phases. As such, this form of transmission tomography is equivalent to a traveltime approach and is dissimilar from approaches which minimize the difference between the observed and modeled waveforms. The finite frequency sensitivity is calculated through the interaction of the forward propagated source field and the backward propagated data residual. The adjoint method constructed for this method is described by Figure 3-5.

Figures 3-6 (b) and (d) show sensitivity kernels for an overturning wave produced at depth and recorded at a single receiver at the surface. The kernel in Figure 3-6 (d) was created in a velocity model containing caustics, which causes a distortion in the travel path. The two advantages that this method has over traditional ray theoretical traveltime tomography is that it is stable in the presence of caustics and the contribution to different scales in the model updates from different frequencies are handled more accurately.

3.4.3 Reflection tomography

Reflection tomography, or migration velocity analysis, exploits redundancy in the reflected wavefield in order to update a smooth background velocity model (Biondi & Sava, 1999). Instead of assessing the model fitness by applying a data-domain error function, fitness is determined by judging the success of subsurface image formation. Curvilinear one-way propagation will be useful in reflection tomography in two very different settings: active source experiments where vertical or sub-vertical reflections occur and teleseismic studies using free surface reflected phases where the curvature of the Earth cannot be ignored

In the active source case, curvilinear propagation can be easily applied to a number of methods. The Rytov-based schemes of Xie & Yang (2008) and Wang et al. (2010), in particular, offer a strong connection to between reflection tomography and the finite-frequency traveltime tomography presented in the above section. Instead of correlating forward modeled and observed wavefields at the receiver locations in time, the method of Xie & Yang (2008) correlates images between different sources in depth. The optimal smooth model is then the one that minimizes the depth moveout between all of the images. Wang et al. (2010) takes another step towards and compares the phase of the images in time. Figure 3-7 demonstrates the sensitivity of a traveltime measure for reflection tomography in ellipsoidal coordinates. The contribution from each event has two legs. The source to reflector leg (Figure 3-7(a)) retains the same of a traveltime kernel, while the second leg (Figure 3-7(b)) fans out between the reflector and all receivers.

Alternatively, analysis using wave-equation angle transform annihilators as the error criteria (De Hoop et al., 2006) has the advantage that it can be used to estimate the reflection coefficient induced by the background velocity, and it remains artifact free in the presence of caustics. Curvilinear versions of these annihilators (Stolk & de Hoop, 2007) have been developed for the purpose of performing reflection tomography in curved coordinates. If the data has been imaged using an acceptable background velocity, the angle gathers should be independent of the slowness. The annihilator is fundamentally a derivative in ray parameter, and thus the background model is optimized by minimizing the annihilated gather. The problem can then be cast as an adjoint method problem .

In the teleseismic setting, the nature of global data makes it difficult to apply conventional reflection tomography methods. The sparse, irregular sources do not contain enough angular information, and the complicated, unknown source-time functions make it difficult to compare traveltime or moveout. Burdick et al. (2013) develops a teleseismic reflection tomography method using a cross-correlation power norm error function. The power norm approach was developed for transmission tomography by Van Leeuwen & Mulder (2008) as an alternative for the error function presented here in Appendix 3.A. Extended to reflection tomography, the error function is robust enough to deal with the shortcomings of teleseismic data. The results in Burdick et al. (2013) use a 2-D Helmholtz propagator (Wang et al., 2010) on Cartesian coordinates, but in application to larger arrays and data sets, a computational advantage could be gained by employing curvilinear one-way propagation.

3.5 Discussion and future directions

We have developed a technique for one-way wave propagation on curvilinear coordinates using a rational approximation. This approximation yields high angular accuracy with only a few terms in the expansion, thereby allowing for accurate propagation at relatively low computational expense. The generalization of the one-way equation extends the application of tomography and migration velocity analysis to a broad array of complex environments and array geometries. The ability to handle turning waves makes it possible to use the same computational framework for problems ranging from transmission tomography from local microseismicity to reflection tomography using underside and free surface reflections. A change of coordinates also makes it possible to apply migration methods to global seismology problems where the curvature of the Earth cannot be ignored.

The Earthscope Project presents a number of interesting geological questions and a wealth high quality seismic data with which to answer them. At least three projects would benefit from the application of finite-frequency tomography using curvilinear one-way propagators. First, USArray Flex Array data from the near-linear sections of the CAFE Array in Washington state can be used to illuminate the subduction of the Juan de Fuca slab and upper mantle structure, and could help refine background models for use in investigating episodic tremor and slip. Local seismicity from the subduction could be used with our methodology in a transmission sense, or multiple reflections off of the slab or Moho could be used for reflection tomography. Second, reflection tomography using double square root propagation would also be useful for the linear array in the SAFOD Project, where exploration-style active sources create reflections off of the near-vertical San Andreas Fault. An enhanced tomographic model would give helpful information about small-scale compositional heterogeneity or volatile content that could affect fault motion.

The third, and the broadest, potential application of tomography with curvilinear one-way propagation in three dimensions is to the continental scale arrays like USArray Transportable Array data (Figure 3-8). Tomography with USArray could be used to investigate questions such as the nature of the subducted Farallon slab, the variation in lithospheric thickness between tectonic provinces, and the structure of the slow anomaly related to the Yellowstone hotspot. An array of this scope allows for a myriad of possible propagation geometries. Using the P-wave travel time result of Burdick et al. (2014) as a starting model, the scattered wavefield accompanying teleseismic phases such as the $P_{410}p$ or $P_{660}p$ could be used in reflection tomography. Underside scattered phases such as the PP wavefield could additionally be incorporated by using separate coordinate systems for source-side and receiver-side calculations. Direct body wave arrivals could be used in a transmission case with a sufficiently deformed coordinate system. Coordinate systems for particular parts of the wavefield could potentially be determined automatically for given domain in source-receiver space via ray tracing.

Before application to Earthscope is possible, several computational concerns will need to be addressed. First, accuracy may be lost when the size of the curvilinear numerical grid varies too much. For example, using a polar coordinate system with θ ranging from 0 to π, it is possible to model large offset transmission data or underside reflections. In cases like this, it is vital to ensure the computational grid size at the outer radius meets the Nyquist criterion. It may be prudent to carry out propagation on a variable-size grid with sections of smaller $d\theta$ at greater radius. Regions requiring grid refinements could be made using mortar cells. Second, in order to ensure accurate wavefield amplitude when the velocity model varies strongly with $\tilde{x}$, it will be necessary to add the subprinciple part to the propagation operator (Stolk & de Hoop, 2007). Third, for use on the 2-D Transportable Array it will be necessary to move to a three dimensional propagator. There is no theoretical difficulty in doing so, but an explicit version of the finite difference discretization of the propagation and normalization operators must be developed. Finally, in order to accommodate the large volumes of seismic data recorded by USArray, it may be useful to institute a checkpointing algorithm within the propagator. This will allow the wavefield to be stored in memory only at certain depths, then rapidly recalculated for the others when needed in the kernel calculation.

3.A One-way transmission tomography

For a single source function, $f(\tilde{x}_s, \tilde{z}_s, t)$, the solution to the one-way wave equation in a smooth velocity model $c(\tilde{x}, \tilde{z})$ can be expressed as

$$\tilde{U}(\tilde{x}, \tilde{z}, \omega) = Q_+(\tilde{z}, \omega) \int G_+(\tilde{x}, \tilde{z}, \omega; \tilde{x}, \tilde{z}_s) Q_+(\tilde{z}_s, \omega)^{-1} f(\tilde{x}_s, \tilde{z}_s, \omega) d\tilde{z}_s, \tag{3.16}$$

where $G_+(\tilde{x}, \tilde{z}, \omega; \tilde{x}_s, \tilde{z}_s)$ is the fundamental solution to the upgoing one-way equation. For simplicity's sake, we redefine the source and wavefield to work in the decoupled domain, $Q_+^{-1}\tilde{U} \to \tilde{U}$ and $Q_+^{-1} f \to f$.

In Finite frequency travel-time tomography, we seek to minimize the L_2 norm of all travel-time residuals for i in the set of all sources and receivers:

$$\mathcal{J}[c] = \frac{1}{2} \sum_{i \in R \times S} (T_i[c] - T_{obs,i})^2, \tag{3.17}$$

where $T_i[c]$ is the estimated travel-time based on wavespeed model c, and T_{obs} is the observed traveltime.

In the following analysis we suppress the dependency on source. In the finite frequency context, the residual is best determined by the maximum of the cross-correlation between the observed and estimated waveforms,

$$\mathcal{C}(t) = \int_{\Re} \overline{\tilde{U}_{obs}(\tilde{x}_r, \tilde{z}_r, \omega)} \tilde{U}(\tilde{x}_r, \tilde{z}_r, \omega) e^{i\omega t} d\omega. \tag{3.18}$$

To find the local maximum, we take a derivative of the cross-correlation function, which amounts to a multiplication by $i\omega$ in the frequency domain:

$$F(t) = \int_{\Re} i\omega \overline{\tilde{U}_{obs}(\tilde{x}_r, \tilde{z}_r, \omega)} \tilde{U}(\tilde{x}_r, \tilde{z}_r, \omega) e^{i\omega t} d\omega. \tag{3.19}$$

$F(t)$ is equal to zero at $t = \Delta t$. If we are using the correct wavespeed model, $c = c_{true}$, then we should have $\Delta t = 0$ for all data. F is perturbed under c, then expanded about

$\Delta t = 0$:

$$\delta F(\Delta t) = \frac{\partial}{\partial c} F(\Delta t)\delta c \approx \frac{\partial}{\partial c} F(0)\delta c + \frac{\partial}{\partial t} F(0) \frac{\partial}{\partial c} \Delta t \delta c = 0. \tag{3.20}$$

This allows us to find an expression for δt, the perturbation of the traveltime residual Δt under δc:

$$\delta t = \frac{\partial}{\partial c} \Delta t \delta c = \frac{-\frac{\partial}{\partial c} F(0)\delta c}{\frac{\partial}{\partial t} F(0)} = \frac{\int_{\Re} i\omega \overline{\tilde{U}_{obs}} \delta \tilde{U} e^{i\omega 0} d\omega}{\int_{\Re} \omega^2 \overline{\tilde{U}_{obs}} \tilde{U} e^{i\omega 0} d\omega} \tag{3.21}$$

Using the Born approximation, we will estimate that $\tilde{U}_{obs} \approx \tilde{U}$ for the purposes of finding the Fréchet derivative.

$$\delta t = \frac{\int_{\Re} i\omega \overline{\tilde{U}} \delta \tilde{U} d\omega}{\int_{\Re} \omega^2 |\tilde{U}|^2 d\omega} = \frac{1}{N_s} \int_{\Re} i\omega \overline{\tilde{U}} \delta \tilde{U} d\omega, \tag{3.22}$$

where we define N as $\int_{\Re} \omega^2 |\tilde{U}|^2 d\omega$.

$\delta \tilde{U}$ represents the perturbation of the wavefield with regards to a perturbation of the velocity model. Following the Born approximation, this wavefield is the solution to the perturbed one-way wave equation:

$$\left(\frac{\partial}{\partial \tilde{z}} - i\Gamma_+ \right) \delta \tilde{U} = i\delta \Gamma_+ \tilde{U}. \tag{3.23}$$

Taking the first term of the expansion of the perturbed square root equation, we find $\delta \Gamma =\approx \partial_c \Gamma \cdot \delta c$. Our discretization scheme for the $\partial_c \Gamma$ operator is derived in Appendix 3.B. Suppressing the dependency of the Green's function on $\tilde{x}$ and ω, we have:

$$\delta \tilde{U}(\tilde{x}, \tilde{z}, \omega) = \int_{\tilde{z}_s}^{\tilde{z}} G_+(\tilde{z}, \tilde{z}') \left(i\partial_c \Gamma_+(\tilde{x}', \tilde{z}', \omega) \right) \tilde{U}(\tilde{x}', \tilde{z}', \omega) \delta c(\tilde{x}', \tilde{z}') d\tilde{z}' \tag{3.24}$$

In essence, the forward-propagated source wavefield is acted upon by the perturbed curvilinear one-way operator at each depth slice. The sum of these singly-perturbed wavefield contributions is then the perturbed source field.

The perturbation to the traveltime can then be formulated as

$$\delta t = \frac{1}{N} \int_{\Re} \int_{\tilde{z}_s}^{\tilde{z}_r} \overline{\tilde{U}(x, z, \omega)} G_+(\tilde{z}, \tilde{z}') \left(i\partial_c \Gamma_+ \right) \tilde{U}(\tilde{x}, \tilde{z}', \omega) \delta c(\tilde{x}', \tilde{z}') d\tilde{z}' d\omega. \tag{3.25}$$

From this, we can extract the sensitivity kernel for each ,

$$\mathcal{K}(\tilde{x},\tilde{z},\omega;\tilde{x}_s,\tilde{z}_s)=\frac{1}{N_s}\int_{\Re}\int_{\tilde{z}_s}^{\tilde{z}_r}\overline{\tilde{U}(x,z,\omega)}G_+(\tilde{z},\tilde{z}')\left(i\partial_c\Gamma_+\right)\tilde{U}(\tilde{x},\tilde{z}',\omega)d\omega, \tag{3.26}$$

and

$$\delta t = H\delta c \equiv \int_{\tilde{z}_s}^{\tilde{z}_r}\mathcal{K}(\tilde{x}',\tilde{z}',\omega;\tilde{x}_s,\tilde{z}_s)\delta c(\tilde{x}',\tilde{z}')d\tilde{z}' \tag{3.27}$$

where H is an integral operator defined by the kernel $\mathcal{K}$. These kernels can be used to solve directly for an update to the velocity by means of a Least Squares inversion, but the relatively large computational cost of perturbing each $\delta c(x,z)$ motivates an alternative approach using the seismic adjoint method. The optimization problem is naturally formulated as:

$$\langle\delta t\rangle = arg\ min\frac{1}{2}\sum_{i\in R\times S}\left(T_{obs,i}-\delta t_i\right)^2, \tag{3.28}$$

The gradient of the correlation error function can then be found by solving an adjoint equation. Using that the one-way operator and its derivative are self-adjoint, we can find the tomographic image:

$$\mathcal{I}(\tilde{x},\tilde{z})=\int_{\Re}\int_{\tilde{z}_r}^{\tilde{z}_s}\overline{\tilde{U}(\tilde{x}',\tilde{z}',\omega)}\left(-i\partial_c\Gamma_-\right)\tilde{U}^{\dagger}(\tilde{x}',\tilde{z}',\omega)d\tilde{z}'d\omega, \tag{3.29}$$

where the adjoint wavefield $\tilde{U}^{\dagger}$ is the solution to the adjoint one-way propagation:

$$\left(\frac{\partial}{\partial\tilde{z}}+i\Gamma_-\right)\tilde{U}^{\dagger}(\tilde{x},\tilde{z},\omega)=N^{-1}\tilde{U}(\tilde{x},\tilde{z},\omega)\Delta T. \tag{3.30}$$

This amounts to a correlation between the upgoing source field with a downwards going adjoint field which includes the traveltime residual in the adjoint source for each propagation. A graphic representation of the process is shown in Figure 3-5. The sum of these tomographic images over all sources and receiver comprises the gradient which can be used to optimize the model using efficient descent methods.

3.B Perturbed single square root operator

For the purpose of tomography, it is necessary to find the derivative of the square root operator in c.

$$\frac{\partial}{\partial c}\gamma = -2c^{-3}\tilde{g}_{33}\left(c^{-2}\tilde{g}_{33} + \omega^{-2}\tilde{k}_x\tilde{g}^{11}\tilde{g}_{33}\tilde{k}_x\right)^{-1/2} \tag{3.31}$$

An efficient discrete operator can be formulated. Following the analysis in Section 3.3, the self-adjoint discrete equation is:

$$\partial_c\Gamma = \frac{-2\tilde{g}_{33}^{1/4}}{c}(1+\Xi)^{-1/2}\frac{\tilde{g}_{33}^{1/4}}{c} \tag{3.32}$$

An acceptable discretization of the derivative of the square root operator can be found using (2,2) rational approximation:

$$\partial_c\Gamma \approx \frac{-2\tilde{g}_{33}^{1/4}}{c}\frac{1+\beta_1\Xi+\beta_2\Xi^2}{1+\beta_3\Xi+\beta_4\Xi^2}\frac{\tilde{g}_{33}^{1/4}}{c} \tag{3.33}$$

A least squares fit with the principle symbol gives the parameters $\beta_1 = 1.208, \beta_2 = 0.263, \beta_3 = 1.698, \beta_4 = 0.702$.

Bibliography

Biondi, B. & Sava, P., 1999. Wave-equation migration velocity analysis, in *Expanded Abstracts*, pp. 1723–1726, Society of Exploration Geophysicists.

Burdick, S., Li, C., Martynov, V., Cox, T., Eakins, J., Mulder, T., Astiz, L., Vernon, F. L., Pavlis, G. L., & van der Hilst, R. D., 2008. Upper mantle heterogeneity beneath North America from travel time tomography with global and USArray Transportable Array data, *Seismological Research Letters*, **79**, 384–390.

Burdick, S., de Hoop, M. V., Wang, S., & van der Hilst, R. D., 2013. Reverse-time migration-based reflection tomography using teleseismic free surface multiples, *Geophysics Journal International*, **in press**.

Burdick, S., van der Hilst, R. D., Vernon, F. L., Martynov, V., Cox, T., Eakins, J., Karasu, G. H., Tylell, J., Astiz, L., & Pavlis, G. L., 2014. Model update January 2013: Upper mantle heterogeneity beneath North America from traveltime tomography with global and USArray Transportable Array data, *Seismological Research Letters*, **in press**.

Claerbout, J. F., 1970. Coarse grid calculations of waves in inhomogeneous media with application to delineation of complicated seismic structure, *Geophysics*, **35**, 407–418.

Collino, F., 1997. Perfectly matched absorbing layers for the paraxial equations, *Journal of Computational Physics*, **131**, 164–180.

Dahlen, F. A., Hung, S. H., & Nolet, G., 2000. Fréchet kernels for finite-frequency traveltimes - I. Theory, *Geophysical Journal International*, **141**(1), 157–174.

de Hoop, M. V. & de Hoop, A. T., 1992. Scalar space-time waves in their spectral-domain first- and second-order thiele approximations, *Wave Motion*, **15**, 229–265.

De Hoop, M. V. & Van der Hilst, R. D., 2005. On sensitivity kernels for 'wave-equation' transmission tomography, *Geophysical Journal International*, **160**(2), 621–633.

De Hoop, M. V., van der Hilst, R. D., & Shen, P., 2006. Wave-equation reflection tomography: annihilators and sensitivity kernels, *Geophysical Journal International*, **167**(3), 1332–1352.

Golub, G. H. & Van Loan, C. F., 1995. *Matrix Computations*, Johns Hopkins University Press.

Li, C., van der Hilst, R. D., Meltzer, A. S., & Engdahl, E. R., 2008. Subduction of the Indian lithosphere beneath the Tibetan Plateau and Burma, *Earth and Planetary Science Letters*, **274**(1), 157 – 168.

Mitchell, A. R. & Griffiths, D. F., 1985. *The Finite Difference Method in Partial Differential Equations*, Wiley, Chichester.

Pratt, R. G., 1999. Seismic waveform inversion in the frequency domain, Part 1: Theory and verification in a physical scale model, *Geophysics*, **64**(3), 888–901.

Richtmeyer, R. D. & Morton, K. W., 1967. *Difference Methods for Initial-Value Problems*, Wiley, New York.

Sava, P. & Fomel, S., 2005. Riemannian wavefield extrapolation, *Geophysics*, **70**, 45–56.

Sava, P. & Fomel, S., 2008. High-order kernels for Riemannian wavefield extrapolation, *Geophysical Prospecting*, **56**, 49–60.

Sava, P. C., Shragge, J. C., & Fomel, S. B., 2004. One-way Wavefield Extrapolation in Riemannian Coordinates, *AGU Fall Meeting Abstracts*, pp. B1061+.

Stolk, C. C. & de Hoop, M. V., 2007. Curvilinear wave-equation angle transforms: Caustics, turning rays, absence of kinematic artifacts, in *77th Annual Meeting, Society of Exploration Geophysicists, Tulsa, Oklahoma*.

Tarantola, A., 1984. Inversion of seismic-reflection data in the acoustic approximation, *Geophysics*, **49**(8), 1259–1266.

Tromp, J., Komatitsch, D., & Liu, Q. Y., 2008. Spectral-element and adjoint methods in seismology, *Communications in Computational Physics*, **3**, 1–32.

Van Leeuwen, T. & Mulder, W. A., 2008. Velocity analysis based on data correlation, *Geophysical Prospecting*, **56**(6), 791–803.

Van Stralen, M. J. N., de Hoop, M. V., & Block, H., 1998. Generalized Bremmer series with rational approximation for the scattering of waves in inhomogeneous media, *Journal of Acoustic Society of America*, **104**(4), 1943–1963.

Wang, S., de Hoop, M. V., & Xia, J., 2010. Acoustic inverse scattering via Helmholtz operator factorization and optimization, *Journal of Computational Physics*, **229**(22), 8445–8462.

Xie, X.-B. & Yang, H., 2008. The finite-frequency sensitivity kernel for migration residual moveout and its applications in migration velocity analysis, *Geophysics*, **73**(6), S241–S249.

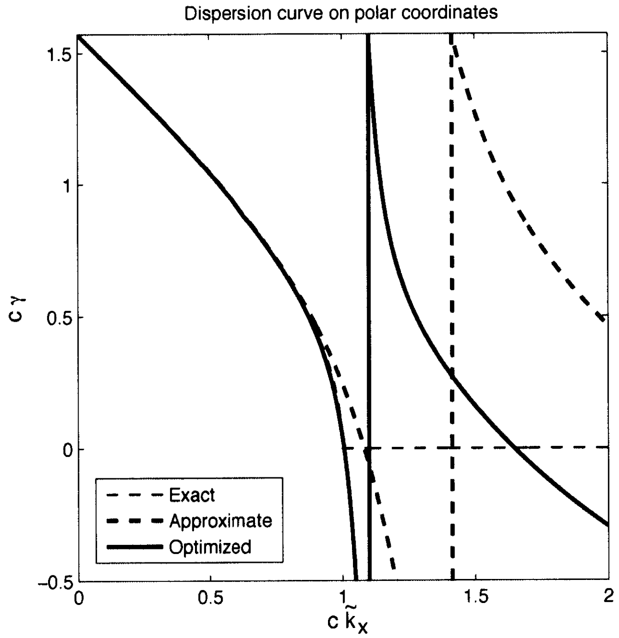

Figure 3-1: Comparison of dispersion curves for rational approximation (dashed) versus optimized parameters (solid), with $\tilde{k}_x^2$ as the pseudodifferential symbol of Ξ. The optimized curve plots on top of the exact curve, demonstrating the high angular accuracy. Plotted in polar coordinates with $\theta = 0$.

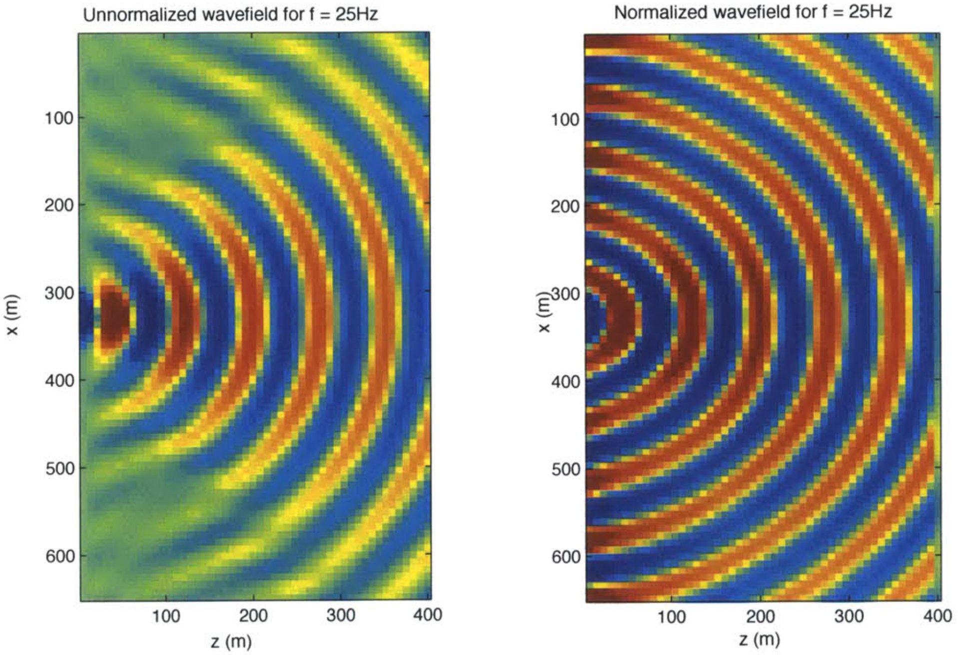

Figure 3-2: The effect normalizing the propagation operator is demonstrated for a 25 Hz source. On the left, the square root operator alone leads to an anisotropic propagation of the source function. On the right, the square root operator is normalized, leading to an accurate, 180° propagation.

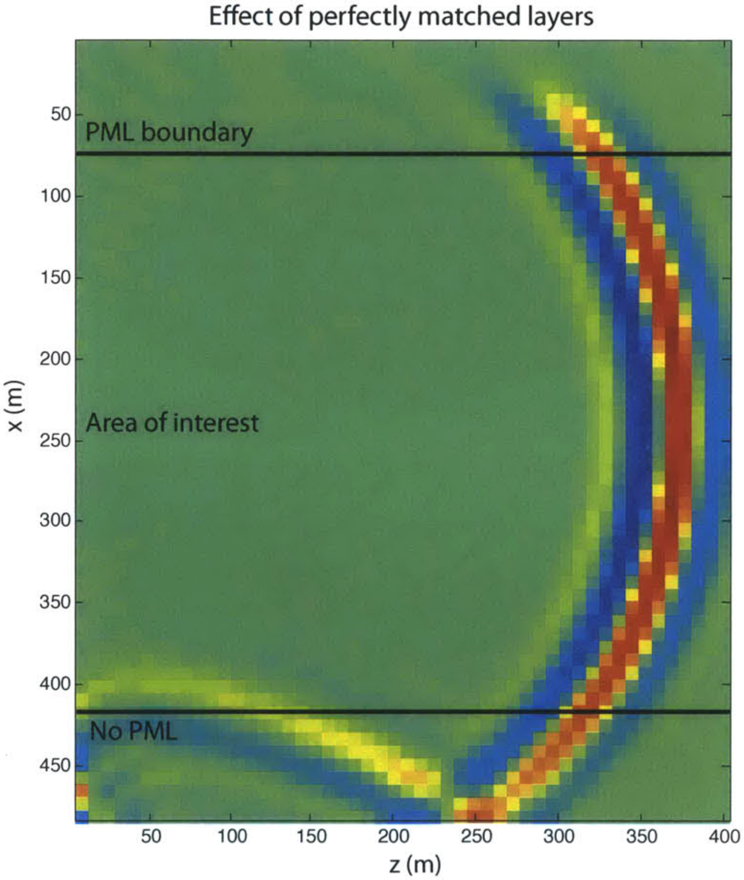

Figure 3-3: Absorbing boundary conditions prevent nonphysical reflections from the edge of the computational grid from contaminating the area of interest. The top boundary of the computational grid includes 10 perfectly matched layers, effectively damping out the wave before reflections can be generated. The bottom boundary has no absorbing condition, and reflections are allowed to propagate back into the area of interest.

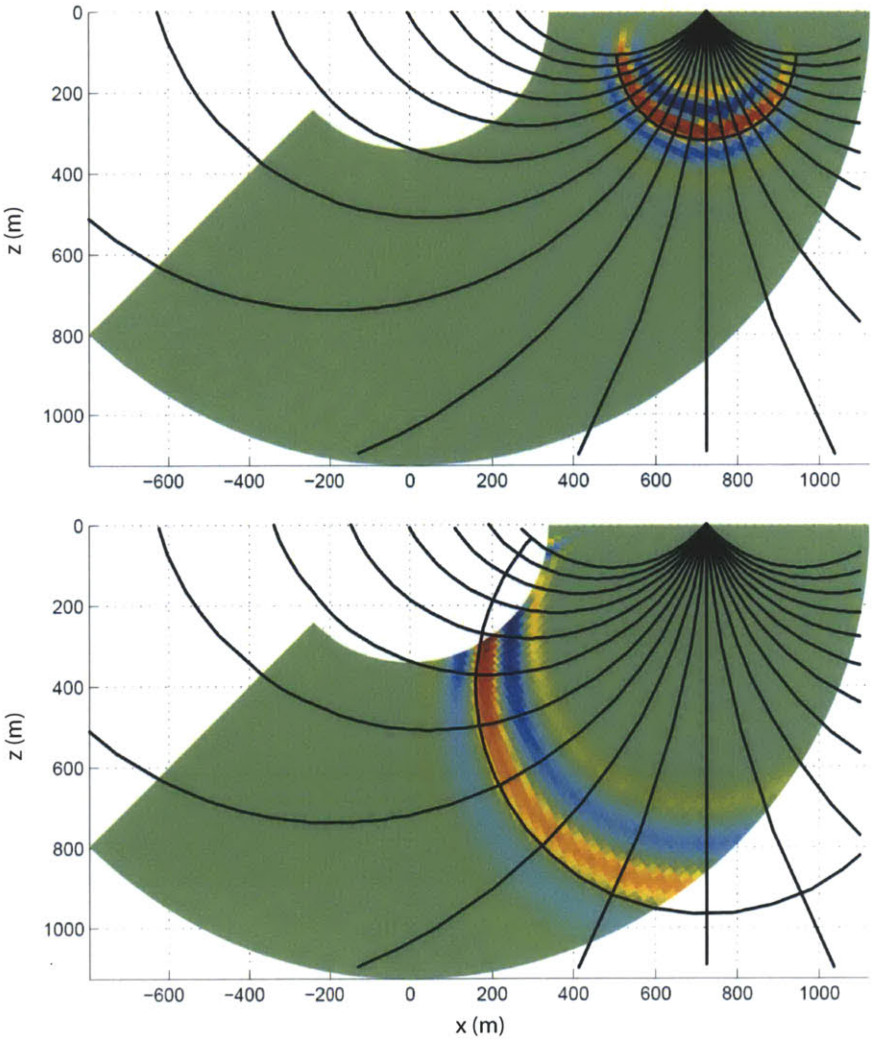

Figure 3-4: Overturning wave in wavespeed model in figure 3-6(a). The source is a wavelet with a Gaussian frequency distribution centered at 25 Hz. Rays and wavefronts are projected on top of the wave, demonstrating the accuracy of propagation in overturning coordinates. Distances are in meters.

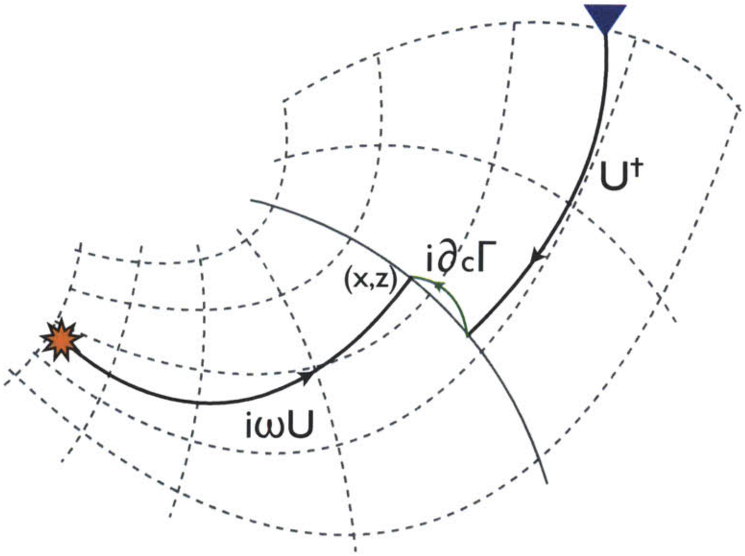

Figure 3-5: The seismic adjoint method for transmission tomography in curvilinear coordinates is described. 1) The source function is propagated forward to the surface from $(\tilde{x}_s, \tilde{z}_s)$ to create $\tilde{U}$. 2) The adjoint source based on the traveltime residual is downward continued from the receivers to any pseudodepth $\tilde{z}$. 3) The perturbed square root operator as allowed to act on the time derivative of the of the adjoint field. 4) An inner product is taken between the conjugate of the forward propagated source and the and the downward continued adjoint.

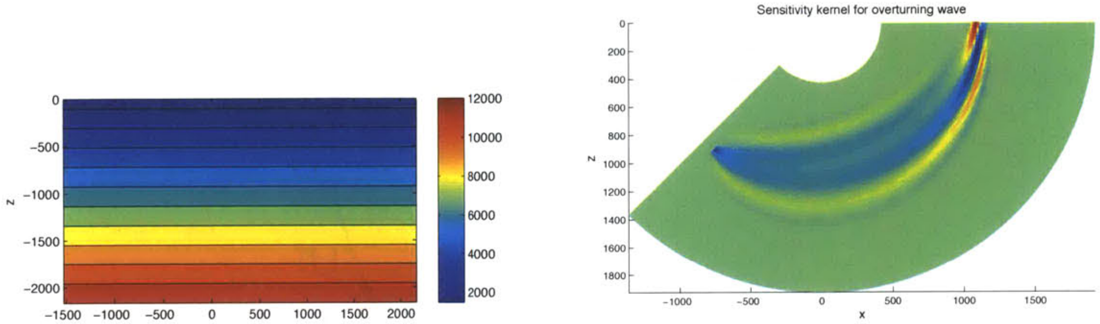

(a) Smooth model

(b) Sensitivity kernel in model (a)

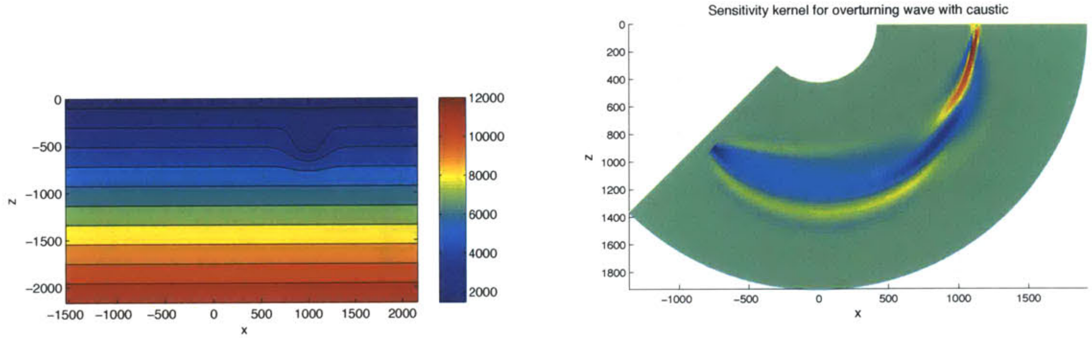

(c) Model with Gaussian lens

(d) Sensitivity kernel with caustic in model (c)

Figure 3-6: (a) Wavespeed model with gradient in z. (c) Similar to wavespeed model in (a) with a -1500 m/s Gaussian lens added. (b) Sensitivity kernel for source/receiver pair in model (a). (d) Sensitivity kernel for model in (c) demonstrating both caustics and overturning rays. The development of the caustics causes a distortion in the kernel. (All distances in meters)

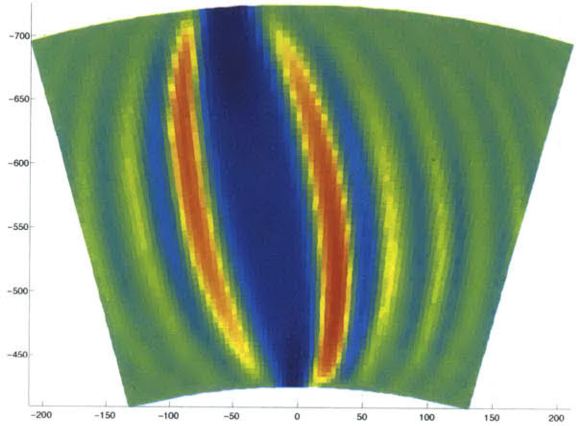

(a) Kernel from source to scattering point

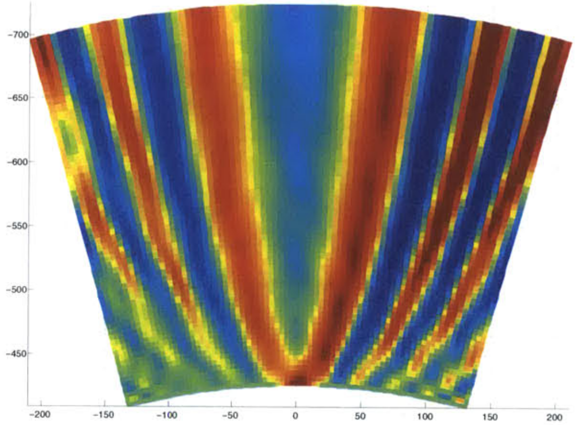

(b) Kernel from scattering point to array

Figure 3-7: Reflection kernel in elliptic coordinates $(x = cos\ \tilde{x}\ cosh\ \tilde{z}, z = sin\ \tilde{x}\ sinh\ \tilde{z})$ for frequency band 40-55 Hz. Distances are in meters. Source side kernel goes between a source at the surface and a scattering point at the bottom center. Receiver side kernel goes from scatterer to array at every point of the surface $\tilde{z} = 0$. Such a setup would be useful in looking at teleseismic wavefield scattered at and around the mantle transition zone.

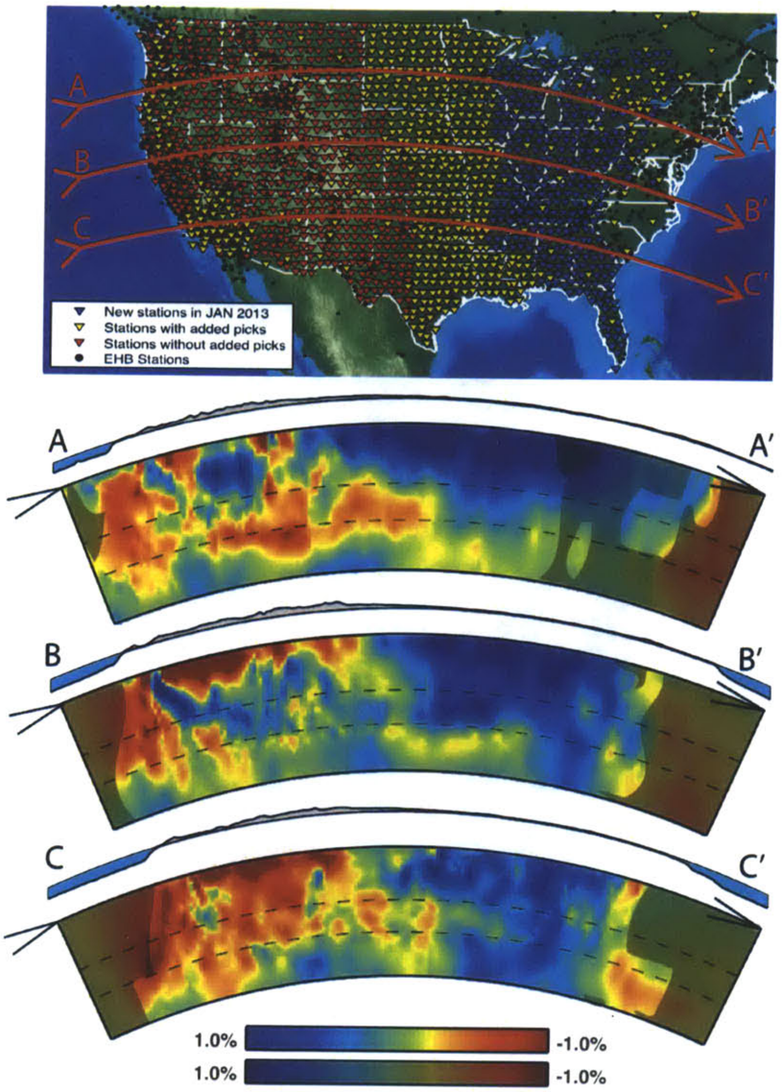

Figure 3-8: Current USArray data coverage with cross sections down to 1000 km through MITP_USA_2013JAN. Continental scale seismic experiments like USArray provide the the high volumes of broadband data that necessitate the development of fast wave-equation methods for tomography.

Chapter 4

Reverse-time migration-based reflection tomography using teleseismic free surface multiples[1]

Abstract

Converted and multiply reflected phases from teleseismic events are routinely used to create structural images of the crust-mantle boundary (Moho) and the elasticity contrasts within the crust and upper mantle. The accuracy of these images is to a large extent determined by the background velocity model used to propagate these phases to depth. In order to improve estimates of 3-D velocity variations and, hence, improve imaging, we develop a method of reverse-time migration-based reflection tomography for use with wavefields from teleseismic earthquakes recorded at broad-band seismograph arrays. Reflection tomography makes use of data redundancy – that is, the ability to generate numerous structural images of the subsurface with different parts of the wavefield. In exploration seismology (where it is known as migration velocity analysis) reflection tomography typically involves the generation of an extended image (e.g. offset- or angle-gathers), and the fitness of the background model is evaluated through the application of image-domain annihilators. In regional-scale passive source seismology, however, annihilation-based methods are inadequate because the sparse and irregular distribution of teleseismic sources is not likely to produce illumination over a sufficient range of angles. To overcome this problem we turn towards a source-indexed moveout scheme. Instead of extended image annihilation, we determine the success of the tomographic velocity model by cross correlating images produced with multiply-scattered waves from different teleseismic sources. The optimal velocity model is the one that minimizes correlation power between windowed images away from zero depth shift. We base our inversion scheme on the seismic adjoint method and a conjugate gradient solver. For each image pair, the update direction is determined by correlations between downgoing wavefields with upgoing adjoint wavefields for both images. The sensitivity

---

[1] Published as: Burdick, S., de Hoop, M. V., Wang, S. van der Hilst, R. D., 2013. Reverse-time migration-based reflection tomography using teleseismic free surface multiples, *Geophysics Journal International*, In Press.

kernels used in this method is similar to those found in other forms of adjoint tomography, but their shapes are controlled by the spatial distribution of the error function. We present the method and a proof-of-concept with 2-D synthetic data.

4.1 Introduction

Since the pioneering papers by Langston (1979) and Vinnik et al. (1979), receiver function analysis of teleseismic free-surface multiples and phase conversions has become the staple of regional scale crust and upper mantle studies with data from seismograph arrays. With this method, structural images are created using data where the direct teleseismic P and S arrivals have been separated from phases that have converted or multiply scattered at discontinuities in velocity. To provide an image of the discontinuities at depth, these so-called receiver functions used to be subjected to simple stacking at common conversion points (CCP stacks), but lately more sophisticated imaging methods like the generalized Radon transform (Bostock et al., 2001) have been put to use. Several recent studies focused with substantial success on wave-equation migration of converted phases and multiples (Shragge et al., 2006; Chen et al., 2009; Shang et al., 2012).

In most studies to date, the accuracy of the images is controlled by the velocity variations in and simplifying assumptions about the background medium. For instance, popular methods for receiver function analysis of crustal structure (Rondenay, 2009) or upper mantle transition zone studies with SS precursors (Deuss, 2009) assume that the medium is 1D and involve stacking across interfaces that are locally planar. In order to use the wealth of broadband data recorded at increasingly dense arrays and image more complex heterogeneity we must bypass these obstructions and use explicitly 2- or 3-D methods that are able to handle irregular discontinuities. Reflection tomography is one such method that can be used to estimate both the 3-D background velocities in addition to the locations of discontinuities.

Reflection tomography based on reverse time migration (RTM) optimizes a smooth velocity model using the redundancy in reflection data. This redundancy allows for the creation of extended images – that is, image gathers formed using different angular or subsurface offset components of the data – via RTM in a 3-D model. The fitness of the model can then be judged through the application of so-called annihilators. In effect, these annihilators provide a measure of image consistency (in the angle domain) or image focusing (in the offset domain). In the absence of caustics this is equivalent to differential semblance (Symes & Carazzone, 1991). Explicit constructions and implementations of annihilators for cases with caustics in the wavefield can be found in (Stolk & de Hoop, 2006; De Hoop et al., 2006), which use the principle of downward continuation (Claerbout, 1985). For more recent implementations of annihilators developed for hydro-carbon exploration and production we refer to Shen & Symes (2008) and Sava & Vasconcelos (2011). The method of teleseismic reflection tomography developed here adopts concepts from these active source applications. The regional teleseismic applications that we have in mind are lithospheric studies with dense linear and areal arrays or the upper mantle studies with USArray or similar such arrays in Europe and Asia.

The formation and annihilation of offset or angle gathers requires a continuous range of source incidences. Due to the nature of global seismicity, it is unlikely that this requirement can be met using teleseismic data, though it is possible that an interferometric approach could fill in the gaps in arrival angle with the scattered wavefield (Schuster, 2010). Furthermore, the low frequency and roughly planar geometry of the teleseismic arrival can cause crosstalk in the offset gathers which renders the degree of focusing an insensitive measure of error. Annihilation-based approaches are, therefore, inadequate for wave-equation tomography with wavefields produced by teleseismic earthquakes.

Xie & Yang (2008) present a method for using source redundancy based on measuring residual moveout (RMO), or the difference in depth between structure imaged with different sources. The measurement of RMO relies on the determination of a correlation maximum between these single-source images. In active source experiments, where the source signature is similar for all events, the correlation maximum reliably yields the moveout. In the teleseismic case, however, differences in the source signatures between different events can map into unwarranted moveout in spite of efforts to deconvolve them from the data. Additionally, the RMO method is intrinsically asymptotic. In order to build an inversion scheme, we must know the direction that the images move due to the perturbation. This moveout direction is not generally normal to the reflector, and must be solved for via a continuation ray tracing system (Duchkov & de Hoop, 2009).

For application to teleseismic wavefields we propose an alternate approach using a misfit criterion in the image domain. The wave equation reflection tomography presented here is based on a RTM inverse scattering transform (Op 't Root et al., 2012) and aims to use the similarity of images produced from different sources as the criteria to find a smooth velocity model that best explains the data. To avoid problems arising from unknown finite-bandwidth source functions, we move towards a correlation power norm in the image domain; here, we adapt the cross correlation power measure introduced by Van Leeuwen & Mulder (2008, 2010). When used in the image domain, this power norm approach penalizes correlation power between images away from zero depth shift. The resulting error function is robust and has a broad basin of attraction. We note that the cross correlation power has some similarities with the criterion used in wave-equation shear-wave splitting tomography (Long et al., 2008).

This paper consists of two main parts. In Section 2 we describe the geometry and mathematical analysis of the problem. Here we develop an inverse scattering theory based on the scalar Helmholtz equation and an image correlation power error function. We also develop an adjoint method for determining the gradient of the error function that is to be optimized, which we present in the Appendix. In Sections 3 and 4, which contain synthetic "experiments," we investigate the error function and present inversion results from 2-D synthetic subduction model.

4.2 RTM-based reflection tomography: Geometry and theory

4.2.1 Teleseismic free-surface reflections

We apply RTM-based reflection tomography to teleseismic P-wave free-surface multiple reflections. The geometry of this problem is shown in Figure 4-1. We consider incident P-waves from earthquakes recorded at seismograph arrays at epicentral distances between 30° and 90°. The surface-reflected waves then propagate downwards, scatter at major discontinuities like the Moho, subducted oceanic crust, or the mantle transition zone, and the back-scattered waves (or teleseismic multiples) are recorded at the same array. We use the incident wavefield as a "source" and the multiple wavefield as "data" to perform RTM and estimate the non-smooth contrasts in elastic properties beneath the array. Since the incident field used for reflection tomography can be estimated directly from the recorded wavefield, we do not need to know the precise location or focal mechanism of the earthquakes.

In the teleseismic setting we incorporate the free surface boundary condition in the fundamental solution to the wave equation. That is, the solution to the source-side problem includes both the initial teleseismic leg of propagation and the downward propagation between the free surface and the target discontinuities. Here, however, we suppress the propagation of the incident field along the teleseismic leg for simplicity of computation and to limit the sensitivity of the method outside of the area of interest. Instead, we intercept the source wavefield as a single-layer potential field at the surface estimated from the data, and we only consider its propagation following the free-surface reflection.

For the purposes of establishing a bridge between previous work in the active source setting and future application to teleseismic data, we restrict the analysis in this paper to *P*-polarized waves and, hence, use the scalar wave equation. While *P* to *S* converted phases dominate the teleseismic scattered field, recent studies (Chen et al., 2009; Pearce et al., 2012) have shown that it is possible to create images using *P* backscattered phases such as Pp_mp. Future development of this method will consider the elastic case so that converted phases can be included.

Teleseismic sources tend to have complicated source-time functions. Owing to rupture processes and reverberation from near-source structure, the length of these source-time functions can exceed the difference in arrival time between the direct phase and multiples from structures in the lithosphere and upper mantle. This fact makes it difficult to decouple the direct *P* from *P* backscattered phases, particularly for flat discontinuities. Common preprocessing approaches (as in Rondenay 2009) address this by separating the phases using cross correlation based alignment and principle component analysis and removing the source time function by deconvolution. Images created with such preprocessed data will inevitably still have some coupling between imaged structures and source-time functions.

Our search for a robust reflection tomography error measure is in part motivated by this limitation.

4.2.2 Inverse scattering

We introduce coordinates $(\mathbf{x}, z)$ such that $\mathbf{x} = (x_1, \ldots, x_{n-1})$ and $x_n = z$, with n the dimension of the problem (that is, n= 2 or 3) and z the depth coordinate. We assume that the data are recorded at $z = 0$. For the purposes of the analysis and proof of concept below, we develop our inverse scattering theory with a point source in mind. Absent polarity effects due to the double couple source – a reasonable assumption for measurements at a regional-scale array at teleseismic distances – we can treat an earthquake source (with its source-time function deconvolved) as a Dirac pulse at $(\mathbf{x}_\mathrm{s}, z_\mathrm{s})$. With G the Green's function, the fundamental solution of the wave equation is then given by

$$\begin{gathered}[c(\mathbf{x}, z)^{-2}\partial_t^2 - \Delta]G(\mathbf{x}, z, t) = \delta(\mathbf{x} - \mathbf{x}_\mathrm{s}, z - z_\mathrm{s})\delta(t), \\ \text{subject to initial values } G(\mathbf{x}, z, 0) = 0 \text{ and } \quad \partial_t G(\mathbf{x}, z, 0) = 0.\end{gathered} \tag{4.1}$$

Here, c is a smooth wavespeed, which we expand into basis functions ψ_k (wavelets or splines, for example):

$$c(\mathbf{x}, z) = \sum_{k=1}^{N_k} \gamma_k \psi_k(\mathbf{x}, z), \tag{4.2}$$

with the weights γ_k to be determined by inversion. As mentioned above, we will suppress the teleseismic leg of propagation and represent G as single-layer potential at the free surface.

Following the Born approximation we represent the medium as a combination of smooth wavespeed variations c and a non-smooth perturbation δc. That is, the scattering problem is obtained by linearization of (4.1) with velocity $(1 + r(\mathbf{x}, z))c(\mathbf{x}, z)$, where $r(\mathbf{x}, z) = \delta c(\mathbf{x}, z)/c(\mathbf{x}, z)$ is the (frequency independent) reflectivity function. The non-smooth character of $r(\mathbf{x}, z)$ gives rise to the scattered or reflected wave exploited here. We multiply (4.1) with $c(\mathbf{x}, z)^2$ and find

$$\begin{gathered}[\partial_t^2 - c(\mathbf{x},z)^2\Delta]u(\mathbf{x},z,t) = 2r(\mathbf{x},z)\,\partial_t^2 G(\mathbf{x},z,t),\\ \text{subject to } u(\mathbf{x},z,0) = 0 \text{ and } \quad \partial_t u(\mathbf{x},z,0) = 0.\end{gathered} \tag{4.3}$$

The scattered wave field $u(\mathbf{x}, z, t)$, caused by interactions of the surface reflected waves with subsurface contrasts $r(\mathbf{x}, z)$, is defined as the solution of this problem and will be the synthetic analog the observed wavefield. The mapping of $r(\mathbf{x}, t)$ to u can be represented by a forward (modeling) operator, say $\mathcal{F}$. Since we develop the theory here with a point source in mind, we make the common RTM assumption (Stolk, 2000) that no caustics or multi-pathing occur between the source and the scatter points. For the application of source-indexed reflection tomography this is of particular importance since artefacts created due to caustics will not average out through stacking. Note that in practice, by intercepting the source field at the surface with three component receivers, we can determine directional information about the wavefield. This effectively allows us to determine which path is taken between the surface and the scatterer, and we then would not need to make the no-caustic assumption.

We then define Σ as the set of receiver locations at $z = 0$, so that R_Σ is an operator that restricts the wavefield to the part that is actually recorded at the receiver array. The modeled data are then $d(\mathbf{x}, t) = R_\Sigma u(\mathbf{x}, z, t)$.

We now introduce the reverse-time propagated field, u_r, as the anticausal solution to

$$[c(\mathbf{x},z)^{-2}\partial_t^2 - \Delta]u_\mathrm{r}(\mathbf{x},z,t) = \delta(z)(Nd)(\mathbf{x},t), \tag{4.4}$$

with the operator N acting on data d the composition of preprocessing operators (which will be described below) and the up/down decomposition operator (De Hoop, 1996)

$$-2\mathrm{i}D_t\, c_0(\mathbf{x})^{-1}\sqrt{1 - c_0(\mathbf{x})^2 D_t^{-2} D_x^2} \tag{4.5}$$

that acts on the wavefield at the free surface. Here, $D_t = \mathrm{i}^{-1}\partial_t$, $D_x = \mathrm{i}^{-1}\partial_x$, and $c_0(\mathbf{x}) = c(\mathbf{x}, 0)$ is the wavespeed at the surface (which is assumed to be fixed).

We proceed from here in the frequency domain, but where our method is concerned there are no inherent advantages or disadvantages to propagation and inverse scattering using time versus frequency domain formulation. We then obtain the image, $\mathcal{I}$, from the action of the inverse scattering transform, say $\mathcal{H}$, on the data:

$$
\begin{aligned}
\mathcal{I} = (\mathcal{H}d)(\mathbf{x}, z) &= \frac{1}{2\pi} \int_B \frac{\chi(\omega)}{\mathrm{i}\omega} \left(\frac{1}{\widehat{G}(\mathbf{x}, z, \omega)} \widehat{u}_{\mathrm{r}}(\mathbf{x}, z, \omega) - \frac{c(\mathbf{x}, z)^2}{\omega^2} \nabla \frac{1}{\widehat{G}(\mathbf{x}, z, \omega)} \cdot \nabla \widehat{u}_{\mathrm{r}}(\mathbf{x}, z, \omega) \right) \mathrm{d}\omega \\
&\approx \frac{1}{2\pi} \int_B \frac{\chi(\omega)}{\mathrm{i}\omega |\widehat{G}(\mathbf{x}, z, \omega_0)|^2} \frac{|\omega_0|^{n-3}}{|\omega|^{n-3}} \left(\overline{\widehat{G}(\mathbf{x}, z, \omega)}\, \widehat{u}_{\mathrm{r}}(\mathbf{x}, z, \omega) - \frac{c(\mathbf{x}, z)^2}{\omega^2} \nabla \overline{\widehat{G}(\mathbf{x}, z, \omega)} \cdot \nabla \widehat{u}_{\mathrm{r}}(\mathbf{x}, z, \omega) \right) \mathrm{d}\omega,
\end{aligned}
\tag{4.6}
$$

where $\widehat{\ }$ denotes the Fourier transform with respect to time, $\overline{\ }$ denotes the complex conjugate, $\chi(\omega)$ is a smooth function that ensures that zero frequency is left out of the integration, and B signifies the available bandwidth. The approximation to the inverse scattering transform (right hand side of (4.6)) is introduced here for ease in calculating the adjoint state below. In effect, we choose the wavefield $\widehat{G}(\mathbf{x}, z, \omega_0)$ for one frequency ω_0 in the upper part of our frequency band to provide the source illumination factor, $|\widehat{G}(\mathbf{x}, z, \omega_0)|^{-2}$.

Op 't Root et al. (2012) show that, for a given source, the inverse scattering transform $\mathcal{H}$ is asymptotically the inverse of the modeling operator $\mathcal{F}$. We note that $\mathcal{H}$ and $\mathcal{F}$ both depend on the given data set (that is, the configuration of the array). The gradient terms in Equation 4.6 are important for the suppression of low-frequency artifacts (Wang et al., 2010).

4.2.3 Correlation power functional

As mentioned above, the sparse and irregular distribution of teleseismic sources requires pairwise comparison between images formed with different sources. The construction of single-source images is, therefore, critical for the development of an error function using teleseismic data.

We indicate the dependencies on the source as follows. For a source i located at $(\mathbf{x}_{s;i}, z_{s;i})$, and which generates data $d_i(\mathbf{x}, t)$, with $i = 1, \ldots, N_s$, we write G_i and $u_{\mathrm{r};i}$ for G and u_{r}, respectively. For source i the image $\mathcal{I}_i$ – the reconstruction of the non-smooth medium perturbations $r(\mathbf{x}, z)$ – is

$$\mathcal{I}_i(\mathbf{x}, z) = \frac{1}{2\pi} \int_B \frac{\chi(\omega)}{\mathrm{i}\omega|\widehat{G}_i(\mathbf{x}, z, \omega_0)|^2} \frac{|\omega_0|^{n-3}}{|\omega|^{n-3}} \\ \left(\overline{\widehat{G}_i(\mathbf{x}, z, \omega)}\, \widehat{u}_{\mathrm{r;i}}(\mathbf{x}, z, \omega) - \frac{c(\mathbf{x}, z)^2}{\omega^2} \nabla \overline{\widehat{G}_i(\mathbf{x}, z, \omega)} \cdot \nabla \widehat{u}_{\mathrm{r;i}}(\mathbf{x}, z, \omega) \right) \mathrm{d}\omega, \quad i = 1, \ldots, N_s. \tag{4.7}$$

We note that the set of receiver locations used can also depend on the source location, that is, on i.

In the case of idealized illumination, the location of the images $\mathcal{I}_i(\mathbf{x}, z)$ should be equal for different sources i . That is, the imaging is redundant in $(\mathbf{x}_s, z_s)$. We exploit this redundancy to estimate $c(\mathbf{x}, z)$. To this end, we identify $N_{\mathcal{I}}$ target reflection points in particular depth intervals. We let $\varphi_\alpha(\mathbf{x}, z)$ be the spatial tapers which will effectively act as correlation windows that localize the relevant parts of the image:

$$(\varphi_\alpha \mathcal{I}_i)(\mathbf{x}, z) = \varphi_\alpha(\mathbf{x}, z) \mathcal{I}_i(\mathbf{x}, z).$$

We then form cross correlation between the images for different sources i and j,

$$\mathcal{C}_{ij}^\alpha(\mathbf{x}, \Delta z) = \int_{\mathbb{R}_{\geq 0}} (\varphi_\alpha \mathcal{I}_i)(\mathbf{x}, z)\, (T_{\Delta z}(\varphi_\alpha \mathcal{I}_j))(\mathbf{x}, z)\, \mathrm{d}z, \quad i \neq j,\ i, j = 1, \ldots, N_s,\ \alpha = 1, \ldots, N_{\mathcal{I}}, \tag{4.8}$$

where

$$(T_{\Delta z}(\varphi_\alpha \mathcal{I}_j))(\mathbf{x}, z) = (\varphi_\alpha \mathcal{I}_j)(\mathbf{x}, z + \Delta z)$$

represents a translation in depth.

We introduce the weighted correlation power $\mathcal{J}$ – as a function of wavespeed or, according to (4.2), as a function of γ – as the energy functional that is to be optimized:

$$\mathcal{J}[\gamma] = \sum_{\alpha=1}^{N_{\mathcal{I}}} \sum_{i \neq j, i, j=1}^{N_s} \frac{1}{S_{ij}^\alpha} \int_X \int_E W_B(\Delta z) \left| \mathcal{C}_{ij}^\alpha(\mathbf{x}, \Delta z) \right|^2 \mathrm{d}\Delta z\, \mathrm{d}\mathbf{x}. \tag{4.9}$$

where E is a closed interval containing 0 over which we vary Δz and W_B is a Gaussian weighting function which penalizes correlation energy away from zero depth shift:

$$W_B(\Delta z) = -\exp\left[-\frac{\Delta z^2}{\sigma_B^2}\right] \tag{4.10}$$

This weighting function is dependent on the frequency content of the data. In order to best capture shifts in depth, we choose σ_B such that W_B has a width that is of the same order as the first peak of the frequency-dependent correlation. Furthermore,

$$S_{ij}^{\alpha} = \int_X \int_E \left|C_{ij}^{\alpha}(\mathbf{x}, \Delta z)\right|^2 \mathrm{d}\Delta z \, \mathrm{d}\mathbf{x} \tag{4.11}$$

represents a normalization which ensures that the functional is not minimized simply by correlating low-amplitude background and shifting the relevant reflectivity in the images outside the correlation windows.

For the error measure described here we develop a model gradient using the augmented Lagrangian method and optimize the velocity iteratively by a conjugate gradient algorithm. The details of the gradient construction can be found in Appendix A.

4.3 Inversion example – subduction model

4.3.1 Generation of synthetic dataset

For a first test of our inversion method we consider a target structure (figure 4-2(a)) based loosely on the subduction model of Audet et al. (2007). The model consists of a slow continental crust, a subducted slab with a relatively slow oceanic crust and faster lithosphere, and a mantle wedge between the slab and the continental crust. Since modeling the initial teleseismic leg of the wave propagation is difficult to achieve without resorting either to high frequency approximations or a great computational expense, we limit our computational domain to the area beneath the array. The model domain is spanned by a 300 km offset at the surface and a depth range of 100 km with grid spacing of 250 m.

We illuminate the model structure with planar waves arriving with different angles of incidence from the bottom of the domain. We use the 2-D Helmholtz solver (Wang et al.,

2010) to generate a dataset up to 2 Hz that includes 29 different teleseismic events with incoming incidence angles between -30° and 30°. The Helmholtz solver accounts for multiple forward and backscattering. The direct incoming wave is altered by velocity heterogeneity as it travels through the model. It is then reflected back downwards at the top of the domain by a free surface boundary condition, and the back-scattered surface-reflections are recorded at the surface. We store data at every computational node at the free surface within the bounds of the array.

Following the generation of synthetic data, several preprocessing steps are needed before the data can be used for reflection tomography. We first time-shift the traces according to their predicted arrival times based on the 1D model so that they are nearly aligned according to the direct *P*. Next, we use multichannel cross correlation on a window around the first arrival to align the wavefield and then perform a principal component analysis. The incoming wavefront is only affected weakly by the model heterogeneity before it reaches the array. Empirically, then, we find that retaining the first two eigenvectors as the incident "source-side" wavefield yields the best results. The rest of the eigenvectors are used as the scattered multiple field. In the presence of horizontal reflectors in the medium, the estimate of the incident field will contain arrivals of the multiples. Both wavefields are then shifted back to their absolute times. The results of this process are displayed in Figure 4-3.

Since the incident field and the multiply scattered field are both recorded at the free surface, they are each the composition of an upgoing incoming field and downgoing reflected field. We wish to utilize the downgoing component of the incident field and the upgoing component of the multiples for our imaging. It is therefore necessary to perform a directional decomposition to separate these components. This is accomplished through application of the decomposition operator described in Equation 4.5. We follow Van Stralen et al. (1998) and chose a discretization of this operator in the frequency domain based on a symbol approximation in order to ensure proper amplitudes for our propagations.

We note that for the application of this method to thre-component teleseismic data from regional scale arrays, other preprocessing steps are needed as outlined in Section 4.4.

4.3.2 Imaging with synthetic data

As the first step in the inversion procedure, an RTM is performed on the data from each separate teleseismic source. Using the inverse scattering transform (equation 4.7) we are able to recover an accurate estimate of the non-smooth part of the velocity model (Figure 4-2(b)) up to illumination effects. Figure 4-4(a) shows the image resulting from the traditional stacking approach for the true smooth model (Figure 4-2(c)). Figure 4-4(b) shows the imaging result when using a 1D reference model. Due to the overestimation of the model velocity near the top of the region, the upper reflectors (continental Moho, top of slab and slab Moho) come in below the correct location while the bottom reflector (base of slab) registers as too shallow due to the underestimation of velocities in the slab. Note that without *a priori* knowledge of the reflector locations it would be difficult to distinguish which of the two images is correct based on the stacked images alone.

The accuracy of the imaging for a given bandwidth of data depends on the spacing of the stations and the ability to interpolate the wavefield between them. For a station spacing of greater than 2.5 km, images formed with data with 2 Hz peak frequency exhibit aliasing. At shallow depths, where the Fresnel zones do not overlap, the sparsity of stations introduces artifacts which makes it both difficult to interpret the image and to use the result to perform tomography. For the frequency content prevalent in teleseismic data, however, a station spacing or interpolation of 5 km is sufficient for forming an accurate image. In practice, this interpolation can be effectively done via a shearlet decomposition (Häuser & Steidl, 2013). For the imaging results presented here, the wavefield at the surface is defined on all grid nodes within the array area.

In order to apply the tomographic error function to the image, we eschew stacking it over the whole dataset and instead compare between images formed by different events. Figure 4-5 show single source images formed in the true model for a variety of incidence angles. Events with high angles of incidence (Figure 4-5(a) and (c)) have difficulty illuminating the discontinuity between the oceanic lithosphere and the mantle due to the geometry of the incoming wave and baseline length of the array.

4.3.3 Error function

It can be expected that, given the correct background model, images from different events will form images focused at the same locations, up to illumination effects. Figure 4-6 demonstrates the effect of the background model on the source-indexed image gathers. The image gathers display the residual moveout between different single-source images by setting them side by side. The shape of these gathers gives information on the success of the imaging. If the model is correct, as in Figure 4-6(b), the image gathers should be essentially flat. If the model is incorrect, moveout appears in the image gathers – a slow model leads to images from high incidence angle events forming at shallower depths than low incidence angle events. The reality of teleseismic data dictates that these images will, however, have differing shape due to varied frequency content, stretching effects, and coupling between imaged structure and imperfectly deconvolved source-time functions. For this reason, we look for an image-based error function sensitive only to the kinematics of the image.

Van Leeuwen & Mulder (2010) introduced the correlation power norm as a robust way to characterize the differences in depth moveout in between images. This is illustrated by Figure 4-6(a). In practice, we pairwise cross correlate partial images generated by distinct sources. The images essentially vary continuously with source position along a curve (in 2.5D, or surface in 3-D) in any reasonable velocity model. Thus, even if the velocity model used for imaging is far from the true model, we need not ensure that the images generated by different sources are sufficiently close to one another.

The efficacy of the correlation power measure depends on a variety of parameters. Foremost among these is weighting function, $W_B(\Delta z)$. The purpose of the weighting function is to penalize correlation energy far away from zero shift, but at the same time we wish to avoid penalizing the image for the shape of its reflectors. We therefore look for a weighting function with a width of the same order as the first correlation peak which depends on the bandwidth of the data.

Figure 4-8 illustrates the error function using the correlation power in depth. This correlation is multiplied by the weight function, and the sum of the weighted correlation is added to the error function. In order to ensure that we are not mapping noise into the error function we must limit the image correlation to areas where a strong, consistent image exists for the events considered. The selection of correlation windows is based on the amplitude, coherence, and linearity of the images. Typically, we take into account image points where the sum of the correlation power between two images exceeds a threshold value relative to the average strength of image autocorrelation. This set of image points can be updated during the iterative optimization if necessary. Figure 4-7 shows the location of image points and the correlation windows around them that were used in our inversion.

The use of a correlation error function in depth only may bias the inversion towards reflectors with shallow dips. In principle, the correlation should ideally take place in the direction that the image moves under a perturbation of the velocity model, as determined by the solution of the velocity continuation ray tracing system (Duchkov & de Hoop, 2009). While it is possible to adjust the correlations in this way, if the target reflectors are horizontal or near horizontal and if the moveout of the images is almost completely in the vertical direction, it is sufficient to consider only vertical shifts in the correlations and apply this measure iteratively. For the case of non-planar scattering points or steeply-dipping reflectors it is also possible to design a correlation function in two dimensions, which will allow for a measurement of image moveout in a general direction. The weighting function in equation 4.10 then takes the form:

$$W_B(\Delta x, \Delta z) = -\exp\left[-\frac{\Delta x^2}{\sigma_{B,x}^2}\right] - \exp\left[-\frac{\Delta z^2}{\sigma_{B,z}^2}\right] \tag{4.12}$$

where weighting parameters $\sigma_{B,x}$ and $\sigma_{B,z}$ can be fixed based on frequency content and reflector dip (and need not be the same).

To demonstrate the effectiveness of the error function we test its ability to distinguish the correct model from an incorrect model, which, however, retains the general 1-D structure of the model. We vary the strength a perturbation δc given by

$$\delta c[\alpha] = c_{true}(x, z) - \alpha c_{true}(X - x, z) \tag{4.13}$$

by a parameter α from -1 to 1. In effect, we start with an initial guess that is the mirror image of the actual subduction model since $c_{true} + \delta c[-1] = c_{true}(X - x, z)$. Figure 4-9 shows the endmember models and their resulting error measures. Even for such a severe model perturbation, the correlation power error function proves to be convex and robust.

4.3.4 Adjoint calculation

We construct the model gradient using the seismic adjoint method. For each image pair correlation, there are four contributions to the gradient – one from the source-side leg of propagation (Equation 4.25) and one from the receiver-side (Equation 4.26) for both images involved. The construction of these gradients involves a solution to the Helmholtz equation for each of the four contributions with an adjoint source that is distributed over the entire correlation window. Correlation of these adjoint fields with each of their respective forward fields then determines the gradient. For a single correlation window, these four contributions to the gradient take the form of deformed "bananas", where the kernel extends in the direction of propagation, widening at the surface since all receivers are included in the calculation for both source- and receiver-side gradients.

Previous methods use such adjoint calculations to determine a sensitivity kernel that allows the projection of an error measure, for example, traveltime delay (Dahlen et al., 2000; De Hoop & Van der Hilst, 2005), residual moveout (Xie & Yang, 2008) or extended image annihilation (De Hoop et al., 2006), back onto a model space. For the reflection tomography considered here, the shape of the sensitivity kernel is inextricably linked to the error measurement itself. The spatial extent and characteristics of the "sources" in equations 4.25 and 4.26 are determined by the correlations and choices of weighting functions.

To confirm the accuracy of our inverse theory, we compare the kernels determined by an adjoint state calculation with ones computed via a finite difference approach. Beginning with a smooth 1D model, c_0, we solve the forward problem once with a perturbation of $\delta\gamma_k = 50$ m/s to each basis function $\psi_k(\mathbf{x}, z)$ and find the perturbed error function. The finite difference gradient,

$$\frac{\partial \mathcal{J}}{\partial \gamma_k} = \delta\gamma_k^{-1} \left(\mathcal{J}[c_0] - \mathcal{J}[c_0 + \delta\gamma_k \psi_k(\mathbf{x}, z)] \right), \tag{4.14}$$

should then be approximately equal to the one computed by the adjoint method. The kernels for one correlation pair are shown in Figure 4-10 with the adjoint method gradient projected onto the basis functions for comparison. Above the correlation window, the kernels are quite similar, but the finite difference version does not include a sensitivity below and directly beside the correlation window due to a lack of backscattering from the smooth perturbations. These kernels demonstrate the sensitivity of the error function to scattering in the transmission regime between the discontinuities and the surface. It is this sensitivity that renders the method apt for optimizing the smooth, long wavelength velocity model.

4.3.5 Inversion results

We ran a series of test inversions to examine the resolving power of the method. For the first series of tests, we consider updates only the central 150 km of the model where the structure is illuminated by all sources. The initial model (Figure 4-11(a)) has 1D structure in the target region and a smooth version of the true subduction zone model in Figure 4-2(a) elsewhere. The perturbation between the true and initial models is shown in Figure 4-11(b). To cover the target region we choose as our basis functions quadratic B-splines with 6 km spacing, with 23 bases in offset and 14 in depth.

Figure 4-12 shows several iterations from the inversion with the most complete set of data parameters. This inversion was performed using data up to 2 Hz in frequency and for the full set of events with incident angles ranging from -30° to 30°. The error function correlation windows used, shown in Figure 4-7, were picked based on coherent single-source image formation in the starting model and are not updated during the process. The error function parameters $\sigma_{B,z}$ were of the order of 0.5-1.0 km. The maximum Δz for the correlations was typically ± 10 km but varied according to the width of the image and nearness of other reflectors.

We perform the inversion via non-linear conjugate gradient. After 5 iterations (Figure 4-12(a)), the general outline of the test perturbation comes into picture. The boundary between the crust and mantle wedge on the right side of the model begins to be delineated and the subducted oceanic crust can be seen clearly. In general, the amplitudes are underestimated and the perturbation below the second reflector has yet to fill in. After 16 iterations the continental crust and wedge outlines begin to become well defined. A fast "hole" remains in the center of the crust due to the complexity of the image below. The connection between the tip of the mantle wedge and the subducted lithospheric mantle is a consistent feature in all high-frequency inversions. After 23 iterations the hole in the crust is ameliorated, and the boundaries of the model sections are sharpened. The spurious connection remains even if the inversion is near its final result. By this point, the amplitudes of the inferred perturbations are already quite accurate. Further iterations result in minor improvements, notably the fine structure of the upper subducted crust and its connection to the lower part of the slab, as seen in Figure 4-12(d). The final result has limited accuracy above the bottommost reflector where only one set of crossing sensitivities are available. Figure 4-13 shows the updates to the image and image gathers based on the model iterations shown in Figure 4-12. Although the stacked images (a and e) do not appear to change dramatically, the image gathers (b and f) become noticeably flatter. Figure 4-13(a) gives the error function reduction during the optimization.

The sensitivity of the error function to model perturbations depends on the model used for propagation and thus changes with each iteration. Figure 4-14 shows the evolution of the sensitivity kernel for one correlation pair between the first and final iterations.

4.4 Discussion

4.4.1 Effects of limited incidence angles

Studies using teleseismic free surface multiples typically include data from earthquake sources between 30° and 90° epicentral distance from the array. Arrivals from these events have incident angles between 15° and 30°, which leaves a considerable gap in angular coverage compared to the above best-case scenario. Although the absence of the near vertical incidence events from the data leads to a decrease in model resolution, the advantage of a source-indexed approach is the ability to handle sparse coverage. The quality of the inversion will degrade near the base of the model and around the edges of the array due to inadequate illumination by multiple reflected events. However, the center of the model remains well resolved due to the existence of multiple crossing paths.

Figure 4-15 shows the results of the inversion with a realistic distribution of teleseismic sources, including one vertically incident phase, such as *PKIKP*. Though the number of image correlations done for the limited dataset is halved, the misfit for this case is not much worse than for the model derived with the full sweep of incident angles. The spurious connection between the mantle wedge and slab mantle is stronger, and the inversion fails to resolve the bottom of the slab at the right side of the target, but the result is not otherwise degraded.

4.4.2 Effects of limited array aperture

The capability to produce tomography updates of the model at certain depths derives from the ability to form images using a variety of incidence angles. For tomography with reflections in the upper mantle we require an array baseline long enough to ensure both the direct wave and the multiples will be recorded from these reflectors. To illustrate this point we perform an inversion with an array limited to only the central 130 km of the model space. The image created with this truncated array is displayed in Figure 4-16(a). The color of the image points represents the log of the total number of image correlations that were performed at each image point. The lack of angular illumination reduces the number of correlations that can be done, particularly at the deeper reflectors, beneath the mantle wedge and towards the edges of the image, as shown by the colored points at the centers of the windows. The resulting model reconstruction 4-16(b) remains accurate at shallower depths and where the distribution of correlations is similar to the previous inversions, but is degraded in the lower half and at the margins. The subducted crust, visible in the other inversions, is not recovered here.

4.4.3 Effects of source spectrum

Due to the nature of the teleseismic problem, data must be gathered from events with a variety of source-time functions and frequency content. Even with sophisticated techniques for deconvolving the source signature from the scattered wavefield, images from different events will be formed using different frequency peaks and noise content. This can be mediated, in part, by stacking images from common source regions prior to applying the image correlation. To simulate the difficulties involved with teleseismic data we create an alternate series of images with different frequency content.

Figure 4-17(a) shows an image created using data only up to 1Hz, a reasonable bandwidth for teleseismic data. A new set of error parameters were determined for use with this image. The correlation windows are widened and $\sigma_{B,z}$ and Δz both scale roughly linearly with frequency. The number of correlations performed is similar to the higher frequency case except in regions where the new, "thicker" images of reflectors are more likely to overlap, as in the tip of the mantle wedge. The resulting model (b) has some advantages over the high frequency inversions. The connection between the upper and lower sections of the subducted crust is more continuous and the shape of the subducted mantle is better recovered. The hole-like anomalies in the center of the crust are filled in earlier in the iterative process. Areas with spottier correlation coverage are somewhat worse, as in the mantle wedge, and the fine structure of the subducted crust on the left side of the model is not recovered.

As a final test of the method, we generate a series of single source images with different frequency characteristics for every source. The amplitude spectra used in the test fall between the endmembers from the previous inversions, with peak frequencies ranging between 0.7 and 1.2 Hz, as shown in figure 4-18 (a). The resulting source-time functions vary by a factor of 2 in length. The bandwidth is simply indexed to the source number, with the lowest frequency event coming from -30° and the highest frequency event coming from 30°.

Inversions were performed for these images using the sets of error parameters both from the 2 Hz tests and 1 Hz tests, and the results are displayed in Figure 4-18(b) and (c), respectively. 4-18(b) shows the result from (c) iterated further with the 2 Hz error parameters. All model results share characteristics with the other inversions using the same error functions. While none perform quite as well as the uniform frequency cases, both manage to reconstruct the major elements of the test model. The inversion using high frequency error parameters recovers the sharply defined boundaries between the model elements, but suffers from a greater prevalence of holes within them. The inversion done with the low frequency parameters does well at recovering the smooth variations of the model, but it retains the anomaly between the wedge and subducted mantle common to inversions with high frequency data. While this points to a tradeoff in the selection of the error function parameters, the fact that both sets reconstructed the models with low misfit demonstrates the robustness of the method. Figure 4-18(d) shows the model from (c) updated for another 10 iterations with the high frequency set of parameters. In this paper we have focused on using uniform sets of error functions, but in practice these results could be further improved by selecting parameters based on individual source pairs.

4.4.4 Preprocessing for application to regional-scale array data

For the application of the method presented here to broadband 3-component array data, additional preprocessing is required. Before we can separate the incident and multiple wavefields, we must separate the data by polarization. This can be done by rotating the three-component data into P, SV, and SH directions through the application of a free-surface transfer operator (Rondenay, 2009). Such analysis would allow for the application of the method to either P to P or SV to SV free surface multiples while still using the scalar wave equation. Additionally, the source-time function of teleseismic events must be estimated from the data and carefully deconvolved from the incident and multiple wavefields. The source-time function can most accurately be represented by the (time-windowed) first principal component. Deconvolution can then be performed in using a number of approaches, including the frequency domain method with optimized water levels (Chen et al., 2010).

4.4.5 Comparison with Full Waveform Inversion

Although they have characteristics in common, the reflection tomography method presented here is fundamentally different from full waveform inversion (FWI). FWI seeks to find a model of elastic properties that best explains the phase and amplitude of seismic observations (Pratt, 1999; Virieux & Operto, 2009). Indeed, the inverse scattering computation that comprises the first step of our inversion method is identical to the initial gradient in a waveform inversion (Wang et al., 2010), but the two approaches diverge thereafter. While an FWI approach would use the results of inverse scattering to model data to compare with observations, reflection tomography uses an image-domain scheme to measure the fitness of the background velocity. The gradient in FWI is thus sensitive to backscattering generated by sharp contrasts in elastic properties while the reflection tomography gradient is sensitive forward scattering between the discontinuities and the surface that are due to smooth variations in the background model.

Each method has advantages and disadvantages with regards to teleseismic data. As currently implemented, reflection tomography can only deal with singly backscattered free surface multiples, while a full waveform approach (Pageot et al., 2013) implicitly incorporates forward scattering along the initial teleseismic leg, in addition to higher order multiples. One of the most persistent difficulties encountered in FWI is cycle skipping, that is, the initial estimate of the velocity structure must model data within a quarter wavelength of observations or the optimization problem will not be convex. Reflection tomography in principle avoids this issue by considering image correlation over an adequate range of depth shifts, which allows for convergence starting from relatively less suitable starting models. For this reason, reflection tomography and FWI are often used in tandem in exploration seismics, with the reflection tomography inversion recovering a model adequate to avoid cycle skipping. In the application to the teleseismic problem, the cycle skipping issue may be ameliorated due the long wavelength content of the data compared to lithospheric scales, but the problem likely persists on scales that include the mantle transition zone.

Due to the difficult properties of teleseismic, reflection tomography may be more apt as a starting point for model building than FWI. The long baselines of teleseismic arrays can lead to variable noise and amplitude properties from receiver to receiver, making the amplitude estimation of the discontinuities (and thus the modeled data) less reliable. For this reason, the reflection tomography seeks only to match the phase information of the images. Additionally, both methods rely on estimation of the source time function. Since some coupling inevitably remains between the source time function and near-receiver structure, the power norm based tomographic error function seeks to reduce its impact. A simple

L2 minimization of data residuals for FWI would be strongly influenced by this coupling, although Pageot et al. (2013) suggests alternative metrics that would be more robust.

4.4.6 Treatment of *P* to *S* conversions

We have considered only *P* to *P* free surface multiples in order to link our work with acoustic studies performed in exploration seismology. In fact, imaging with *P* to *S* (and *S* to *P*) converted phases play a much larger role in teleseismic studies. Furthermore, mixed-phase free surface multiples like Pp_ms and Ps_ms can provide strong additions to the image. The extension of our methodology to the elastic case is therefore a first-order priority for future work.

This can be accomplished in one of two ways. The more straightforward route is to separate the *P* and *S* wavefields and propagate both using a scalar wave equation and the *P* and *S* velocity models can be updated independently of each other or with constraints. *P* to *S* multiple scattering can then be treated in much the same way as *P* multiples, while upgoing parts of both of the incident *P* and *Ps* arrivals can be backpropagated to produce an image from the converted phase.

Another way would be to backpropagate both polarizations at once using an elastic solver Wang et al. (2011). *Ps* converted phases can be treated using the methodology of Shang et al. (2012), wherein the (source-time function deconvolved) three component data are propagated in reverse time. The resulting wavefield is then subjected to a polarization decomposition, and an image is obtained by applying the elastic inverse scattering transform (Brytik et al., 2012) to the separated *P* and *S* wavefields.

4.4.7 Extension to 3-D

In 2-D, the applicability of this method is limited to arrays with earthquakes at a variety of epicentral distances aligned with the strike of the array. Events at too great an angle to the strike will necessitate an onerous 2.5D assumption. An relatively high density linear array like the LA RISTRA experiment in New Mexico (Gao et al., 2004), which has major earthquakes generated at subduction zones at the teleseismic distances along its great circle arc, is ideal for our application, but for many linear arrays sufficient coverage will be unavailable.

Fortunately, this limitation will be ameliorated by the extension to 3-D. Tomography using areal array data will be able to consider events from all azimuths, and no matter how sparse that set is, it is more likely to generate paths crossing at a variety of different directions beneath the array. Figure 4-19 illustrates the geometric requirements of the 3-D problem. The tomographic update, as is true for body wave tomography, does not rely on a full set of incoming incidences and backazimuths, but rather a sufficiently variable set of crossing paths.

The extension to 3-D will be aided by the advantages in illumination the teleseismic geometry has over exploration geometry. The locally planar geometry of the "source" we use ensures each source more or less illuminates the subsurface evenly across the entire array. This is only limited by the incidence angle the lower the incidence angle, the more the illumination tapers off at high offsets at depth. The result for 3-D applications is that there will be a hemisphere-like region where the subsurface is illuminated by multiple events sufficiently for tomography, similar to the 2-D case shown in Figure 4-16(b).

4.5 Conclusions

We have developed a method for RTM-based wave equation reflection tomography using teleseismic free surface multiples that is able to handle several issues with teleseismic data. In response to the sparsity of source locations due to the limits of global seismicity we have based our error function not on waveform fits but on the similarity of images formed from single sources or sets of sources in the same location. In order to deal with irregular source-time functions and frequency content, as well as limitations of preprocessing in removing these effects, we compare different single source images by means of a weighted correlation of image windows which penalizes correlation power away from zero depth shift.

The robustness of the error measure in the face of large deviations from the correct model gives this method an advantage over full waveform inversion in regions where an accurate starting model cannot be defined. Synthetic tests show that we can begin with a 1-D model and still recover the correct heterogeneity in the parts of the model where multiple events are reflected. The smooth model resulting from this method can be used in tandem with the model of singular velocity variations given by inverse scattering to achieve a complete characterization of the heterogeneity.

4.6 Acknowledgments

Support for this project was provided by NSF CMG Grant 1025302 and Total E&P. The authors thank the editor, Prof. Jean Virieux and Stephane Operto and the two anonymous reviewers for their constructive comments which improved this manuscript.

4.A The gradient

To efficiently optimize the smooth velocity model, we develop an adjoint method for determining the gradient of the error function with respect to the model parameters. We first extend the computational domain Ω to $\mathbb{R}^n$ and describe the gradient in terms of solutions to the Helmholtz equation. To begin with, the fields $\widehat{G}_i(\mathbf{x}, z, \omega)$ and $\widehat{u}_{\mathrm{r};i}(\mathbf{x}, z, \omega)$ satisfy the inhomogeneous Helmholtz equations supplemented with the Sommerfeld radiation condition,

$$\begin{aligned} &[\Delta + \omega^2 c(\mathbf{x}, z)^{-2}]\widehat{G}_i(\mathbf{x}, z, \omega) = -\delta(\mathbf{x} - \mathbf{x}_{s;i}, z - z_{s;i}), \\ &\lim_{r\to\infty} r^{(n-1)/2}\left(\frac{\partial}{\partial r} + \mathrm{i}\frac{\omega}{c_\infty}\right)\widehat{G}_i = 0, \end{aligned} \tag{4.15}$$

and

$$\begin{aligned} &[\Delta + \omega^2 c(\mathbf{x}, z)^{-2}]\widehat{u}_{\mathrm{r};i}(\mathbf{x}, z, \omega) = -\delta(z)\widehat{N_\Sigma d_i}(\mathbf{x}, \omega), \\ &\lim_{r\to\infty} r^{(n-1)/2}\left(\frac{\partial}{\partial r} + \mathrm{i}\frac{\omega}{c_\infty}\right)\widehat{u}_{\mathrm{r};i} = 0, \end{aligned} \tag{4.16}$$

respectively. By introducing an exterior Dirichlet-to-Neumann map on $\partial\Omega$, we can restrict our analysis to Ω (Keller & Givoli, 1989).

We follow the techniques from the theory of optimization with equality constraints (Plessix, 2006), and introduce the Lagrangian, $\mathcal{L}[c]$, associated with our minimization problem. The quantities, λ, below are Lagrange multipliers. Following the building up of the cross correlation power, we introduce

$$
\begin{aligned}
\mathcal{L} = & \sum_{\alpha=1}^{N_{\mathcal{I}}} \sum_{i\neq j,i,j=1}^{N_s} \frac{1}{S_{ij}^{\alpha}} \int_X \int_E W_B(\Delta z)\, \left|\mathcal{C}_{ij}^{\alpha}(\mathbf{x}, \Delta z)\right|^2 \mathrm{d}\Delta z\, \mathrm{d}\mathbf{x} \\
& + \sum_{\alpha=1}^{N_{\mathcal{I}}} \sum_{i\neq j,i,j=1}^{N_s} \int_X \int_E \lambda_{\mathcal{C};ij,\alpha}(\mathbf{x}, \Delta z) \Big\{ \mathcal{C}_{ij}^{\alpha}(\mathbf{x}, \Delta z) \\
& \qquad\qquad - \int_{\mathbb{R}_{\geq 0}} (\varphi_\alpha \mathcal{I}_i)(\mathbf{x}, z)\, (T_{\Delta z}(\varphi_\alpha \mathcal{I}_j))(\mathbf{x}, z)\, \mathrm{d}z \Big\} \mathrm{d}\Delta z\, \mathrm{d}\mathbf{x} \\
& + \sum_{i=1}^{N_s} \int_\Omega \lambda_{\mathcal{I};i}(\mathbf{x}, z) \Big\{ \mathcal{I}_i(\mathbf{x}, z) - \frac{1}{2\pi} \int_B \frac{\chi(\omega)}{\mathrm{i}\omega} \Big(\frac{1}{\widehat{G}_i(\mathbf{x}, z, \omega)} \widehat{u}_{\mathrm{r};i}(\mathbf{x}, z, \omega) \\
& \qquad\qquad - \frac{c(\mathbf{x}, z)^2}{\omega^2} \nabla \frac{1}{\widehat{G}_i(\mathbf{x}, z, \omega)} \cdot \nabla \widehat{u}_{\mathrm{r};i}(\mathbf{x}, z, \omega) \Big)\, \mathrm{d}\omega\, \Psi_{\Omega_0}(\mathbf{x}, z) \Big\} \mathrm{d}\mathbf{x}\mathrm{d}z \\
& + \sum_{i=1}^{N_s} \int_B \int_\Omega \overline{\lambda_{G;i}(\mathbf{x}, z, \omega)} \Big\{ [\Delta + \omega^2 c(\mathbf{x}, z)^{-2}] \widehat{G}_i(\mathbf{x}, z, \omega) + \delta(\mathbf{x} - \mathbf{x}_{s;i}, z - z_{s;i}) \Big\} \mathrm{d}\mathbf{x}\mathrm{d}z\, \mathrm{d}\omega \\
& + \sum_{i=1}^{N_s} \int_B \int_\Omega \overline{\lambda_{\mathrm{r};i}(\mathbf{x}, z, \omega)} \Big\{ [\Delta + \omega^2 c(\mathbf{x}, z)^{-2}] \widehat{u}_{\mathrm{r};i}(\mathbf{x}, z, \omega) + \delta(z) \widehat{N_\Sigma d_i}(\mathbf{x}, \omega) \Big\} \mathrm{d}\mathbf{x}\mathrm{d}z\, \mathrm{d}\omega \\
& \qquad\qquad + \int_\Omega \lambda_c(\mathbf{x}, z) \Big\{ c(\mathbf{x}, z) - \sum_{k=1}^{N_c} \gamma_k \psi_k(\mathbf{x}, z) \Big\} \mathrm{d}\mathbf{x}\mathrm{d}z.
\end{aligned}
\tag{4.17}
$$

To the inverse scattering term in the Lagrangian we have added a cutoff term $\Psi_{\Omega_0}(\mathbf{x}, z)$ with support contained in $\Omega_0 \subset \Omega$. We now derive the adjoint state equations. The derivatives follow to be:

$$
\begin{aligned}
\frac{\partial \mathcal{L}}{\partial \mathcal{C}_{ij}^{\alpha}} = & \, 2\frac{1}{S_{ij}^{\alpha}} \Big[W_B(\Delta z) \\
& - \sum_{\alpha=1}^{N_{\mathcal{I}}} \sum_{i\neq j,i,j=1}^{N_s} \frac{1}{S_{ij}^{\alpha}} \int_X \int_E W_B(\Delta z)\, \left|\mathcal{C}_{ij}^{\alpha}(\mathbf{x}, \Delta z)\right|^2 \mathrm{d}\Delta z\, \mathrm{d}\mathbf{x} \Big] \mathcal{C}_{ij}^{\alpha}(\mathbf{x}, \Delta z) + \lambda_{\mathcal{C};ij,\alpha}(\mathbf{x}, \Delta z),
\end{aligned}
\tag{4.18}
$$

for the state variable C^{α}_{ij}, and

$$\frac{\partial \mathcal{L}}{\partial \mathcal{I}_i} = -\sum_{\alpha=1}^{N_{\mathcal{I}}} \sum_{j=1}^{N_s} \int_E \Big\{ \lambda_{C;ij,\alpha}(\mathbf{x}, \Delta z)\varphi_\alpha(\mathbf{x}, z)\; (T_{\Delta z}(\varphi_\alpha \mathcal{I}_j))(\mathbf{x}, z) \\ + \lambda_{C;ji,\alpha}(\mathbf{x}, \Delta z)(T^*_{\Delta z}(\varphi_\alpha \mathcal{I}_j))(\mathbf{x}, z)\; \varphi_\alpha(\mathbf{x}, z) \Big\} \mathrm{d}\Delta z + \lambda_{\mathcal{I};i}(\mathbf{x}, z), \tag{4.19}$$

for the state variable $\mathcal{I}_i$. Here, $T^*_{\Delta z}$ is obtained through a change of variable of integration. We use that the supports of φ_α do not contain a neighborhood of the acquisition surface. For obtaining the adjoint state equation for the state variable $\widehat{G}_i$, we first rewrite the terms containing the gradient of $\widehat{G}_i$:

$$\int_\Omega \lambda_{\mathcal{I};i}(\mathbf{x}, z)\; \Psi_{\Omega_0}(\mathbf{x}, z)\, \frac{1}{2\pi} \frac{\chi(\omega)}{\mathrm{i}\omega}\, \frac{c(\mathbf{x}, z)^2}{\omega^2} \nabla \frac{1}{\widehat{G}_i(\mathbf{x}, z, \omega)} \cdot \nabla \widehat{u}_{\mathrm{r};i}(\mathbf{x}, z, \omega)\, \mathrm{d}\mathbf{x}\mathrm{d}z \\ = \int_{\partial\Omega} \lambda_{\mathcal{I};i}(\mathbf{x}, z)\; \Psi_{\Omega_0}(\mathbf{x}, z)\, \frac{1}{2\pi} \frac{\chi(\omega)}{\mathrm{i}\omega}\, \frac{c(\mathbf{x}, z)^2}{\omega^2}\, \frac{1}{\widehat{G}_i(\mathbf{x}, z, \omega)}\, \frac{\partial \widehat{u}_{\mathrm{r};i}}{\partial \nu}(\mathbf{x}, z, \omega)\, \mathrm{d}A(\mathbf{x}, z) \\ - \int_\Omega \frac{1}{\widehat{G}_i(\mathbf{x}, z, \omega)}\; \nabla \cdot \Big[\, \lambda_{\mathcal{I};i}(\mathbf{x}, z)\; \Psi_{\Omega_0}(\mathbf{x}, z)\, \frac{1}{2\pi} \frac{\chi(\omega)}{\mathrm{i}\omega}\, \frac{c(\mathbf{x}, z)^2}{\omega^2} \nabla \widehat{u}_{\mathrm{r};i}(\mathbf{x}, z, \omega)\, \Big]\, \mathrm{d}\mathbf{x}\mathrm{d}z, \tag{4.20}$$

and

$$\int_\Omega \overline{\lambda_{G;i}(\mathbf{x}, z, \omega)}\, [\Delta + \omega^2 c(\mathbf{x}, z)^{-2}] \widehat{G}_i(\mathbf{x}, z, \omega)\, \mathrm{d}\mathbf{x}\mathrm{d}z = \\ \int_{\partial\Omega} \Big[\, \overline{\lambda_{G;i}(\mathbf{x}, z, \omega)}\, \frac{\partial \widehat{G}_i}{\partial \nu}(\mathbf{x}, z, \omega) - \overline{\frac{\partial \lambda_{G;i}}{\partial \nu}(\mathbf{x}, z, \omega)}\, \widehat{G}_i(\mathbf{x}, z, \omega)\, \Big]\, \mathrm{d}A(\mathbf{x}, z) \\ + \int_\Omega \overline{([\Delta + \omega^2 c(\mathbf{x}, z)^{-2}]\lambda_{G;i})(\mathbf{x}, z, \omega)}\, \widehat{G}_i(\mathbf{x}, z, \omega)\, \mathrm{d}\mathbf{x}\mathrm{d}z. \tag{4.21}$$

Using the exterior Dirichlet-to-Neumann map, we find that the boundary integral on the right-hand side of this equation does not play a role. In view of the cut-off function, Ψ_{Ω_0}, the boundary integral in (4.20) vanishes. Hence,

$$\frac{\partial \mathcal{L}}{\partial \widehat{G}_i} = \lambda_{\mathcal{I};i}(\mathbf{x}, z) \frac{1}{2\pi} \frac{\chi(\omega)}{\mathrm{i}\omega \widehat{G}_i(\mathbf{x}, z, \omega)^2} \Big(\mathit{\Psi}_{\Omega_0}(\mathbf{x}, z)\, \widehat{u}_{\mathrm{r};i}(\mathbf{x}, z, \omega)$$
$$+ \nabla \cdot \Big[\lambda_{\mathcal{I};i}(\mathbf{x}, z)\ \mathit{\Psi}_{\Omega_0}(\mathbf{x}, z)\, \frac{c(\mathbf{x}, z)^2}{\omega^2}\, \nabla \widehat{u}_{\mathrm{r};i}(\mathbf{x}, z, \omega) \Big] \Big) + [\Delta + \omega^2 c(\mathbf{x}, z)^{-2}] \overline{\lambda_{G;i}(\mathbf{x}, z, \omega)}. \tag{4.22}$$

In a similar fashion, we first rewrite the terms containing the gradient of $\widehat{u}_{\mathrm{r};i}$,

$$\int_{\Omega} \lambda_{\mathcal{I};i}(\mathbf{x}, z)\ \mathit{\Psi}_{\Omega_0}(\mathbf{x}, z)\, \frac{1}{2\pi} \frac{\chi(\omega)}{\mathrm{i}\omega}\, \frac{c(\mathbf{x}, z)^2}{\omega^2}\, \nabla \frac{1}{\widehat{G}_i(\mathbf{x}, z, \omega)} \cdot \nabla \widehat{u}_{\mathrm{r};i}(\mathbf{x}, z, \omega)\, \mathrm{d}\mathbf{x}\mathrm{d}z$$
$$= - \int_{\partial\Omega} \lambda_{\mathcal{I};i}(\mathbf{x}, z)\ \mathit{\Psi}_{\Omega_0}(\mathbf{x}, z)\, \frac{1}{2\pi} \frac{\chi(\omega)}{\mathrm{i}\omega \widehat{G}_i(\mathbf{x}, z, \omega)^2}\, \frac{c(\mathbf{x}, z)^2}{\omega^2}\, \frac{\partial \widehat{G}_i}{\partial \nu}(\mathbf{x}, z, \omega)\, \widehat{u}_{\mathrm{r};i}(\mathbf{x}, z, \omega)\, \mathrm{d}A(\mathbf{x}, z)$$
$$- \int_{\Omega} \nabla \cdot \Big[\lambda_{\mathcal{I};i}(\mathbf{x}, z)\ \mathit{\Psi}_{\Omega_0}(\mathbf{x}, z)\, \frac{1}{2\pi} \frac{\chi(\omega)}{\mathrm{i}\omega}\, \frac{c(\mathbf{x}, z)^2}{\omega^2}\, \nabla \frac{1}{\widehat{G}_i(\mathbf{x}, z, \omega)} \Big]\ \widehat{u}_{\mathrm{r};i}(\mathbf{x}, z, \omega)\, \mathrm{d}\mathbf{x}\mathrm{d}z, \tag{4.23}$$

and then obtain

$$\frac{\partial \mathcal{L}}{\partial \widehat{u}_{\mathrm{r};i}} = -\lambda_{\mathcal{I};i}(\mathbf{x}, z) \frac{1}{2\pi} \frac{\chi(\omega)}{\mathrm{i}\omega} \Big(\mathit{\Psi}_{\Omega_0}(\mathbf{x}, z)\, \frac{1}{\widehat{G}_i(\mathbf{x}, z, \omega)}$$
$$+ \nabla \cdot \Big[\lambda_{\mathcal{I};i}(\mathbf{x}, z)\ \mathit{\Psi}_{\Omega_0}(\mathbf{x}, z)\, \frac{c(\mathbf{x}, z)^2}{\omega^2}\, \nabla \frac{1}{\widehat{G}_i(\mathbf{x}, z, \omega)} \Big] \Big) + [\Delta + \omega^2 c(\mathbf{x}, z)^{-2}] \overline{\lambda_{\mathrm{r};i}(\mathbf{x}, z, \omega)}. \tag{4.24}$$

The computation of the adjoint sources in equations (4.22) and (4.24) become somewhat complicated by the presence of the divergence terms. For practical purposes, we can instead follow the approximation introduced in Equation (4.6). In this approximation, we need not take the derivative of terms containing $\widehat{G}_i(\mathbf{x}, z, \omega_0)$. This substitution modifies the first right hand side terms of (4.22) and (4.24). Furthermore, finite difference tests (Figure 4-10) show that the divergence terms are negligible, and we therefore omit the second right hand side terms from the calculations. The source side adjoint field in equation (4.22) then becomes:

$$\begin{aligned}\frac{\partial \mathcal{L}}{\partial \widehat{G}_i} = \lambda_{\mathcal{I};i}(\mathbf{x}, z)\frac{1}{2\pi}\frac{\chi(\omega)}{\mathrm{i}\omega|\widehat{G}_i(\mathbf{x}, z, \omega_0)|^2}\frac{|\omega_0|^{n-3}}{|\omega|^{n-3}}\varPsi_{\Omega_0}(\mathbf{x}, z)\, \widehat{u}_{\mathrm{r};i}(\mathbf{x}, z, \omega) \\ + [\Delta + \omega^2 c(\mathbf{x}, z)^{-2}]\overline{\lambda_{G;i}(\mathbf{x}, z, \omega)}\end{aligned} \tag{4.25}$$

and the receiver side adjoint field in (4.24) becomes:

$$\begin{aligned}\frac{\partial \mathcal{L}}{\partial \widehat{u}_{\mathrm{r};i}} = \lambda_{\mathcal{I};i}(\mathbf{x}, z)\frac{1}{2\pi}\frac{\chi(\omega)}{\mathrm{i}\omega|\widehat{G}_i(\mathbf{x}, z, \omega_0)|^2}\frac{|\omega_0|^{n-3}}{|\omega|^{n-3}}\varPsi_{\Omega_0}(\mathbf{x}, z)\, \overline{\widehat{G}_i(\mathbf{x}, z, \omega)} \\ + [\Delta + \omega^2 c(\mathbf{x}, z)^{-2}]\overline{\lambda_{\mathrm{r};i}(\mathbf{x}, z, \omega)}\end{aligned} \tag{4.26}$$

Finally, we have

$$\frac{\partial \mathcal{L}}{\partial c} = \sum_{i=1}^{N_s}\int_B \left(-\frac{2\omega^2}{c^3}\right)\left\{\,\overline{\lambda_{G,i}(\mathbf{x}, z, \omega)}\,\widehat{G}_i(\mathbf{x}, z, \omega) + \overline{\lambda_{\mathrm{r},i}(\mathbf{x}, z, \omega)}\,\widehat{u}_{\mathrm{r};i}(\mathbf{x}, z, \omega)\,\right\}\mathrm{d}\omega + \lambda_c(\mathbf{x}, z), \tag{4.27}$$

and

$$\frac{\partial \mathcal{L}}{\partial \gamma_k} = \frac{\partial \mathcal{J}}{\partial \gamma_k} - \int_\Omega \lambda_c(\mathbf{x}, z)\psi_k(\mathbf{x}, z)\,\mathrm{d}\mathbf{x}\mathrm{d}z. \tag{4.28}$$

At a stationary point, all of these derivatives go to zero, and we can obtain the model update direction, $\frac{\partial \mathcal{J}}{\partial \gamma_k}$, by eliminating the multipliers through successive substitution. In other words, we solve (A.4) for $\lambda_{\mathcal{C};ij,\alpha}$ and substitute it into (A.5), which is then solved for $\lambda_{\mathcal{I};i}$. We then need to solve two Helmholtz equations, (4.25) and (4.26), with $\overline{\lambda_{G;i}}$ corresponding to the adjoint "source field" and $\overline{\lambda_{r;i}}$ corresponding to the adjoint "receiver field." Equation (4.27) has the form of a traditional cross correlation imaging condition between these adjoint fields and their corresponding forward fields. Finally, equation (4.28) just entails a projection onto the relevant basis functions. Thus, from (4.18), (4.19), (4.25), (4.26), (4.27) and (4.28) we obtain a system of equations which we solve from top to bottom; in this process we encounter the fields which make up the images of $r(z, \mathbf{x})$ as well as the images themselves.

Bibliography

Audet, P., Bostock, M. G., & Mercier, J.-P., 2007. Teleseismic waveform modelling with a one-way wave equation, *Geophysical Journal International*, **171**(3), 1212–1225.

Bostock, M. G., Rondenay, S., & Shragge, J., 2001. Multiparameter two-dimensional inversion of scattered teleseismic body waves 1. Theory for oblique incidence, *Journal of Geophysical Research-Solid Earth*, **106**(B12), 30771–30782.

Brytik, V., de Hoop, M. V., & van der Hilst, R. D., 2012. Elastic-wave inverse scattering based on reverse time migration with active and passive source reflection data, in *Inverse Problems and Applications: Inside Out II*, vol. 60, pp. 411–453, Cambridge Univ. Press, Cambridge, U. K.

Chen, C. W., Miller, D. E., Djikpesse, H. A., Haldorsen, J. B. U., & Rondenay, S., 2010. Array-conditioned deconvolution of multiple-component teleseismic recordings, *Geophysical Journal International*, **182**(2), 967–976.

Chen, L., Cheng, C., & Wei, Z., 2009. Seismic evidence for significant lateral variations in lithospheric thickness beneath the central and western North China Craton, *Earth and Planetary Science Letters*, **286**(1-2), 171–183.

Claerbout, J. F., 1985. *Imaging the Earth's Interior*, Blackwell Scientific Publications, Inc., Palo Alto, CA.

Dahlen, F. A., Hung, S. H., & Nolet, G., 2000. Fréchet kernels for finite-frequency traveltimes - I. Theory, *Geophysical Journal International*, **141**(1), 157–174.

De Hoop, M. V., 1996. Generalization of the Bremmer coupling series, *Journal of Mathematical Physics*, **37**, 32463282.

De Hoop, M. V. & Van der Hilst, R. D., 2005. On sensitivity kernels for 'wave-equation' transmission tomography, *Geophysical Journal International*, **160**(2), 621–633.

De Hoop, M. V., van der Hilst, R. D., & Shen, P., 2006. Wave-equation reflection tomography: annihilators and sensitivity kernels, *Geophysical Journal International*, **167**(3), 1332–1352.

Deuss, A., 2009. Global observations of mantle discontinuities using SS and PP precursors, *Surveys in Geophysics*, **30**(4-5), 301–326.

Duchkov, A. A. & de Hoop, M. V., 2009. Velocity continuation in the downward continuation approach to seismic imaging, *Geophysical Journal International*, **176**(3), 909–924.

Gao, W., Grand, S. P., Baldridge, W. S., Wilson, D., West, M., Ni, J. F., & Aster, R., 2004. Upper mantle convection beneath the central Rio Grande rift imaged by P and S wave tomography, *Journal of Geophysical Research-Solid Earth*, **109**(B3).

Häuser, S. & Steidl, G., 2013. Convex multiclass segmentation with shearlet regularization, *International Journal of Computer Mathematics*, **90**(1), 62–81.

Keller, J. B. & Givoli, D., 1989. Exact non-reflecting boundary-conditions, *Journal of Computational Physics*, **82**(1), 172–192.

Langston, C. A., 1979. Structure under Mout Rainier, Washington, inferred from teleseismic body waves, *Journal of Geophysics Research*, **84**, 4749–4762.

Long, M. D., de Hoop, M. V., & van der Hilst, R. D., 2008. Wave-equation shear wave splitting tomography, *Geophysical Journal International*, **172**(1), 311–330.

Op 't Root, T. J. P. M., Stolk, C. C., & de Hoop, M. V., 2012. Linearized inverse scattering based on seismic reverse time migration, *Journal De Mathematiques Pures Et Appliquees*, **98**(2), 211–238.

Pageot, D., Operto, S., Vallee, M., Brossier, R., & Virieux, J., 2013. A parametric analysis of two-dimensional elastic full waveform inversion of teleseismic data for lithospheric imaging, *Geophysical Journal International*, **193**(3), 1479–1505.

Pearce, F. D., Rondenay, S., Sachpazi, M., Charalampakis, M., & Royden, L. H., 2012. Seismic investigation of the transition from continental to oceanic subduction along the western Hellenic Subduction Zone, *Journal of Geophysical Research-Solid Earth*, **117**.

Plessix, R. E., 2006. A review of the adjoint-state method for computing the gradient of a functional with geophysical applications, *Geophysical Journal International*, **167**(2), 495–503.

Pratt, R. G., 1999. Seismic waveform inversion in the frequency domain, Part 1: Theory and verification in a physical scale model, *Geophysics*, **64**(3), 888–901.

Rondenay, S., 2009. Upper mantle imaging with array recordings of converted and scattered teleseismic waves, *Surveys in Geophysics*, **30**(4-5), 377–405.

Sava, P. & Vasconcelos, I., 2011. Extended imaging conditions for wave-equation migration, *Geophysical Prospecting*, **59**(1), 35–55.

Schuster, G. T., 2010. *Seismic interferometry*, Cambridge University Press.

Shang, X., de Hoop, M. V., & van der Hilst, R. D., 2012. Beyond receiver functions: Passive source reverse time migration and inverse scattering of converted waves, *Geophysical Research Letters*, **39**.

Shen, P. & Symes, W. W., 2008. Automatic velocity analysis via shot profile migration, *Geophysics*, **73**(5), VE49–VE59.

Shragge, J., Artman, B., & Wilson, C., 2006. Teleseismic shot-profile migration, *Geophysics*, **71**(4), SI221–SI229.

Stolk, C. C., 2000. Microlocal analysis of a seismic linearized inverse problem, *Wave Motion*, **32**(3), 267–290.

Stolk, C. C. & de Hoop, M. V., 2006. Seismic inverse scattering in the downward continuation approach, *Wave Motion*, **43**(7), 579–598.

Symes, W. & Carazzone, J., 1991. Velocity inversion by differential semblance optimization, *Geophysics*, **56**, 654–663.

Van Leeuwen, T. & Mulder, W. A., 2008. Velocity analysis based on data correlation, *Geophysical Prospecting*, **56**(6), 791–803.

Van Leeuwen, T. & Mulder, W. A., 2010. A correlation-based misfit criterion for wave-equation traveltime tomography, *Geophysical Journal International*, **182**(3), 1383–1394.

Van Stralen, M. J. N., de Hoop, M. V., & Block, H., 1998. Generalized Bremmer series with rational approximation for the scattering of waves in inhomogeneous media, *Journal of Acoustic Society of America*, **104**(4), 1943–1963.

Vinnik, L. P., Mikhailova, N. G., & Avetisian, R. A., 1979. Analysis of observations of the mantle PS waves, *Doklady Akademii Nauk Sssr*, **248**(3), 573–576.

Virieux, J. & Operto, S., 2009. An overview of full-waveform inversion in exploration geophysics, *Geophysics*, **74**(6), WCC1–WCC26.

Wang, S., de Hoop, M. V., & Xia, J., 2010. Acoustic inverse scattering via Helmholtz operator factorization and optimization, *Journal of Computational Physics*, **229**(22), 8445–8462.

Wang, S., de Hoop, M. V., & Xia, J., 2011. On 3D modeling of seismic wave propagation via a structured parallel multifrontal direct Helmholtz solver, *Geophysical Prospecting*, **59**(5), 857–873.

Xie, X.-B. & Yang, H., 2008. The finite-frequency sensitivity kernel for migration residual moveout and its applications in migration velocity analysis, *Geophysics*, **73**(6), S241–S249.

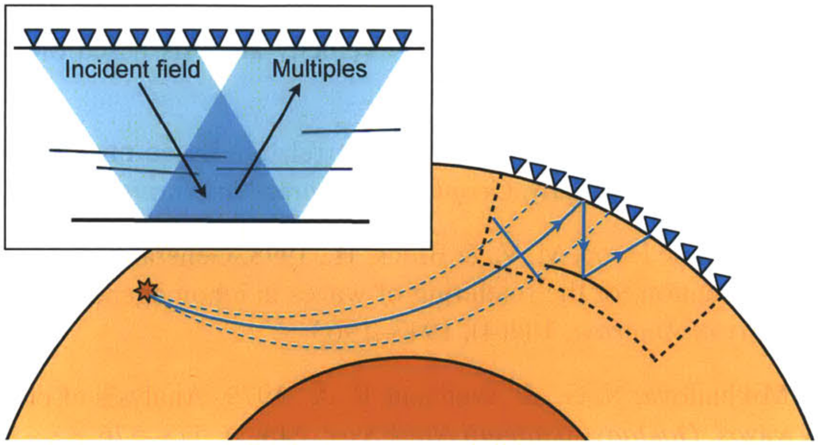

Figure 4-1: Geometry of the teleseismic problem. The direct P waves from distant earthquakes travel through the mantle and are recorded at a seismic array. The waves are reflected at the free surface, are scattered at discontinuities, and are recorded again by the same array. The teleseismic RTM approach uses the direct incident field as a source and the scattered field as data. For the synthetic teleseismic data presented in this paper, we omit the initial leg of travel and give the teleseismic source as a localized plane wave within the computational domain, represented here by the dashed black box.

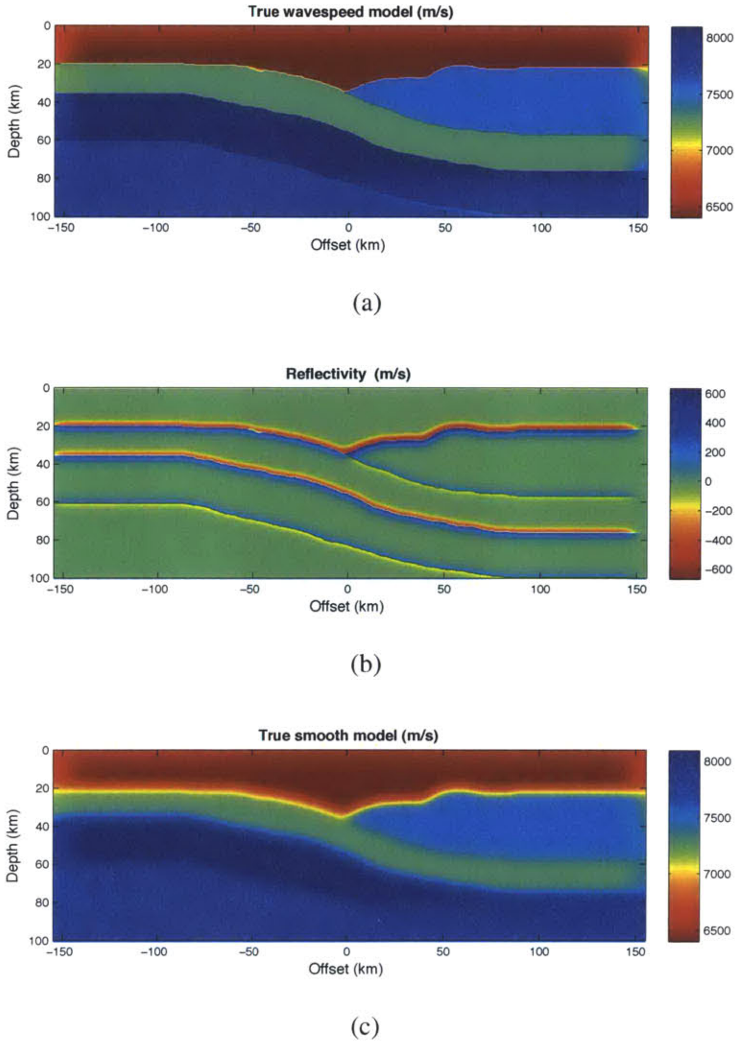

Figure 4-2: (a) Subduction zone model used to create synthetic teleseismic data. (b) Singular part of the subduction zone model. Values in percent perturbation from smooth model. (c) Smooth wavespeed perturbation to the smoothed 1D model.model used for wave propagation in imaging.

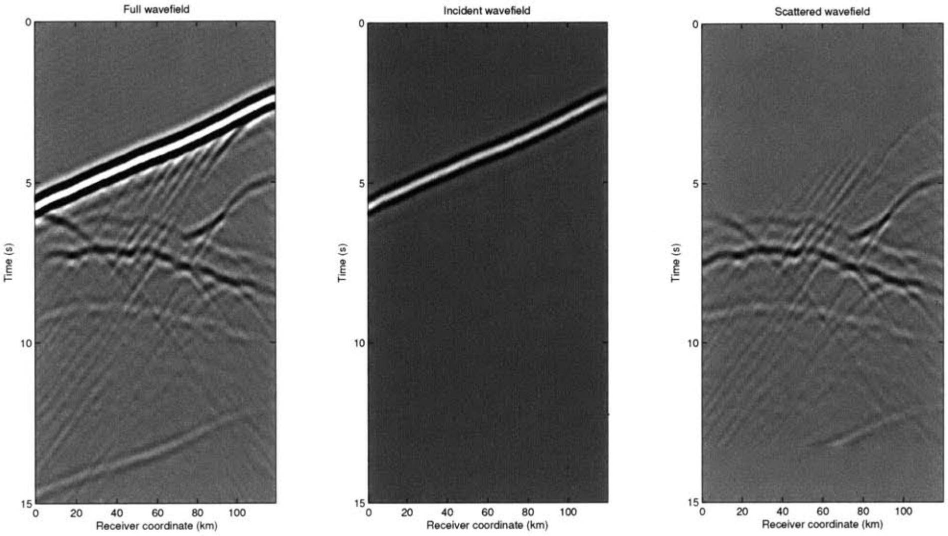

(a) (b) (c)

Figure 4-3: Synthetic data (a) generated by a Helmholtz solver in the velocity model displayed in 4-2(a) is split into the direct arrival, (b) and the free surface multiples, (c). The model is illuminated using a plane wave with horizontal slowness 5×10^{-5} s/m impinging on the bottom of the domain. The wave travels upwards, is reflected by the free surface boundary condition on at the top of the domain and is multiply scattered. The direct and multiple fields are separated by aligning the traces by cross correlation and eigenvalue analysis. Since the source-time function is known in this synthetic case, we do not deconvolve for the source-time function.

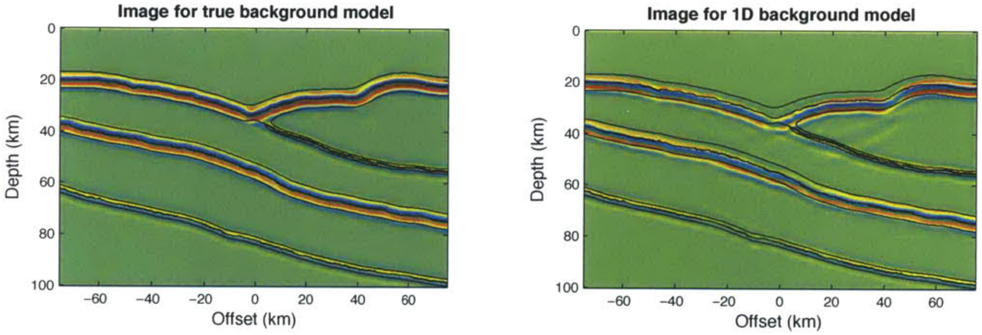
Image for true background model

Image for 1D background model

(a)

(b)

Figure 4-4: (a) The central 150 km of stacked image formed in the true model. Black outlines represent contours of reflectivity in the subduction model as shown in Figure 4-2(b). The image fits well within the contours in this case. (b) Stacked image for 1D model. The top reflectors are shifted downwards from their true location due to an overestimated velocity.

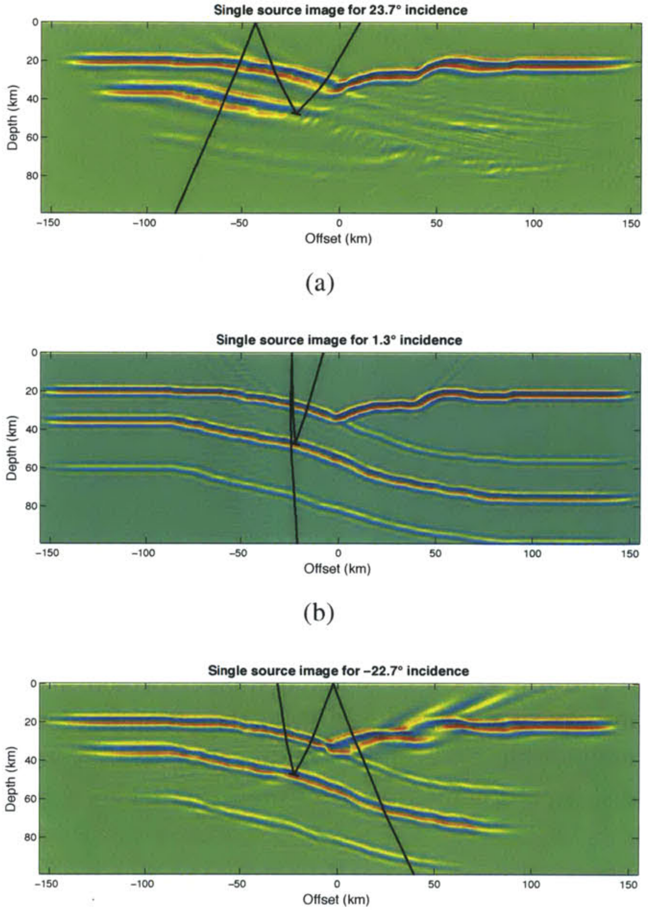

(a)

(b)

(c)

Figure 4-5: Single source images formed using inverse scattering in true model for teleseismic sources arriving from (a) 23° from the left, (b) near vertical incidence, and (c) 23° from the right. The black lines show the ray geometry for one reflection point.

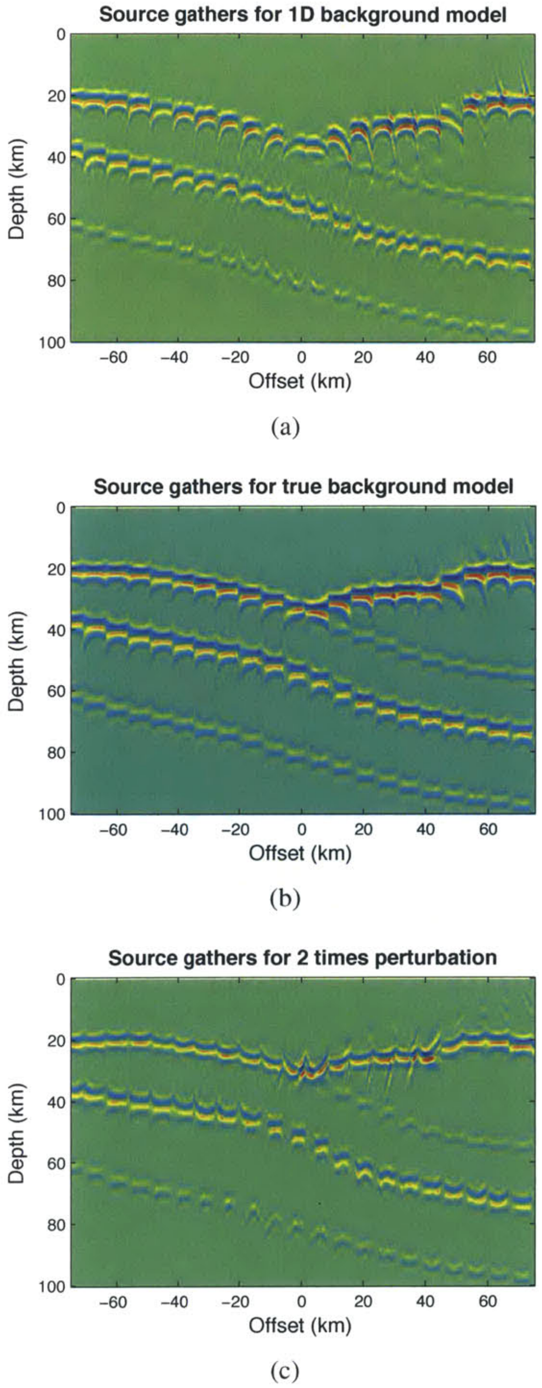

Figure 4-6: Source gathers from the central 150 km section of the image. For a series of horizontal offsets spaced 7.5 km apart, the single-source images from all events are set next to each other to visualize difference in depth moveout in the images. (In the inversion process, measurements are made at all illuminated points along the discontinuities.) (a) Gathers formed using the 1D model. Due to the overestimated velocity in the crust, the images of the uppermost reflector from lower incidence events form deeper. (b) Source gathers for correct smooth model show no residual depth moveout between images. (c) Source gathers for model with double the smooth perturbation from 1D model. The under-estimated crustal velocity leads to a convex gathers for the uppermost reflector.

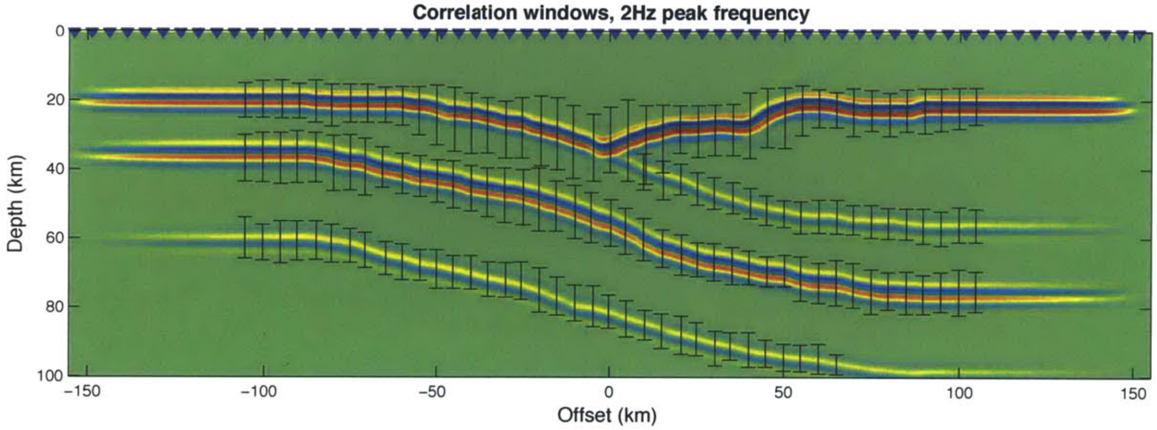

Figure 4-7: Map of correlation windows. Black bars correspond to representative window locations. Correlations are taken at every offset where coherent structure is imaged. Triangles indicate the extent of the receiver array.

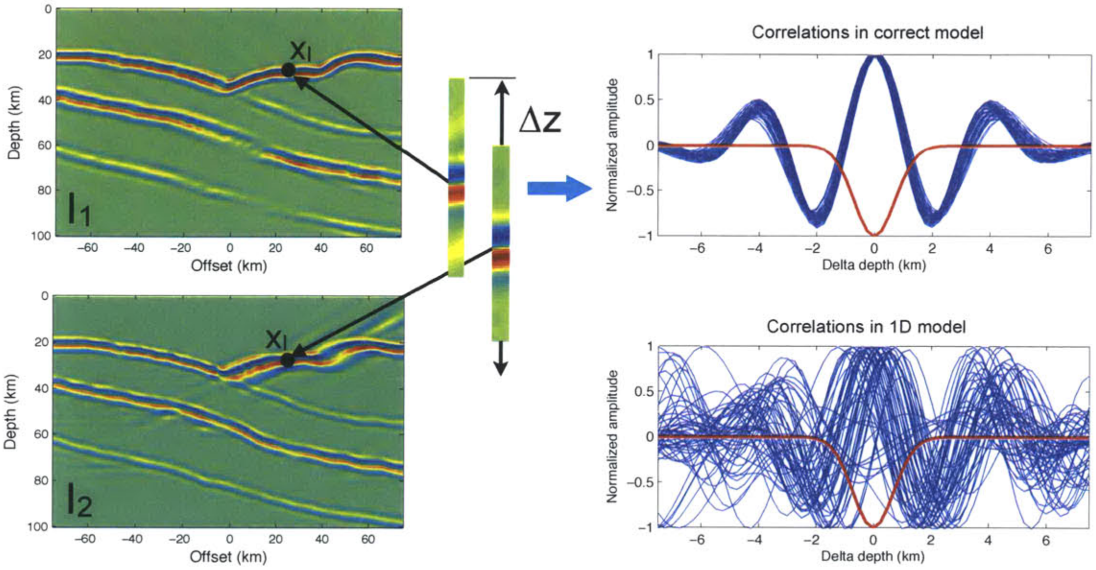

Figure 4-8: An explanation of the correlation power error metric. At each relevant image point, pairs images are correlated on a depth window over Δz. This correlation is multiplied by a weighting function $W_B(\Delta z)$ (shown as a red line) which is chosen based on the bandwidth of the data used to form the image. If the smooth velocity used to propagate the wavefields is correct, the two images should best align at zero depth shift and the sum of the weighted correlation should be at its minimum value. If the model is incorrect along the paths of the waves, the correlations will typically not be centered at zero shift, as shown in the bottom plot.

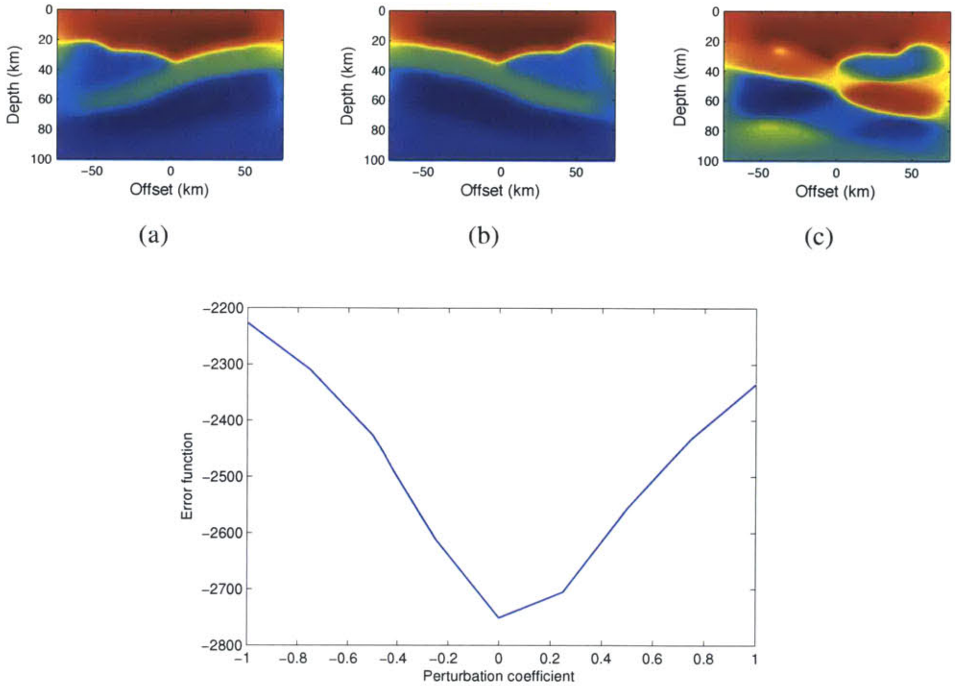

(a) (b) (c)

(d)

Figure 4-9: We test the error function by varying a perturbation to the true model. The perturbation is the difference between true model and the true model flipped from left to right-hand side. (a) True model minus perturbation. (b) True model. (c) True model plus perturbation. (d) Correlation power norm error function with weighting function displayed in figure 4-8. The error function is minimized by the correct subduction model and has a broad basin of attraction.

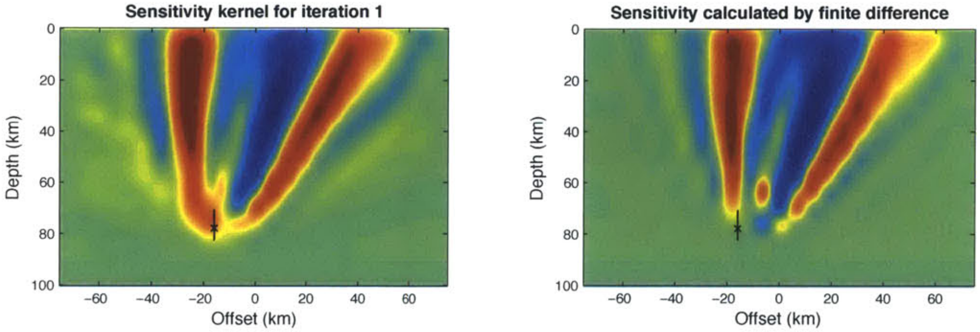

(a) (b)

Figure 4-10: Sensitivity kernels for one correlation window and a single pair of events with incidence angles of 0° and 23° from the right-hand side, as shown in Figure 4-5. Black **x**'s represent location of image point centered on bottommost reflector and line shows extent of correlation window. The red indicates areas where a positive perturbation to the velocity results in an increase in the error function while the blue indicates that the perturbation will reduce the error function. (a) Kernel computed with adjoint method and projected on to spline basis. (b) Kernel computed via finite differences for same correlation window. For each basis function, the smooth starting model in figure 4-11 is perturbed by the function with an amplitude of 50 m/s.

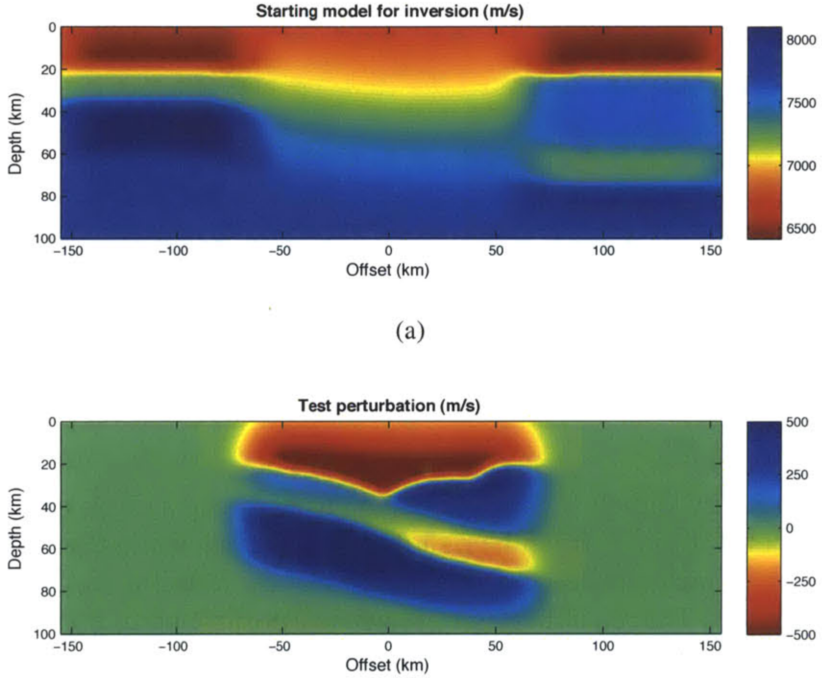

(a)

(b)

Figure 4-11: (a) The initial model for test inversions has 1D structure in the 150 km target region at the center of the model and a smooth version of the true subduction model elsewhere. Tomographic updates are performed in the target region. (b) The perturbation between the true smooth model and the initial model that will be recovered by the inversion.

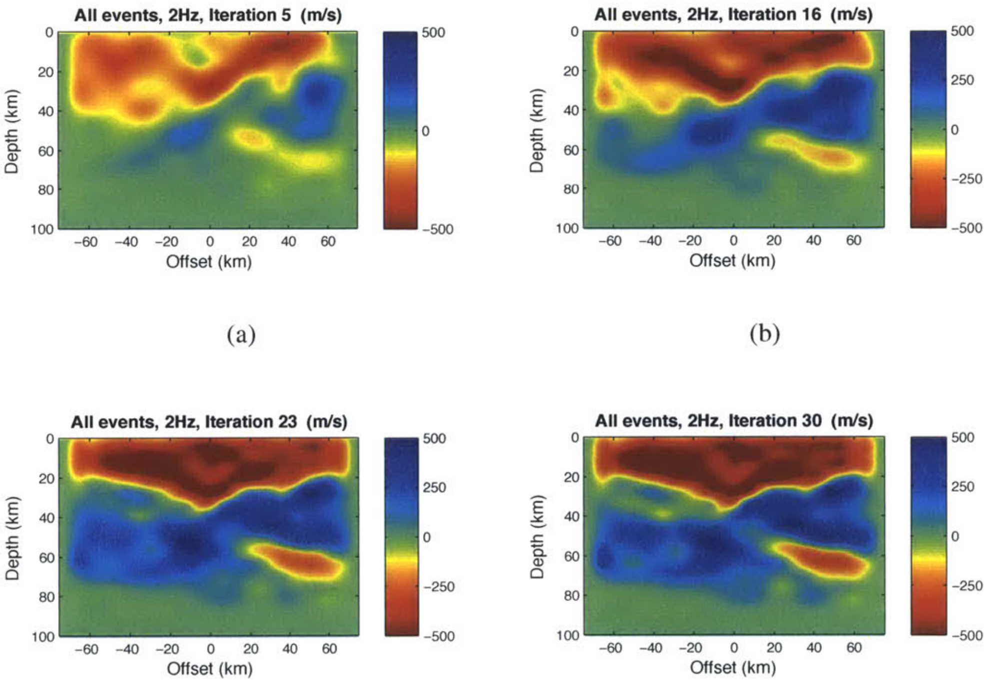

(a) (b)

(c) (d)

Figure 4-12: Inversions results for set of parameters shown in Figure 4-7 using full range of incidence angles and data bandwidth up to 2 Hz. All results are plotted only for the spatial extent of test perturbation for clarity.

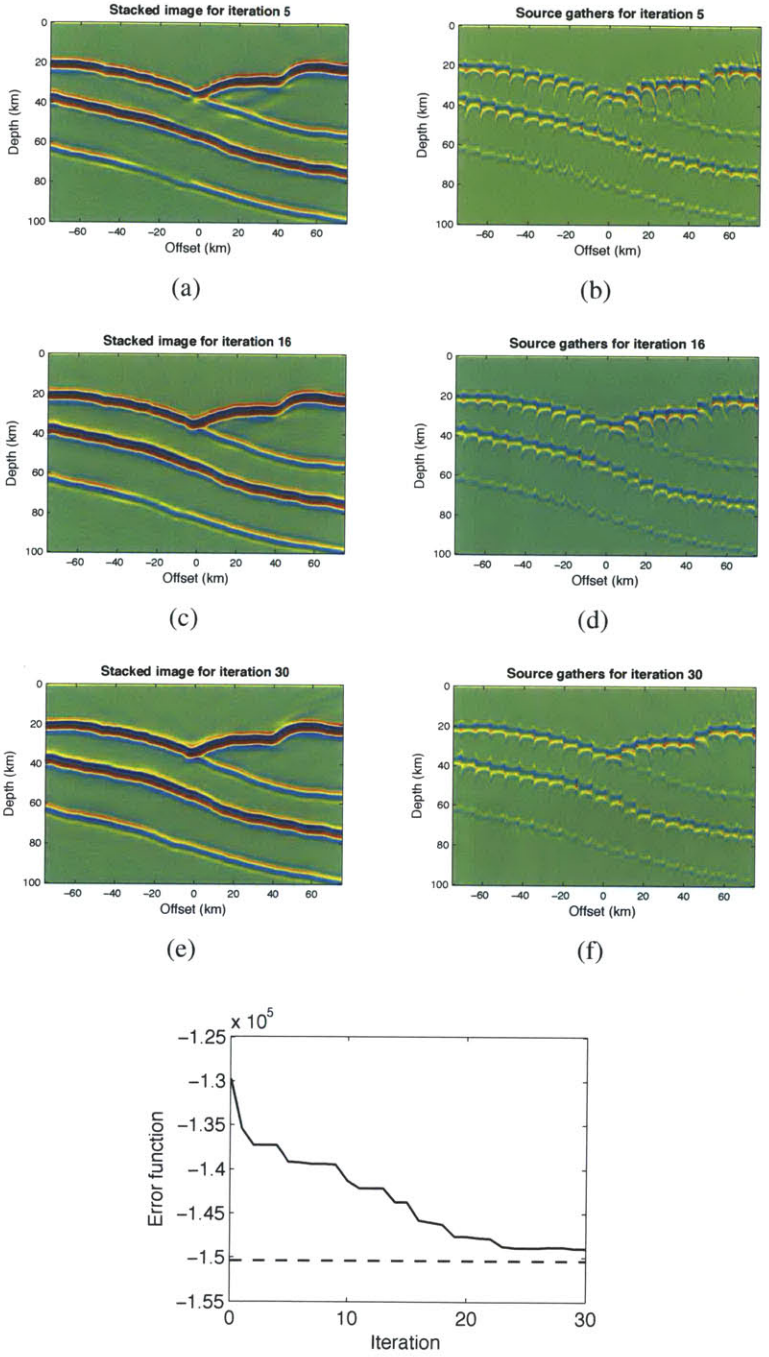

(a) (b)

(c) (d)

(e) (f)

(g)

Figure 4-13: (a),(c) and (e) Stacked images for model iterations corresponding to figure 4-12. (b),(d) and (f) Image gathers for same model iterations. For gathers formed in the starting model, refer to figure 4-6(a). (g) Error function reduction for all iterations. Dashed line represents the error measure for the true model.

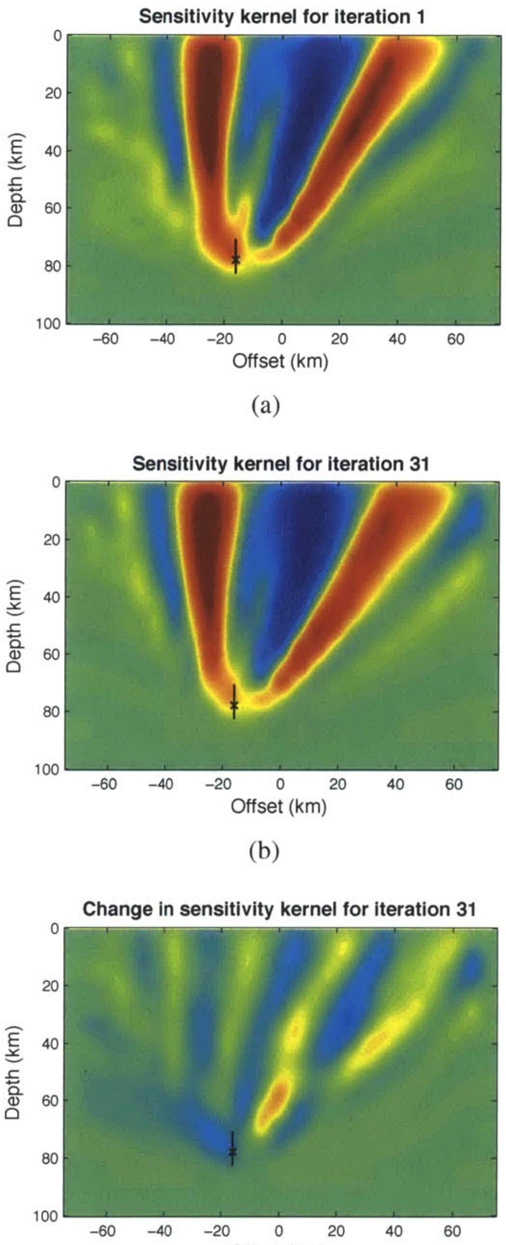

(a)

(b)

(c)

Figure 4-14: Evolution of the sensitivity kernel for correlation window from Figure 4-10 after (a) the first iteration and (b) the final iteration. (c) The difference between the first and final iterations.

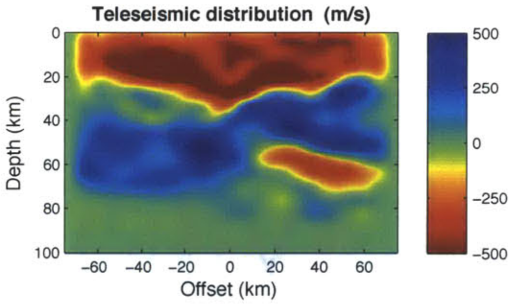

Figure 4-15: Inversion result for more realistic teleseismic distribution of incidence angles. Arrivals range from $15-30°$ from normal, in addition to one vertically incident *PKIKP*.

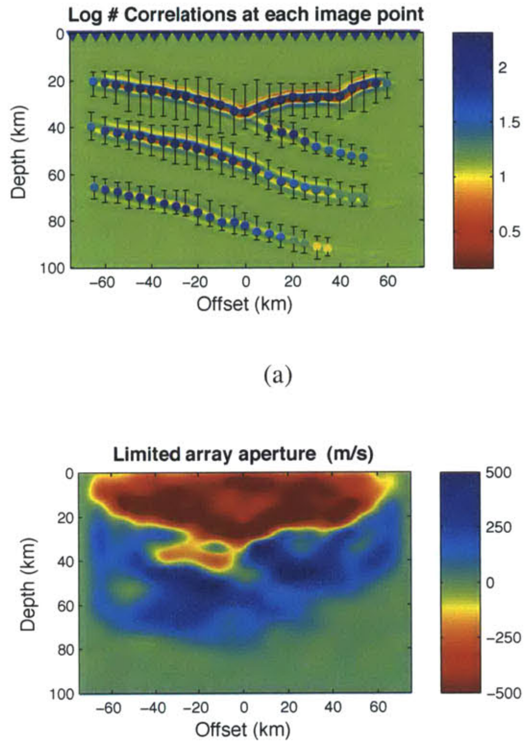

(a)

(b)

Figure 4-16: Effects of a limited array aperture on the inversion. (a) Map of correlation windows projected over image formed with limited aperture array. Inverted triangles show the extent of the recordings. The number of error function measurements is severely decreased at the bottom reflector and towards the edges. (b) Inversion result.

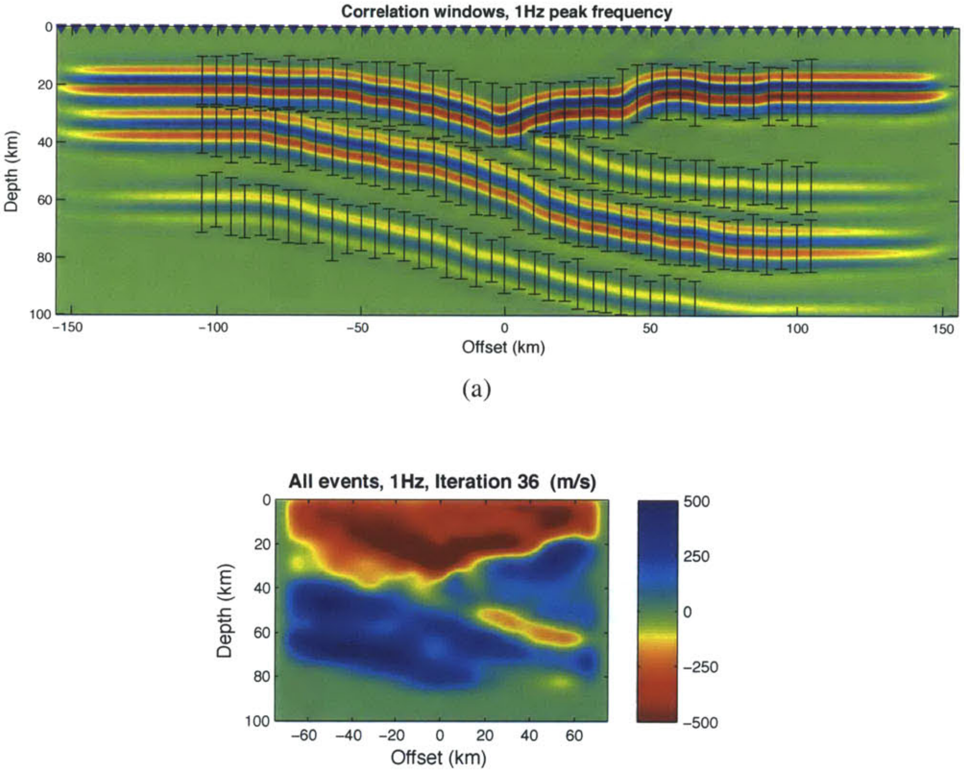

(a)

(b)

Figure 4-17: (a) Map of correlation windows for lower frequency image. Black bars correspond to window extent. The limited bandwidth of the image reduces the number of acceptable windows relative to the 2 Hz image in areas where reflectors are close together. (b) Inversion result with data up to 1 Hz after 36 conjugate gradient iterations.

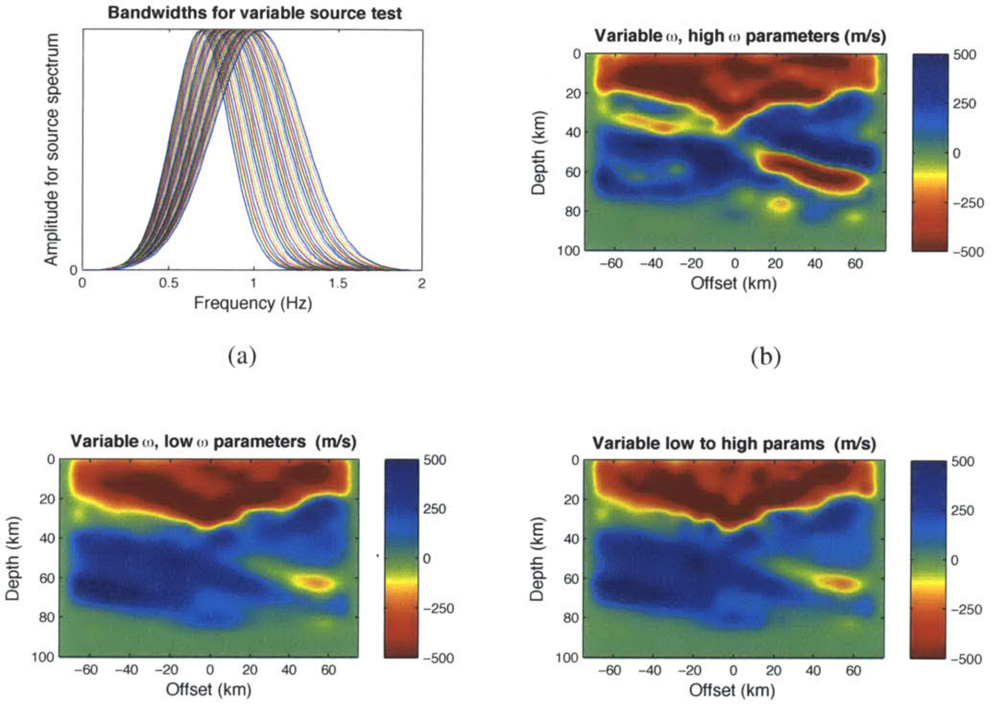

(a)

(b)

(c)

(d)

Figure 4-18: Inversion results with variable frequency information. (a) Source spectra for the 29 incident wavefields vary with peak frequencies between 0.7 and 1.2 Hz. Inversions were performed with the error function parameters displayed in (b) Figure 4-7 and (c) Figure 4-17. (d) Beginning from the result with low frequency parameters in (c), additional iterations were performed with high frequency parameters as in (b).

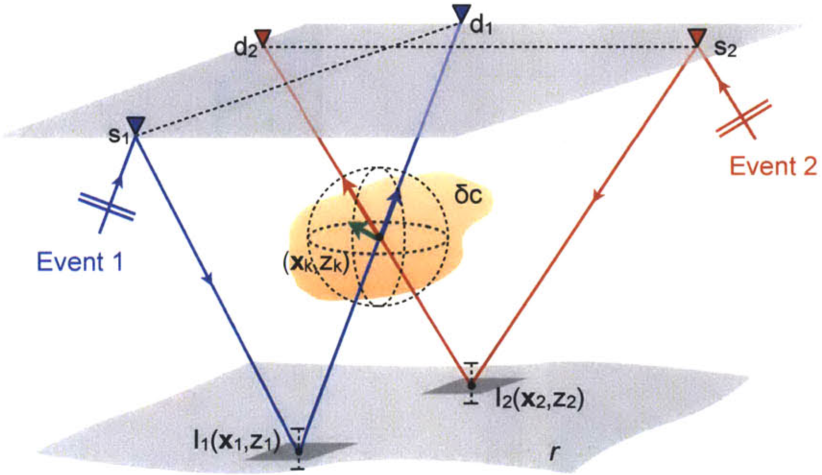

Figure 4-19: Geometry of 3-D reflection tomography problem. A teleseismic wave from event 1 (blue) is recorded at s_1, reflects off of the free surface, scatters off discontinuity *r* at $(\mathbf{x}_1, z_1)$ and is recorded at d_1. A wave from event 2 (red) arrives from a different back-azimuth, reflects downward at s_2, is scattered at $(\mathbf{x}_2, z_2)$ and is recorded again at d_2. The two "rays," in addition to a third "ray" shown in green, intersect at a point $(\mathbf{x}_k, z_k)$ within a smooth velocity heterogeneity δc. In order to constrain the heterogeneity at $(\mathbf{x}_k, z_k)$, we require wavepaths through the point in three sufficiently different directions.

Chapter 5

Smooth and discontinuous structure beneath Tibet from teleseismic reflection tomography

Abstract

The Reverse Time Migration (RTM) based teleseismic reflection tomography method developed in Chapter 4 (Burdick et al., 2013) makes use of images formed with free surface multiples to better constrain smooth variations in wavespeed. As a first real-world test of the method we apply it to broadband data recorded by the Hi-CLIMB array in Tibet. The Hi-CLIMB array was deployed to investigate the collision between the Indian and Eurasian plates and determine the ultimate fate of their respective mantle lithospheres. A number of seismic analyses for recovering either the smooth or the discontinuous velocity structure have been performed using data from the experiment. Our reflection tomography has advantages over the conventional teleseismic transmission tomography previously employed on the Hi-CLIMB data in that it deals intrinsically with the multi-scale nature of wave propagation and can limit updates of the smooth model to within the crust.

Here, we apply reflection tomography to *SsPmp* phases that have undergone post-critical reflection, including waves that arrive at a high angle of obliquity with the strike of the array. In spite of the reduction in resolving power, these events help provide the angular coverage needed to perform a tomographic inversion. We present both the preliminary results of RTM imaging of the Moho and crustal discontinuities and the estimate of smooth velocity structure in the crust recovered by reflection tomography.

5.1 Introduction

The increasing volumes of high-quality broadband passive data from densely-spaced regional seismic arrays call for improved methods for inverting both the smooth and discontinuous velocity structure of the crust and upper mantle. Reverse Time Migration (RTM) imaging-based reflection tomography provides one such opportunity. Compared with the common conversion point (CCP) stacking method regularly used to determine discontinuities in seismic velocity, RTM imaging handles caustics and multi-pathing in the data and does away with assumptions about the linearity and continuity of reflectors. In contrast with the conventional body wave tomography routinely employed to determine the smooth velocity structure, RTM reflection tomography deals with the frequency-dependent nature of the inverse problem and improves depth resolution by constraining updates to structure above the imaged reflectors.

Originally developed for use for seismic exploration in the active source setting, wave-equation reflection tomography exploits redundancy in the data in order to estimate the smooth velocity model used to project reflected phases to depth. The ability of this smooth model to explain the data is judged by whether the images of reflectivity are well-focused (Shen & Symes, 2008) or consistent for different sources (Xie & Yang, 2008) or incidence angles (De Hoop et al., 2006). Due to the unknown source-time functions and sparse, irregular source and receiver locations inherent in the teleseismic setting, reflection tomography approaches developed for exploration purposes are insufficient for use with regional scale passive arrays.

Burdick et al. (2013) presented a reflection tomography method suitable for application to teleseismic array data. To deal with the lack of continuous source coverage, the method uses pairwise comparison of images created using an single-source inverse scattering transform (Op 't Root et al., 2012). In response to the difficulty in removing the source signature from teleseismic data, a robust error measure was developed based on an image correlation power norm (Van Leeuwen & Mulder, 2008). If the smooth velocity model is acceptable, images created with data from different events should be focused about the same depth. The fitness of the model is measured by multiplying the correlations between image pairs by a weighting function that penalizes power away from zero depth shift. Based on this error measure, the gradient of the smooth model is determined using the seismic adjoint method and the model is updated using a conjugate gradient algorithm.

The linear Hi-CLIMB array (Nabelek et al., 2005) in Tibet, with its dense spacing and wide aperture, provides an attractive first application for the teleseismic reflection tomography method in 2-D. The Hi-CLIMB array was deployed to investigate structures associated with the active continental collision between the Eurasian and Indian plates responsible for the uplift of the Himalaya and the broad, flat Tibetan Plateau. The array spans the Himalaya in the south, passing through the Lhasa block and ending in the Qiangtang terrane in the north. It covers two major sutures between the terranes – the Indus-Yarlung suture (IYS) marks the present boundary between Indian and Eurasian crust and the Bangong-Nunjiang suture (BNS) delineates the Lhasa and Qiangtang terranes which fused during a Jurrasic-Cretaceous collision.

One of the major questions the Hi-CLIMB experiment seeks to address is the ultimate fate of the mantle lithosphere from the colliding plates. The Tibetan plateau in the vicinity of the Hi-CLIMB array has undergone a high degree of shortening, and the uplift of the plateau does not account for the total amount of crustal mass involved. Previous tomography results suggest that lithosphere from both plates has descended into the mantle. Body wave (Li et al., 2008; Hung et al., 2010; Zhang et al., 2012) and surface wave (Sun et al., 2010) tomography show a northward dipping fast anomaly beneath the Lhasa terrane and, perhaps, a less pronounced southward dipping fast structure beneath the Qiangtang terrane interpreted to be the downwelling Indian and Eurasian lithospheres, respectively. Between these structures, the lithosphere and upper mantle directly beneath the BNS is seen as a slow region.

Several studies have performed receiver function analysis on converted and free-surface reflected phases culled from the Hi-CLIMB dataset. Nabelek et al. (2009) follows the common conversion point stacking method using P to S converted phases augmented with mixed-phase free-surface multiples. The resulting images show a strong Moho reflection at 40 km depth to the south of the Himalaya, plunging to 70-75 km beneath the Lhasa terrane. They also find evidence for a continuous reflection from the top of the subducted Indian crust which terminates at 31° N. Gaussian-beam migration of converted phases (Nowack et al., 2010) reveals strong, coherent Moho reflections beneath both the Lhasa and Qiangtang terranes, separated by a 200 km section of disrupted reflectivity around the Bangong-Nujiang suture. Elastic reverse-time migration (Shang, 2013) agrees with the depth of structures and shows a weak but more continuous Moho structure beneath the suture.

Both Nabelek et al. (2009) and Nowack et al. (2010) present stacked images illuminated by different clusters of teleseismic events. Stacked images using converted phases coming from the north and south broadly agree south of 31° N. The lack of Moho conversions north of 31° N in waves arriving from the north suggests a northward dipping interface. Gaussian-beam migration results from three event clusters furthermore agree with each other over a broad range of frequency bandwidths. This overall consistency between images formed with different incidences indicates that the teleseismic data collected by the Hi-CLIMB array is suitable for reflection tomography.

For the application of teleseismic reflection tomography to the Hi-CLIMB array, we initially focus on imaging using the *SsPmp* arrival from the section of the array north of the Indus-Yarlung suture. For a range of epicentral distances, the *SsPmp* undergoes a post-critical reflection at the Moho, creating a reflected phase strong and continuous enough to be seen in individual data sections. However, due to the relatively narrow band of distances where this occurs, we must make use of earthquakes that happen at a high degree of obliquity to the strike of the array. The addition of this data requires minor developments in the 2-D formulation of our method.

The structure of this paper is as follows: first, we discuss the selection and preprocessing of *SsPmp* data, including the application of sparse wavefield reconstruction with curvelets. Next, we summarize the reflection tomography approach. Finally, we present the results of RTM imaging and reflection tomography from Hi-CLIMB. The appendix contains modifications to the reflection tomography that are needed to implement for the application to oblique events.

5.2 Data and Methods

5.2.1 Event coverage

The current implementation of teleseismic reflection tomography requires that the downgoing free-surface reflected phase and the upgoing scattering at subsurface heterogeneity must be the same polarization. This means that currently only phases that are P-to-P or S-to-S scattered after reflecting off the free surface can be used. Due to the large depth to the crust-mantle interface beneath the Tibetan Plateau, most of these phases come late in the coda of the direct arrivals and are overwhelmed by noise, near source effects, and mixed-phase arrivals. The *SsPmp* phase, however, has been used to great success for estimating the Moho depth by Tseng et al. (2009) and Yu et al. (2013).

The *SsPmp* phase is the result of a conversion of the direct S wave into P at the free surface. The P then propagates downward and is backscattered at discontinuities in the crust and upper mantle and is recorded at the array. Within a certain epicentral distance, the *SsPmp* undergoes a total reflection at the Moho and all downgoing energy is reflected back towards the array. For reflection tomography, this is something of a blessing and a curse. On one hand, the strong amplitude of the arrival means that highly consistent images can be formed using individual events, which is the cornerstone of the source-indexed approach. On the other hand, since all of the energy reflects upwards at the Moho, deeper interfaces cannot be imaged. Fine-scale reconstruction of smooth heterogeneity requires multiple intercutting reflectors, so the resolution of tomography using totally-reflected *SsPmp* arrivals is limited to the crust.

Figure 5-1 (a) shows the distribution of the events used. Large circles show the epicenters of earthquakes used in the imaging and tomography below and are grouped into different regions by color. Events that give strong *SsPmp* arrivals come from four major clusters: the Sumatra subduction, which is along the strike of the array, the Philippines, the Mediterranean, and Japan. In all, 51 events provided *SsPmp* arrivals sufficient for single-source image formation, 22 from Sumatra, 12 from the Philippines, 22 from Japan, and 3 from the Mediterranean.

In order for reflection tomography to be effective, we require incoming arrivals with a variety of incidence angles. All of the events used are between 30° and 45° from the center of the array, which translates to incidence angles between 25° and 35°. However, the high obliquity of the events leads to a set of apparent incidences between 0° and 35°, which Burdick et al. (2013) shows to be sufficient for reflection tomography. The black contours in 5-1 (a) show the apparent incidence angles.

5.2.2 Preprocessing

The section of the Hi-CLIMB experiment used in this study (Figure 5-1 b) is a near-linear array with an aperture of around 500 km and irregular station spacing that varies between 5 and 15 km. The relative topography on the section of the Tibet Plateau occupied by the array is minor. Prior to the application of our reflection tomography method, we must preprocess the raw data in order to recover the Green's function of the free surface reflected phase, reduce the signal to noise ratio, and project the data onto a grid suitable for wave-equation propagation. The preprocessing contains four major steps – trace alignment, interpolation onto a regular grid, source signature estimation, and deconvolution.

After removing the mean and trend of each trace, the data are rotated into P and SV frame based on the analysis of particle motion (Yu et al., 2013). In this case, the SV trace contains the direct S arrival and the P trace contains the *SsPmp*. Next, all of the traces for a single earthquake event are shifted based on their theoretical S traveltime. Multichannel cross-correlation (VanDecar & Crosson, 1990) is then performed on the first peaks of the band-filtered direct arrival to estimate the residual traveltime delay and optimally align the traces for interpolation and source signature estimation.

Curvelet interpolation

For the application of reverse time migration to the data, we require that the data be distributed on a regular grid that meets the Nyquist criteria for the frequencies pertinent to teleseismic data. We therefore regularize the data by means of a curvelet interpolation.

The 1-D line that best fits the station locations is determined by a least squares regression, and a grid is created with 2 km spacing. The data traces are projected onto the nearest offset point on the line (the blue dots in Figure 5-1 b). Figure 5-3 (a) shows the projected raw *S* wavefield for a representative event coming from the subduction beneath Japan.

The irregularly spaced data coverage is then interpolated using the method proposed by Hennenfent et al. (2010) and applied to *Ps* converted phases from Hi-CLIMB by Shang (2013). We apply a 2-D curvelet Lasso optimization scheme to reconstruct the wavefield with a sparse set of curvelet coefficients. The interpolated data de-noised by discarding curvelet coefficients smaller than 1.0% of the maximum. Since the structure we image here is relatively flat, we further eliminate spurious horizontally propagating waves by discarding the corresponding vertically-oriented curvelet coefficients. Figure 5-3 (b) gives a representative result of the interpolation for the event shown inFigure 5-3.

Source-time function deconvolution

For the purposes of imaging and reflection tomography it is necessary to remove the signature of the source-time function, as well as any near-source reverberations such as depth phases from the direct and scattered fields. This source-side signature is estimated by a singular value decomposition of the incident *S* wavefield. The first eigenvector is retained as the signature of the incoming wave (Figure 5-3) for use in deconvolution In the case where a reliable estimation can be made for its temporal extent (i.e. for impulsive source functions and deep events), the source signature is tapered off to prevent artefacts in the deconvolution. In order to further prevent artefacts from edge effects from forming during wavefield propagation, we normalize the amplitude of the incident field across the array and the scattered field according to the same factor.

The source-time function is then optimally removed from the incident and scattered fields using Wiener deconvolution (Chen et al., 2010). Figure 5-4 shows the results of the deconvolution for the incident *S* and scattered *P* fields. Following a shift back into absolute time, these data are used as the input to the imaging algorithm.

5.2.3 RTM reflection tomography

The methodology for RTM teleseismic reflection tomography was developed in Burdick et al. (2013) but we summarize the relevant details here. The tomographic approach is comprised of three major steps – (1) forward propagation and imaging, (2) application of an error measure to the images, and (3) adjoint propagation for gradient construction and inversion.

In order to accommodate the limitations inherent to the passive teleseismic reflection problem, our reflection tomography was developed using an source-by-source approach. As a first step, we therefore follow the seismic inverse scattering approach of Op 't Root et al. (2012) for creating single-source images. We modify the active source approach here, using the direct arrival as the source field and free surface multiples as the receiver field. Using a scalar Helmholtz solver (Wang et al., 2010), the "source field" (source-deconvolved *Ss*) is propagated forward in time and the "receiver field" (*SsPmp*) is propagated backwards in time for each individual earthquake. The fields are subjected to an inverse scattering transform to form images of reflectors at depth.

We next apply an error measure to the single-source images in order to judge the fitness of the background model for forming consistent images. The high degree of difficulty in completely deconvolving the source-time function from the incoming and scattered wavefield leaves some variability in the imaged reflectors, making a simple comparison of their shape or the moveout between them infeasible for measuring imaging success. Instead, we turn to a correlation power measurement. Pairs of images are correlated in depth over a set of correlation windows selected according to illumination by the source field and continuity and linearity of the imaged reflector. If the two images form at the same location, most of the power in the correlation should be centered around zero depth shift. To measure this, the correlation power is multiplied by a weighting function that progressively penalizes power with increasing depth shift. Based on synthetic tests, we choose as our weighting function a negative Gaussian with a standard deviation on the order of the first peak in the correlation. The resulting error measure is then the sum of the weighted correlation power over all windows and all image pairs.

Finally, we follow the Augmented Lagrangian method (Plessix, 2006) to construct a model gradient to be used in an iterative optimization scheme. The weighted correlations are used to build an adjoint source function for each earthquake, two Helmholtz solutions are performed to find the adjoint "source" and "receiver" fields. The interaction between these two fields and their respective forward fields gives us the model gradient. The model is then updated using the conjugate gradient method until convergence is found.

Previous synthetic 2-D applications of reflection tomography assumed that the epicenters of the events used for imaging were along the great circle arc of the array, limiting out-of plane effects. The limited number and incidence range of events available within the strike of the Hi-CLIMB array necessitates the use of events with high angles of obliquity, which requires a number of additional assumptions and an alteration to the imaging and velocity update steps. We follow and modify the approach proposed by Pageot et al. (2013). The details are presented in Appendix 5.A.

5.3 Model results

5.3.1 Inverse scattering results

As a first step in our reflection tomography algorithm, we propagate the data through an initial smooth model and apply an inverse scattering transform to create single-source images. The initial smooth model used for imaging (Figure 5-5) is a 1-D model based on the velocity estimates from Nowack et al. (2010). It contains a crustal layer with a P wave velocity of 6.3 km/s and a thickness of 70 km, similar to the Moho depth beneath the Lhasa terrane imaged in previous studies. Beneath 100 km depth the wavespeed is set to 8.1 km/s, and between the two layers the velocity is determined by a linear interpolation. The computational domain extends 100 km from either end of the array in order to allow for the absorbing boundary conditions of the Helmholtz solver (Wang et al., 2010).

Figure 5-6 shows the results of imaging in the initial model for the different event clusters. Image (a) corresponds to the events originating in the Mediterranean, image (b) from Sumatra, image (c) from the Philippines, and image (d) from Japan. The differences in incidence angle and obliquity lead to different characteristics between these four images. All images apart from the one made with the Japan events exhibits effects from the edge of array coverage. The upward turn towards the edge of the array is not physical, and these offsets are not taken into account during the tomographic inversion. The stacked image from earthquakes near Japan does not exhibit this feature due to the near-vertical apparent incidence.

The images from events at high obliquity also have longer wavelength content. This is because, in effect, the obliquity correction increases the velocity for high obliquity events. For the same frequency content in the data, this increased velocity will result in a wavelength in the finite frequency image for these events.

The results of the critical reflection can be seen most clearly in the events from the Sumatra cluster. Since the phenomenon only occurs when the incidence S wave has horizontal slowness less than the inverse of the mantle P velocity, the *SsPmp* from events closer to the array only undergoes the total reflection beneath the Northern part of the array. For the events at $\sim$40° epicentral distance, a strong Moho reflection is available across the entire array. The stacked image result is biased towards the events closer to the array, leading to a physically meaningless increase in amplitude beneath the Qiangtang terrane.

Apart from the Sumatra cluster, the other three images show the Moho reflection to be fairly continuous and have constant amplitude across the array. In the initial model, the Moho runs from 80 km depth in the south to 60 km in the north in the Japan image, $\sim$65 km depth with an upward bulge near the BNS in the Philippines and Mediterranean images.

5.3.2 Tomographic results

Following the inverse scattering step, we apply the correlation power norm to pairs of images. The parameters used in the error measure are selected based on the illumination and frequency content of the single-source images. Previous synthetic tests (Burdick et al., 2013) have shown that the error function and inversion is most potent when using a depth window centered around each individual reflection point, but the method remains effective when one large window is used for all offsets. Given the difficulty in discerning the Moho from other intracrustal crustal reflectors within the frequency band used, as well as the dearth of deeper reflectors due to the critical reflection of the *SsPmp*, we draw our windows around the Moho and crust. The extent of the windows is shown in Figure 5-7.

During the inversion, correlations are made at all offsets along the illuminated Moho. Figure 5-8 shows a source-gathers for the the offsets shown in Figure 5-7. The images used in the error function are set side-by-side in each division of the plot, demonstrating the variation in depth from region to region. Our inversion seeks to flatten these gathers by improving the smooth 2-D model.

Synthetic tests show that the error measure is most effective when the weighting function has a width of the same order as the first peak in the image correlation. Due to variation in image wavelength between sources from the obliquity correction, we consider a weighting function with a width more suited to the longer wavelength images based on the conclusions drawn in Burdick et al. (2013). Given the wavelength of the images produced from Hi-CLIMB we choose a negative Gaussian with a standard deviation of 8 km.

In order to ensure that there is no scattering forward and adjoint propagation for the purposes of tomography, we project our model updates onto a basis of smoothing splines. For our initial inversion, we choose a relatively sparse set of bases due to (1) the limited number of reflectors illuminated by the *SsPmp* phase and (2) the limitations in resolution due to the obliquity assumptions. We cover the region directly below the array with quadratic B-splines with 48 km spacing, with 11 bases in offset and 3 in depth.

The total reflection at the Moho prevents deep reflectors from being imaged. Although the chosen bases extend below the estimated depth of Moho, they are within the bounds of the correlation window depth. The update is effected by the smooth at these depths because it has an effect on the shape of the reconstructed finite-frequency image, and therefore on the error function.

Due to the limitations imposed by the high obliquity (see Appendix 5.A) of the majority of events used, we limit our analysis here to one update of the model beginning from the 1-D model starting model. Figure 5-9 shows the result of one iteration. The recovered heterogeneity shows a fast region extending from the center of the Lhasa block to the Qiangtang block with a slow anomaly at shallow depths beneath the Bangong-Nujiang suture. At the edge of the method's resolution beneath the Lhasa block, there is a slow anomaly bordering the fast region. We interpret the fast structure as the northward dipping Indian lithosphere beneath Lhasa coinciding with a southward dipping downwelling of the Eurasian lithosphere beneath Qiangtang.

The optimization of the smooth model simultaneously improves the focusing of the image. Figure 5-10 shows one image gather created in the initial model and after one iteration. Each gather plot shows the single source images used in the inversion at offsets marked by the colored dots in Figure 5-7. If the tomographic model is correct, the gathers at each offset should be flat, indicating that all images estimate the Moho at the same depth. In the initial model, there is significant vertical moveout within the gather, particularly between clusters of events with different apparent incidences. The updated gather window shows an improvement in the alignment of the images.

5.4 Discussion

5.4.1 Comparison with previous imaging and tomography results

Contrary to the imaging results of Nabelek et al. (2009) and Nowack et al. (2010), we find the Moho signature to be relatively continuous beneath the BNS in images illuminated from each direction. This result agrees with the findings of Shang (2013). The single-event result of Tseng et al. (2009) also shows slight variation in depth, but continuous structure beneath the suture. The continuity of the image is aided by the total reflection undergone by the *SsPmp*. There may also be a tradeoff between the particularly sparse and irregular sampling of the array in the neighborhood of the BNS and the regularizing effects of the curvelet interpolation.

Figure 5-11 compares between the *SsPmp* imaging result from this study and the elastic RTM imaging with P to S converted phases from Shang (2013). The two images evince somewhat different illumination of the subsurface – the conversions used in the *Ps* study come primarily from the Sumatran subduction zone and during RTM both wavefields are propagated back towards the south so they have better resolution of the ITS and the edge of the Himalaya. The aperture for *SsPmp* is smaller because the two wavefields are propagated in opposite directions and only form an image where the two interact. The *SsPmp* image displays longer wavelength structure at the Moho due in part to the lower frequency content of the incident *S* and in part to the stretching effects of the obliquity correction.

Previous *P*-wave tomography results from Hi-CLIMB (Zhang et al., 2012) and elsewhere on the Tibetan Plateau (Li et al., 2008; Tilmann et al., 2003) show two downgoing fast anomalies beneath the Hi-CLIMB array – a northward dipping structure beneath the Lhasa block inferred to be the Indian lithosphere and a steep, southward dipping structure inferred to be Eurasian lithosphere. Between the two structures, the models typically a slow zone beneath the BNS.

Figure 5-12 shows a comparison of the reflection tomography model with teleseismic transmission models from Tibet. Due the poor vertical resolution in the crust and increased resolution in the mantle provided by the teleseismic transmission approach, these models are complementary to the reflection tomography results. The reflection tomography result is in excellent agreement with Zhang et al. (2012) on the lateral heterogeneity beneath the Hi-CLIMB but estimate that the lithospheric slabs bottom out a shallower depth. Li et al. (2008) reveals that the fast structures related to the downwelling lithosphere to the top of the mantle transition zone.

5.4.2 Future work

In this study we consider only the *P* scattering following the direct *S* arrival since it gives a strong reflection that can be used to form a consistent image on a source-to-source basis. Within the scalar Helmholtz framework, images from other scattered phases including the *PpSms* and *PpPmp*, while noisy, could be stacked together by region to provide additional information for the inversion. Future extension of the reflection tomography method to the elastic case will make it further possible to consider the strong *Ps* conversions used for imaging in Nabelek et al. (2009), Nowack et al. (2010), and Shang (2013).

Figure 5-13 shows the single-source image gathers from the elastic *Ps* RTM study of Shang (2013). The images are arranged in the gathers by event latitude from south to north.

These gathers demonstrate a high degree of consistency in structure between sources, indicating that they would be viable for use in a reflection tomography inversion. Tomography will allow for the minor moveout in the gathers to be iteratively reduced.

5.A Appendix: Obliquity correction

This appendix presents a modification to the work of Pageot et al. (2013). In order to treat arrivals with non-zero obliquity within the 2-D framework of our reflection tomography, we apply an correction term to the velocity model based on the obliquity and incidence angle of each event.

Figure 5-14 shows the geometry of the obliquity problem. The array lies along the x_1 axis. An incident *S* wave travels along the x_1' axis and arrives at the free surface at some distance in the x_2 away from the plane of the array. The obliquity, θ, is defined as the angle between the x_1 and x_1' axes. The reflected *P* phase travels downwards, reflects at a subsurface discontinuity, and is recorded at the array with incidence angle ϕ. In order to remove the effect of the obliquity of the arrivals, we flatten the particle motion in the x_1' axis into the x_1 axis.

We make the assumption that the velocity c model varies only in the z direction. We also assume that the incoming *S* wave is in the form of a plane wave and has a constant horizontal slowness $p = sin\phi/c$ over the entire array. Due to the teleseismic distance of the events used in this study, this is a relatively safe assumption, particularly for arrivals with high obliquity. The distance to individual stations, and therefore the slowness, is more variable for events closer the strike of the array (as seen with the critical reflection reflects for the event cluster in Sumatra in Figure 5-6 b), but the effect of the obliquity correction is reduced.

These assumptions are reasonable given interfaces with relatively minimal dip and tomography and for smooth velocity structure that varies little in the x_2 direction. Over the range of reflection points from events orthogonal to the Hi-CLIMB array, previous studies show relatively consistent reflector depth and heterogeneity, so the approximation is justified here.

Given the assumptions, the compressional particle velocity V in (x'_1, z) plane is

$$\begin{aligned} V_{x'_1}(z) &= A\ sin\phi(z)\ exp\left[-i\omega\left(\frac{x'_1 sin\phi(z)}{c(z)} + \frac{z\ cos\phi(z)}{c(z)} - t\right)\right] \\ V_z(z) &= A\ cos\phi(z)\ exp\left[-i\omega\left(\frac{x'_1 sin\phi(z)}{c(z)} + \frac{z\ cos\phi(z)}{c(z)} - t\right)\right]. \end{aligned} \tag{5.1}$$

After rotating into the (x_1, z) plane by substituting $x'_1 = x_1\ cos\theta + x_2\ sin\theta$ we look at the motion in the plane defined $x_2 = 0$:

$$\begin{aligned} V_{x_1} &= A\ sin\phi\ cos\theta\ exp\left[-i\omega\left(\frac{x_1\ sin\phi\ cos\theta}{c} + \frac{z\ cos\phi}{c} - t\right)\right] \\ V_z &= A\ cos\phi\ exp\left[-i\omega\left(\frac{x_1\ sin\phi\ cos\theta}{c} + \frac{z\ cos\phi}{c} - t\right)\right]. \end{aligned} \tag{5.2}$$

We search for an apparent velocity $c_a(z)$ and an apparent incidence angle $\phi_a(z)$ that will give the equivalent particle motion for a phase traveling in the x_1 axis. Thus, we get the system of equations:

$$\begin{aligned} \frac{sin\phi_a}{c_a} &= \frac{sin\phi\ cos\theta}{c} \\ \frac{cos\phi_a}{c_a} &= \frac{cos\phi}{c}. \end{aligned} \tag{5.3}$$

This gives:

$$\begin{aligned} tan\phi_a(z) &= tan\phi(z)\ cos\theta \\ c_a(z) &= c(z)\frac{1}{\sqrt{1 - sin^2\theta\ sin^2\phi(z)}} = c(z)\xi(z). \end{aligned} \tag{5.4}$$

The obliquity correction factor, $\xi(z)$ is determined in a velocity model that varies only in the z direction. In practice, a more accurate correction factor cannot be found without solving for the for the raypaths of arrivals in the 2.5-D model. For this reason, the approximation derived here can only be applied to a velocity updates beginning from a 1-D model. For additional updates, high frequency approximations must be introduced, reducing the benefits of working in the finite frequency framework.

During the velocity update process, We multiply the smooth model for each event by its corresponding obliquity correction. The adjoint step thus results in a gradient for the c_a model for each event. In order to update the proper c instead, we add a term to the Augmented Lagrangian presented in Burdick et al. (2013). This results in an additional adjoint term that sets Lagrange multipliers $\lambda_c = \lambda_{c_a}\xi$.

While the approximations necessary for using incoming waves that arrive at a high angle to the strike of the array reduces their resolving power in our method, there is a beneficial side to using these arrivals. The range of incidence angles available for tomography using only the-along strike events is limited to $\sim$ 15° to 35° at the most for compressional phases. The introduction of events that arrive orthogonal to the array increases the possible range of apparent incidence angles to 0° to 35°, improving illumination towards the edges of the array and the sensitivity of the error measure to coarse variations in velocity.

Bibliography

Burdick, S., de Hoop, M. V., Wang, S., & van der Hilst, R. D., 2013. Reverse-time migration-based reflection tomography using teleseismic free surface multiples, *Geophysics Journal International*, **in press**.

Chen, C. W., Miller, D. E., Djikpesse, H. A., Haldorsen, J. B. U., & Rondenay, S., 2010. Array-conditioned deconvolution of multiple-component teleseismic recordings, *Geophysical Journal International*, **182**(2), 967–976.

De Hoop, M. V., van der Hilst, R. D., & Shen, P., 2006. Wave-equation reflection tomography: annihilators and sensitivity kernels, *Geophysical Journal International*, **167**(3), 1332–1352.

Hennenfent, G., Fenelon, L., & Herrmann, F. J., 2010. Nonequispaced curvelet transform for seismic data reconstruction: A sparsity-promoting approach, *Geophysics*, **75**(6), WB203–WB210.

Hung, S.-H., Chen, W.-P., Chiao, L.-Y., & Tseng, T.-L., 2010. First multi-scale, finite-frequency tomography illuminates 3-D anatomy of the Tibetan Plateau, *Geophysical Research Letters*, **37**(6).

Li, C., van der Hilst, R. D., Meltzer, A. S., & Engdahl, E. R., 2008. Subduction of the Indian lithosphere beneath the Tibetan Plateau and Burma, *Earth and Planetary Science Letters*, **274**(1), 157 - 168.

Nabelek, J., Vergne, J., & Hetenyi, G., 2005. Project Hi-CLIMB: a synoptic view of the Himalayan collision zone and Southern Tibet, in *AGU Fall Meeting*.

Nabelek, J., Hetenyi, G., Vergne, J., Sapkota, S., Kafle, B., Jiang, M., Su, H., Chen, J., Huang, B.-S., & Hi, C. T., 2009. Underplating in the Himalaya-Tibet collision zone revealed by the Hi-CLIMB experiment, *Science*, **325**(5946), 1371–1374.

Nowack, R. L., Chen, W.-P., & Tseng, T.-L., 2010. Application of Gaussian-beam migration to multiscale imaging of the lithosphere beneath the Hi-CLIMB array in Tibet, *Bulletin of the Seismological Society of America*, **100**(4), 1743–1754.

Op 't Root, T. J. P. M., Stolk, C. C., & de Hoop, M. V., 2012. Linearized inverse scattering based on seismic reverse time migration, *Journal De Mathematiques Pures Et Appliquees*, **98**(2), 211–238.

Pageot, D., Operto, S., Vallee, M., Brossier, R., & Virieux, J., 2013. A parametric analysis of two-dimensional elastic full waveform inversion of teleseismic data for lithospheric imaging, *Geophysical Journal International*, **193**(3), 1479–1505.

Plessix, R. E., 2006. A review of the adjoint-state method for computing the gradient of a functional with geophysical applications, *Geophysical Journal International*, **167**(2), 495–503.

Shang, X., 2013. *Inverse Scattering: Theory and Application to the Images of the Earth's Seismic Discontinuities*, Ph.D. thesis, Massachusetts Institute of Technology.

Shen, P. & Symes, W. W., 2008. Automatic velocity analysis via shot profile migration, *Geophysics*, **73**(5), VE49–VE59.

Styron, R., Taylor, M., & Okoronkwo, K., 2010. Database of active structures from the Indo-Asian collision, *Eos Trans. AGU*, **91**(20), 0–1.

Sun, X., Song, X., Zheng, S., Yang, Y., & Ritzwoller, M. H., 2010. Three dimensional shear wave velocity structure of the crust and upper mantle beneath China from ambient noise surface wave tomography, *Earthquake Science*, **23**(5), 449–463.

Tilmann, F., Ni, J., & INDEPTH III Seismic Team, 2003. Seismic imaging of the downwelling Indian lithosphere beneath central Tibet, *Science*, **300**(5624), 1424–1427.

Tseng, T.-L., Chen, W.-P., & Nowack, R. L., 2009. Northward thinning of Tibetan crust revealed by virtual seismic profiles, *Geophysical Research Letters*, **36**.

Van Leeuwen, T. & Mulder, W. A., 2008. Velocity analysis based on data correlation, *Geophysical Prospecting*, **56**(6), 791–803.

VanDecar, J. & Crosson, R., 1990. Determination of teleseismic relative phase arrival times using multi-channel cross-correlation and least squares, *Bulletin of the Seismological Society of America*, **80**(1), 150–159.

Wang, S., de Hoop, M. V., & Xia, J., 2010. Acoustic inverse scattering via Helmholtz operator factorization and optimization, *Journal of Computational Physics*, **229**(22), 8445–8462.

Xie, X.-B. & Yang, H., 2008. The finite-frequency sensitivity kernel for migration residual moveout and its applications in migration velocity analysis, *Geophysics*, **73**(6), S241–S249.

Yu, C.-Q., Chen, W.-P., & van der Hilst, R. D., 2013. Removing source-side scattering for virtual deep seismic sounding (VDSS), *Geophysical Journal International*, **195**, 1932–1941.

Zhang, H., Zhao, J., & Xu, Q., 2012. Crustal and upper mantle velocity structure beneath central Tibet by P-wave teleseismic tomography, *Geophysical Journal International*, **190**(3), 1325–1334.

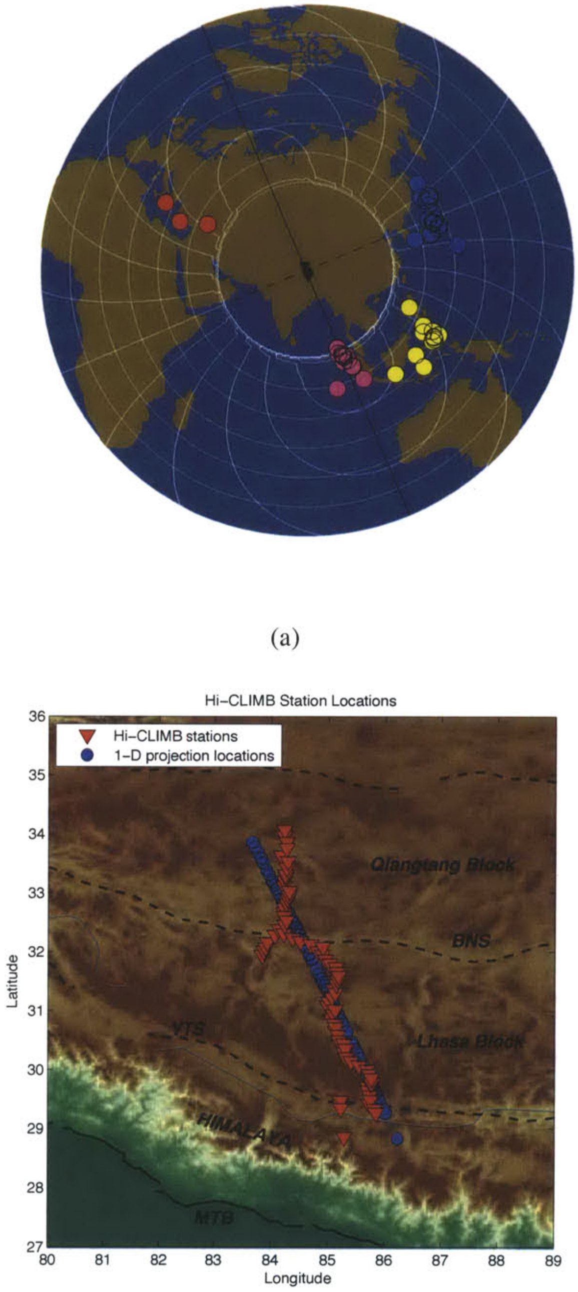

(a)

(b)

Figure 5-1: (a) Locations of teleseismic events recorded at Hi-CLIMB array. Map is centered around Hi-CLIMB (triangles) and the solid black line shows the strike of the array. Grey circles show epicentral distances from 30° to 90° Colored show event locations divided into four main regions for comparison. White contours show the apparent incidence angle of the *SsPmp* generated by events. (b) Red triangles give locations of Hi-CLIMB stations and blue circles show the projection of the locations onto a 1-D line for interpolation. Black dashed lines show locations of sutures and terranes given by Styron et al. (2010) BNS–Bangong-Nujiang suture, YTS–Indus-Yarlung suture, MTB–main thrust belt of the Himalaya.

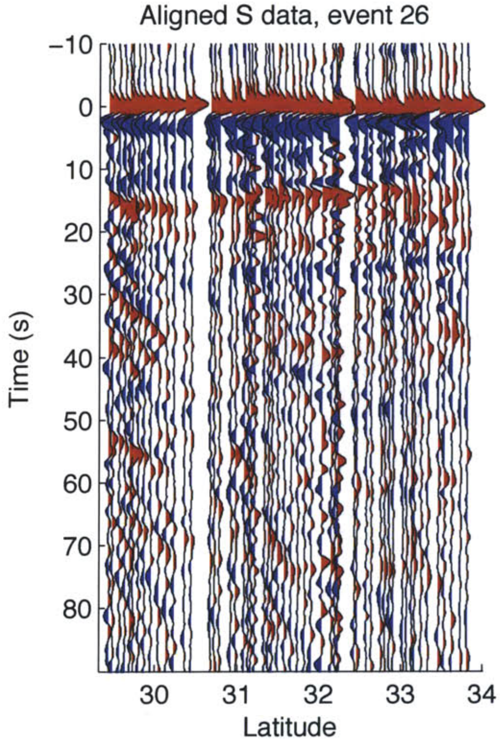

Figure 5-2: Left: Bandpass filtered *S* traces. Right: interpolated wavefield from an event from Japan. The x-axis corresponds to the latitude along the projection line shown in Figure 5-1 (b). Traces are projected onto the 1-D grid with 2 km spacing and interpolated using a Lasso algorithm.

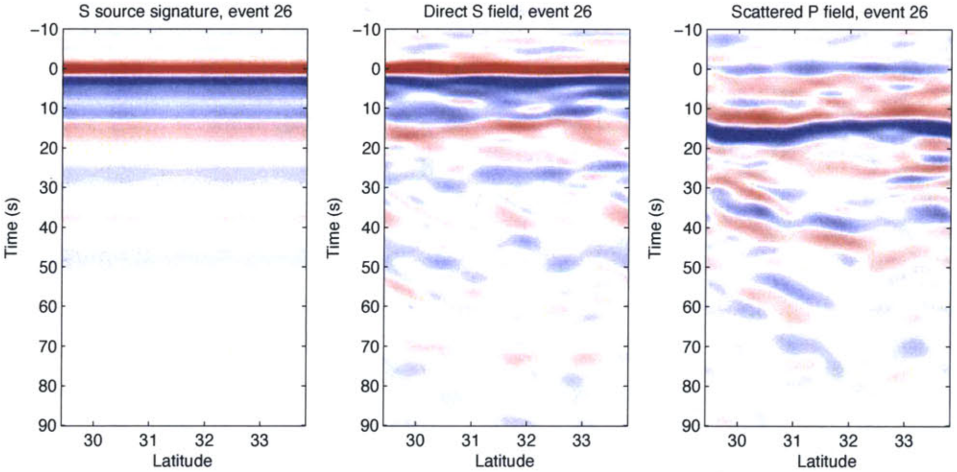

Figure 5-3: Left: The source signature recovered from the direct *S* wavefield (Center) by singular value decompostion and the *P* scattered wavefield(Right) following the *S* arrival for the event from Japan shown in Figure 5-2.

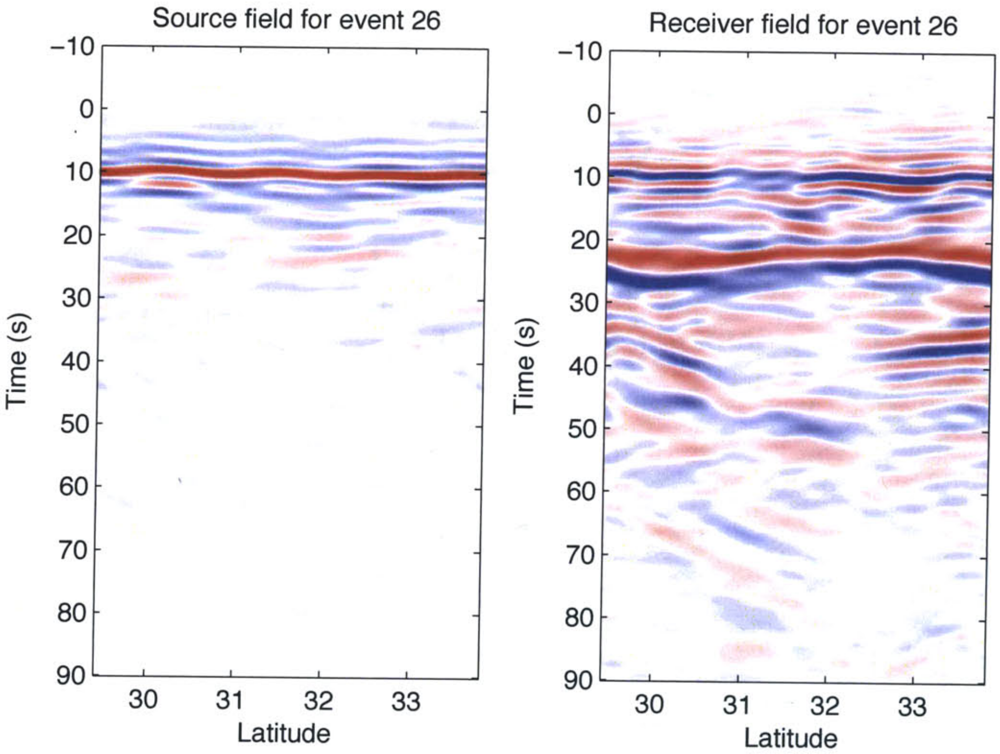

Figure 5-4: The incident *S* (Left) and scattered *P* (Right) wavefields from Figure 5-3 with the source-time function removed by Wiener deconvolution. Following a shift back into the absolute time frame, these fields are used as the input to the reverse time migration algorithm as the "source" field and "receiver" field.

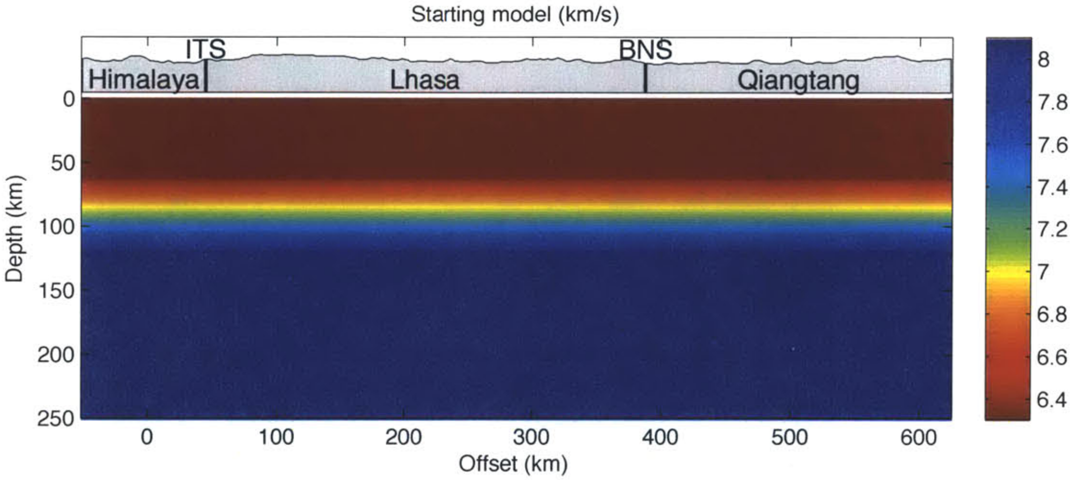

Figure 5-5: Initial smooth *P* velocity model used for propagation.

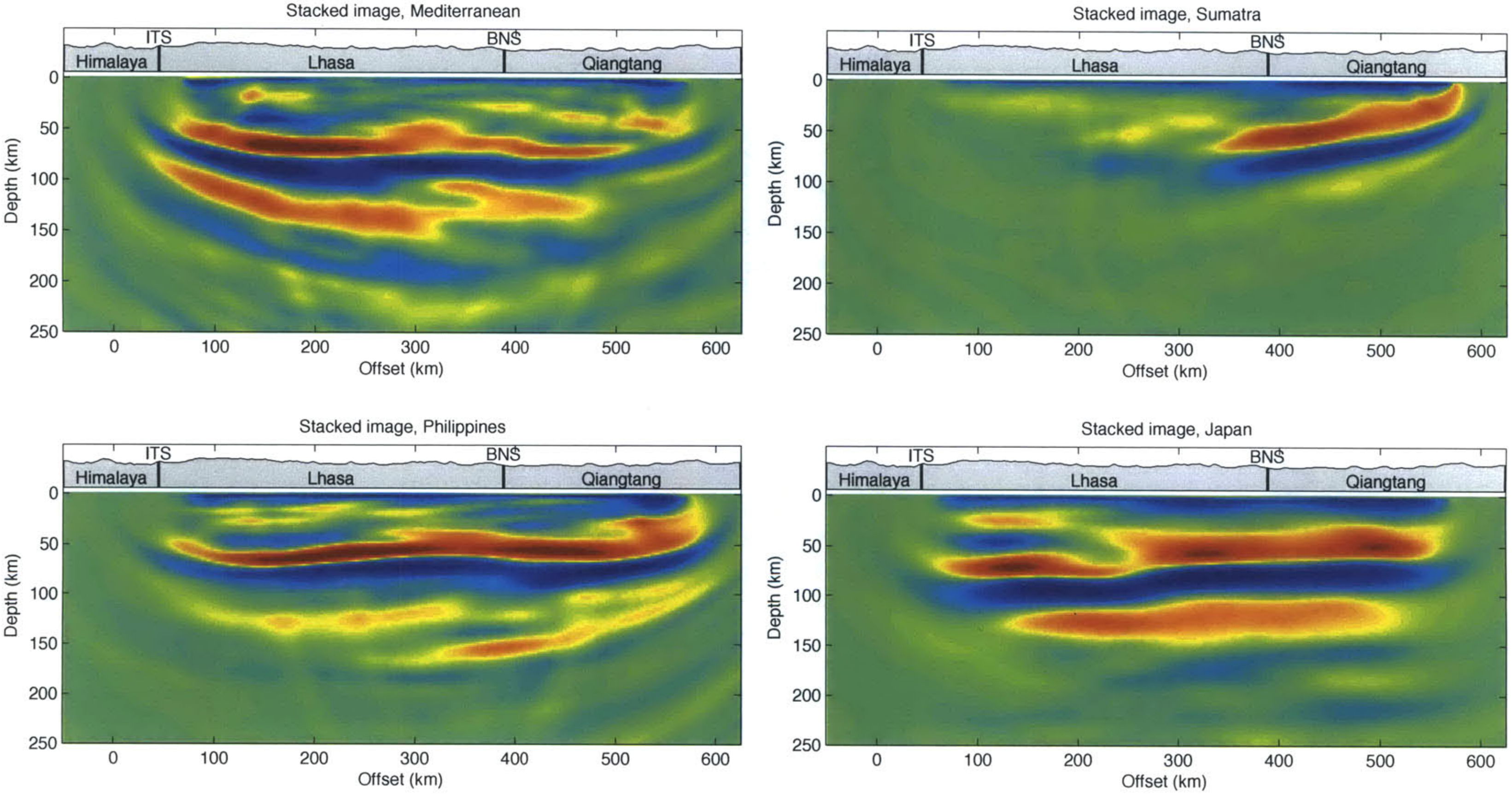

Figure 5-6: Stacked images by region created using the initial model shown in Figure 5-5. Images correspond to clusters of events (5-1 a) from the Mediterranean, Sumatra, the Philippines, and Japan. In the images, red structures correspond to lower velocities and blue to higher velocities.

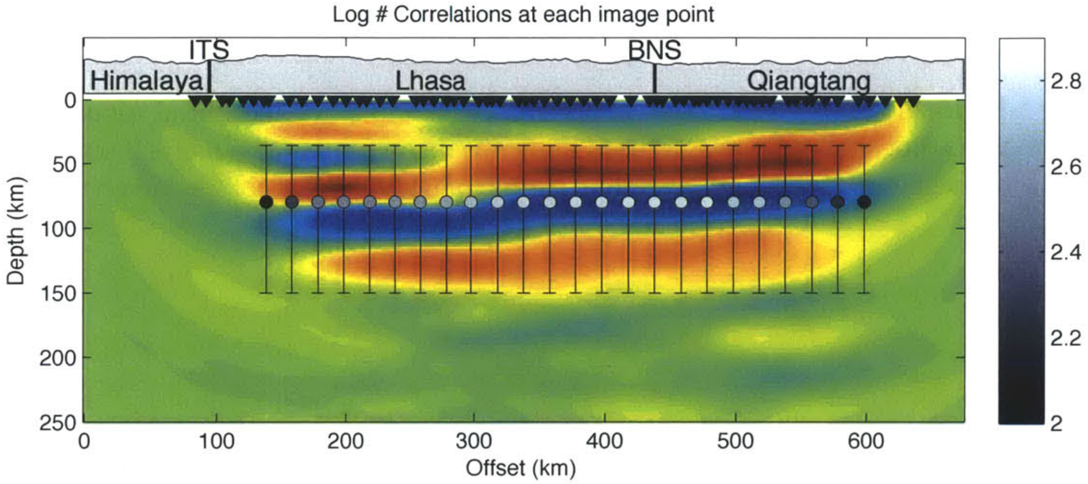

Figure 5-7: The recovered image stacked over all equally-weighted sources. The colored dots show a selection of image points at which image correlations are performed (correlation are performed at each offset for the inversion), and black bars show the extent of the windows. The color of the circle indicates the number of correlations made at each window. Triangles show the extent of the array. The number of error function measurements decreases sharply towards the edges due to the geometry of the arrivals.

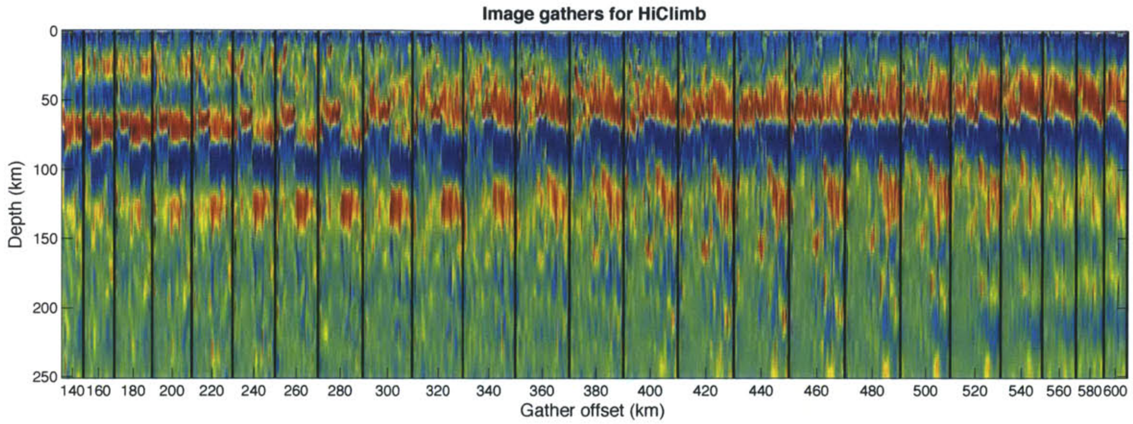

Figure 5-8: Image gather with offsets shown in Figure 5-7 for the initial model. Each division of the plot shows the images used in the inversion for that given offset set side-by-side. Each image window is normalized by its maximum value for comparison here.

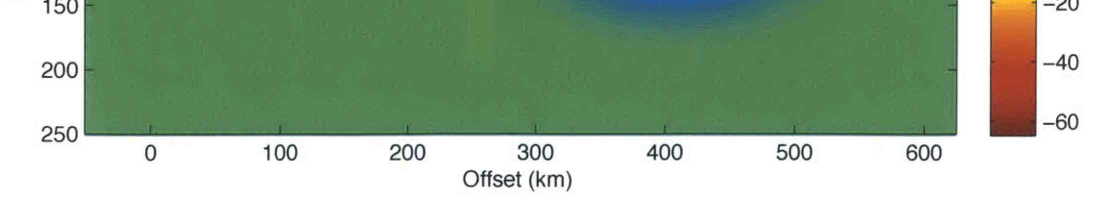

Figure 5-9: Velocity heterogeneity recovered by the first iteration of reflection tomography.

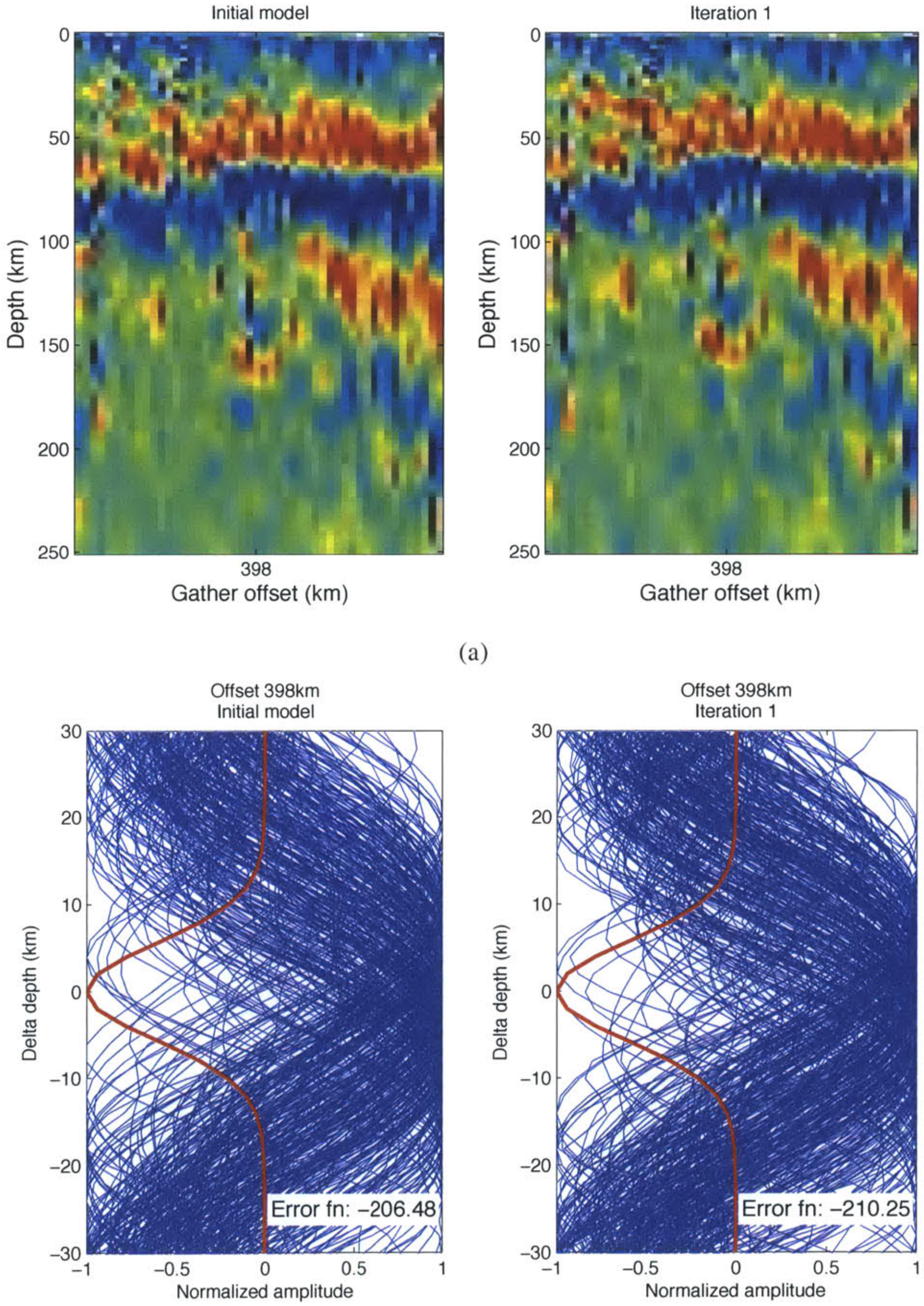

(a)

(b)

Figure 5-10: (a) One image gather at 398 km offset as shown in 5-7 for the initial model (Left) and the final model (Right). The velocity update improves the alignment of single-source images from different regions. (b) Correlations (blue lines) at this offset that comprise the error function. Each power of each correlation is multiplied by the weighting function (red line) and the summed. The contribution from the error function shown at the bottom right is reduced after one iteration.

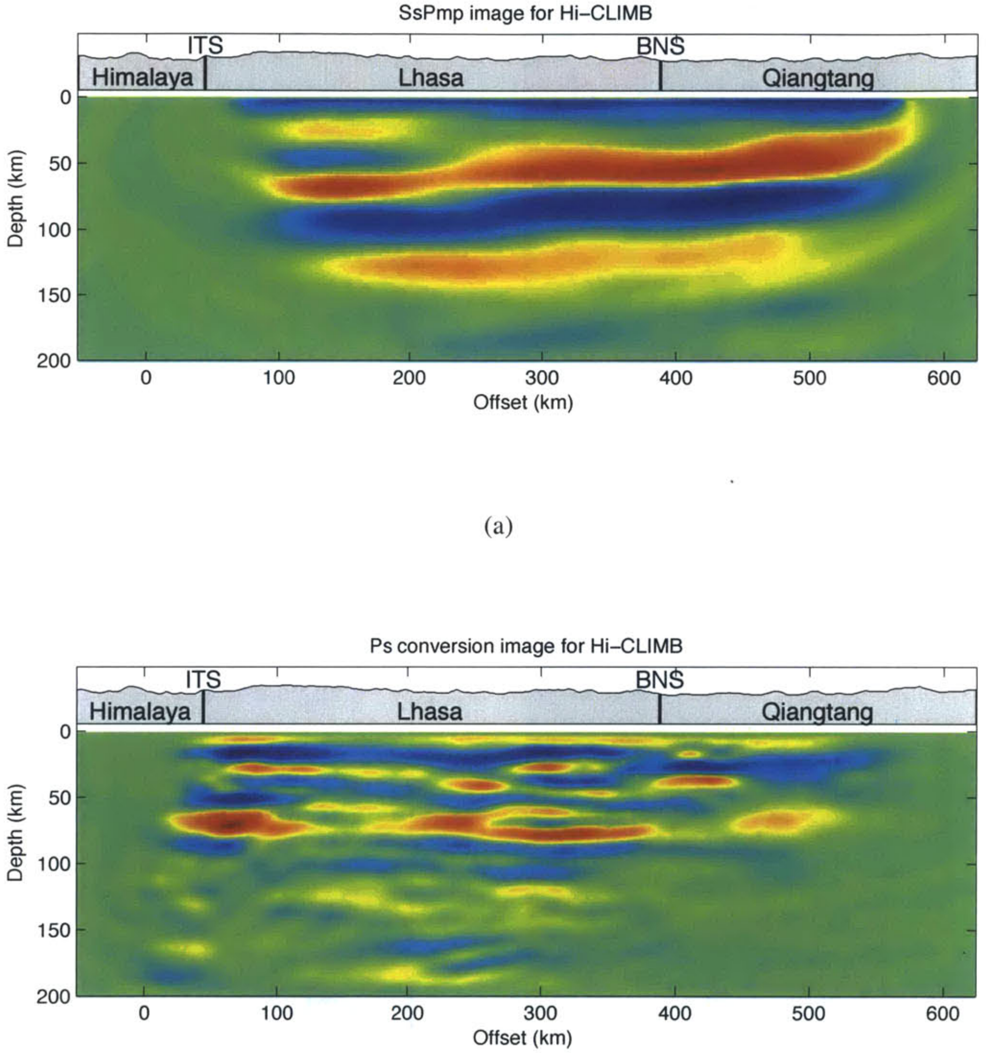

(a)

(b)

Figure 5-11: (a) Image result using *SsPmp*. (b) Image result from elastic RTM with *Ps* converted phases (Shang, 2013).

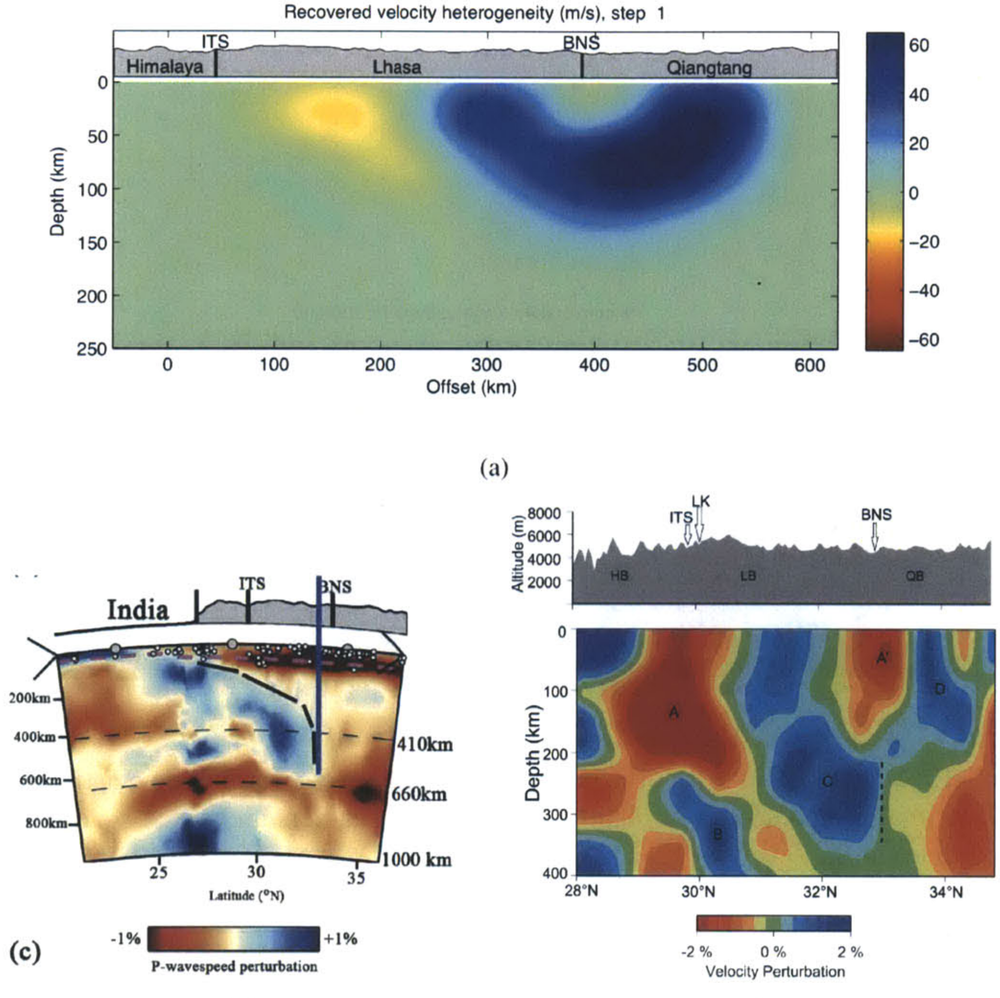

(a)

(b)

(c)

Figure 5-12: (a) Reflection tomography result. (b) Slice through global *P* wave model (Li et al., 2008) along the axis of the INDEPTH III experiment (two degrees east of Hi-CLIMB). (c) Teleseismic traveltime tomography using Hi-CLIMB data (Zhang et al., 2012).

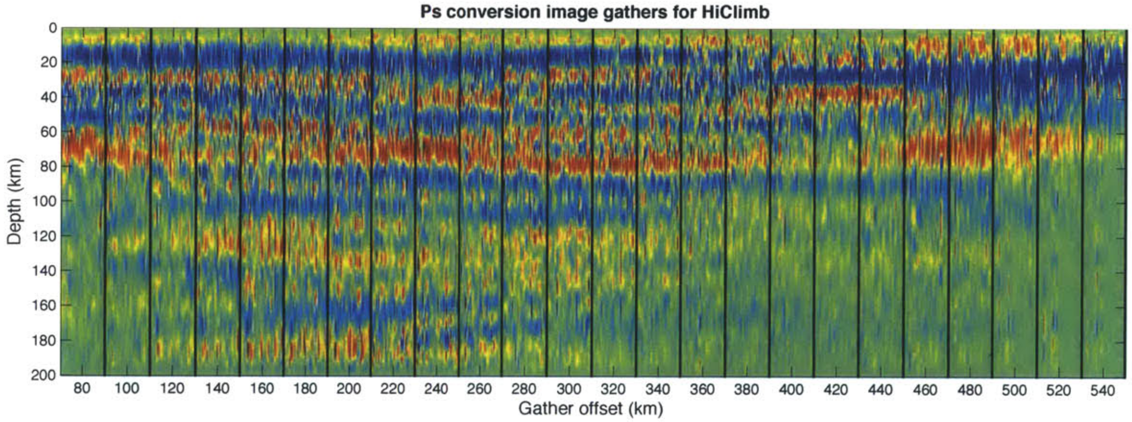

Figure 5-13: Image gather with offsets similar to those in 5-8 for the the elastic *Ps* conversion RTM imaging presented in Shang (2013). Image gathers are sorted by event latitude from south to north.

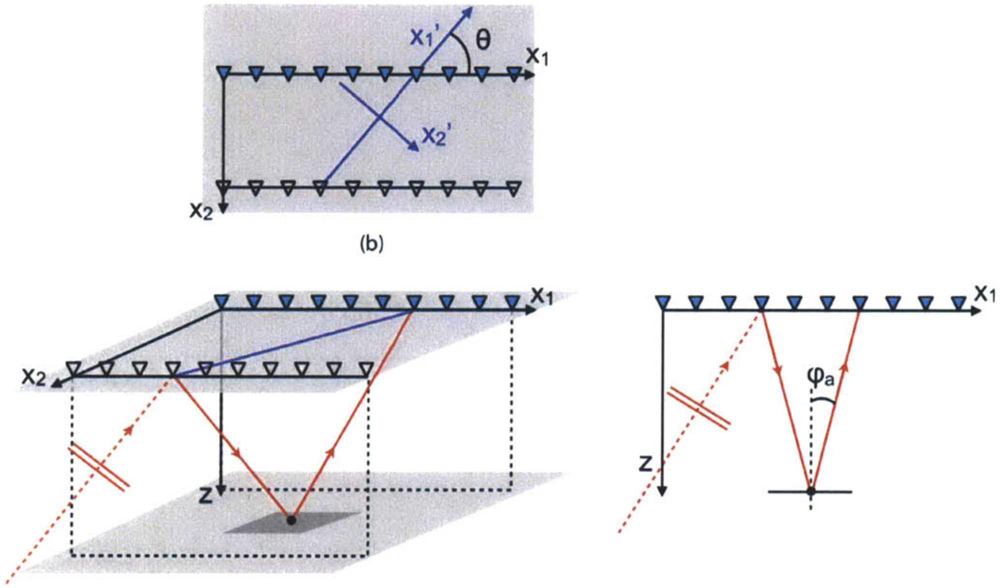

(b)

(a)

(c)

Figure 5-14: (a) 3-D view of an incoming SsP_mp arrival. The incident *S* wave (dotted red line) reflects off the free surface in front of the array (clear triangles). The *P* phase from the reflection is reflected again at the Moho and arrives at the array (blue triangles) at $x_2 = 0$ with incidence ϕ. (b) Top down view. The blue line shows the direction of the arrival between the free-surface reflection point and the recorded arrival. The angle between the two is the obliquity (θ). (c) View in depth plane shows the projection of the geometry into the 2-D $x_2 = 0$ plane. ϕ_a is the apparent angle of incidence in this plane.

Chapter 6

Concluding Remarks

6.1 Summary

In this thesis, we dealt with three widely varying methods for seismic tomography. **Chapter 2** presented an application of global ray-theoretical body wave tomography to millions of traveltime picks from USArray Transportable Array and global catalogues. **Chapter 3** presented an efficient one-way wave propagator on curvilinear coordinates and a formulation of finite-frequency transmission tomography for use with it. **Chapter 4** develops a novel method for reflection tomography using teleseismic free surface multiples and **Chapter 5** offered an application of the method to the Hi-CLIMB array in Tibet. Although the three projects contained here rest on different tomographic approaches, each deals with the questions of how to balance physical accuracy and computational feasibility and how to improve upon previous results through the innovative use of the seismic wavefield.

As the volumes of data available for tomographic inversions continue to increase apace with theoretical developments and computational capacity, the question of wave physics accuracy versus data quantity remains a vital one. The methods presented in this thesis lean towards the increased data quantity side of the scale. The global body wave tomography presented in Chapter 2 puts the resolving power of massive data volumes first and foremost. With over 13 million P phase picks involved in the inversion, there is no choice but to build the sensitivity matrix using a ray theoretical approximation. The adaptable parameterization and the high frequency approximation applied in this chapter allow for the construction of a fine-scale global model that agrees well with regional models using more sophisticated methods.

The other two methods attempt to strike more of a balance between numerical accuracy and data volume, but both choose to approach the wave propagation and data usage selectively rather than with brute-force computation. In Chapter 3, we developed a curvilinear one-way wave-equation propagator able to handle overturning teleseismic phases. By using waveform data in this approach, we can improve upon the high frequency assumptions of the traveltime picks in the previous chapter while still determining the sensitivity considerably more efficiently than full wave methods like SPECFEM (Tromp et al., 2008). Although somewhat slower than the one-way propagator, the optimized Helmholtz solver (Wang et al., 2010) used in Chapters 4 and 5 strikes the balance of accuracy and efficiency required for the reflection tomography method. Furthermore, developments in inverse theory in Chapters 3 and 4 allow us to address an increased volume of data using wave equation methods. The calculation of the model gradient with the seismic adjoint method drastically reduces the number of relatively expensive forward computations required and allows us to consider more events than would be possible with a direct computation of the Fréchet derivative.

This thesis also dealt with the application of tomography to alternate parts of the seismic wavefield in order to resolve new features in the Earth. Chapter 4 presented the development of a novel method for using teleseismic free surface reflections in order to constrain the smooth velocity of the crust and upper mantle. Teleseismic studies of regional seismic structure have typically performed analysis on the smooth and the discontinuous velocity structures separately. The depth of the discontinuities and smooth 3-D velocity structure are closely tied, and reflection tomography exploits the relationship in order to iteratively improve both. This has the effect of increasing vertical resolution in the lithosphere compared to body wave approaches. The curvilinear propagator in Chapter 3 was developed in part for the application of exploration-scale reflection tomography to waves reflection off of near vertical or overturning structures. Previous applications of reflection tomography using one-way propagation were limited to shallowly dipping structure – a restrictive assumption in the reservoir setting. The extension of the method to overturning coordinate systems makes it possible to resolve previously unconstrained structure.

Although the bulk of this thesis dealt with new theoretical developments, ultimately the goal of tomography is to gain a better understanding of processes that effect smooth velocity heterogeneity. Chapters 2 and 5 presented the applications of these tomography methods to teleseismic data. The global *P* wave models in Chapter 2 provided fine scale resolution of the North American continent thanks to continuously increasing volumes of traveltime picks from the USArray Transportable Array. The latest model reveals tectonic structures to the east of the Rocky Mountains that were unresolved using global data sets. The slow signature of the Mid-Continental Rift corresponds spatially to the continental gravity high. The Reelfoot Rift and the New Madrid Seismic Zone see a slow anomaly that extends into the upper mantle, suggesting mantle control of rifting processes. Wavelet analysis of the model demonstrates that the structures in the tectonically stable east of the continent contain elements of the same spatial scale as those in the west, but with lower relative amplitude.

In Chapter 5, the inaugural application of reflection tomography to array data targeted *SsPmp* phases from the Hi-CLIMB array in central Tibet. The strong arrivals of these phases at their critical reflection distance allowed for a robust comparison between different different single-source images. The imaging component of the method found a continuous Moho reflection across the entire array at depths of $\sim$75 km beneath the Lhasa block, trending upwards to 60 km beneath the Qiangtang terrane. The velocity inversion found two downgoing fast elements corresponding to Indian and Eurasian lithosphere separated by a shallow slow anomaly beneath the Bangong-Nujiang suture.

6.2 Future Work

6.2.1 Routine inversion of global tomography model

With the completion of the Transportable Array's campaign across the coterminous United States in 2015, the regular updates to the MITP global model will come to an end. Data will continue to roll in from the USArray stations in Alaska and other arrays elsewhere, but improvements to the model due to uniform station spacing in the continental US will cease. It is vital to transition the global tomography method from an active research code into a routine part of seismic data processing.

As it currently stands, the global tomography inversion is accomplished by a loose amalgamation of C routines, MATLAB scripts, and shell commands. Future work with the codes will be centered around creating a streamlined, automated version with an emphasis towards portability. This task is primarily technical, and therefore not suitable for Ph.D. thesis work. In the end, we desire a product that automatically computes a new irregular grid and performs an inversion based on the addition of new arrivals. I have begun work with the Array Network Facility, the team responsible for producing the *P* arrival picks, on installing our inversion as part of their routine processing.

6.2.2 Wavelet analysis of USArray models

The *P* models presented in Chapter 2 and Appendices A, B, C, D, and E are only a handful of the plethora of models of seismic properties created primarily using USArray TA data. As discussed in Section 2.5, these models are solve for different seismic properties, use different components of the wavefield, and employ a number of different forward modeling and inversion methods. All models have a number of major features – The Basin and Range province, the fast craton, a linear slow anomaly along the Snake River Plain, the Cascadia subduction, and many more – but they vary strongly in amplitude and somewhat in structure across all scales. Several studies have compared the range of models using different criteria – in particular Becker (2012) sought to determine what features are consistently present based on correlation.

In Chapter 2 we applied basic wavelet analysis to investigate the scale of heterogeneity in the mantle beneath the United States. Although our investigations here were limited to the MITP model itself, Carannante (2008) has shown wavelet analysis to be a useful tool to explore the differences between global tomography models. Models using USArray TA data localized to the continental United States are ripe for such analysis. Following Becker (2012), it would be possible to construct a composite model of mantle heterogeneity beneath the USA based on points and scales where all models agree.

6.2.3 Reflection tomography outlooks

Chapters 4 and 5 of this thesis presented the theoretical formulation of reflection tomography based on source-pair image correlations and the application of the method to synthetic and 2-D array data. Both the synthetic and data applications were limited to the exploitation of P to P multiple scattering in order to bridge the gap between exploration practices and teleseismic problems, but this phase is typically weak and temperamental. Vast improvements can be made in the applicability of reflection tomography by extending it to the elastic case and to 3-D propagation. The work in this thesis then represents a step forward into a burgeoning field, and the potential applications and extensions are numerous.

Elastic reflection (and conversion) tomography

The inversions presented in Chapters 4 and 5 were based solely on images formed using P to P free surface multiples. Although this approach allowed us to connect our novel application of reflection tomography back to established exploration results, this reliance on same-phase scattering will be an overwhelming and unnecessary limitation moving forward. Myriad studies have shown that converted phases and mixed-phase free surface multiples are stronger and relatively better suited to imaging than P to P multiples, including studies using Hi-CLIMB data (Nabelek et al., 2009; Nowack et al., 2010). The same studies, in addition to wave equation imaging work by Shang (2013) have shown the ability to generate coherent images from these phases using subsets of the teleseismic events from different regions.

For this reason, the next logical step in the development of teleseismic reflection tomography is the extension to the elastic case. Broadly speaking, there are two possible approaches to an elastic-wave application. The first approach bears more similarity to the method established in Chapter 4, and involves considering each leg propagation separately by means of single scattering. Thus, for instance, for the Ps conversion, the two phases would be propagated downwards using separate solutions to the scalar Helmholtz equation with their respective velocity models and imaged by applying the elastic inverse scattering transform (Brytik et al., 2012). Updates could then be made to one or both models, with or without constraints on each other. The alternative is to propagate both polarizations at once in the manner of Shang et al. (2012). The resulting three-component wavefield would then be subject to a polarization decomposition before imaging.

One potential setback in using the *Ps* and *Sp* converted phases is that the direct phase and conversion travel along similar paths with a relatively small difference in incidence angle in the crust and lithosphere, and therefore will be relatively poor vertical resolution. Deeper conversion points, such as the 410 and 660 km mantle discontinuities, may generate sufficiently different paths for upper mantle tomography, but lithospheric studies may need to be augmented with free surface reflected phases. Further investigation of this concern with inversions using synthetic data is merited before the application to seismic data.

The ultimate target for reflection tomography will be the upper mantle and transition zone beneath the USArray Transportable Array (TA). Numerous studies have shown success imaging the Lithosphere-Asthenosphere Boundary (Lekic & Fischer, 2013) and the mantle transition zone discontinuities (Gilbert, 2012; Pavlis et al., 2012; Schmandt, 2012) using TA data, particularly with converted phases. This application will require the method to be upgraded to consider the elastic case. Furthermore, due to the very long baseline of the array, we will no longer be able to consider a Cartesian approximation, and therefore our implementation must be done in spherical coordinates. Appendix F provides the spherical elastic Helmholtz equation and its discretization along the lines of Wang et al. (2010).

Extension to 3-D

After the extension to elastic phases, the next most vital improvement to be made to our reflection tomography algorithms is the expansion to 3-D problems. Although the theoretical development in Chapter 4 does in fact account for two or three dimensions, the implementation and application of a 3-D version may be difficult. The computational intensity will increase necessarily, though the fast 3-D elastic Helmholtz solver of Wang et al. (2011) makes inversion problems on the order of 1000^3 feasible without extraordinary (but with still rather high) cost. The areal arrays available typically have a shorter baseline or greater station spacing than linear arrays, which will limit the depths resolvable and/or usable frequency bandwidth.

The benefits of an expansion of the method to 3-D are numerous enough to make the endeavor worthwhile. In the 2-D case, applications are limited to linear arrays that either have numerous teleseismic sources along their great-circle arc or are deployed to image structure that changes little in the direction normal to the array. The structure beneath Hi-CLIMB has comparatively weak variation perpendicular to the array and the LA RISTRA experiment in New Mexico sees teleseismic events from a wide range of sources along strike, but many linear arrays may not meet these requirements. The extension to 3-D will assuage this limitation through the consideration of data from all azimuths and inversion for 3-D structure, both smooth and discontinuous. It should be noted that for the source-indexed approach we do not need full azimuthal coverage in order to constrain the smooth velocity. Consistent with other tomographic approaches, we only need a sufficiently varied set arrivals from linearly independent directions.

Bibliography

Becker, T. W., 2012. On recent seismic tomography for the western United States, *Geochemistry Geophysics Geosystems*, **13**.

Brytik, V., de Hoop, M. V., & van der Hilst, R. D., 2012. Elastic-wave inverse scattering based on reverse time migration with active and passive source reflection data, in *Inverse Problems and Applications: Inside Out II*, vol. 60, pp. 411–453, Cambridge Univ. Press, Cambridge, U. K.

Carannante, S., 2008. *Multiresolution spherical wavelet analysis in global seismic tomography*, Ph.D. thesis, Univeresita di Bologna.

Gilbert, H., 2012. Crustal structure and signatures of recent tectonism as influenced by ancient terranes in the western United States, *Geosphere*, **8**(1), 141–157.

Lekic, V. & Fischer, K., 2013. Contrasting lithospheric signatures across the western United States revealed by Sp receiver functions, *Earth and Planetary Science Letters*, **submitted**.

Nabelek, J., Hetenyi, G., Vergne, J., Sapkota, S., Kafle, B., Jiang, M., Su, H., Chen, J., Huang, B.-S., & Hi, C. T., 2009. Underplating in the Himalaya-Tibet collision zone revealed by the Hi-CLIMB experiment, *Science*, **325**(5946), 1371–1374.

Nowack, R. L., Chen, W.-P., & Tseng, T.-L., 2010. Application of Gaussian-beam migration to multiscale imaging of the lithosphere beneath the Hi-CLIMB array in Tibet, *Bulletin of the Seismological Society of America*, **100**(4), 1743–1754.

Pavlis, G. L., Sigloch, K., Burdick, S., Fouch, M. J., & Vernon, F. L., 2012. Unraveling the geometry of the Farallon plate: Synthesis of three-dimensional imaging results from USArray, *Tectonophysics*, **532**, 82–102.

Schmandt, B., 2012. Mantle transition zone shear velocity gradients beneath USArray, *Earth and Planetary Science Letters*, **355**, 119–130.

Shang, X., 2013. *Inverse Scattering: Theory and Application to the Images of the Earth's Seismic Discontinuities*, Ph.D. thesis, Massachusetts Institute of Technology.

Shang, X., de Hoop, M. V., & van der Hilst, R. D., 2012. Beyond receiver functions: Passive source reverse time migration and inverse scattering of converted waves, *Geophysical Research Letters*, **39**.

Tromp, J., Komatitsch, D., & Liu, Q. Y., 2008. Spectral-element and adjoint methods in seismology, *Communications in Computational Physics*, **3**, 1–32.

Wang, S., de Hoop, M. V., & Xia, J., 2010. Acoustic inverse scattering via Helmholtz operator factorization and optimization, *Journal of Computational Physics*, **229**(22), 8445–8462.

Wang, S., de Hoop, M. V., & Xia, J., 2011. On 3D modeling of seismic wave propagation via a structured parallel multifrontal direct Helmholtz solver, *Geophysical Prospecting*, **59**(5), 857–873.

Appendix A

Upper mantle heterogeneity beneath North America from travel time tomography with global and USArray Transportable Array data[1]

A.1 Introduction

The large volumes of broadband waveforms that are being acquired by *USArray* (*http://www.iris.edu/USArray/*), the seismology component of the national Earth science program *Earthscope* (*http://www.earthscope.org/*), offer unique opportunities for seismic imaging. Constraining structures on a range of length scales and understanding their physical and chemical causes is a prerequisite for understanding the relationship between near surface and deeper mantle processes. One can expect that, eventually, full wave tomography (e.g., De Hoop & Van der Hilst (2005); De Hoop et al. (2006); Tromp et al. (2005); Zhao & Jordan (2006)) with broad-band *USArray* waveforms will produce superior insight into the structure of the mantle beneath North America, but linearized tomographic inversion of phase arrival time data readily yields exciting results in regions where data from dense seismograph networks is available. We will use travel times from the transportable component of *USArray*, hereinafter referred to as *USArrayTA*, and from other sources, such

---

[1] Published as: Burdick, S., Li, C., Martynov, V., Cox, T., Eakins, J., Mulder, T., Astiz, L., Vernon, F., Pavlis, G., van der Hilst, R., 2008. Upper mantle heterogeneity beneath North America from travel time tomography with global and USArray Transportable Array data, Seismological Research Letters, 79.

as the EHB data base (Engdahl et al., 1998), to constrain 3-D mantle heterogeneity beneath North America.

Tomographic images based on *USArrayTA* data will help us understand first-order geological structure of and processes in the mantle beneath North America. Examples include, but are not restricted to: (1) the transition from the stable continental lithosphere at the center of the North American continent to the tectonically active domains further west, (2) the Cascadia subduction system, (3) the Yellowstone hotspot, and (4) the relationship between current and past episodes of subduction and upper mantle upwellings and processes deeper in the mantle. Before the advent of *USArrayTA*, insight into mantle structure beneath the western United States was either obtained from (pieced-together) regional *P*-wave studies (e.g., Figure 1a, after Dueker et al. (2001) or from global travel time or surface wave tomography (Figures 1b,c,d, after Ritzwoller et al. (2002), Montelli et al. (2004), and Grand (2002), respectively). The use of *USArray* data allows systematic tomographic imaging of the entire continent at or near the resolution of the best currently available regional studies.

We intend to update our tomographic mantle model every 6 months or so with new USArrayTA data from the Array Network Facility (ANF), and these model updates will be available to the community. This paper summarizes our procedures for data analysis and tomographic inversion and provides a reference point for users of this "community product". To illustrate the potential of our approach we present results from data from *USArrayTA* up to November 2007. We note, however, that more spectacular improvements over currently available models are anticipated when the transportable arrays reach the central and eastern states, where station distribution has traditionally been more sparse than in the western part of the continental U.S.

A.2 Data

For our travel time tomography we use travel time residuals from regional and teleseismic distance *P*-wave phases using the method described by Li et al. (2006, 2008a). We compute travel time residuals relative to the times calculated in some reference Earth model (here we used *ak135* by Kennett et al. (1995)) using a global hypocenter catalog and corrections for ellipticity.

The largest single data source for such residuals is the bulletin of the International Seismological Centre (ISC). We use the reprocessed ISC data described by Engdahl et al. (1998), hereinafter referred to as the EHB data set. The global distribution of stations contributing data to this data set is depicted in Figure 2, and Figure 2a (inset, lower left) depicts the North American stations from which data were available for global tomography before the advent of USArray. The EHB data already includes travel time residuals from regional arrays in, for instance, from the SKIPPY project in Australia.

The global data used in our tomography currently consists of over 10 million teleseismic *P*, *pP*, *Pn*, and *PKP* EHB data, with earthquake origin times between 1964 and 2004, and over 20,000 (differential) travel-time residuals of long-period *PP-P* phases (Bolton & Masters, 2001). We augment this data with handpicked travel time residuals, also measured against *ak135*, from USArrayTA stations (Figure 2b, inset lower right) produced by the ANF. The results shown here include ∼600,000 USArrayTA data from 2004 to November 2007.

A.3 Tomographic method

For the joint inversion of USArrayTA data we adopt the method developed by Li et al. (2006) for the study of the upper mantle structure beneath Tibet. An iterative least squares method is used to minimize the cost function

$$E = ||\mathbf{Am} - \mathbf{d}||^2 + k_1||\mathbf{Lm}||^2 + k_2||\mathbf{m}||^2 + k_3||\mathbf{C} - \mathbf{M}_c||^2, \tag{A.1}$$

where **A** is the sensitivity matrix, **m** is the model, **d** is the data, and **C** and $\mathbf{M}_C$ as defined under (II), below. The model **m** includes the wave speed perturbations (in non-overlapping, constant-slowness blocks) relative to *ak135* (Kennett et al., 1995) and parameters associated with hypocenter mislocation. In order to deal with noisy data and possible singularity in the inversion, both norm and gradient damping are applied. The norm damping seeks to find the best model with small variations from the original model, and gradient damping smoothes the model. The weights for gradient and norm damping are k_1 and k_2, respectively, and $\mathbf{L}$ is a smoothing operator.

For the calculation of the sensitivity matrix A we have been using geometrical ray theory (in the spherically symmetric reference model *ak135*) to calculate ray paths associated with short period data measured by phase picking (e.g., *P, Pn, PKP*) and 3-D sensitivity kernels for the long period data measured by waveform cross-correlation (such as *PP-P*). In contrast to smoothing in the model space (e.g., through regularization), back projection along such kernels allows constraining long wavelength structure with long period data without sacrificing spatial resolution in regions of dense coverage by short-period data (Kárason & van der Hilst, 2001). We use an approximation to finite frequency kernels that is different from the approximation that has become known as the banana doughnut kernel (e.g., Dahlen et al. (2000)). With the data, parameterization, and linearization used such differences are of minor importance (e.g., Kárason (2002); De Hoop et al. (2006)), and neither type of kernel should be regarded as a finite frequency sensitivity kernel proper. Indeed, multi-scale tomography with (broad-band) *USArrayTA* data requires consideration of full wave dynamics (e.g., De Hoop & Van der Hilst (2005); De Hoop et al. (2006); Tromp et al. (2005)).

Li et al. (2008a) describe the full details of this methodology, but two aspects of the method are of particular interest for the application to *USArrayTA* data:

A.3.1 Adaptive parameterization

To mitigate uneven data coverage and benefit optimally from the addition of array and regional network data we adapt grid-size to the local density of data coverage (Figure 3). The smallest grid used is currently 0.3 x 0.3 x 45km near the surface, which is appropriate for the 70 km station spacing used in USArrayTA, but the minimum size increases with depth to reflect the change in width of associated Fresnel zones. In this application, the density of data coverage is determined by the number of ray path segments in a specified mantle volume. Higher spatial resolution is attained in areas such as the Western US that have smaller grid spacing whereas (currently) only longer wavelength heterogeneity can be observed further to the east. Upon availability of more and more *USArrayTA* data, this grid will be adapted to the changes in data coverage. Such adaptive parameterization allows the global inversion to approach the resolution of a regional study in areas of high data coverage (see also, for instance, Bijwaard et al. (1998)).

A.3.2 Crust correction

Without remedial action, structures in the crust that cannot be resolved by the travel time data used here may produce artifacts in the images of the upper mantle. To prevent this from happening we apply a crust correction based on an independent reference model for the crust. In our inversion, this is accomplished through addition of a regularization term - $k_3||\mathbf{C} - \mathbf{M}_C||^2$ - to the cost function (Li et al., 2008b). Here, $\mathbf{C}$ is the projection of the reference crust model onto the irregular grid, $\mathbf{M}_C$, is the crustal part of our model, and k_3 is weight factor (Lagrangian multiplier) that controls the effect of this correction. Ideally, for $\mathbf{C}$ one uses a detailed regional model, but the current results have been obtained with the projection of the global reference CRUST 2.0 (Bassin et al. (2000), available online at *http://mahi.ucsd.edu/Gabi/crust2.html*) onto our fine grid. This regularization of the model space has distinct advantages over making explicit time corrections. In particular, new data can easily be added and updates of the crust model do not require recalculating time corrections. Indeed, when better crust models become available for regions involved in *USArrayTA* we will simply update $\mathbf{M}_C$ and re-run the inversion.

A.4 Model Updates - "Community Product"

We will update the tomography model periodically and make it readily available to the community. The update process is illustrated in Figure 4. Broadband data from *USArrayTA* stations is constantly collected at the ANF. Travel times for several seismic phases are then handpicked. Every six months we plan to take the new arrival times and combine them with extant *USArrayTA* and *EHB* data. At the same time a new irregular grid will be determined from the new ray path density. Finally, crustal corrections are projected onto the new grid, and new inversions done.

The updated models (that is, the velocity values for North America to 1000km depth) will be accompanied by a brief announcement in SRL, which will include pertinent information about the update (including model date, revision number, technique refinements, and the time span and station locations of the *USArrayTA* data used). Each model will be available electronically at the SRL website, along with information on data format and model parameters. Additionally, the model and a series of selected maps and cross sections will be available at http://web.mit.edu/sburdick/www/tomography.html.

We expect to receive around 200,000 new residuals from *USArrayTA* every six months. The effect on the images of four months worth of *USArrayTA* data is illustrated in Figure 5. We note, however, that image improvement will become even more significant as *USArray* extends into the Great Plains, where data coverage from existing stations is sparse.

A.5 Preliminary Results

The main purpose of this paper is to document our tomographic method and provide information about the model updates. While a detailed discussion of the results is beyond the scope of the paper, we call attention to a few first order observations.

For a depth of 200 km, Figure 5 illustrates the spatial resolution for February (5a), June (5b), and November 2007 (5c) for models based on USArrayTA data only as well as the model using all data (5d). A comparison of the current iteration with USArrayTA only and with all data is shown in 6e and 5f. Because many stations reporting to EHB are present in the western US (Figure 2b), the beneficial effect of adding USArrayTA data is likely to be smaller here than further east (Figure 2b,c). Indeed, in the western states the final model (5f) is similar to the USArrayTA-only model (5e), but the difference are larger further to the east. The low velocity basin and range province, the subduction of the Juan de Fuca plate beneath the Pacific NW, and the wavespeed variations beneath the Colombia plateau all appear very similar in the two models, but we lack, for instance, the ability to resolve the Yellowstone hotspot with only USArrayTA data recorded to November 2007. Even a few months of USArrayTA data, however, the resolution of velocity variations in the first several hundred kilometers beneath the western US noticeably improved. Indeed, adequate resolution of checkerboard structures expands progressively eastward after each four-month iteration. Between June and November, for instance, the data have begun to resolve (beneath Wyoming and Colorado) the western edge of the craton.

In map views (figure 7), the subduction of the Juan de Fuca plate can be seen as a distinct high velocity shallow mantle feature that extends from British Columbia to California. It is a pronounced feature in the Cascadian subduction zone (6a), but then becomes significantly weaker beneath the High Lava Plains in Oregon, an area notable for its lack of seismicity. As it increases with depth, the high velocity slab broadens and extends westward, with a "hole" in the slab between 400 and 600 km to the west of Oregon. The slab returns to strength at shallow depths in Northern California (6b) before ending abruptly at the Mendocino Triple Junction. At greater depths, the slab structure continues south past the triple junction, and the slab window created by the northward motion of the triple junction is apparent. We note that preliminary results of finite frequency tomography with USArray data reveals similar structures (Sigloch et al., 2008). At around 350 km depth, the maps suggest that the high velocity zone broadens and continues further to the east. This trend is also visible in vertical cross sections (Figure 6b). The Yellowstone hotspot is seen distinctly in map views up to $\sim$350 km depth, where it appears to be cut off by a high velocity feature that is connected to structure beneath California. It is possible that the source of the Yellowstone hotspot is shallow; but if the source were deeper, this observation suggests a complex interplay of the upwelling associated with the hotspot and deeper mantle structures.

In the vertical sections (Figure 6) the upper mantle beneath the basin and range province and the Colorado plateau is marked by very low wavespeeds. At the western edge of the low wavespeed zone is a fast area beneath the Sierra Nevada, and to the east, there is a sharp cutoff where the Rocky Mountains begin (Figure 6b). Beyond the Rockies, to the east, the cratonic center of the continent is generally quite high velocity, but here the resolution of the inversion is still low due to poor data coverage. As *USArrayTA* continues to the east, it will be possible to see whether the mantle beneath the stable craton has the same degree of heterogeneity as the tectonically active west coast.

A.6 A brief model comparison

A comparison of the maps views in Figures 1, 6, and 7 suggests that the main structures detected by our tomographic inversion (e.g., Figure 5 and 6) are largely in agreement with the previous generation of global tomography models, for surface waves (Ritzwoller et al., 2002), *P*-waves (e.g., Montelli et al. (2004)) and *S*-waves (Grand, 2002), but our multi-scale model reveals much more detail. By combining (high resolution) regional and (lower resolution) global models Dueker et al. (2001) provided tantalizing depictions of mantle structure beneath the western US (Figure 1a), but a problem arises when results from different regions are to be combined or when a quantitative comparison is needed between different models. The results shown here (e.g., Figure 6 and 7) demonstrate that our multi-scale tomography can reach the resolution of a regional study in areas of high data coverage. For example, the two-pronged structure of the Yellowstone hotspot is shown with similar resolution to that of a study using a high-density regional array (Yuan & Dueker, 2005).

A.7 Conclusion, outlook, and model availability

We have described the aspects of data processing and travel time tomography insofar they are directly relevant for the tomographic inversion of travel time data from *USArrayTA* stations. Because of the expected interest in tomographic models of the mantle beneath the continental regions involved in *USArrayTA* deployments, we will update our model on a regular basis and make it publicly available at the SRL website and at http://web.mit.edu/sburdick/www/tomography.html.

Already, there is a strong improvement in the resolution of mantle structures in the Western US in spite of the fact that the area is already well represent in the global data set. As *USArrayTA* marches across the various geological terrains in the United States, adding data in areas with traditionally lower station coverage, the updated multi-scale images will afford unique new insight into the lateral variations in upper mantle structures and the geological and geodynamical processes that cause them.

A.8 Acknowledgements

The authors thank the National Science Foundation Earthscope program and all the personnel supported through the USArray component operated by the Incorporated Research Institutions for Seismology who made this study possible.

Bibliography

Bassin, C., Laske, G., & Masters, G., 2000. The current limits of resolution for surface wave tomography in North America, *EOS*, **81**(B4).

Bijwaard, H., Spakman, W., & Engdahl, E. R., 1998. Closing the gap between regional and global travel time tomography, *Journal of Geophysical Research-Solid Earth*, **103**(B12), 30055–30078.

Bolton, H. & Masters, G., 2001. Travel times of P and S from the global digital seismic networks: Implications for the relative variation of P and S velocity in the mantle, *Journal of Geophysical Research-Solid Earth*, **106**(B7), 13527–13540.

Dahlen, F. A., Hung, S. H., & Nolet, G., 2000. Fréchet kernels for finite-frequency traveltimes - I. Theory, *Geophysical Journal International*, **141**(1), 157–174.

De Hoop, M. V. & Van der Hilst, R. D., 2005. On sensitivity kernels for 'wave-equation' transmission tomography, *Geophysical Journal International*, **160**(2), 621–633.

De Hoop, M. V., van der Hilst, R. D., & Shen, P., 2006. Wave-equation reflection tomography: annihilators and sensitivity kernels, *Geophysical Journal International*, **167**(3), 1332–1352.

Dueker, K., Yuan, H., & Zurek, B., 2001. Thick structured Proterozoic lithosphere of Western North America, *GSA Today*, **11**(12), 4–9.

Engdahl, E. R., van der Hilst, R., & Buland, R., 1998. Global teleseismic earthquake relocation with improved travel times and procedures for depth determination, *Bulletin of the Seismological Society of America*, **88**(3), 722–743.

Grand, S. P., 2002. Mantle shear-wave tomography and the fate of subducted slabs, *Philosophical Transactions of the Royal Society of London Series a-Mathematical Physical and Engineering Sciences*, **360**(1800), 2475–2491.

Humphreys, E. D. & Dueker, K. G., 1994. Physical state of the Western United-States upper-mantle, *Journal of Geophysical Research-Solid Earth*, **99**(B5), 9635–9650.

Kárason, H., 2002. *Constraints on Mantle Convection from Seismic Tomography and Flow Modeling*, Ph.D. thesis, Massachusetts Institute of Technology.

Kárason, H. & van der Hilst, R. D., 2001. Tomographic imaging of the lowermost mantle with differential times of refracted and diffracted core phases (PKP, P-diff), *Journal of Geophysical Research-Solid Earth*, **106**(B4), 6569–6587.

Kennett, B. L. N., Engdahl, E. R., & Buland, R., 1995. Constraints on seismic velocities in the Earth from travel-times, *Geophysical Journal International*, **122**(1), 108–124.

Li, C., van der Hilst, R. D., & Toksöz, A. N., 2006. Constraining P-wave velocity variations in the upper mantle beneath Southeast Asia, *Physics of the Earth and Planetary Interiors*, **154**(2), 180–195.

Li, C., van der Hilst, R. D., Engdahl, E. R., & Burdick, S., 2008a. A new global model for P wave speed variations in Earth's mantle, *Geochemistry Geophysics Geosystems*, **9**, Q05018.

Li, C., van der Hilst, R. D., Meltzer, A. S., & Engdahl, E. R., 2008b. Subduction of the indian lithosphere beneath the Tibetan Plateau and Burma, *Earth and Planetary Science Letters*, **274**(1-2), 157–168.

Montelli, R., Nolet, G., Masters, G., Dahlen, F. A., & Hung, S. H., 2004. Global P and PP traveltime tomography: rays versus waves, *Geophysical Journal International*, **158**(2), 637–654.

Ritzwoller, M. H., Shapiro, N. M., Barmin, M. P., & Levshin, A. L., 2002. Global surface wave diffraction tomography, *Journal of Geophysical Research-Solid Earth*, **107**(B12).

Sigloch, K., McQuarrie, N., & Nolet, G., 2008. Two-stage subduction history under North America inferred from multiple-frequency tomography, *Nature Geoscience*, **1**(7), 458–462.

Tromp, J., Tape, C., & Liu, Q. Y., 2005. Seismic tomography, adjoint methods, time reversal and banana-doughnut kernels, *Geophysical Journal International*, **160**(1), 195–216.

Yuan, H. Y. & Dueker, K., 2005. Teleseismic P-wave tomogram of the Yellowstone plume, *Geophysical Research Letters*, **32**(7).

Zhao, L. & Jordan, T. H., 2006. Structural sensitivities of finite-frequency seismic waves: a full-wave approach, *Geophysical Journal International*, **165**(3), 981–990.

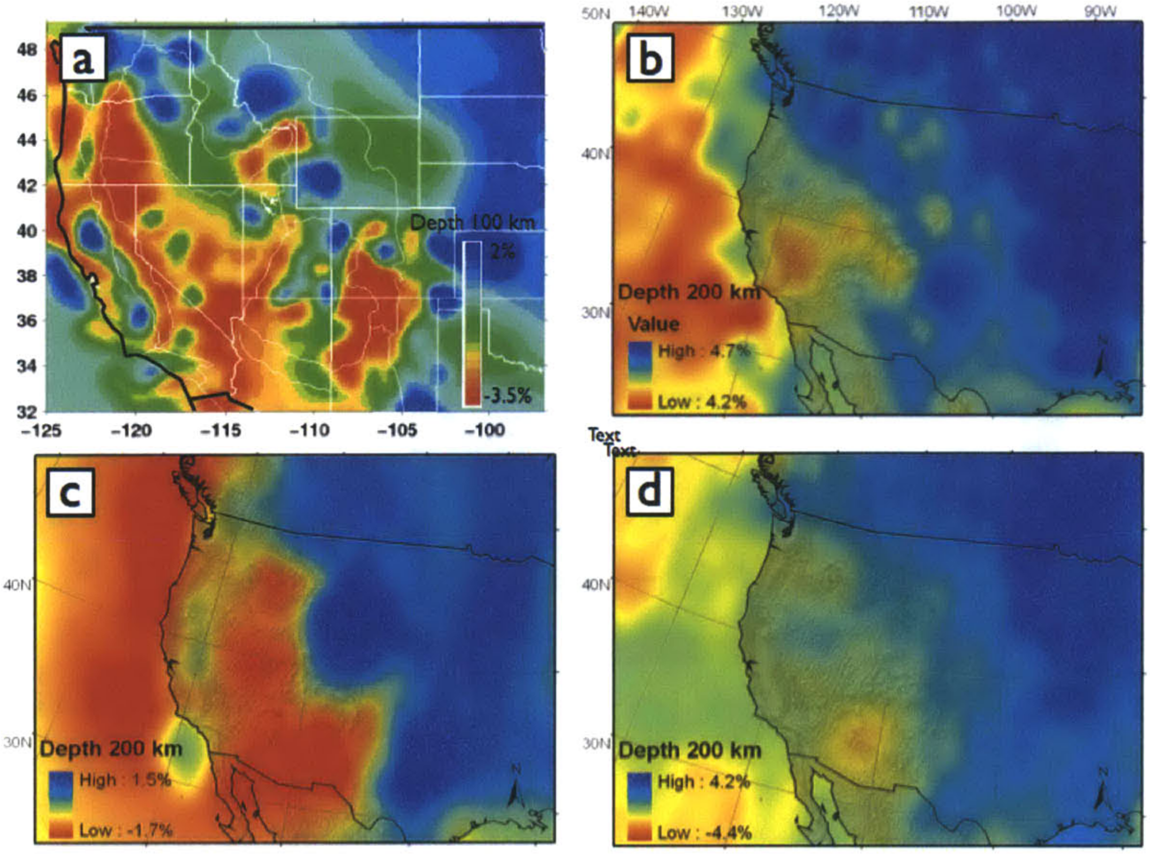

Figure A-1: a.) Model made by piecing together local tomography studies from Humphreys & Dueker (1994) and inverting with global data set (after Dueker et al. (2001)). b.) Global S-wave model from surface wave diffraction (Ritzwoller et al., 2002) c.) Global P-wave model using finite frequency kernels (Montelli et al., 2004). d.) Global S-wave travel-time model (Grand, 2002).

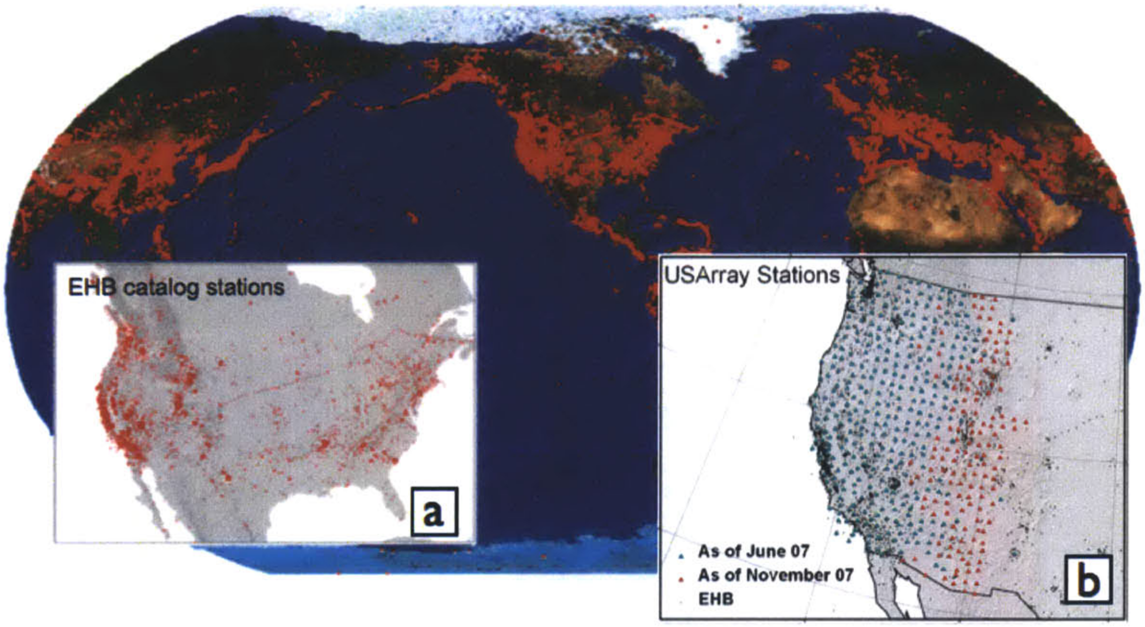

Figure A-2: Distribution of seismic stations from which data is used for travel time tomography. Background map: global distribution of stations reporting to the International Seismological Centre (ISC) and the US Geological Survey's National Earthquake Information Center (NEIC). These data are used by Engdahl et al (1998) to produce the EHB data base. (a) Locations of North American stations in EHB catalogue. (b) Station locations for USArrayTA data used in June 2007 iterations are shown in green, while locations added for November are shown in red.

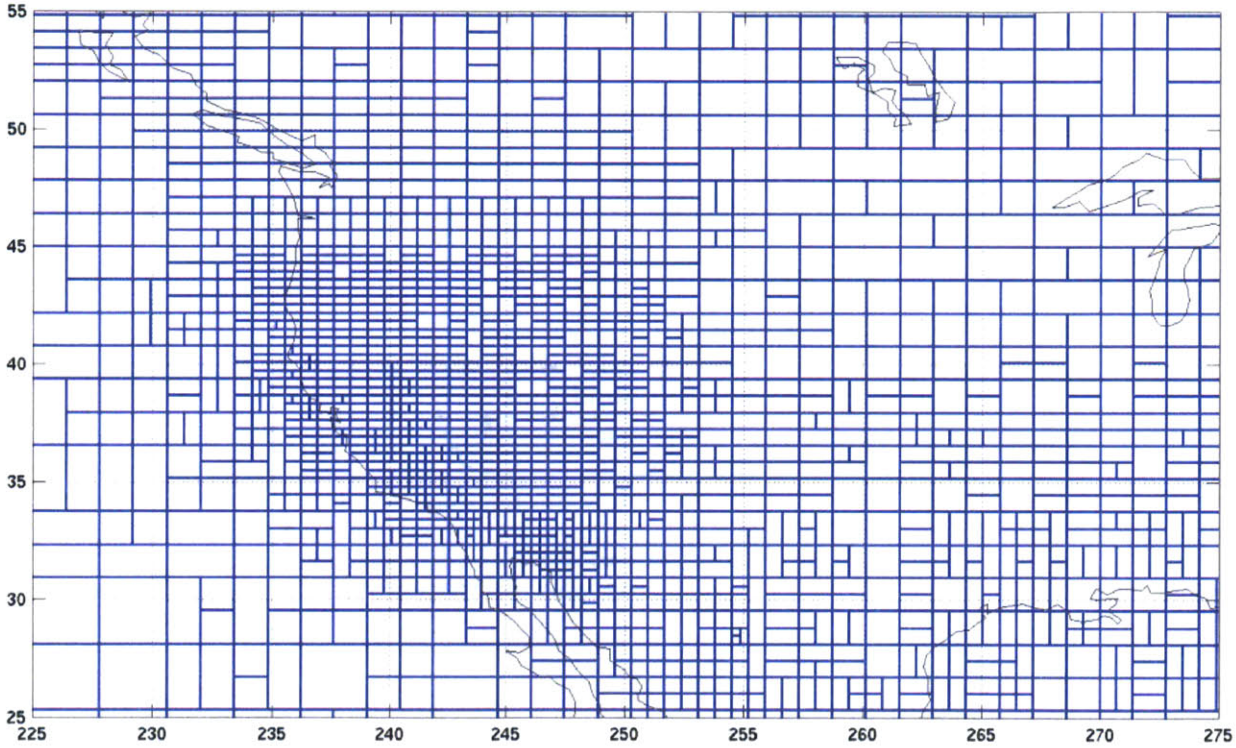

Figure A-3: Irregular grid used in inversion at a depth of 200km.

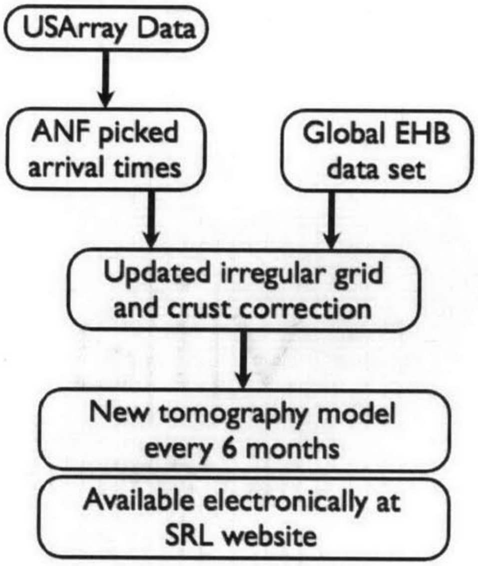

Figure A-4: Description of data flow and model update process.

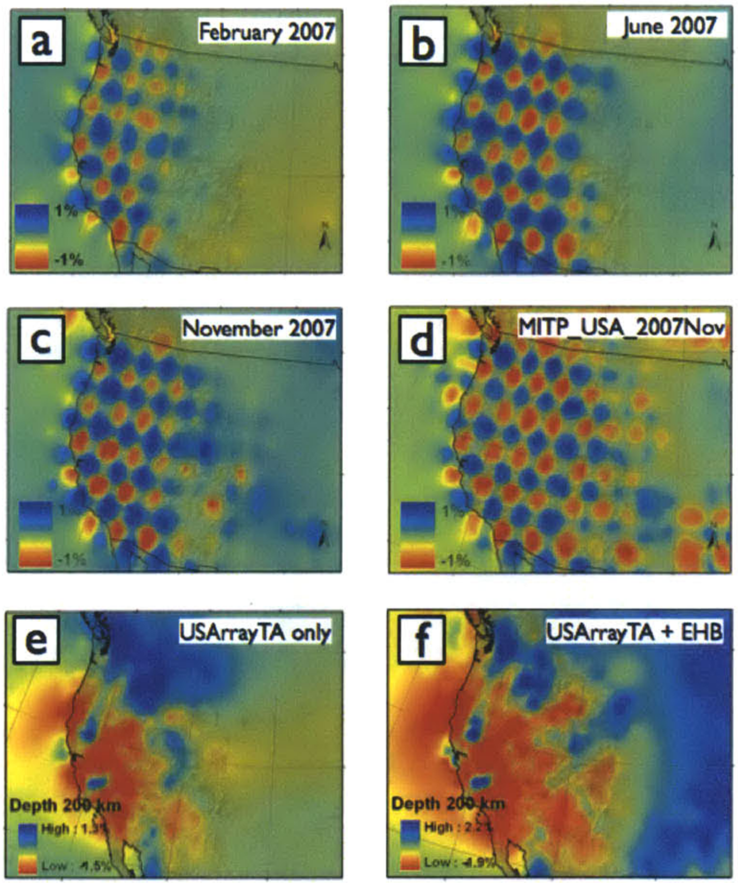

Figure A-5: Comparison of model with and without EHB data (all at 200 km depth). Resolution tests performed in a.) February 2007, b.) June 2007, and c.) November 2007 show the results that increasing the USArray data has on resolving structure in the Western US. d.) Resolution test using both EHB and USArray data improve on USArray only tests to the southwest and north of USArray. e.) Model from USArray data only. f.) Model from USArray and EHB data (MITP_US_2007NOV)

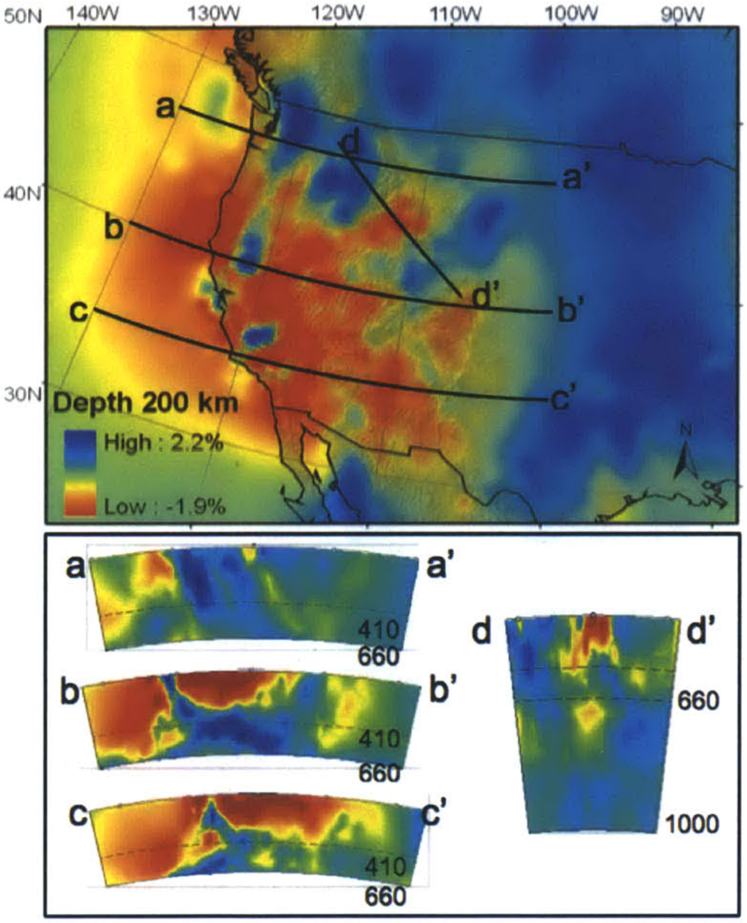

Figure A-6: Cross sections generated from latest model, MITP_USA_2007NOV. a.) Section across Cascadia subduction and Columbia plateau. b.) Section across southern extent of Juan de Fuca subduction. c.) Section across Sierra Nevada and Basin and Range province. d.) Section through Yellowstone hotspot track.

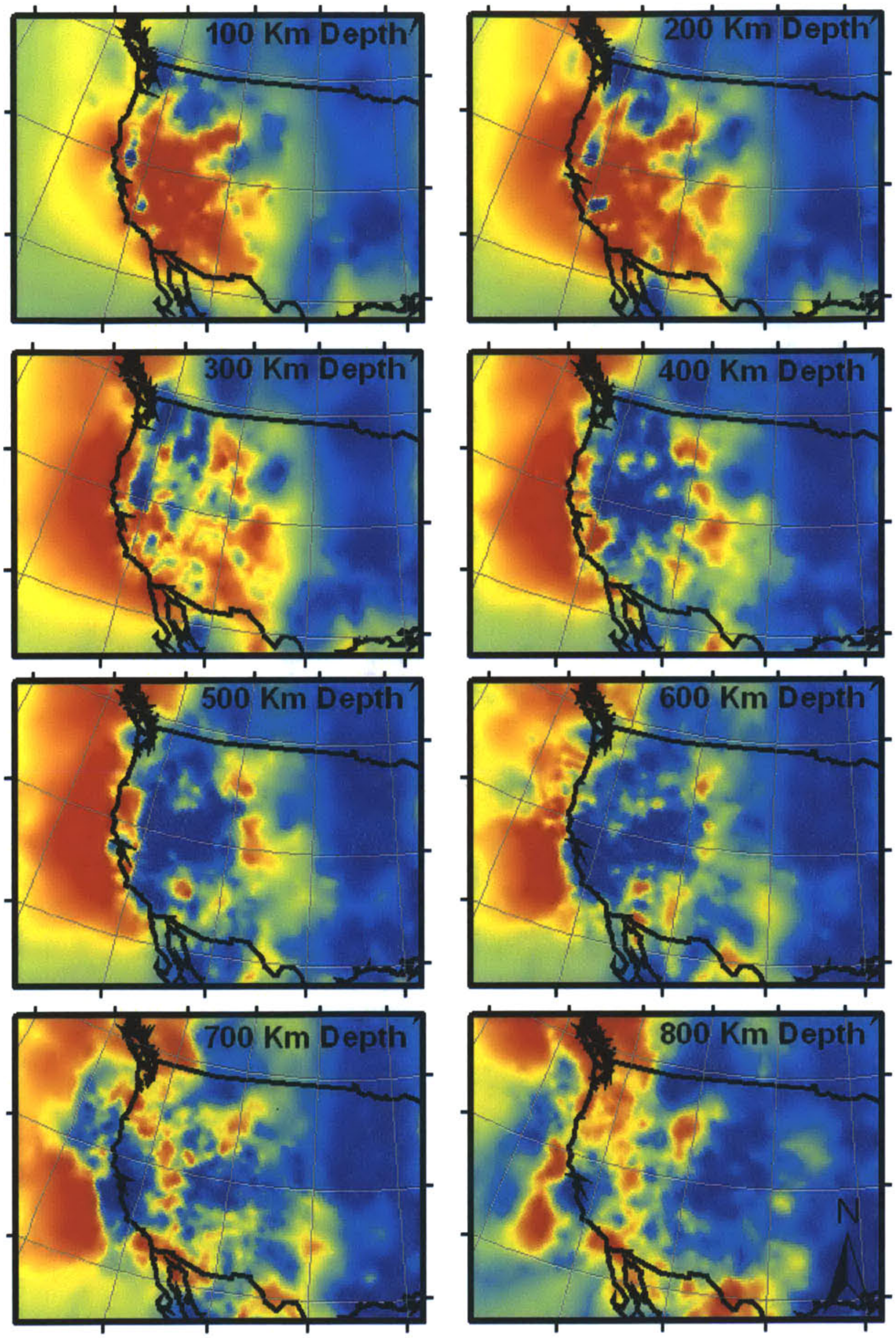

Figure A-7: Depth sections through MITP_USA_2007NOV. Red represents a change from the background model of -2.0% and blue a change of +2.0%.

Appendix B

USArray P-wave Model Update December 2008[1]

B.1 Introduction

As the Transportable Array of USArray (*http://www.iris.edu/USArray/*), the seismology component of EarthScope (*http://www.earthscope.org/*), progresses eastward across the USA, the seismological database available for studies of mantle heterogeneity beneath the North American continent is rapidly expanding. Burdick et al. (2008) published a tomographic model of mantle heterogeneity beneath North America based on USArrayTA *P*-wave travel time data through November 2007. The purpose of this article is to announce the availability (as an electronic supplement through the SRL web site) of model MITP_USA_2008DEC, which is based on USArrayTA data through December 2008.

By the end of 2008 USArrayTA had begun to illuminate mantle structure below the center of the continent, where systematic high-resolution tomography was previously unavailable. Specifically, data from stations east of the Rocky Mountains provides new constraints on the heterogeneity of the stable North American craton and allows for direct comparison with mantle heterogeneity beneath the tectonically active western margin. Compared to the previous version (Burdick et al., 2008), the current model update refines estimates of man-

---

[1] Published as: Burdick, S., van der Hilst, R.D., Vernon, F.L., Martynov, V., Cox, T., Eakins, J., Mulder, T., Astiz, L., and Pavlis, G.L. (2009). Model Update December 2008: Upper Mantle Heterogeneity beneath North America from P-wave Travel Time Tomography with Global and USArray Transportable Array Data. Seismological Research Letters 80, 638-645.

tle heterogeneity around Yellowstone hotspot, better defining its boundaries and revealing a strong slow anomaly beneath the transition zone. Large-scale structural features in the west, such as the Basin and Range and the Cascadia subduction zone, where data coverage was already good, remain similar to those in the original model, which suggests that the tomographic images of them are now robust

B.2 Methodology

Our tomographic inversions of USArray data are based on the method developed by Kárason (2002) and described by Li et al. (2008). We perform global inversions in order to account properly for mantle heterogeneity outside the study area and use an adaptable grid to enhance resolution in mantle volumes densely sampled by the seismic data used. For details pertinent to application to USArray we refer to Burdick et al. (2008). Of most interest for the model updates are (i) the addition of new USArrayTA data and (ii) the grid refinement in response to this addition of this new data. The smallest grid used is currently 0.3 0.3 45 km near the surface, which is appropriate for the 70-km station spacing used in USArrayTA. The minimum size increases with depth, however, to reflect the change in width of associated Fresnel zones of the transmitted waves. As in our previous paper, a crustal correction is applied to reduce the smearing of strong crustal heterogeneity into the mantle (Li et al., 2006). The least squares (tomographic) inversions yield wavespeed variations relative to reference model *ak135* (Kennett et al., 1995).

Our USArray models are inferred from three principal sources of data: (1) the global data base of $\sim$10 million *P*, *pP*, *Pn*, and *PKP* traveltime residuals reported to the International Seismological Centre (ISC) and the US Geological Center's National Earthquake Information Center (NEIC) and reprocessed by Engdahl (Engdahl et al., 1998) - hereinafter EHB data; (2) $\sim$20,000 long period *PP-P* differential travel time data (interpreted by means of approximate finite frequency sensitivity kernels), and (3) the rapidly growing data base of *P*-wave travel times from USArrayTA stations picked and subjected to rigorous quality control at the Array Network Facility (Burdick et al., 2008).

B.3 New data, Model Update, and Current Results.

The current USArray data base of $\sim$990,000 ANF picks includes sim390,000 P-wave traveltime residuals from 247 new USArrayTA stations (figure 1) from almost 2,000 teleseismic events between October 2007 and December 25, 2008. The new stations improve coverage in areas that are poorly sampled by data from stations represented in the EHB catalog, particularly in Eastern Wyoming and much of Montana and Colorado. Figure 2 shows the distribution of seismic events used in the new dataset (in red and green) added to the 3600 events from the previous USArrayTA dataset (in blue).

In response to the addition of new USArrayTA data we refined the model grid (shown in figure 3 for 200 km depth). Compared to Burdick et al. (2008), the most significant grid refinements occur in (1) the Pacific Northwest, where data has continued to accumulate and (2) West Texas and New Mexico, where stations were being installed around the time of our first report. Near the (current) leading edge of the array, for instance in Wyoming and Montana, grid refinements are still subtle because the recently installed stations have not yet recorded many events. Figure 4 demonstrates the ability of our method to resolve features on the order of 3 by 3 with currently available data.

Although new data have been added, the major structures imaged in the Pacific Northwest have not changed significantly compared to Burdick et al. (2008). This suggests that the geometry of the Cascadia subduction and the Idaho Batholith observed in the earlier paper are robust when viewed through the resolution window of this representation of the data. Likewise, features beneath California, where the grid was already at the highest level of refinement considered here, appear consistent between the old and new model. On the other hand, new data has increased the contrast between the slow anomaly related to the Yellowstone hotspot and the surrounding craton. Beneath Colorado and New Mexico, grid refinement (and increased spatial resolution) has not affected the scale of inferred mantle heterogeneity but the shape seems better defined. Previous tomography revealed a decrease in scale length of heterogeneity east of the eastern margin of the Rocky Mountains ($\sim$ 105W) but this variation coincided with a change in the spatial resolution of the data, with lower resolution of structure in the east owing to sparser station distribution. Inversion of USArray data demonstrates that the change in scale is real and not due to degraded resolution. Also notable in the present model is the emergence of a localized, slow anomaly at the base of the transition zone associated with the surface location of Yellowstone (figure 5f). For comparison with our previous model, MITP_USA_2007NOV, in Figure 6 we present mantle slices through MITP_USA_2008DEC in the same positions as the sections in Figure 7 of Burdick et al. (2008).

B.4 Model Comparison

Several groups have been using USArray data to produce high-resolution *P*-wave tomography models for the Western USA (Roth et al., 2008; Sigloch et al., 2008; Xue & Allen, 2007). See Figure 7 for a display of some of these models along one upper mantle section. Roth et al. (2008) produced a large regional model combining selected TA data with closely spaced arrays in the Northwest whereas Sigloch et al. (2008) incorporates TA data, measured at different frequencies, into a global finite-frequency tomography inversion. In spite of the differences in parameterization, the similarities between the models are encouraging, though there exist also substantial differences in details that will require further discussion.

The three models agree quite well in much of the western United States and at shallow depths the lateral positioning of strong anomalies associated with large-scale tectonic features seems to be robust, but their depth extend does not yet seem to be well constrained by the travel time inversions. We note that none of these models used the additional constraints provided by surface waves. Each model shows an image of the Cascadian subduction zone, terminating at the Mendocino triple junction and attenuating in Central Oregon. The Yellowstone-Snake River Plain hotspot track consistently shows as a very slow anomaly to below 200 km depth and the Idaho Batholith can be seen as a fast anomaly extending beyond 300 km. All models show evidence of a fast wavespeed anomaly in central Nevada between 200 and 300 km depth.

As in Sigloch et al. (2008) and Roth et al. (2008), our model shows a weakening of the anomaly from the subducted slab to 300 km depth beneath the High Lava Plain, trending eastward to below Central Oregon (Figure 5a-c). Roth *et al.* suggest that this feature, which is commonly referred to as the slab window, may be an inversion artifact due to poor ray coverage. However, our resolution tests (Figures 4 and 8) suggest that it may be a robust feature. The window/weak slab structure appears to extend deeper and further to the east than in other models, perhaps even connecting to the slow anomaly beneath Idaho down to 600 km depth.

B.5 Conclusions

The updated version of the MIT USArrayTA *P* model now incorporates close to 1,000,000 *P*-wave traveltime residuals from 2004 through December 2008 for $\sim$700 USArrayTA stations. The addition of over a year of traveltime data has led to refinements in our tomography model, particularly the Northwestern United States and in the western end of the Great Plains. A first look suggests that the difference in scale length of mantle heterogeneity beneath the stable center of the continent and the more tectonically active western margin is real and not an artifact of spatial resolution. A comparison with other high-resolution models of the western United States shows encouraging similarities but also substantial differences.

Our new model (MITP_USA_2008DEC) and simple MATLAB scripts for making cross sections is publicly available at the SRL website and at http://web.mit.edu/sburdick/www/tomography.html.

Acknowledgements

The authors thank the National Science Foundation for continued funding of the Earthscope program, the USArray team for their superb efforts in array installation and data quality control, and the Incorporated Research Institutions for Seismology for continued leadership and data storage and dissemination. We would also like to thank Karin Sigloch and Matt Fouch for providing their respective P-wave models for comparison.

Bibliography

Burdick, S., Li, C., Martynov, V., Cox, T., Eakins, J., Mulder, T., Astiz, L., Vernon, F. L., Pavlis, G. L., & van der Hilst, R. D., 2008. Upper mantle heterogeneity beneath North America from travel time tomography with global and USArray Transportable Array data, *Seismological Research Letters*, **79**, 384–390.

Engdahl, E. R., van der Hilst, R., & Buland, R., 1998. Global teleseismic earthquake relocation with improved travel times and procedures for depth determination, *Bulletin of the Seismological Society of America*, **88**(3), 722–743.

Kárason, H., 2002. *Constraints on Mantle Convection from Seismic Tomography and Flow Modeling*, Ph.D. thesis, Massachusetts Institute of Technology.

Kennett, B. L. N., Engdahl, E. R., & Buland, R., 1995. Constraints on seismic velocities in the Earth from travel-times, *Geophysical Journal International*, **122**(1), 108–124.

Li, C., van der Hilst, R. D., & Toksoz, N. M., 2006. Constraining spatial variations in P-wave velocity in the upper mantle beneath SE Asia., *Physics of the Earth and Planetary Interiors*, **154**, 180–195.

Li, C., van der Hilst, R. D., Engdahl, E. R., & Burdick, S., 2008. A new global model for P wave speed variations in Earth's mantle, *Geochemistry Geophysics Geosystems*, **9**, Q05018.

Roth, J. B., Fouch, M. J., James, D. E., & Carlson, R. W., 2008. Three-dimensional seismic velocity structure of the northwestern United States, *Geophysical Research Letters*, **35**(15).

Sigloch, K., McQuarrie, N., & Nolet, G., 2008. Two-stage subduction history under North America inferred from multiple-frequency tomography, *Nature Geoscience*, **1**(7), 458–462.

Xue, M. & Allen, R. A., 2007. The fate of the Juan de Fuca plate: Implications for a Yellowstone plume head, *Earth and Planetary Science Letters*, **264**, 266–276.

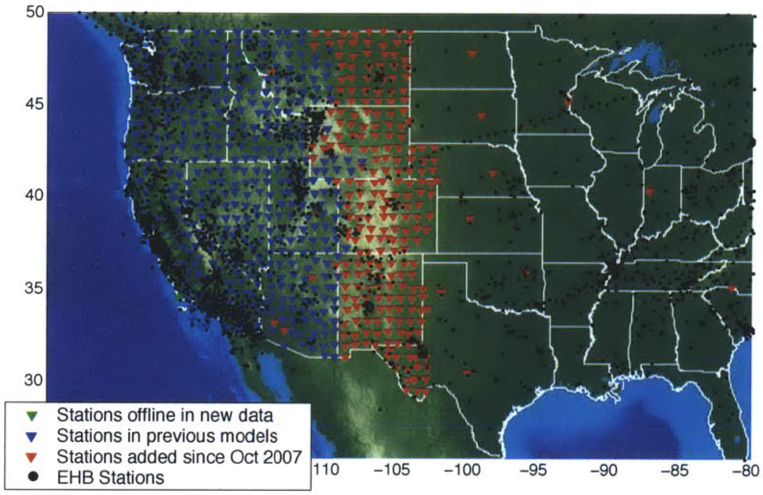

Figure B-1: Map of stations used in the western half of the United States. Black dots represent the current distribution of stations for the EHB dataset. For worldwide station distribution, please refer to Burdick *et al.* 2008 or Li *et al.* (2008). Blue triangles represent USArrayTA station locations from the previous model update for data between 2002 and October 2007. Red triangles represent USArray stations added to the dataset during the latest model run. Green triangles represent stations that were removed prior to the start date of the new dataset. Note the addition of stations in areas that previously had sparse data coverage.

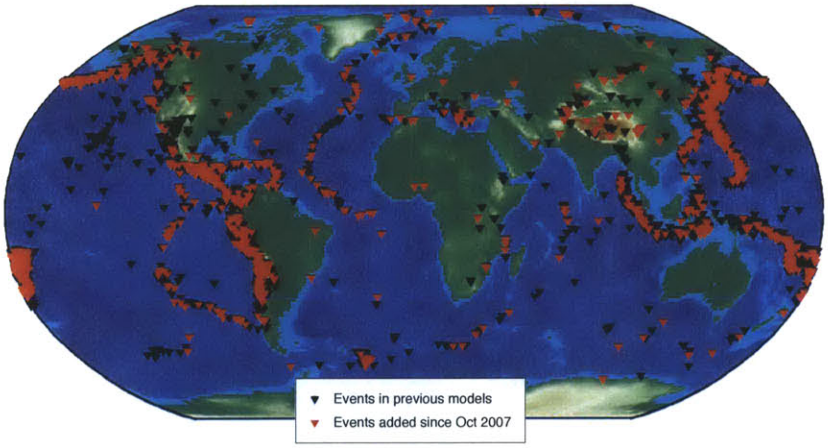

Figure B-2: Map of events recorded by USArray used in creating the current model. Blue triangles denote earthquakes recorded up to October 2007. Red triangles denote events recorded since the previous update.

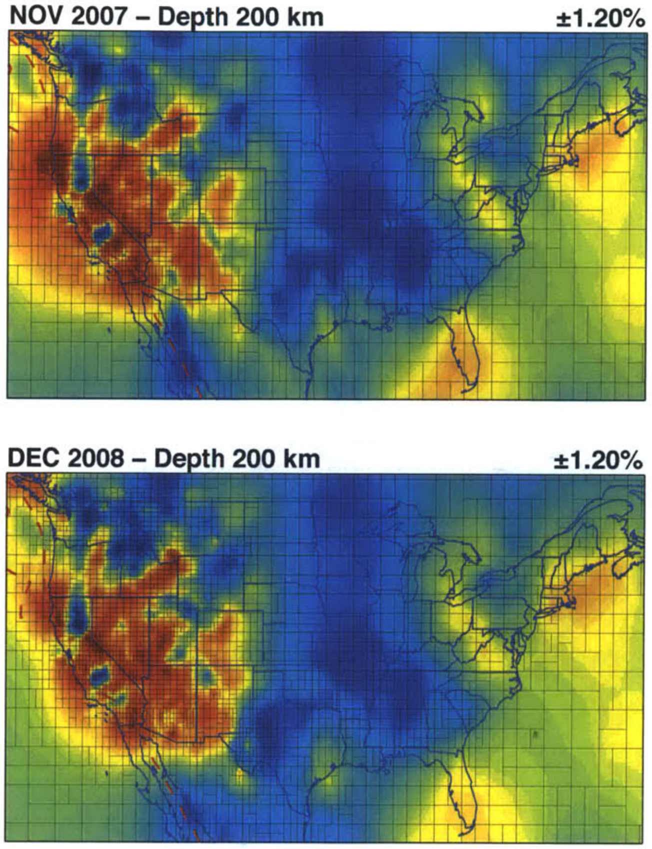

Figure B-3: Refinements to the model grid. The irregular grid used in the tomographic inversion is overlain on depth slices from the current and previous models at 200 km depth. The top image shows the grid from the October 2007 model update while the bottom shows the grid for the current model. Grid spacing is representative of the adequate data density within each cell.

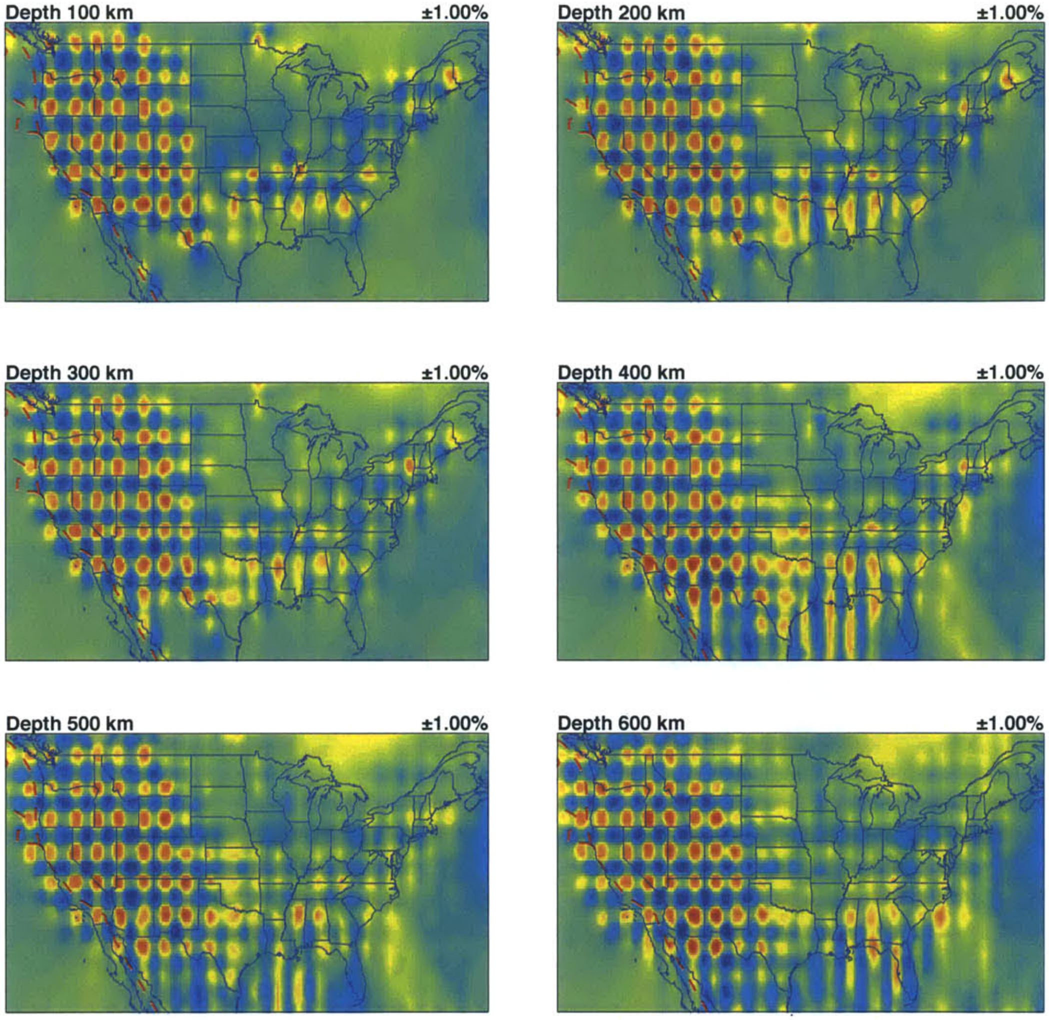

Figure B-4: Resolution tests using the current full dataset. The current model inversion shows the ability to resolve features on the scale of 3 by 3 beneath the current extent of the USArray Transportable Array. Resolution tests show that greater than half of the amplitude of the heterogeneity is recovered in this region. Elsewhere beneath the US - and beneath areas where USArrayTA was recently deployed - amplitude recovery is less successful. The elongated checkerboard squares in the Gulf of Mexico below 300 km depth show the effect of low data density on the irregular grid. The current data is unable to constrain longitudinal variations in that region on the order of three degrees.

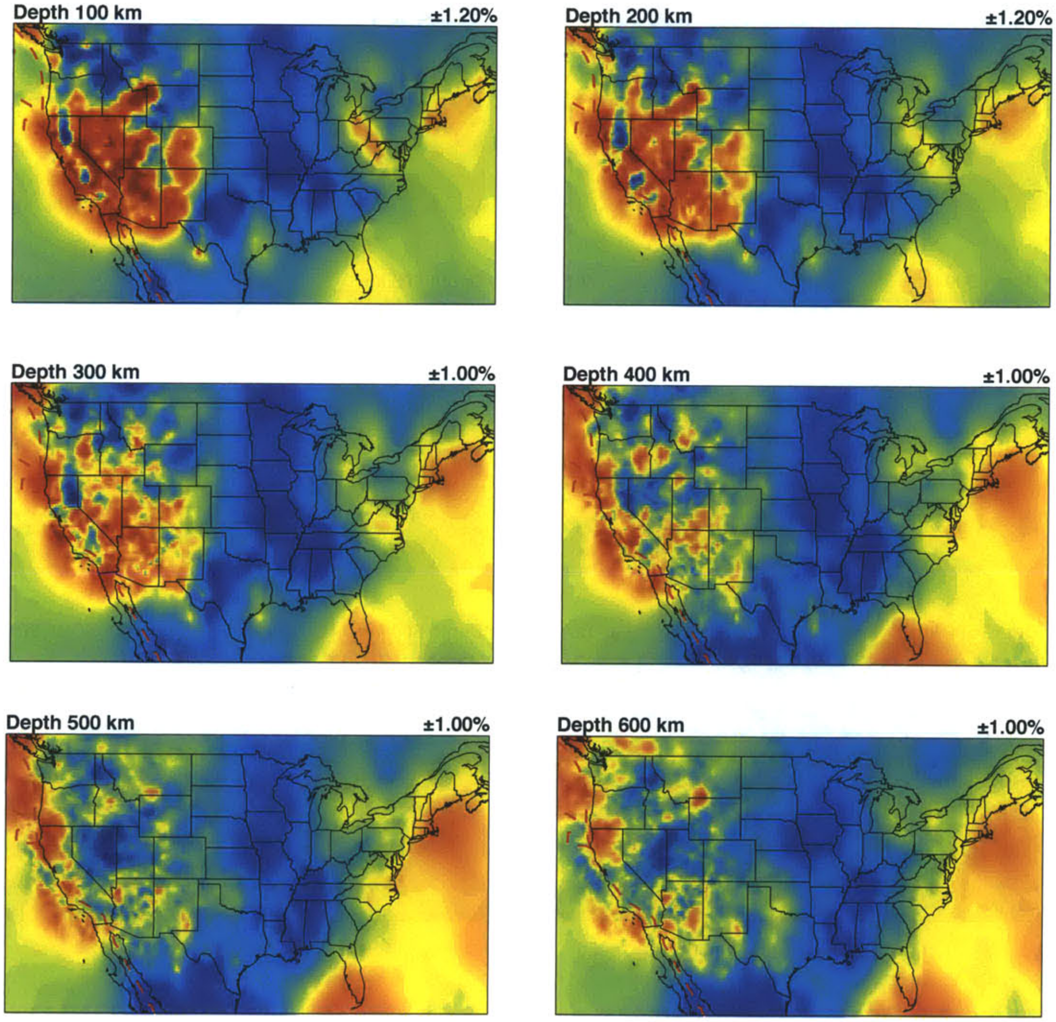

Figure B-5: Lateral variations in *P* wavespeed according to model MITP_USA_2008DEC for 6 different depths in the mantle beneath North America.

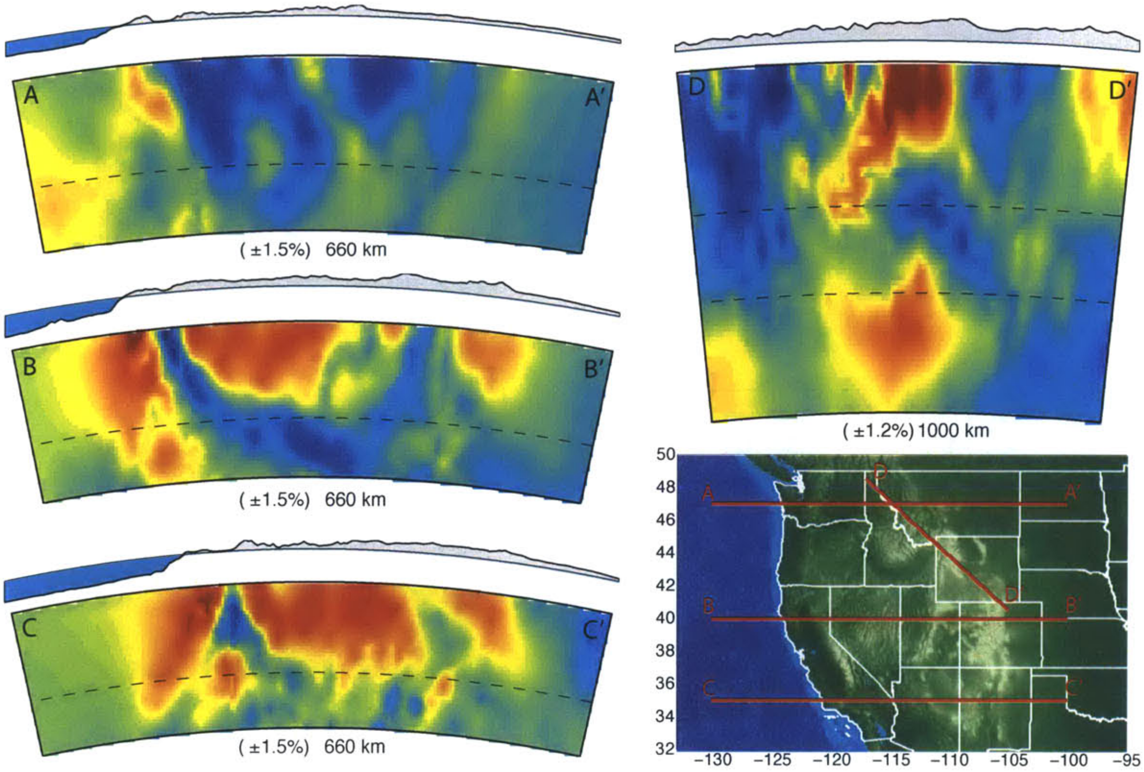

Figure B-6: Cross sections through MITP_USA_2008DEC for the same locations as in Fig. 7 of Burdick *et al.* (2008), which displayed model MITP_USA_2007NOV The three east-west sections reveal additional heterogeneity to the east, while the updated D-D' section shows a greater degree of heterogeneity at shallow depths.

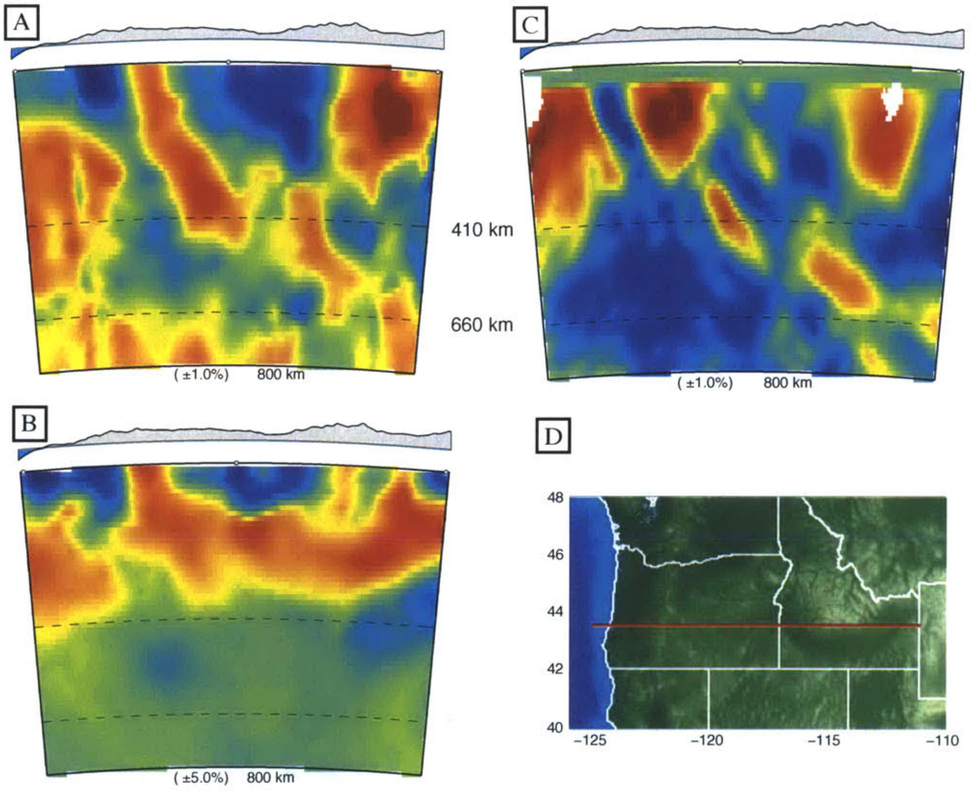

Figure B-7: A comparison between models of P-wave heterogeneity in the western US: (A) model MITP_USA_2008DEC (this paper), (B) *P*-wave model due to Sigloch *et al.* 2008, and (C) *P*-wave model due to Roth *et al.* 2008. The line of section is shown on the map in (D). Cross sections from the west coast to Wyoming are shown crossing the High Lava Plain and the eastern Snake River Plain. Note that the color scale is 1% deviation for A and C, and 5% for B.

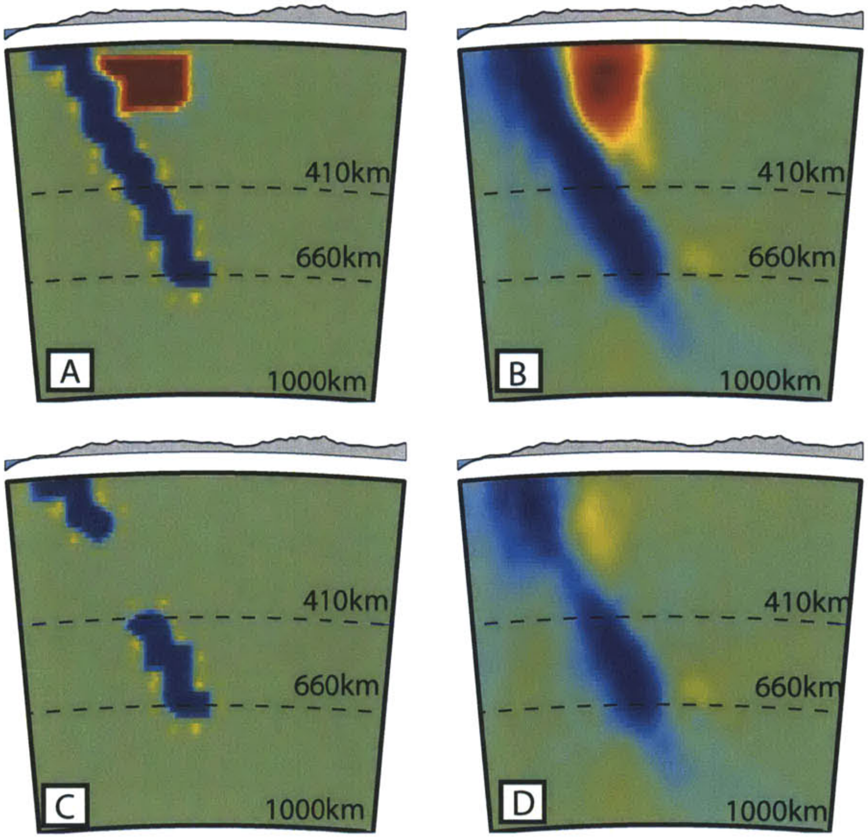

Figure B-8: Results of inversions with synthetic data to test the hypothesis that the "gap" in the slab could be an imaging artifact caused by the presence of slow anomalies on either side of the slab. Section is the same as in figure 7. (A) model with a continuous slab and a slow mantle wedge, (B) result of inversion with synthetic data calculated from model slab in panel (A). (C) input model of slab with "gap", (D) result of inversion with synthetic data calculated from model slab in panel (C). These test inversions demonstrate that a continuous slab can be resolved by the data used and that the image produced by a slab wit a "gap" resembles the image obtained from the observed data. This test suggests that the "gap" in the slab is real.

Appendix C

USArray P-wave Model Update January 2010[1]

C.1 Introduction

The Transportable Array of USArray (*http://www.iris.edu/USArray/*), the seismological component of EarthScope (*http://www.earthscope.org/*), is producing an impressive database of seismological observations for use in exploring mantle structure beneath North America. By early 2010, USArrayTA had made its way into the Great Plains states where the availability of seismic data was previously very sparse. In our previous papers (Burdick et al., 2008, 2009) we presented 3-D tomographic models of mantle P-wavespeed from global and USArrayTA traveltime data through November 2007 and December 2008, respectively. Here we present a model update using additional USArrayTA data through January 2010. The new community model, MITP_USA_2010JAN, is available as an electronic supplement to this research note.

---

[1] Published as: Burdick, S., van der Hilst, R. D., Vernon, F. L., Martynov, V., Cox, T., Eakins, J., Karasu, G. H., Tylell, J., Astiz, L., Pavlis, G. L., 2010. Model update January 2010: Upper mantle heterogeneity beneath North America from traveltime tomography with global and USArray Transportable Array data, *Seismological Research Letters*, 81(5), 689-693.

C.2 Methodology

The method for traveltime tomography used here is described in detail by Li et al. (2008) and Burdick et al. (2008). In short, we perform global inversions of P-wave travel time residuals using an adaptable grid with a minimum grid spacing of 0.3° 0.3° 45 km near the surface. The spacing of the adaptable grid is adjusted based on adequate raypath coverage in each mantle volume. The data included in the inversion consist of ~10 million P-wave residuals from the International Seismological Centre and the National Earthquake Information Center processed using the algorithms developed by Engdahl et al. (1998) - henceforth referred as the EHB catalog - and the database of USArrayTA P-wave residuals picked by the Array Network Facility (available online at ANF site). For the model update, we refine our grid in response to the addition of new USArrayTA traveltime residuals. The model values are reported as percentage P-wavespeed variation relative to reference model *ak135* (Kennett et al., 1995).

C.3 New data, Model Update, and Current Results.

Compared to Burdick et al. (2009), the updated dataset includes ~280,000 new USArrayTA picks from ANF for a total of ~1,390,000 traveltime residuals. These include residuals at 214 new USArrayTA stations (figure 1) from almost 1,500 teleseismic events between December 2008 and January 2010. The new stations improve data coverage throughout the Great Plains and central Texas, areas that are poorly sampled by data in the EHB catalog.

We have adapted the model grid (shown in figure 2) to benefit from the denser sampling provided by the new USArrayTA data. Compared to the previous update in Burdick et al. (2009) the most significant grid refinements concern (1) Eastern Montana and the western parts of the Dakotas, where data have continued to accumulate at existing stations, and (2) in Central Texas and Oklahoma. Figure 3 demonstrates the ability of our method to resolve features on the order of 3° by 3° with the current USArrayTA data plus the EHB catalog.

Compared to the previous model, the addition of new data has had little - if any - effect on the shape and strength of the heterogeneity west of the Rocky Mountains, suggesting that the model in this region is now robust at the scale of our inversion. East of the Rockies, however, the effects of improved resolution can be seen. In figures 4 and 5, the broad fast regions beneath the center of the continent begin to have a greater level of heterogeneity than in previous models. The distinction between anomalies due to the craton and to remnants of the Farallon slab, in particular, has become better defined. Additionally, the fast anomalies at shallow depths beneath Texas and those beneath Nebraska starting at 400 km stand out in sharper relief compared to the adjacent regions. The current model also shows a greater continuity between the deep, fast anomalies beneath the Plain states and anomalies due to slab structure in the west.

C.4 Conclusions

The updated version of the MIT USArrayTA *P* model now incorporates close to 1,400,000 *P*-wave traveltime residuals from 2004 through January 2010 for over 900 USArrayTA station locations. The addition of over a year of new traveltime data has led to refinements in our tomography model, particularly beneath the Great Plains states, Texas, and Oklahoma. Additional data coverage to the east of the Rocky Mountains reveals well defined boundaries between fast anomalies and surrounding structure, where previous models could only resolve large scale fast regions.

Our new model (MITP_USA_2010JAN) and simple scripts for making cross-sections is publicly available as an electronic supplement to this note and at *http://web.mit.edu/sburdick/www/esup10/*. ANF phase data are available to community as CSS monthly files at *http://anf.ucsd.edu/tools/events/download.php* or at the IRIS DMC thorough their Product section at *http://www.iris.edu/dms/products/*.

Acknowledgements

The authors thank the National Science Foundation for continued funding of the EarthScope program, the USArray team for their superb efforts in array installation and data quality control, and the Incorporated Research Institutions for Seismology for continued excellence and leadership in data storage and dissemination.

Bibliography

Burdick, S., Li, C., Martynov, V., Cox, T., Eakins, J., Mulder, T., Astiz, L., Vernon, F. L., Pavlis, G. L., & van der Hilst, R. D., 2008. Upper mantle heterogeneity beneath North America from travel time tomography with global and USArray Transportable Array data, *Seismological Research Letters*, **79**, 384–390.

Burdick, S., Hilst, R. D., Vernon, F., Martynov, V., Cox, T., Eakins, J., Mulder, T., Astiz, L., , & Pavlis, G., 2009. Model update December 2008: Upper mantle heterogeneity beneath North America from travel time tomography with global and USArray Transportable Array data., *Seismological Research Letters*, **80**, 638–645.

Engdahl, E. R., van der Hilst, R., & Buland, R., 1998. Global teleseismic earthquake relocation with improved travel times and procedures for depth determination, *Bulletin of the Seismological Society of America*, **88**(3), 722–743.

Kennett, B. L. N., Engdahl, E. R., & Buland, R., 1995. Constraints on seismic velocities in the Earth from travel-times, *Geophysical Journal International*, **122**(1), 108–124.

Li, C., van der Hilst, R. D., Engdahl, E. R., & Burdick, S., 2008. A new global model for P wave speed variations in Earth's mantle, *Geochemistry Geophysics Geosystems*, **9**, Q05018.

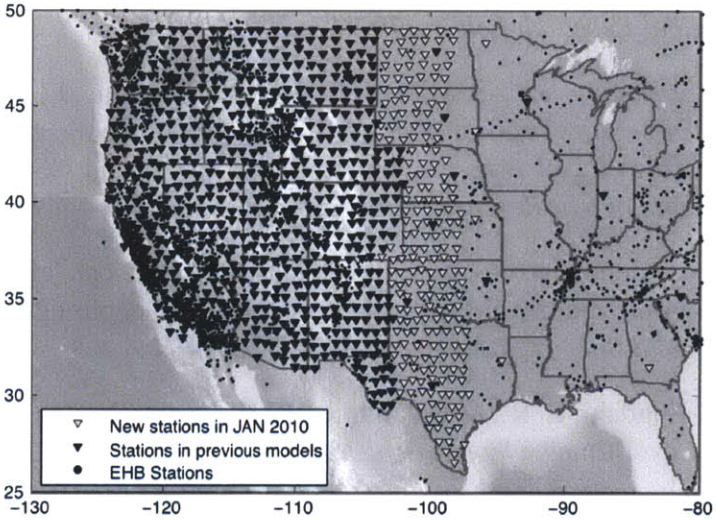

Figure C-1: Map of stations in the western United States from which data is used in the inversion. Black dots represent stations contributing to the EHB dataset - the worldwide station distribution can be found in Burdick et al. (2008) or Li et al. (2008). Dark triangles represent USArrayTA station locations from the previous model update for data between 2002 and December 2008 used in Burdick et al. (2009). Light triangles represent TA stations added to the dataset for the latest inversion.

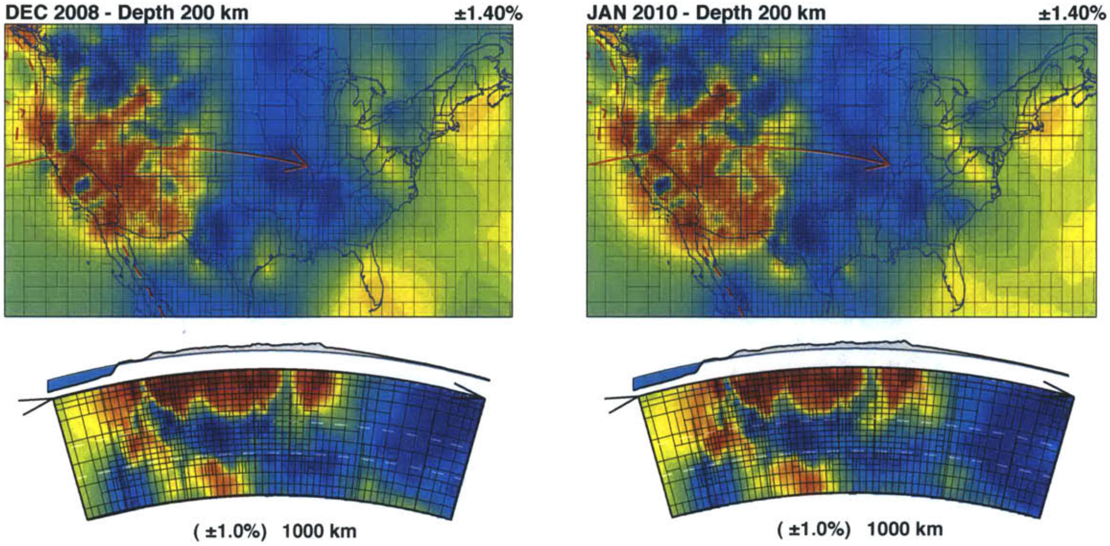
DEC 2008 - Depth 200 km

JAN 2010 - Depth 200 km

Figure C-2: Refinements to the model grid. Map sections at 200 km and cross-sections through the irregular grids used in the tomographic inversion for the current and previous models. The images on the left show the grid from the December 2008 model update. The red arrow indicates the location of the cross-section. The images on the right show the grid for the current model. Grid spacing is representative of the adequate raypath density within each cell.

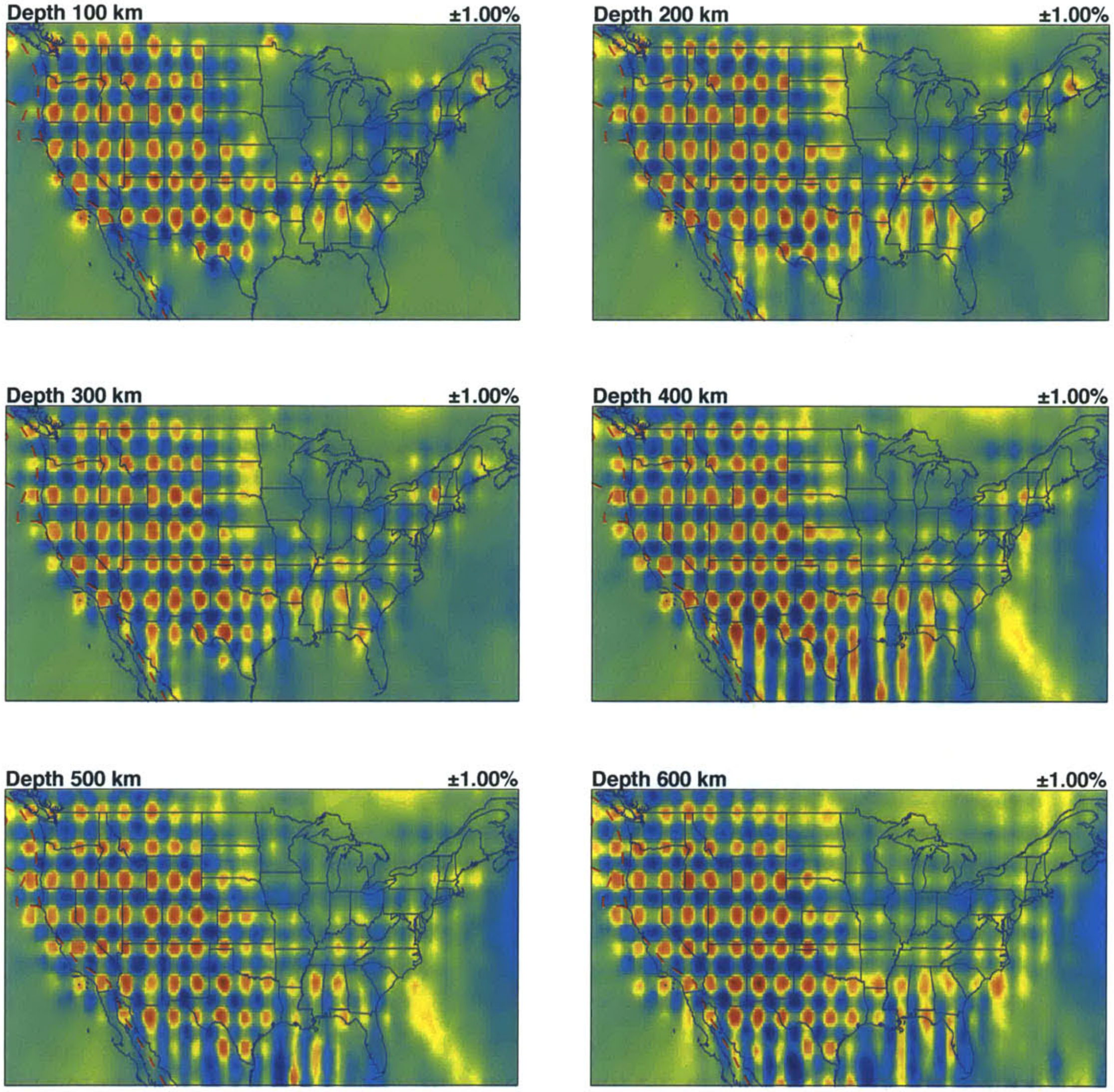

Figure C-3: Resolution tests using the current full dataset. The current model inversion shows the ability to resolve features on the scale of 3 by 3° beneath the current extent of the USArray Transportable Array. Tests were able to resolve most of the amplitude of the heterogeneity. Just to the east of the current extent of USArrayTA and beneath recently deployed portions, the shape of the heterogeneity can be seen, but lower amplitudes were recovered.

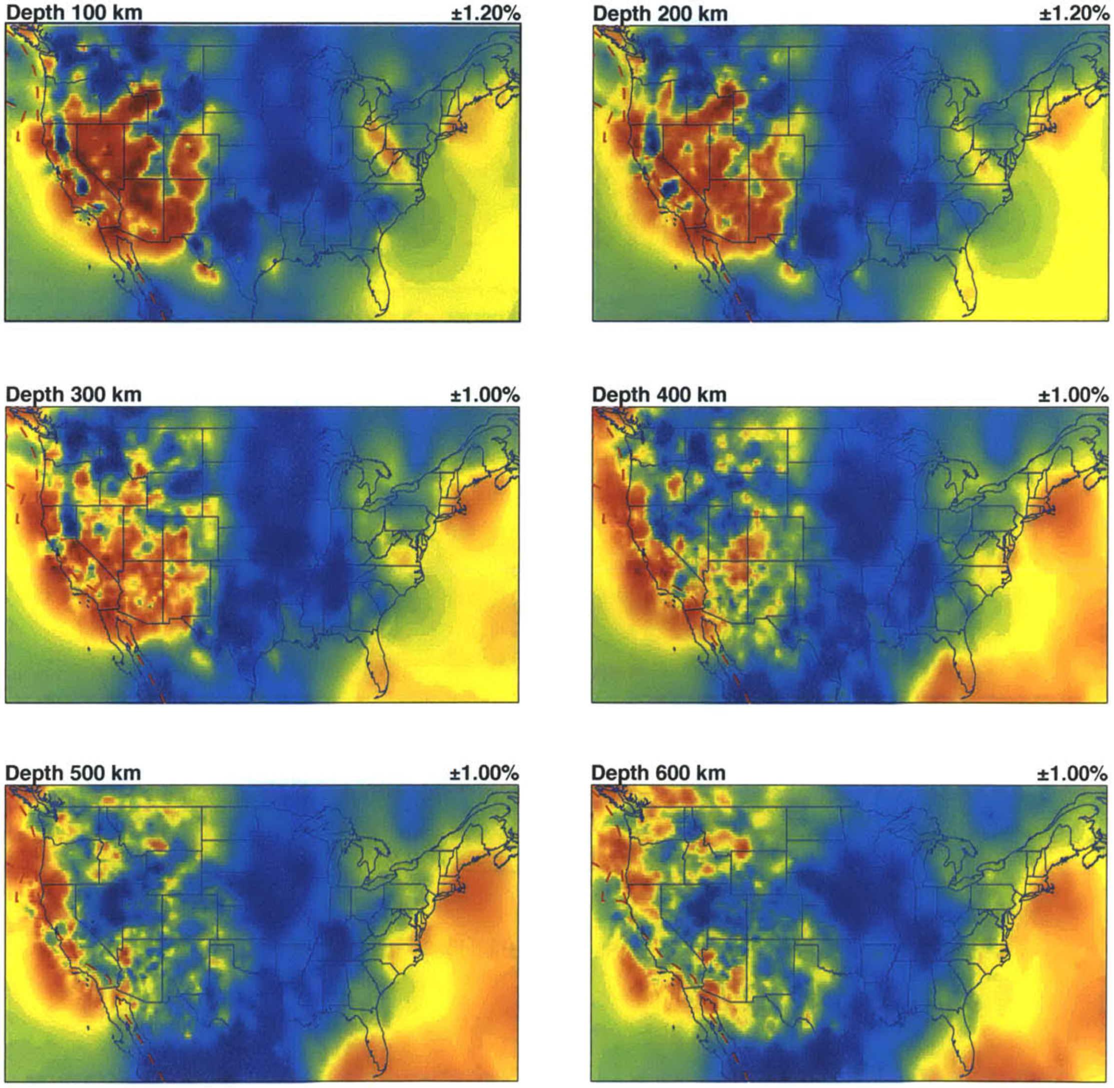

Figure C-4: Lateral variations in *P* wavespeed according to model MITP_USA_2010JAN for 100-600 km depth in the mantle beneath North America.

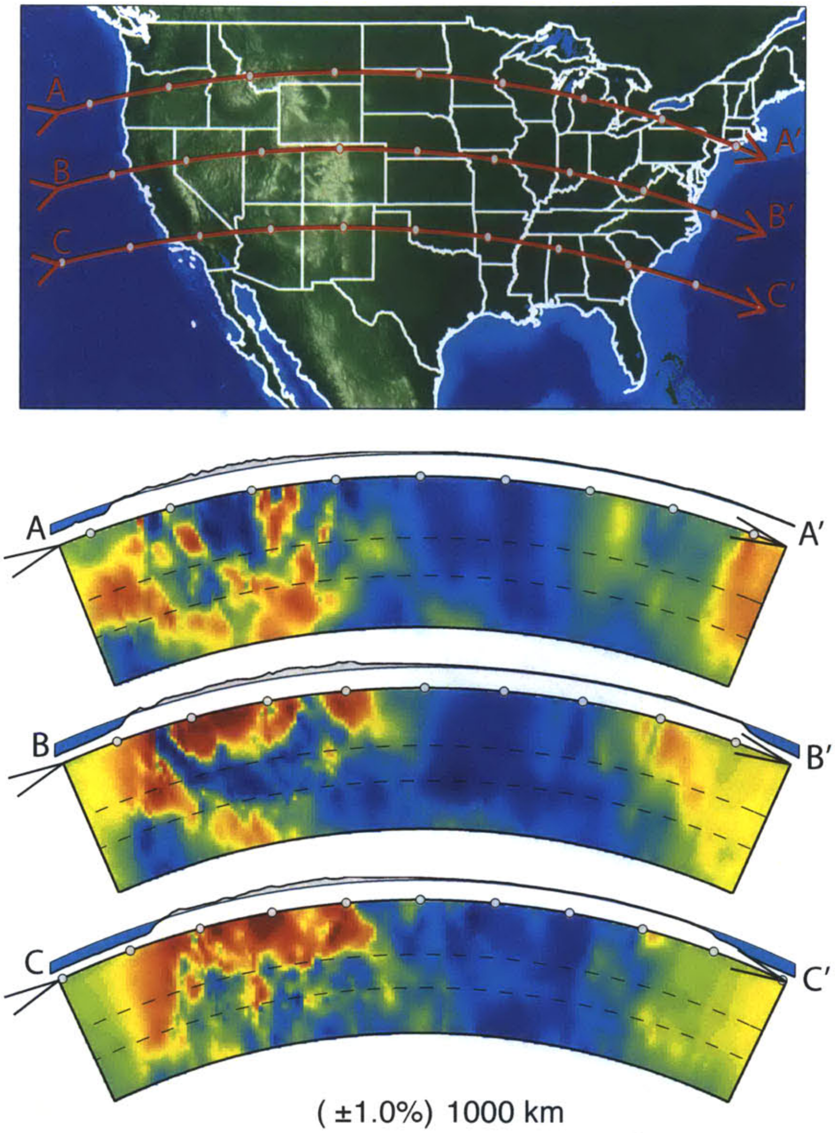

Figure C-5: Cross-sections through MITP_USA_2010JAN. Note that the eastern parts of the cross-sections remain poorly sampled by the current data. Future USArrayTA deployments will be pivotal in (1) establishing whether the smoothness is real or an artifact of current sampling and (2) better resolving the structures associated with the craton and fragments of the Farallon slab in the transition zone.

Appendix D

USArray P-wave Model Update March 2011[1]

D.1 Introduction

In 2011, the Transportable Array of USArray (http://www.iris.edu/USArray/), the seismological component of EarthScope (http://www.earthscope.org/), continued to extend east of the Rocky Mountains and the Great Plains and into the Midwest and Gulf Coast regions where not many routinely processed data were available for previous regional- or global scale travel time inversions. In previous papers (Burdick et al., 2008, 2009, 2010) we presented 3-D tomographic models of mantle P-wavespeed from global and USArrayTA traveltime data through November 2007, December 2008, and January 2010, respectively. Here we present a model update using USArrayTA data through March 2011. The new model, MITP_USA_2011MAR, is available as an electronic supplement. Interpretation of the 3-D tomographic images is beyond the scope of this brief research note.

---

[1] Published as: Burdick, S., van der Hilst, R. D., Vernon, F. L., Martynov, V., Cox, T., Eakins, J., Karasu, G. H., Tylell, J., Astiz, L., Pavlis, G. L., 2012. Model update March 2011: Upper mantle heterogeneity beneath North America from traveltime tomography with global and USArray Transportable Array data, *Seismological Research Letters*, 83(1), 23-28.

D.2 Methodology

The method for traveltime tomography used here is described in previous papers (Li et al., 2008; Burdick et al., 2008), but for the sake of completeness we include a brief summary. We perform global (linearized) inversions of P-wave travel time residuals using an adaptable grid with a minimum grid spacing of $0.3^\circ \times 0.3^\circ \times 45$ km. The spacing of the adaptable grid is adjusted based on raypath coverage in each mantle volume. The data included in the inversion consist of $\sim$10 million P-wave residuals from the International Seismological Centre and the National Earthquake Information Center processed using the algorithms developed by Engdahl et al. (1998) - henceforth referred as the EHB catalog - and the database of USArrayTA P-wave residuals picked by the Array Network Facility (available online at ANF site). For each model update we refine the grid in response to the addition of new USArrayTA traveltime residuals. The tomographic inversion is linearized using the 1-D reference model *ak135* (Kennett et al., 1995); that is, ray paths are calculated in *ak135* and the wavespeed variations respresented in model MITP_USA_2011MAR are relative to the average wavespeed at a given depth according to *ak135*.

D.3 What is new?

Compared to the last update, the March 2011 update of the USArrayTA dataset includes $\sim$260,000 P-wave travel time residuals from around 3,500 teleseismic events mostly occurring between January 2010 and March 2011 and which were recorded at 261 new USArrayTA stations (Figure 1). Some events occurring before 2010 which had not been previously reviewed have also been added to the data set. The total number of USArrayTA picks used in our tomography is now $\sim$1,650,000. The advancing Transportable Array continues to improve data coverage in areas poorly sampled in the EHB catalog as it extends past the Great Plains states and into the Midwest and Gulf Coast regions. New stations also include those installed in Cascadia in 2010.

We adapted the model grid (shown in Figure 2) to the denser sampling provided by the new data. The most significant grid refinements (compared to the 2010 inversions) concern

(i) the shallow mantle beneath the eastern part of the Great Plains (due to continued data accumulation at stations installed before our 2010 update) and East Texas and Arkansas (due to data from new seismograph locations) and (ii) the mantle transition zone beneath the Plains and the western parts of the Midwest and the Gulf states. To obtain a qualitative measure of resolution by the data used we conducted series of so-called checkerboard resolution tests. Figure 3 suggests that beneath the USArray TA footprint the data generally resolve model features of the order of 3° by 3° ($\sim$300 km by 300 km), but resolution is better in several well sampled regions.

Figures 4 and 5 depict mantle heterogeneity according to the latest model update. Beneath the Western US (including Rocky Mountains) the addition of a year's worth of new data has not had a great effect on the tomographic image of upper mantle heterogeneity, but the additional ray paths have refined certain features at transition zone depths and below. The Farallon slab, for instance, appears narrower beneath the Western US than in previously published versions of our model. Beneath the Great Plains and beyond the new data improve constraints on mantle heterogeneity at all depths. At eastern edge of the Great Plains the data are now resolving the base of the zone of fast velocities beneath the craton, and they have begun to distinguish between cratonic lithosphere and the presumed remnants of slabs of subducted lithosphere. With these new data it now also becomes apparent that the smooth, long length-scale structure in the west of the Rocky Mountains seen in previous models is not just a result of difference in data coverage, but indeed is a robust feature of the region.

D.4 Concluding remarks.

In this brief research note we present the latest MIT USArrayTA P model: MITP_USA_2011MAR. This model includes more than 1,650,000 P-wave traveltime residuals (from 2004 through March 2011) obtained from nearly 1200 USArrayTA seismograph sites. A year's worth of new traveltime data has improved the resolution of the model, particularly in the Great Plains and the eastern parts of the Midwest and Gulf states from which little global data was available previously. Beneath the central continent, the data now resolve the subducted slab from the base of the cratonic root.

Model MITP_USA_2011MAR and scripts for making horizontal and vertical cross-sections through it are available as an electronic supplement to this research note and from http://web.mit.edu/sburdick/www/esup11/. ANF phase data are also available to the community as CSS monthly files at http://anf.ucsd.edu/tools/events/download.php or at the IRIS DMC thorough their Product section at http://www.iris.edu/dms/products/.

D.5 Acknowledgements

The authors thank the National Science Foundation for continued funding of the EarthScope program, the USArray team for their superb efforts in array installation and data quality control, and the Incorporated Research Institutions for Seismology for continued excellence and leadership in data storage and dissemination. The construction and dissemination of our model updates is supported by NSF grant EAR-0951901

Bibliography

Burdick, S., Li, C., Martynov, V., Cox, T., Eakins, J., Mulder, T., Astiz, L., Vernon, F. L., Pavlis, G. L., & van der Hilst, R. D., 2008. Upper mantle heterogeneity beneath North America from travel time tomography with global and USArray Transportable Array data, *Seismological Research Letters*, **79**, 384–390.

Burdick, S., Hilst, R. D., Vernon, F., Martynov, V., Cox, T., Eakins, J., Mulder, T., Astiz, L., , & Pavlis, G., 2009. Model update December 2008: Upper mantle heterogeneity beneath North America from travel time tomography with global and USArray Transportable Array data., *Seismological Research Letters*, **80**, 638–645.

Burdick, S., van der Hilst, R. D., Vernon, F. L., Martynov, V., Cox, T., Eakins, J., Karasu, G. H., Tylell, J., Astiz, L., & Pavlis, G. L., 2010. Model update January 2010: Upper mantle heterogeneity beneath North America from traveltime tomography with global and USArray Transportable Array data, *Seismological Research Letters*, **81**(5), 689–693.

Engdahl, E. R., van der Hilst, R., & Buland, R., 1998. Global teleseismic earthquake relocation with improved travel times and procedures for depth determination, *Bulletin of the Seismological Society of America*, **88**(3), 722–743.

Kennett, B. L. N., Engdahl, E. R., & Buland, R., 1995. Constraints on seismic velocities in the Earth from travel-times, *Geophysical Journal International*, **122**(1), 108–124.

Li, C., van der Hilst, R. D., Engdahl, E. R., & Burdick, S., 2008. A new global model for P wave speed variations in Earth's mantle, *Geochemistry Geophysics Geosystems*, **9**, Q05018.

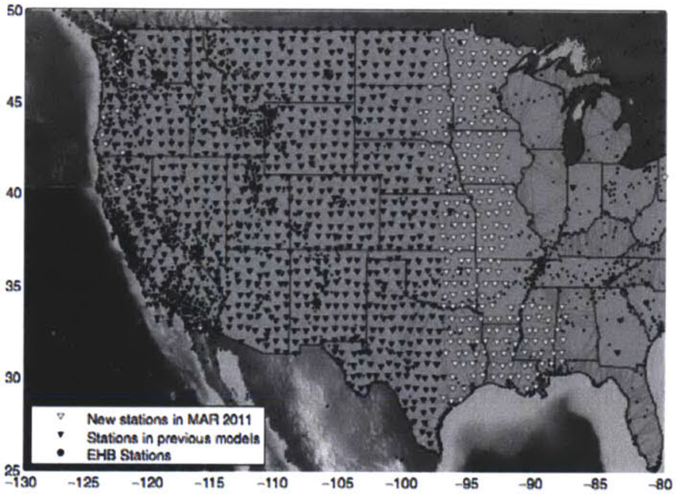

Figure D-1: Geographical distribution of seismograph stations in the western United States from which data is used in the latest model update (MITP_USA_2011MAR). Black dots represent stations contributing to the EHB dataset; the worldwide station distribution is depicted in Li et al. (2008) and Burdick et al. (2008). Black triangles represent USArrayTA station locations from the previous model update for data through January 2010 (Burdick et al., 2010). White triangles represent the new TA stations from which data was not yet available in previous updates.

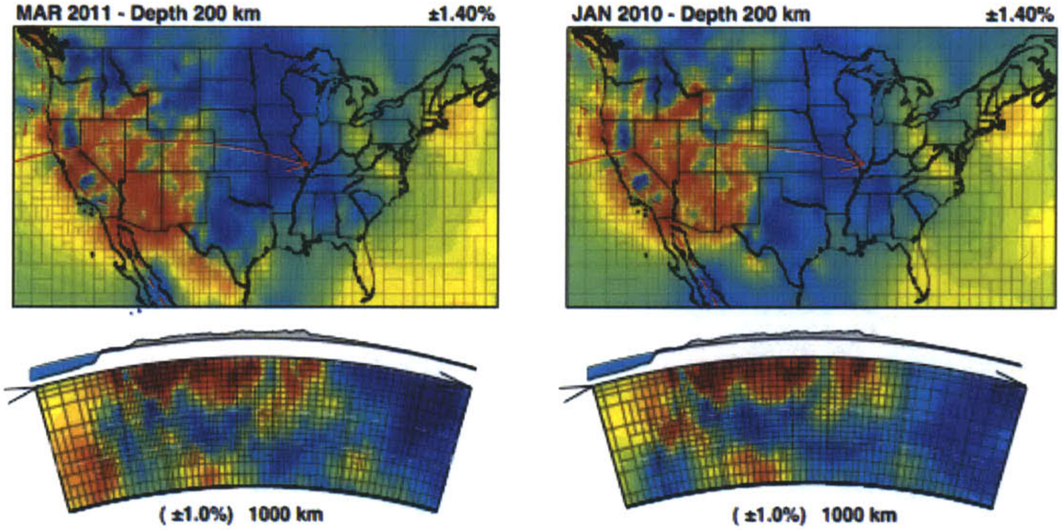

Figure D-2: Illustration of grid refinement. Map views at 200 km depth and mantle cross sections illustrating the grids used for the parameterization of the 2010 and 2011 models (on the right and left, respectively). The red arrow indicates the location of the cross-section. Grid spacing is representative of the adequate raypath density within each cell.

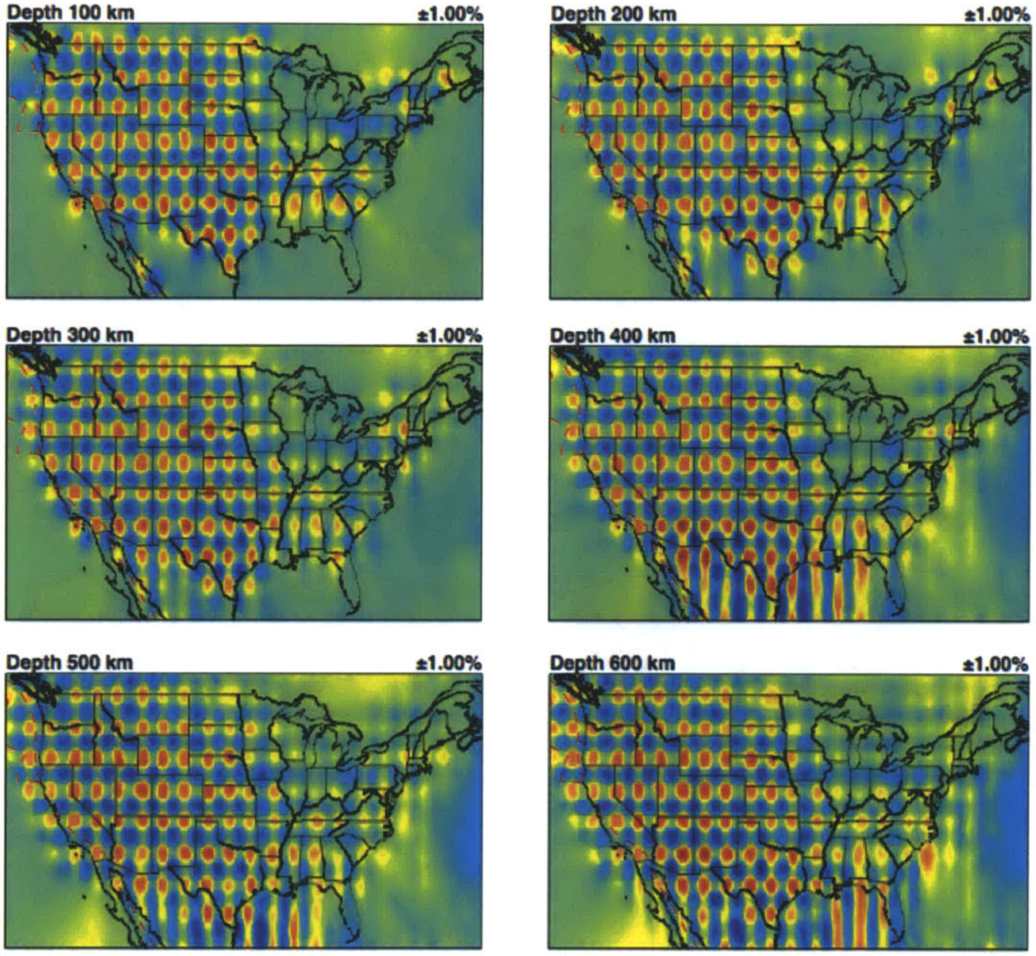

Figure D-3: Checker-board resolution using the current full dataset. With the current parameterization, the data used in the March 2011 model update resolves structural features on a lateral scale of 3° by 3° (that is, around 300 x 300 km) beneath the current footprint of the USArray Transportable Array.

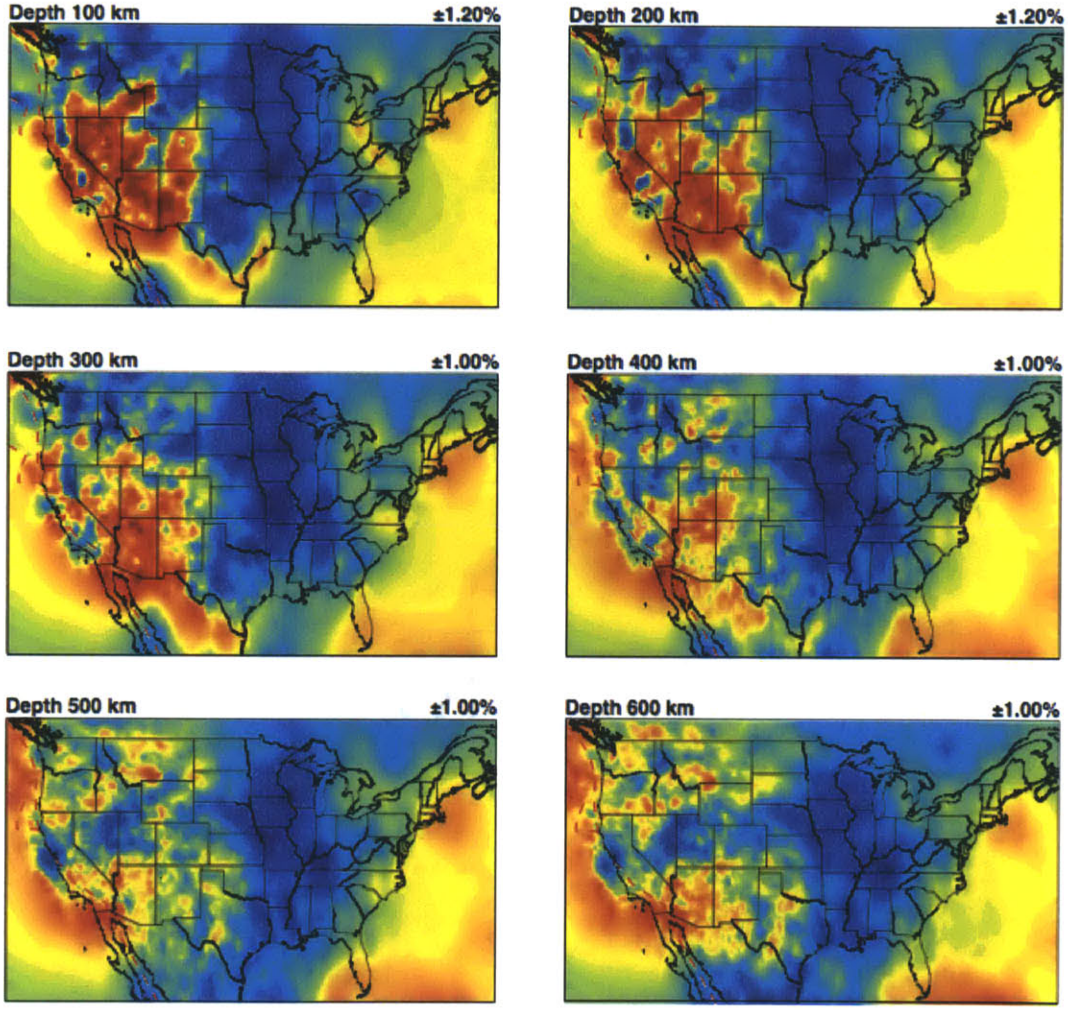

Figure D-4: Lateral variations in *P* wavespeed according to model MITP_USA_2011MAR at 100, 200, 300, 400, 500, and 600 km depth in the mantle beneath North America.

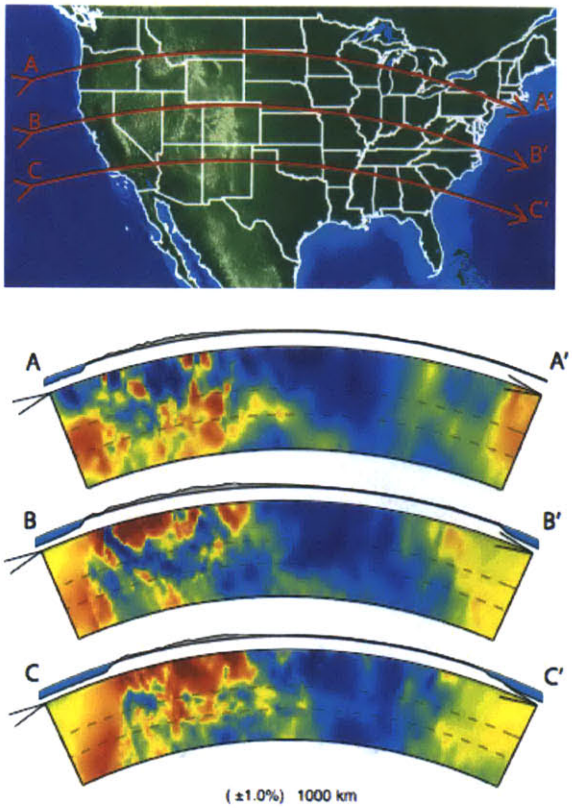

Figure D-5: Cross-sections through MITP_USA_2011MAR. Note that the eastern parts of the cross-sections remains poorly sampled by the current data. Notable in this model is (1) refinement of high velocity anomaly related to the continental root beneath the Great Plains and (2) better resolution between the root and fragments of the Farallon slab in the transition zone.

Appendix E

USArray P-wave Model Update January 2013[1]

E.1 Introduction

As of January 2013, the Transportable Array of USArray (*http://www.iris.edu/USArray/*), the seismological component of EarthScope (*http://www.earthscope.org/*), has extended east of the Great Plains and into the Midwest and Gulf Coast regions, offering routinely processed data for traveltime inversions in regions where little data was previously available. In previous research notes (Burdick et al., 2008, 2009, 2010, 2012) we presented 3-D tomographic models of mantle *P*-wavespeed from global and USArrayTA traveltime data recorded through November 2007, December 2008, January 2010, and March 2011 respectively. Here we present our global model updated with USArrayTA data through January 2013. As before, we make the new model, MITP_USA_2013JAN, available as an electronic supplement. Full interpretation of the 3-D tomographic model is beyond the scope of this brief research note.

---

[1] Published as: Burdick, S., van der Hilst, R. D., Vernon, F. L., Martynov, V., Cox, T., Eakins, J., Karasu, G. H., Tylell, J., Astiz, L., Pavlis, G. L., 2014. Model update January 2013: Upper mantle heterogeneity beneath North America from traveltime tomography with global and USArray Transportable Array data, *Seismological Research Letters*, In press

E.2 Methodology

A full description of the tomographic method used here can be found in Li et al. (2008) and Burdick et al. (2008), but we include a brief summary. We perform global inversions of *P*-wave traveltime residuals using an adaptable grid with a minimum grid spacing of 0.35° × 0.35°× 45 km within 10° of the USArrayTA footprint and 1.4° × 1.4°× 45 km outside. Grid cells are merged into larger ones in poorly sampled mantle volumes. The data included in the inversion consist of ~10 million *P*-wave residuals from the International Seismological Centre and the National Earthquake Information Center which are processed using the algorithms developed by Engdahl et al. (1998), and the database of USArrayTA *P*-wave residuals picked by the Array Network Facility (available online at ANF site). For each update we refine the grid in response to the addition of raypaths associated with new USArrayTA data picks. The tomographic inversion is linearized using the 1-D reference model *ak135* (Kennett et al., 1995). Wavespeed variations represented in model MITP_USA_2013JAN are given as percent difference from the average wavespeed at each depth in *ak135.*

E.3 What is new?

The January 2013 update of the USArrayTA dataset includes ~800,000 new P-wave travel time residuals from around 4,700 teleseismic events mostly occurring between March 2011 and January 2013. The updated set includes data recorded at 415 new USArrayTA stations (Figure 1) and new data from continuously recording stations elsewhere, particularly in the western States. The total number of USArrayTA picks used in the inversion now stands at ~2,560,000. The expansion of the Transportable Array brings the data coverage in the Great Plains region close to parity with that in the west and begins to improve coverage in regions as far east as the Appalachian Range where data in the global catalog is sparse.

Cognizant of the shortcomings of checkerboard tests as a diagnostic tool for assessing spatial resolution, we use them nonetheless to obtain a qualitative measure of the

mantle volumes where data coverage is adequate for resolving structure at a specified spatial wavelength. For this purpose we define the resolving power, R, at all points in the models by comparing the recovered checkerboard model, m, to the input checkerboard, m_0:

$$R = \frac{((m - m_0)^T W (m - m_0))^{1/2}}{(m_0^T W m_0)^{1/2}} \tag{E.1}$$

where W is a function that adds weighted contributions from adjacent cells, chosen here as a Gaussian with width on the order of the checker size. We consider the model resolved if R exceeds a threshold value. A threshold value of R = 0.7 was used for the resolution contours in Figures 2-5. Figure 2 suggests that the data generally resolve model features of the order of 1.5° by 1.5° ($\sim$150 km by 150 km) beneath the USArray TA footprint. Resolution expands eastward with depth, and we begin to resolve structure in the mantle transition zone beneath the eastern margin.

The new model grid (shown in Figure 3) is adapted based on expanded coverage provided by the new data. Compared with the 2011 inversion, the most significant grid refinements center around (i) the shallow mantle beneath the northern Great Plains and the central Gulf Coast (due to continued data accumulation at stations installed at the time of the previous update) and the Midwest and eastern Gulf coast (due to data from new station locations) and (ii) the mantle transition zone beneath the Midwest and Appalachia.

Figures 4 and 5 depict mantle heterogeneity according to the latest model update. To the west of the Great Plains, the addition of a year's worth of new data has not had a great effect on the tomographic image of mantle heterogeneity, but the additional ray paths have refined certain features at transition zone depths and below. Shallow mantle structures related to subduction on the western margin continue to improve with continued data collection. The definition between presumed Farallon slab fragments and the fast structure associated with the craton appears better-defined and more continuous than in previous model updates. Beneath the Midwest and the Gulf Coast, the new data improve constraints on mantle heterogeneity at all depths. The Midcontinent Rift System leaves a slight low velocity signature from Lake Superior to Iowa at depths down to 100 km. The New Madrid Fault Zone and the Reelfoot Rift show as strong slow anomalies and Ozark Plateau as a fast structure. Thanks to the equal coverage provided the Transportable Array, it is apparent that the variability of the structure in the craton is less pronounced than in the tectonically active west, although sharp variations exist between the Midwest and the Gulf region.

E.4 Concluding Remarks

In this brief research note we present the latest MIT USArrayTA *P* model. This model includes more than 2,560,000 *P*-wave traveltime residuals (from 2004 through January 2013) obtained from nearly 1600 USArrayTA seismograph sites. A year's worth of new traveltime data has improved the resolution of the model, particularly in the Midwest and Great Lakes regions and in the Gulf lowlands where little global data was available previously. Beneath the center of the continent, the data continue to define the craton and now reveal it to be more uniform than in the west, but with well defined boundaries.

Model MITP_USA_2013JAN and scripts for making horizontal and vertical cross-sections through it are available as an electronic supplement to this research note. ANF phase data are also available to the community as CSS monthly files at *http://anf.ucsd.edu/tools/events/download.php* or at the IRIS DMC thorough their Product section at *http://www.iris.edu/dms/products/.*

E.5 Acknowledgements

The authors thank the National Science Foundation for continued funding of the Earth-Scope program, the USArray team for their superb efforts in array installation and data quality control, and the Incorporated Research Institutions for Seismology for continued excellence and leadership in data storage and dissemination. The construction and dissemination of our model updates is supported by NSF grant EAR-0951901.

Bibliography

Burdick, S., Li, C., Martynov, V., Cox, T., Eakins, J., Mulder, T., Astiz, L., Vernon, F. L., Pavlis, G. L., & van der Hilst, R. D., 2008. Upper mantle heterogeneity beneath North America from travel time tomography with global and USArray Transportable Array data, *Seismological Research Letters*, **79**, 384–390.

Burdick, S., Hilst, R. D., Vernon, F., Martynov, V., Cox, T., Eakins, J., Mulder, T., Astiz, L., , & Pavlis, G., 2009. Model update December 2008: Upper mantle heterogeneity beneath North America from travel time tomography with global and USArray Transportable Array data., *Seismological Research Letters*, **80**, 638–645.

Burdick, S., van der Hilst, R. D., Vernon, F. L., Martynov, V., Cox, T., Eakins, J., Karasu, G. H., Tylell, J., Astiz, L., & Pavlis, G. L., 2010. Model update January 2010: Upper mantle heterogeneity beneath North America from traveltime tomography with global and USArray Transportable Array data, *Seismological Research Letters*, **81**(5), 689–693.

Burdick, S., van der Hilst, R. D., Vernon, F. L., Martynov, V., Cox, T., Eakins, J., Karasu, G. H., Tylell, J., Astiz, L., & Pavlis, G. L., 2012. Model update March 2011: Upper mantle heterogeneity beneath North America from traveltime tomography with global and USArray Transportable Array data, *Seismological Research Letters*, **83**(1), 23–28.

Engdahl, E. R., van der Hilst, R., & Buland, R., 1998. Global teleseismic earthquake relocation with improved travel times and procedures for depth determination, *Bulletin of the Seismological Society of America*, **88**(3), 722–743.

Kennett, B. L. N., Engdahl, E. R., & Buland, R., 1995. Constraints on seismic velocities in the Earth from travel-times, *Geophysical Journal International*, **122**(1), 108–124.

Li, C., van der Hilst, R. D., Engdahl, E. R., & Burdick, S., 2008. A new global model for P wave speed variations in Earth's mantle, *Geochemistry Geophysics Geosystems*, **9**, Q05018.

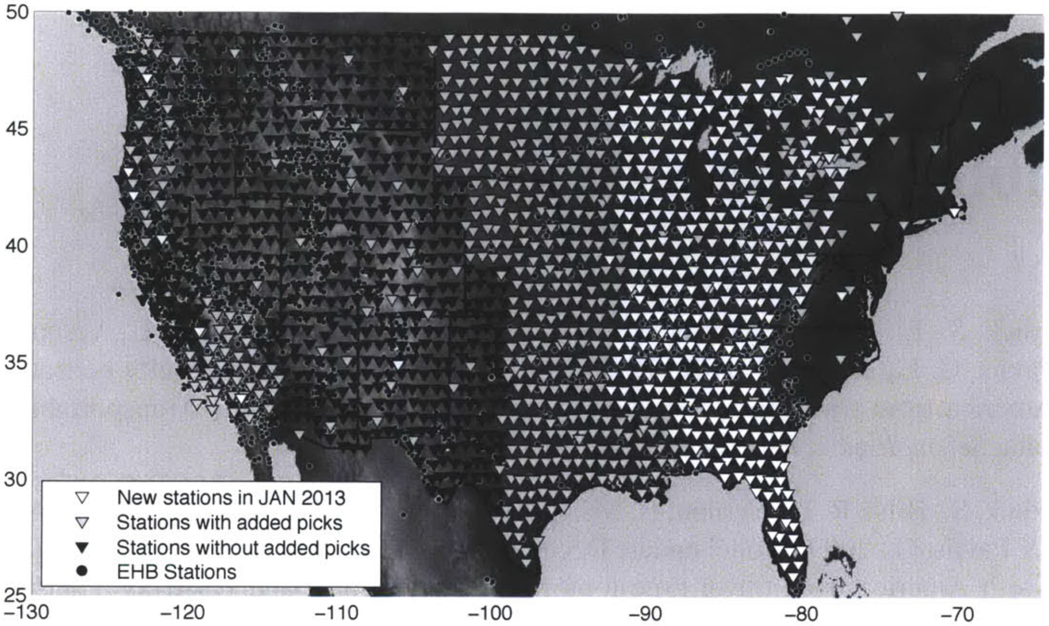

Figure E-1: Geographical distribution of seismograph stations in and around the United States from which data is used. Black dots represent stations contributing to the EHB dataset; the worldwide station distribution is depicted in Burdick *et al.* (2008) or Li *et al.* (2008). Black and gray triangles represent USArrayTA station locations from the previous model update for data through March 2011 (Burdick *et al.* 2012). Gray stations have additional picks made after the previous update while black stations do not. White triangles represent the new TA stations included in the data set.

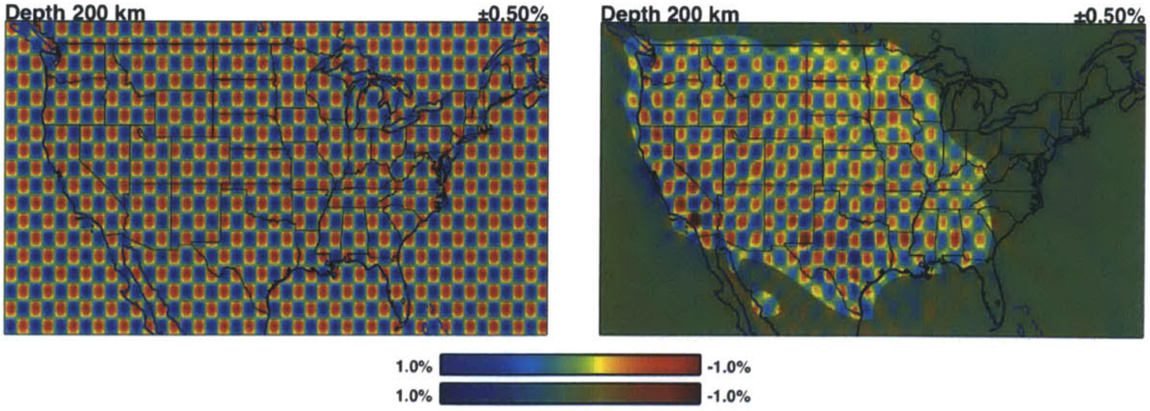

Figure E-2: Checkerboard resolution were used to determine areas of the model with lateral heterogeneity on the scale of 1.5° by 1.5° (that is, around 150 x 150 km.) Left: true checkerboard model at 200 km depth. Right: checkerboard pattern recovered by inversion. The shaded area ($R = 0.7$) represents parts of the model where 1.5° resolution is unavailable at this depth.

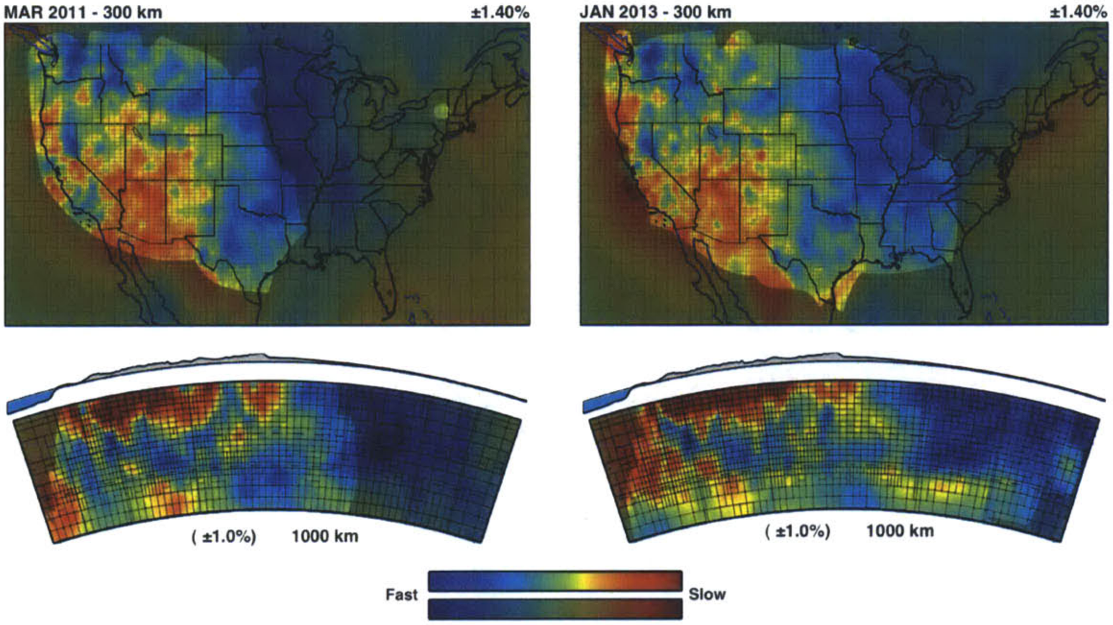

Figure E-3: Illustration of grid refinement. Map views at 200 km depth and mantle cross sections illustrating the grids used for the parameterization of the 2011 and 2013 models (on the right and left, respectively). Cross sections run at 40°N from 82 to 128°W. Grid spacing is representative of the adequate raypath density within each cell. The unshaded areas show where we are able to resolve structures on the order of 1.5° as determined by checkerboard resolution tests.

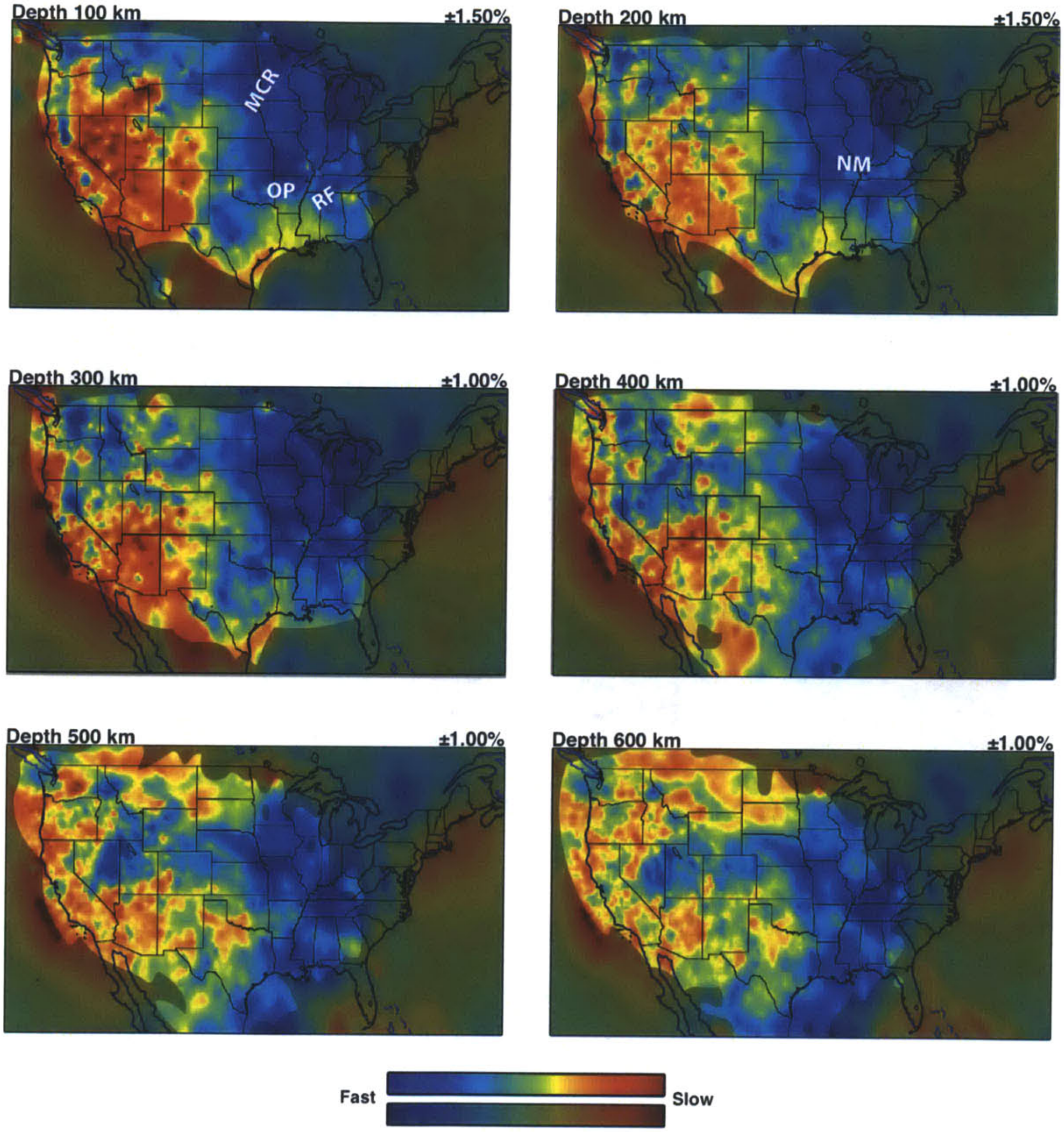

Figure E-4: Lateral variations in *P* wavespeed according to model MITP_USA_2013JAN at 100, 200, 300, 400, 500, and 600 km depth in the mantle beneath North America. Features of note Midcontinent Rift (MCR), Ozark Plateau (OP), Reelfoot Rift (RF), and New Madrid Seismic Zone (NM) are marked.

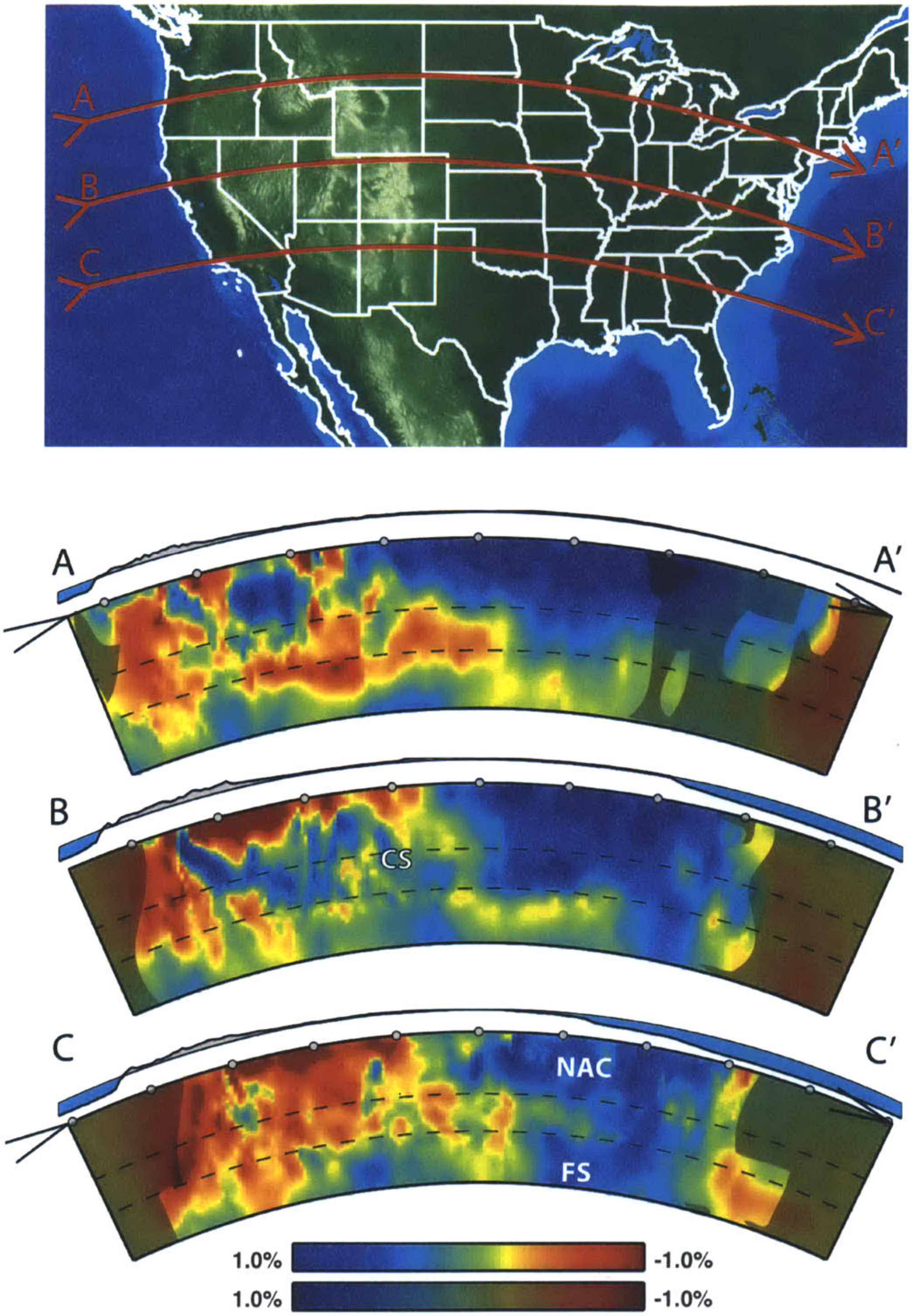

Figure E-5: Cross-sections through MITP_USA_2013JAN down to 1000 km. Dashed lines represent 410 km and 660 km depth. Note that the eastern parts of the cross-sections remains poorly sampled by the current data. Notable in this model is (1) refinement of high velocity anomaly related to the North American cratonic root (NAC) beneath the center of the continent and (2) better resolution between the root and the more heterogeneous mantle, including fragments of the ancient slab (Cascadian Slab - CS, Farallon Slab - FS).